NASA Contractor Report 4769

Numerical Investigation of Hot Gas Ingestion by STOVL Aircraft

S.P. Vanka
University of Illinois at Urbana-Champaign, Urbana, Illinois

Prepared under Grant NAG3–1026

National Aeronautics and
Space Administration

Lewis Research Center

January 1998

Available from

NASA Center for Aerospace Information
800 Elkridge Landing Road
Linthicum Heights, MD 21090-2934
Price Code: A06

National Technical Information Service
5287 Port Royal Road
Springfield, VA 22100
Price Code: A06

Table of Contents

1. Introduction

This report compiles the various research activities conducted under the auspices of the NASA grant NAG3-1026, "Numerical Investigation of Hot Gas Ingestion by STOVL Aircraft" during the period of April 1989 to April 1996. The effort involved the development of multigrid based algorithms and computer programs for the calculation of the flow and temperature fields generated by Short Take-off and Vertical Landing (STOVL) aircraft while hovering in ground proximity. Of particular importance has been the interaction of the exhaust jets with the head wind which gives rise to the hot gas ingestion process. The objective of new STOVL designs is to reduce the temperature of the gases ingested into the engine.

The present work describes a solution algorithm for the multi-dimensional elliptic partial differential equations governing fluid flow and heat transfer in general curvilinear coordinates. The solution algorithm is based on the multigrid technique (Brandt [1,21, Vanka [3], Vanka et al. [4] and Sockol [5]) which obtains rapid convergence of the iterative numerical procedure for the discrete equations. Initial efforts were concerned with the solution of the Cartesian form of the equations. This algorithm was applied to a simulated STOVL configuration in rectangular coordinates (Fricker, Holdeman and Vanka [15]). In the next phase of the work, a computer code for general curvilinear coordinates was constructed. This was applied to model STOVL geometries on curvilinear grids. The code was also validated in model problems. In all these efforts, the standard k-ε model (Launder and Spalding [6])was used.

2. Problem Considered

The ingestion of hot gases into the engine inlets is an important consideration in the design and operation of Short Take-off and Vertical Landing (STOVL) aircraft hovering in ground proximity. Such an ingestion can cause significant problems for the engine performance including reduced thrust and compressor stalls. These problems involve many hazards for the pilots including very hard landings.

A number of interesting fluid dynamic effects have been identified when the lift jets of STOVL aircraft impinge on a ground surface. First, as the lift jets expand, they entrain the surrounding fluid, causing a negative pressure underneath the fuselage and a loss in lift. As the jets impinge on the ground and spread radially outwards, the exhaust jets further entrain external fluid and increase the loss in lift. In a multiple-jet aircraft such as the McDonnell Aircraft Company Model 279-3C, these exhaust jets collide with each other and turn upwards to form an up wash fountain, as shown in Figure 1. This fountain flow has two major effects on the STOVL aircraft

dynamics. First, an increase in lift force is caused when the fountain impinges on the aircraft fuselage. The recovery in lift is a positive effect of the up wash flow. However, this impinging fluid can also flow along the fuselage surface and eventually make its way into the engine inlets, which is the primary source of hot gas ingestion. Because the temperature of the fountain flow is much greater than that of the ambient air, its ingestion by the engine can reduce the power and cause thermal stresses in engine components. In addition to the fountain flow, Figure 1 also shows another mechanism for the hot gas ingestion resulting from the interaction of the forward-moving exhaust jet with the head wind. When the head wind and the exhaust jet collide, a stagnation region is formed, and the exhaust jet is turned into a ground vortex. This ground vortex can subsequently be re- ingested by the engine, resulting in a further loss in power. Far field hot gas ingestion is characterized by a strong dependence on head wind velocity and aircraft height. It can be recognized that the overall flow field governing these fluid dynamic interactions is strongly three-dimensional, as well as turbulent.

The objective of this study is to develop a computational capability to investigate flow fields generated by the impinging lift jets in the presence of cross flow, as applied to the STOVL flow geometry. Numerical simulation of the complete STOVL aircraft flow field requires the solution of nonlinear partial differential equations that govern the transport of mass, momentum, and heat in three dimensional space with boundary conditions that describe the lift jets, the aircraft geometry, and the head wind.

In reality, the flows of practical relevance are almost always turbulent; this means that the fluid motion is highly unsteady and three-dimensional. Due to these complexities, the turbulent motion and the heat and mass-transfer phenomena associated with it are extremely difficult to describe and thus to predict theoretically. Yet, one of the basic tasks of fluid engineering is to predict fluid flow phenomena. Due to the fact that "predictions" by way of experiments are usually very expensive, calculation methods are in demand.

A complete simulation of a turbulent flow requires the solution of the time dependent Navier- Stokes equations. Such a simulation is referred to as a direct numerical simulation (DNS) (Orszag and Patterson [7]). A direct numerical simulation is capable of resolving the temporal and spatial dependencies of the turbulent flow field. However, the ability to resolve the significant time and length scales is achieved at the cost of computational effort. As an example, a fully turbulent isothermal channel flow calculation using a DNS required 250 hours of CPU time on a Cray X-MP super computer (Kim et al. [8]). At present time, DNS is not a viable option for the solution of practical flow fields.

The solution of time averaged equations is currently the most widely used means of simulating an engineering flow problem [6]. In solving a set of averaged equations, a temporally and spatially resolved solution is replaced by a stochastic description of the flow. The dependent variables of the governing equations are time averaged quantities.

The solution of averaged equations is obtained only after certain closure hypotheses have been invoked. The closure hypotheses of turbulence models relate the correlation between the mean fluctuations (Reynolds stresses) to the time averaged flow variables. The degree of sophistication of this closure is dependent on the flow fields which are to be studied. A review of the various models which are in use for predicting internal flows is given by Nallasamy [9]. For wall bounded flows, Patel et al. [10] give an analysis of various low Reynolds number k-ε turbulence models. A review of Reynolds stress models is given by Speziale [11]. The standard k-ε turbulence model is used in the current study.

3. Objectives of Current Research

The scope of the current research project was to develop efficient computational techniques for elliptic fluid flow equations and apply them for studying the mechanisms and extent of hot gas ingestion by Short-Take-off and Vertical Landing (STOVL) aircraft. The efficient computational technique was based on the solution of the Reynolds-averaged equations by a multigrid technique. In a multigrid procedure, in contrast with a single grid procedure, several levels of fine and coarse grids are used to discretize the partial-differential equations. The solution of the discrete equations is sought on the finest grid, but use is made of the coarse grids to accelerate the solution process. The coarse grids are also used to progressively generate better initial guess for the finer grid.

The general objective of the present research was to develop a computer code capable of simulating flow in complex geometries with embedded blocked regions (obstacles and baffles) as well as arbitrary locations where mass and momentum can be injected. These features are necessary to simulate the STOVL configuration and the dynamic interactions occurring during the hovering stage. The construction of the eventual code included an intermediate stage of considering a rectangular (Cartesian) geometry and validation of the algorithm in model problems.

4. Present Contribution

During the course of this research, several versions of the computational algorithm were developed and tested. Initially, a version limited to rectangular coordinates was developed and applied to compute twin-jet impingement (Pegues and Vanka [12]) and flow over a model STOVL aircraft (Tafti and Vanka [13,14]). This version was subsequently used by Fricker, Holdeman and Vanka [15] to study the effects of geometrical and flow parameters on the hot gas ingestion.

The curvilinear code development consisted of first developing an algorithm based on collocated arrangement of the variables. The collocated arrangement has several advantages over other formulations of curvilinear grid equations. The multigrid technique was developed for collocated curvilinear grids as a part of this study. The code and the algorithm were validated in a number of model problems as well as in a STOVL configuration (Smith [16], Smith and Vanka [17], and Smith et al. [18]). However, during further trials with this code in more realistic STOVL configurations, difficulties related to convergence at the end of the calculation were encountered. This was attributed to the complex nature of the multigrid cycling procedure on collocated grids.

As a result, a new staggered arrangement based on previous work by Maliska and Raithby [19] was considered. This scheme was subsequently developed for a multigrid sequence and validated in complex flows (Cope et al. [20], Wang et al. [21] and Wang [22]). Based on the success of these calculations, the STOVL calculations were repeated with this method. However, similar difficulties as encountered with the collocated arrangement were also encountered with this arrangement.

The STOVL problem has several complexities from computational viewpoint that were probably the reason why good performance was not observed in this flow while expected fast rates of convergence were observed in other fairly complex flows. The specific issues of STOVL are:

a) large cell aspect ratios are necessary to represent the large stream wise extent of the flow domain;

b) large rates of strain and turbulence production are encountered at the impingement sites of the jets resulting in questionable performance of the wall-functions;

c) large pressure build-up at stagnation regions (of jets) resulting in severe pressure gradients at the bottom boundary and inconsistencies from pressure extrapolation to the walls;

d) large-scale unsteady behavior of the jets in the impingement region causing difficulties due to representation as a steady flow.

Further research is needed to address these issues and to identify the precise cause for these convergence difficulties. To this end, methods based on unstructured triangular grids may be more beneficial. Also, unsteady calculations in the context of Very Large Eddy Simulations (VLES) may appear to be promising for future studies.

5. Thesis and Reports from this Grant

Theses

1. Smith, K. M. (1992) "Multigrid Calculation of Internal Flows in Complex Geometries", Master's Thesis, University of Illinois at Urbana-Champaign.

2. Wang, G. (1994) "Numerical Simulations of STOVL Hot Gas Ingestion in Ground Proximity Using a Multigrid Solution Procedure", Master's Thesis, University of Illinois at Urbana-Champaign.

Papers and Presentations

1. Pegues, W. J. and Vanka, S. P. (1990) "Numerical Study of Twin-Jet Impingement Upwash Flow", Forum on Turbulent Flows, ASME Spring Meeting of the Fluid Engineering Division, vol. 94, pp. 97-103.

2. Tafti, D. K., and Vanka, S. P. (1990) "Hot Gas Environment Around STOVL Aircraft in Ground Proximity, Part 2: Numerical Study", AIAA-90-2270, AIAA/SAE/ASME/ASEE 26th Joint Propulsion Conference, July 16-18, Orlando, Florida.

3. Fricker, D. M., Holdeman, J. D. and Vanka, S. P. (1992) "Calculations of Hot Gas Ingestion for a STOVL Aircraft Model", AIAA-92-0385, 30th Aerospace Sciences Meeting & Exhibit, January 6-9, Reno, Nevada, AIAA Journal of Aircraft, vol. 31, 1, pp. 236-242.

4. Smith, K. M. and Vanka, S. P. (1992) "Multigrid Calculation of Internal Flows in Complex Geometries", AIAA-92-0096, 30th Aerospace Sciences Meeting & Exhibit, January 6-9, Reno, Nevada.

5. Cope, W. K., Wang, G. and Vanka, S. P. (1994) "A Staggered Grid Multilevel Method for the Simulation of Fluid Flow in 3-D Complex Geometries", AIAA-940778, 32nd Aerospace Sciences Meeting & Exhibit, January 10-13, Reno, NV.

6. Wang, G., Cope, W. K. and Vanka, S. P. (1994) "Multigrid Calculations of Twin Jet Impingement with Crossflow: Comparison of Segregated and Coupled Relaxation Strategies", Advances in Computational Methods in Fluid Dynamics, ASME Fluids Engineering Division Summer Meeting, vol. 196, pp. 233-244.

Journal Articles

1. Tafti, D. K., and Vanka, S. P. (1990) "Hot Gas Environment Around STOVL Aircraft in Ground Proximity, Part 2: Numerical Study", Journal of Aircraft, vol. 29, pp. 20-27.

2. Smith, K. M., Cope, W. K. and Vanka, S. P. (1993) "A Multigrid Procedure for Three-Dimensional Flows on Non-Orthogonal Collocated Grids", International Journal for Numerical Methods in Fluids, vol. 17, pp. 887-904.

6. References

1. Brandt, A., (1977) "Multi-Level Adaptive Solutions to Boundary-Value Problems" Mathematics of Computation, vol. 31, no. 138, pp. 333-390.

2. Brandt, A., (1980) "Multilevel Adaptive Computations in Fluid Dynamics", AIAA Journal, vol. 18, no. 10, pp. 1165- 1172.

3. Vanka, S. P. (1986) "Block Implicit Multigrid Calculation of Navier Stokes Equations in Primitive Variables", Journal of Computational Physics, vol. 65, pp. 138- 158.

4. Vanka, S. P., Krazinski, J. L., and Nejad, A. S., (1989) "Efficient Computational Tool for Ramjet Combustor Research", Journal of Propulsion and Power, vol. 5, no. 4, pp. 431-437.

5. Sockol, P. M., (1993) "Multigrid Solution of the Navier-Stokes Equations on Highly Stretched Grids", International Journal for Numerical Methods in Fluids, vol. 17. pp. 543-566.

6. Launder, B. E. and Spalding, D. B. (1974) "The Numerical Computation of Turbulent Flows", Computer Methods in Applied Mechanics and Engineering, vol. 3. pp. 269- 289.

7. Orszag, S. A., and Patterson, G. S. Jr. (1972) "Numerical Simulation of Three Dimensional Homogeneous Isotropic Turbulence", Phys. Rev. Lett., vol. 28, pp. 76- 79.

8. Kim, J., Moin. P., and Moser, R. (1987) "Turbulence Statistics in Fully Developed Channel Flow at Low Reynolds Number", Journal of Fluid Mechanics, vol. 177, pp. 133-166.

9. Nallasamy, M. (1987) "Turbulence Models and Their Applications to the Prediction of Internal Flows: A Review", Computers and Fluids, vol. 15. no. 2. pp. 151-194.

10. Patel, V. C., Rodi, W., and Scheuerer, G. (1985) "Turbulence Models for Near Wall and Low Reynolds Number Flows: A Review". AIAA Journal, vol. 23. no. 9. pp. 1308-1319.

11. Speziale, C. G. (1991) "Analytical Methods for the Development of Reynolds Stress Closures in Turbulence", Annual Review of Fluid Mechanics, vol. 23. pp. 107-157.

*12. Pegues, W. J. and Vanka, S. P. (1990) "Numerical Study of Twin-Jet Impingement Upwash Flow", Forum on Turbulent Flows, ASME Spring Meeting of the Fluid Engineering Division, vol. 94, pp. 97-103.

*13. Tafti, D. K., and Vanka, S. P. (1990) "Hot Gas Environment Around STOVL Aircraft in Ground Proximity, Part 2: Numerical Study", AIAA-90-2270, AIAA/SAE/ASME/ASEE 26th Joint Propulsion Conference, July 16-18, Orlando, Florida.

*14. Tafti, D. K., and Vanka, S. P. (1990) "Hot Gas Environment Around STOVL Aircraft in Ground Proximity, Part 2: Numerical Study", Journal of Aircraft, vol. 29, pp. 20-27.

*15. Fricker, D. M., Holdeman, J. D. and Vanka, S. P. (1992) "Calculations of Hot Gas Ingestion for a STOVL Aircraft Model", AIAA-92-0385, 30th Aerospace Sciences Meeting & Exhibit, January 6-9, Reno, Nevada, AIAA Journal of Aircraft, vol, 31, 1, pp. 236-242.

*16. Smith, K. M. (1992) "Multigrid Calculation of Internal Flows in Complex Geometries", Master's Thesis, University of Illinois at Urbana-Champaign.

*17. Smith, K. M. and Vanka, S. P. (1992) "Multigrid Calculation of Internal Flows in Complex Geometries", AIAA-92-0096, 30th Aerospace Sciences Meeting & Exhibit, January 6-9, Reno, Nevada.

*18. Smith, K. M., Cope, W. K. and Vanka, S. P. (1993) "A Multigrid Procedure for Three-Dimensional Flows on Non-Orthogonal Collocated Grids", International Journal for Numerical Methods in Fluids, vol. 17, pp. 887-904.

19. Maliska, C. R. and Raithby, G. D. (1984) "A Method for Computing Three Dimensional Flows using Non-orthogonal Boundary Fitted Coordinates", International Journal for Numerical Methods in Fluids, vol. 4. pp.519-537.

*20. Cope, W. K., Wang, G. and Vanka, S. P. (1994) "A Staggered Grid Multilevel Method for the Simulation of Fluid Flow in 3-D Complex Geometries", AIAA-940778, 32nd Aerospace Sciences Meeting & Exhibit, January 10-13, Reno, NV.

*21 Wang, G., Cope, W. K. and Vanka, S. P. (1994) "Multigrid Calculations of Twin Jet Impingement with Crossflow: Comparison of Segregated and Coupled Relaxation Strategies", Advances in Computational Methods in Fluid Dynamics, ASME Fluids Engineering Division Summer Meeting, vol. 196, pp. 233-244.

*22. Wang, G. (1994) "Numerical Simulations of STOVL Hot Gas Ingestion in Ground Proximity Using a Multigrid Solution Procedure", Master's Thesis, University of Illinois at Urbana-Champaign.

* Publications from this project

HOT GAS INGESTION PHENOMENA

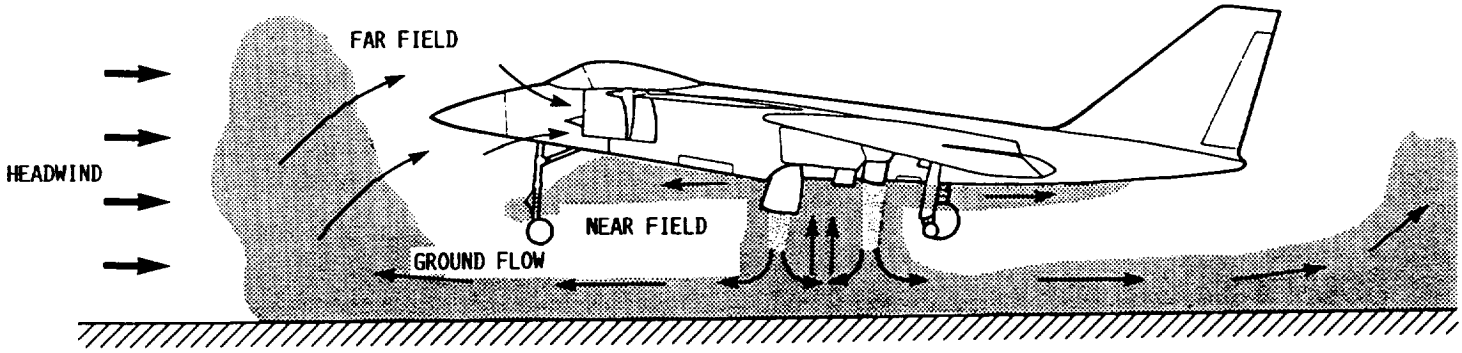

APPENDIX A

NUMERICAL STUDY OF TWIN-JET IMPONGEMENT UPWASH FLOW

NUMERICAL STUDY OF TWIN-JET IMPINGEMENT UPWASH FLOW

W. J. Pegues and S. P. Vanka
Department of Mechanical and Industrial Engineering
University of Illinois at Urbana-Champaign
Urbana, Illinois

Abstract

Two horizontally spaced jets impinging normally on a flat surface create a fountain upwash flow due to the collision of the radially flowing wall jets. This fountain flow is of importance to the dynamics and propulsion of Short Take-off and Vertical Landing(STOVL) aircraft . The fountain flow influences the lift forces on the aircraft and the ingestion of hot gases and debris by the engine inlet. In this paper, a multigrid based finite-difference numerical procedure has been applied to solve the equations governing this three-dimensional flow. The calculations have been performed using a reasonably fine finite-difference mesh and the results have been compared with experimental data of Saripalli (1985). The standard k-ε turbulence model has been used. Comparisons with experimental data reveal that while the mean velocities are predicted with reasonable accuracy, the turbulent kinetic energies are seriously in error. The reasons for this discrepancy could be the intense unsteadiness and large-scale structures of the flow in the near wall region, which can not be captured well by any Reynolds-averaged turbulence model.

Introduction

For the past three decades, there has been a significant amount of research into the understanding and predictability of the flow fields that govern the dynamics of Vertical Take-off and Landing (VTOL) aircraft (Mitchell, 1985 and Gilbert, 1984). The impingement of the lift jets on the ground produce a complex three-dimensional flow consisting of radial wall jets and an upwash flow. The upwash flow subsequently impinges on the fuselage and impacts the lift and moments on the aircraft. Also, part of the hot gases impinging on the fuselage make their way into the engine inlet and can cause thermal loading on the engine components (Kuhn, 1982; Mitchell, 1985 and VanOverbeke and Holdeman, 1988). Therefore, detailed studies of the fountain upwash flow are essential to avoid adverse effects due to the impinging lift jets. Also, the upwash flow presents itself as an interesting fluid flow problem from the viewpoint of basic fluid mechanics.

In recent years, several experimental and computational studies have been conducted to study the fluid mechanics of single and twin impinging jets. Agarwal (1983), Kuhn and Eshelman (1985) and Kotansky (1983) have provided reviews of current understanding and computation of these flow fields. Several complexities of the flow have been pointed out. Foremost of these is the three-dimensionality of the flow which makes numerical computations difficult and time consuming even on today's supercomputers. Also, flow visualization experiments(Kibens et. al.,1987) indicate that the jets and the fountain region are highly unsteady and are dominated by large scale turbulent structures. Thus, attempts to model the effects of turbulence through a Reynolds-averaged approach can be inaccurate and frustrating. In earlier works of Agarwal and Bower(1982) and Kotansky and Bower(1978), the flow was simplified to be two-dimensional and the governing equations were solved by a finite-difference calculation procedure. Turbulence models based on solution of partial-differential equations for turbulence kinetic-energy and another variable such as the turbulence dissipation rate have been used to represent the effects of turbulence. Similar computational studies have also been conducted by other researchers (e.g. Hwang et. al., 1990, and Mitchell, 1985). Despite the difficulties in accurately modelling turbulence, the Reynolds-averaged approach continues to be the preferred approach because time-accurate calculations of the unsteady flow are significantly more expensive (Childs and Nixon, 1986; Rizk and Menon, 1988 and Childs, 1990).

A primary difficulty in performing three-dimensional fluid flow calculations (Bower, et. al, 1979) is the inability to resolve the flow domain with enough mesh points such that the numerical errors in the solution are essentially negligible. In the present work, we have used a multigrid based calculation procedure to compute the three-dimensional flow field generated by the impingement of two horizontally-spaced jets. The multigrid technique possesses the advantage that the discretized elliptic partial differential equations can be solved in a relatively small number of iterations even when the mesh is significantly refined. Therefore, calculations with fine mesh resolutions can be performed in relatively small computer times leading to the possibility of an error free solution.The multigrid concept is explained in several earlier works (Brandt, 1984 and Hackbusch, 1985), and our implementation is documented in Vanka (1988), Vanka et.al. (1988) and Claus and Vanka (1990).

Flow Configuration

Recently, Saripalli and Kroutil (1985) and Saripalli (1981,1985) conducted detailed experiments on the twin jet impingement flow. Initially, flow visualization experiments were conducted in a closed rectangular tank with two water jets attached to a baffle plate (Fig. 1). The water jets impinged normally on the bottom of the tank and created a fountain upwash flow. Subsequently, a laser velocimeter was used to map the mean and fluctuating velocity components. The

effect of jet spacing and the height of the jets from the ground plane were also studied. Although the experiments were isothermal, these data provide valuable information towards developing and validating turbulence models for engineering calculation of STOVL aircraft flow processes under non isothermal conditions.

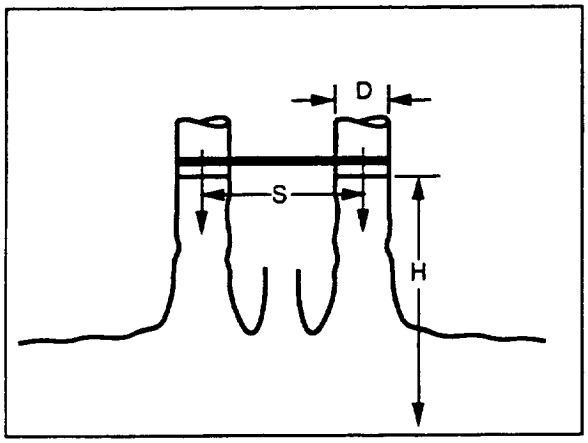

Fig.1 Sketch of the Flow Configuration

Equations and Solution Procedure

The equations governing a three-dimensional steady, elliptic flow of constant density and viscosity can be written as

$$\partial u_i/\partial x_i = 0 \qquad (1)$$

$$\partial/\partial x_j\,(u_i\,u_j) = -\,\partial p/\rho\partial x_i + \nu\,\partial/\partial x_j\,(\partial u_i/\partial x_j)\ ,\ i=1,3 \qquad (2)$$

where summation is implied by the repeated indices. u_i is the component of velocity in the x_i direction and p is the pressure. v is the molecular viscosity. In the Reynolds-averaged approach, the velocities are decomposed into mean and fluctuating components and a turbulence model is used to represent the correlations of the fluctuating velocities. The most popular of these models is the k-ε model and a large amount of research effort has been devoted to its development and validation. Higher order models based on stress transport equations (Launder, 1989) are also available, but at this stage further development efforts are needed before they are applied to three-dimensional flows such as the one considered here.

In the k-ε model, two other partial-differential equations are solved representing the transport of turbulence kinetic energy and its dissipation rate. The model assumes that the turbulent stresses can be related to the mean strain rates through a turbulent viscosity. This turbulent viscosity is evaluated from the distributions of turbulence kinetic energy and its dissipation rate. Validation of this model in a wide variety of flows has been summarized by Rodi (1984), amongst others. Although there are serious doubts on the validity of the assumptions made in deriving this model, it currently represents the best compromise for engineering flows.

Computational Details

The equations are discretized by a first/second order accurate hybrid differencing scheme (Spalding, 1972). Although higher order schemes can be used to improve the accuracy of the discretization, such schemes can be non conservative and may not provide the expected accuracy for complex recirculating flows (Vanka, 1987). In the current differencing scheme, the convective fluxes are discretized such that at high Peclet numbers (>2), the first order scheme is used, whereas for Peclet numbers < 2, the second order accurate central differencing scheme is used. This hybrid scheme currently appears to be the only robust scheme for incompressible, recirculating flows as other proposed schemes have been observed to cause difficulties in convergence and overshoots in the flow variables (Syed et. al., 1985).

The discrete equations are solved by a multigrid solution algorithm. A fine grid consisting of 64 x 32 x 32 finite-difference cells is used to represent the important flow domain. In the experiments of Saripalli (1985), the rectangular tank is closed at all the ends, except for a small outlet to remove the jet fluid. We represented this geometry by placing a baffle inside a rectangular solution domain and included the jets as mass injections to internal cells below the baffle. The jet fluid was extracted above the baffle as a mass and momentum sink. Only one-fourth of the total geometry was simulated because of symmetry about the spanwise mid-plane and the mid-plane of the jets.The jets were considered to be rectangular because it was not currently possible to represent mass injection from a circular orifice.

The multigrid calculation consisted of four grid levels starting from the coarsest grid of 8 x 4 x 4 cells. This grid was progressively doubled (mesh spacing is halved in each direction) to a 64 x 32 x 32 grid. The two jets were spaced nine jet diameters apart, corresponding to the first of the three tests of Saripalli. The jet was discretized with sixteen cells in the x-direction and eight cells in the z-direction. The fountain region between the jets was represented by thirty two cells in the x-direction. In the y-direction, a non-uniform grid with closer spacing in the wall region was used. The calculations were iterated until the sum of the absolute local mass residuals was less than one percent of the jet mass flow.

The multigrid procedure used here is identical to the one reported earlier (Vanka et. al, 1988). The inner relaxation of the continuity and momentum equations is performed simultaneously by a coupled Gauss-Seidel iterative procedure. The turbulence equations are solved decoupled from the momentum and continuity equations and interact with the flow equations through the turbulent viscosity. A Full Multigrid (FMG) algorithm is used in which the solution is initiated at the coarsest grid and progressively developed for finer grids. The nonlinear version of the multigrid procedure is used on any given grid level, with interpolations between grids dictated by a V-cycle. Details of these features are given in Vanka et. al., 1989.

Results

Figure 2 shows the observed convergence history of the mass residuals for S/D = 9.0 and H/D = 3.0 (H = height of jets; S = spacing of jets; and D = jet diameter). It can be seen that the procedure converges rapidly to a satisfactory solution, requiring approximately 80 iterations to reach the one percent level from the initial level of 300 percent. As a result of this superior rate of convergence, the calculations were completed in approximately 8 minutes on a CRAY-2 computer. Although the grid employed here has not been proven to provide error-free results, it is sufficient for conducting parametric studies as well as for any future studies with higher-order discretization schemes. Also, calculations with another finer grid level will be attempted in the near future.

A systematic comparison of the present calculations with data of Saripalli (1985) has been performed both in the jet and in the fountain regions. Saripalli measured the time-averaged mean velocities in the axial and radial directions of the jet and the fountain (his notations were interchanged in the jet and fountain regions). Also measured

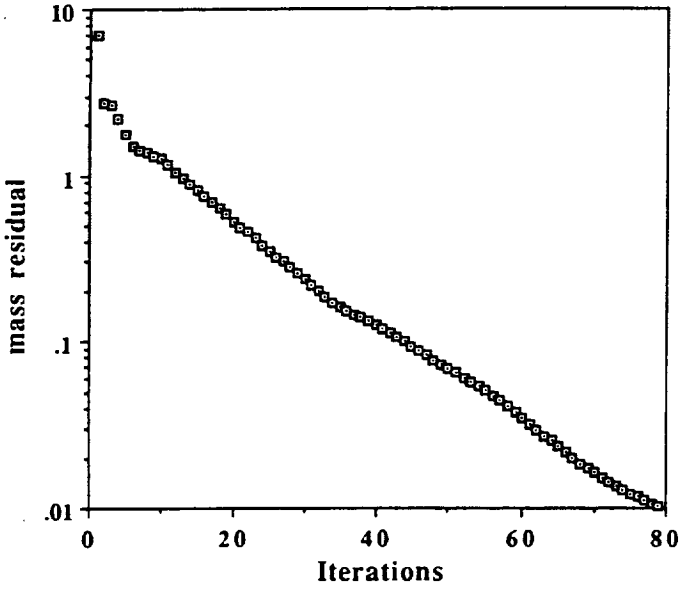

Fig.2 Convergence History for Sum of Mass Residuals

were the fluctuating components ($\overline{u'^2}$ and $\overline{v'^2}$) from which a turbulence kinetic energy could be derived (assuming that $\overline{w'^2}$ is equal to the average of $\overline{u'^2}$ and $\overline{v'^2}$). The turbulence kinetic energy from the solution of the partial differential equation was compared to this value.

Figure 3 provides a comparison of the profiles of axial velocity in the jet region at three different positions from the ground. The heights selected are closer to the ground because the flow does not develop much in the initial region and the agreement with the experiments is very good in that region. For the three different heights shown in Figure 3, we observe that the agreement at y/D = 1.0 is fairly good. The minor differences in the central core region and at the edges of the jet can probably be reduced by more accurate prescription of the inlet conditions and further mesh refinement. At y/D = 0.3, the calculated jet velocities are lower (considering the magnitude) in the core region and higher at the edges. This region is affected by the impingement region and the errors in predicting the latter are propagated upstream. Closer to the wall, there are appreciable differences, particularly to the left of the jet (on the other side of the fountain). It is necessary to point out that this region is affected by the way the boundary conditions are prescribed for extracting the jet mass. In the current calculations, the flow is extracted as a mass sink in the region above the baffle. This makes the flow turn upwards towards the mass sink, influencing the region left of the jet. However, in the region adjacent to the fountain, the calculated velocities show reasonable agreement.

Figure 4 compares the calculated radial velocities in the wall jet region with the measured values. At y/D = 1.0, the radial velocities are relatively small, and the qualitative nature of the velocity profile is accurately captured by the calculations. At y/D of 0.30, the flow on the fountain side is overpredicted but the flow on the free stream side is under-predicted. However, qualitatively, the profile is well predicted. At y/D of 0.05, the velocities are again under-predicted, implying that the wall jet profile is flatter than that in the experiments. This may either be due to insufficient grid refinement in the wall jet region or due to the inaccuracies in the turbulence model.

In Figure 5, the measured and calculated kinetic energies are compared. The trends observed for the velocities are also seen here, but the discrepancies in the near-wall region are much larger. The jet shear layer is fairly well captured at y/D of 1.0. However, at y/D of 0.30, the predicted profile of kinetic energy is flatter than the experiments and significant differences exist. The disagreement is even larger for y/D of 0.05. The experiments indicate large values of kinetic energies on both the fountain side and the free stream side of the jet. However, the calculations substantially under-predict these values, indicating a flat distribution of turbulence energy. Near the wall, the jet impingement region is very violent and unsteady (Childs and Nixon, 1986). This produces large turbulent fluctuations, which are reflected in the measurements as high turbulence kinetic energies. Such fluctuations are not well represented by a Reynolds-averaged turbulence model. Much of the discrepancy observed in the impingement region is believed to be due to the inherently large scale nature of the turbulent flow. However, some improvement in the results may be achieved if a finer mesh is used closer to the wall.

The velocity field in the fountain region is compared with experimental data, in Figures 6 and 7. Figure 6 shows that the horizontal velocity (u) is well predicted in the present calculations. These velocities are approximately 20 percent of the jet velocity, and the agreement is fairly good except at y/D of 0.05. For this location, the axial velocity close to the jet is under-predicted. The agreement in vertical velocity (v), shown in Figure 7 is better than that for the horizontal velocity. The location x/D of zero corresponds to the center of the fountain where the vertical velocity is largest. This value is well predicted. However, significant differences exist between the calculated and measured turbulence kinetic energies shown in Figure 8. The measurements show large values of turbulence kinetic energy in the center of the fountain region. This turbulence is produced by the collision of the two wall jets. The calculations performed with the k-ε model significantly under-estimate these energies. Significant differences exist at all three values of y/D. The disagreements observed in turbulence energies can not be improved easily by the standard k-ε model. Recent studies (Childs, 1990) indicate that several corrections which include effects of streamline curvature, anisotropy and large scale mixing are necessary before good predictions are possible. Alternatively, time accurate simulations which solve for the large scale structures may provide more hope in representing the physics of the flow.

In the present study, calculations for the other two sets of data of Saripalli (1985) in which the S/D and H/D are varied were also made and compared with the measured values. The agreement between the calculations and experiments is similar to that presented above. Therefore, for the sake of brevity, the other results are not presented here.

Summary

This paper demonstrates the applicability and potential of a multigrid procedure for efficiently solving the fountain upwash flow generated by the lift jets of Short Take-off and Vertical Landing(STOVL) aircraft. Numerical computations have been performed for the experimental configuration of Saripalli (1985) with a finite-difference grid consisting of 64 x 32 x 32 cells. Comparisons of the calculated velocities and turbulence energies reveal that while the velocities agree reasonably well with measured values, the turbulence kinetic energies are in significant error. Although some improvement can be achieved by further mesh refinement, it is believed that the fundamental cause for the disagreement may be the unsteadiness of the impingement region which can not be well represented by the Reynolds-averaged concept. Therefore, time-accurate simulations, based on the concept of simulating the large scale structures (LES) may be more appropriate for accurate calculations of this flow.

Acknowledgements

This study was supported by a grant from the NASA Lewis Research Center, Ohio. The authors wish to thank Dr. J. D. Holdeman for his encouragement during this study. Dr. Saripalli generously provided his experimental data in a tabular form for easy comparisons with our results. The computations were performed alternately on the CRAY-2 machines at the NASA Ames NAS facility and the National Center for Supercomputing Applications (NCSA) at the University of Illinois at Urbana-Champaign.

References

Agarwal, R.K., 1983, "Recent Advances in Prediction Methods for Jet-Induced Effects on V/STOL Aircraft", Recent Advances in Aerodynamics, Springer-Verlag, pp. 471-521.

Agarwal, R. K. and Bower, W.W., 1982, "Navier-Stokes Computations of Turbulent Compressible Two-Dimensional Impinging Jet Flowfields," *AIAA Journal*, Vol. 20, No. 5, pp. 577-584.

Brandt, A., 1984, "Multigrid Techniques: 1984 Guide with Applications to Fluid Dynamics", GMD-Studien Nr. 85.

Bower, W. W., Agarwal, R. K. and Peters, G. R., 1979, "A Theoretical Study of Two- and Three-Dimensional Impinging Jets," MDRL 79-22 .

Childs, R. E., and Nixon, D., 1986, "Unsteady Three-Dimensional Simulations of a VTOL Upwash Fountain," AIAA 86-0212.

Childs, R., 1990,"Turbulence Modeling for Impinging Jets," AIAA 90-0022, 28th Aerospace Sciences Meeting, January 8-11, Reno, NV.

Claus, R. W. and Vanka, S. P., 1990, "Multigrid Calculations of a Jet in Crossflow", AIAA-90-0444, 28th Aerospace Sciences Meeting, Reno, NV.

Gilbert, B. L., 1984, "An Investigation of Turbulence Mechanisms in V/STOL Upwash Flowfields," Grumman Aerospace Corporation Report, RE-688.

Hackbusch, W. , 1985, Multigrid Methods and Applications, Springer Verlag, Berlin.

Hwang, C., Yang, S., and Liu, J., 1990, "Numerical Investigations of Airfoil/Jet/Fuselage-Undersurface Flowfields in Ground Effect", AIAA-90-0597, 28th Aerospace Sciences Meeting,Reno, NV.

Kibens, V., Saripalli, K. R., Wiezen, R. W. and Kegelman, J. T., 1987, "Unsteady Features of Jets in Lift and Cruise Modes for VTOL Aircraft," SAE paper number 872359, International Power Lift Conference, Santa Clara, CA .

Kotansky, D. R., 1984, " Multiple Jet Impingement Flow Fields", Special Course on V/STOL Aerodynamics, AGARD Report, No. 710, pp. 7-1 to 7-48.

Kotansky, D. R. and Bower, W. W. , 1978, "A Basic Study of the VTOL Ground Effect Problem for Planar Flow," *Journal of Aircraft*, Vol. 15, vol. 15, No. 4, pp 214-221.

Kuhn, R. E., 1982, "Design Concepts for Minimizing Hot Gas Ingestion in V/STOL Aircraft," *Journal of Aircraft*, Vol. 19, no. 10, pp. 845-850.

Kuhn, R. E. and Eshelman, J., 1985, "Ground Effects on V/STOL and STOL Aircraft --- A Survey, " AIAA Paper, 85-4033, NASA TM-86825.

Launder, B. E., 1989, "Second-moment Closure: Present.... and Future ?," *Heat and Fluid Flow*, Vol. 10, 4, pp. 282-300.

Mitchell, K., 1985, "Proceedingss of the 1985 NASA Ames Research Center's Ground Effects Workshop," NASA CP-2462, NASA, Wasington, D.C.

Rizk, M. H. , and Menon, S., 1988 , "Large-eddy Simulations of Axisymmetric Excitation Effects on a Row of Impinging jets", Physics of Fluids, 31, 7, pp. 1892-1903.

Rodi, W., 1984, "Examples of Turbulence Model Applications", in Turbulence Models and Their Applications, Eyrolles, Paris, pp. 297-401.

Saripalli, K. R. and Kroutil, J. C., 1985, "A Novel Experimental Facility for Conducting Jet Impingement Studies Related to VTOL Aircraft", AIAA-85-0052, 23rd Aerospace Sciences Meeting, January, 14-17, Reno, NV.

Saripalli, K. R., 1981,"Visualization of Multi - Jet Impingement Flow," AIAA-81-1364, AIAA/SAE/ASME 17th Joint Propulsion Conference, July 27-29, Colorado Springs, Colorado.

Saripalli, K. R., 1985, "Laser Doppler Velocimeter Measurements in 3-D Impinging Twin-Jet Fountain Flows", *Turbulent Shear Flows 5*, Springer Verlag.

Spalding, D. B., 1972, " A Novel Finite-Difference Formulation for Differential Expressions Involving First and Second Derivatives," *International Journal for Numerical Methods in Engineering*, Vol. 4, pp. 551-559.

Syed, S. A., Chiapetta, L. M. and Gosman, A. D., 1985, "Error Reduction Program", PWA-5928-25, Pratt & Whitnet Aircraft, East Hartford, CT, NASA-CR-174776.

Vanka, S. P., 1987 "Study of Second Order Upwind Difference Scheme in Recirculating Flows," *AIAA Journal*, Vol. 25, pp. 1435-1444.

Vanka, S. P., 1989, "Analytical Studies of Three-Dimensional Combustion Processes", Aero Propulsion Laboratory Report, AFWAL-TR-88-2140.

Vanka, S. P., Krazinski, J. L. and Nejad, A. S., 1988, "An Efficient Computational Tool for Ramjet Combustor Research", AIAA-88-0060, 26th Aerospace Sciences Meeting, Reno, NV.

VanOverbeke, T. J. and Holdeman, J.D., 1988,"A Numerical Study of the Hot Gas Environment Around a STOVL Aircraft in Ground Proximity", AIAA-88-2882, AIAA/ASME/SAE/ASEE 24th Joint Propulsion Conference, Boston, Mass.

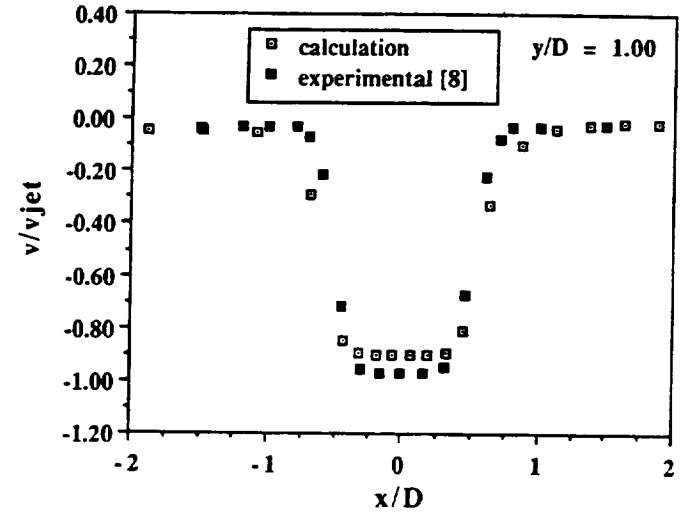

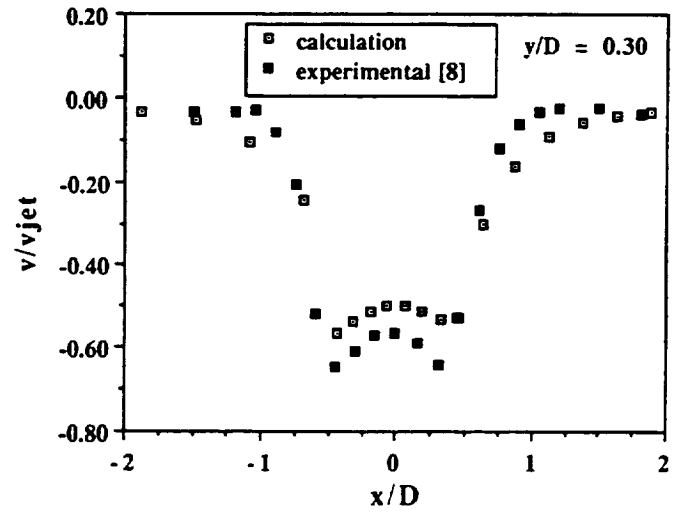

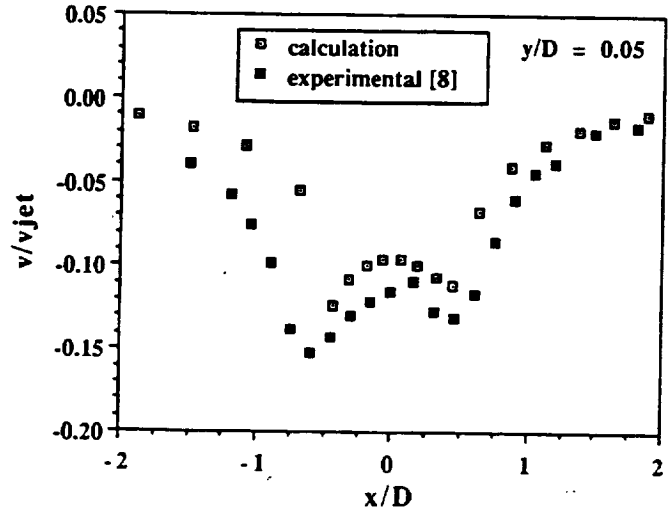

Fig. 3 Axial Velocity Across the Impinging Jet

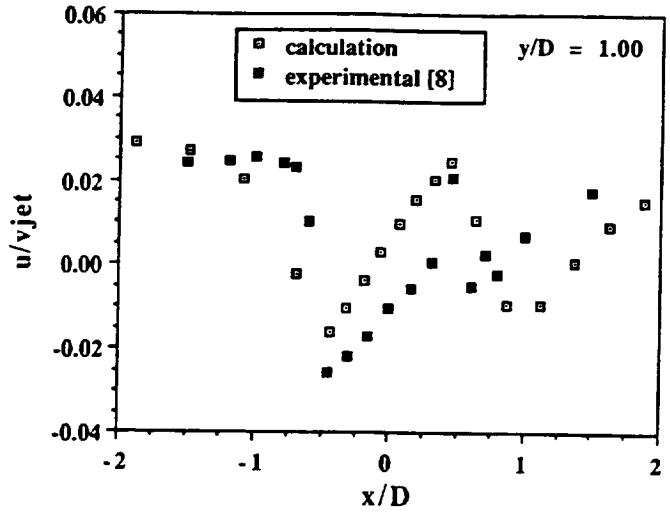

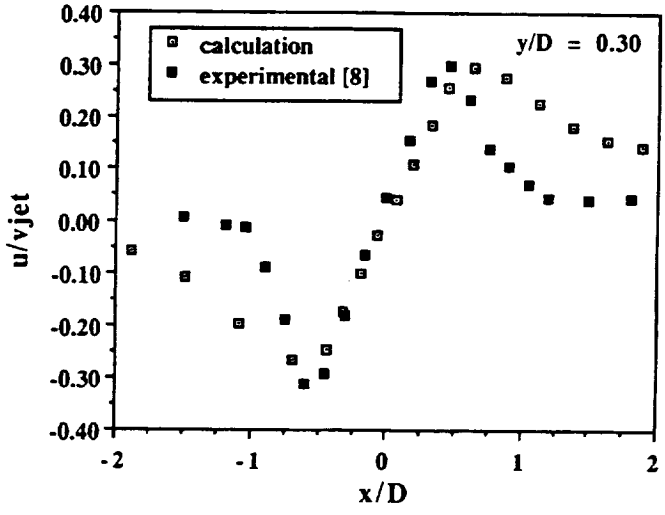

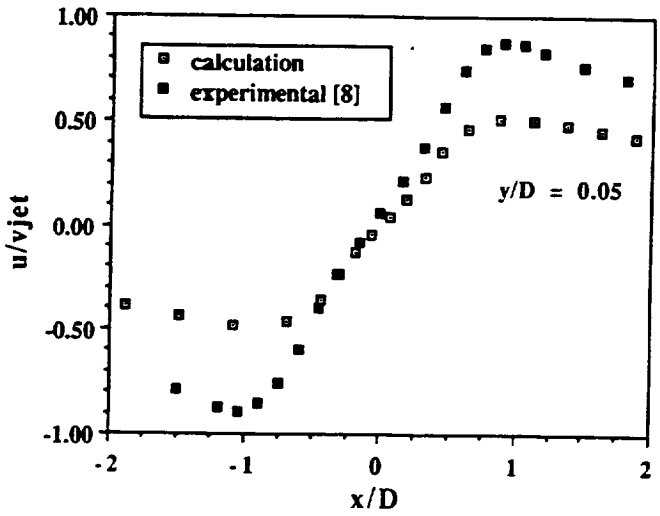

Fig. 4 Radial Velocity Across the Impinging Jet

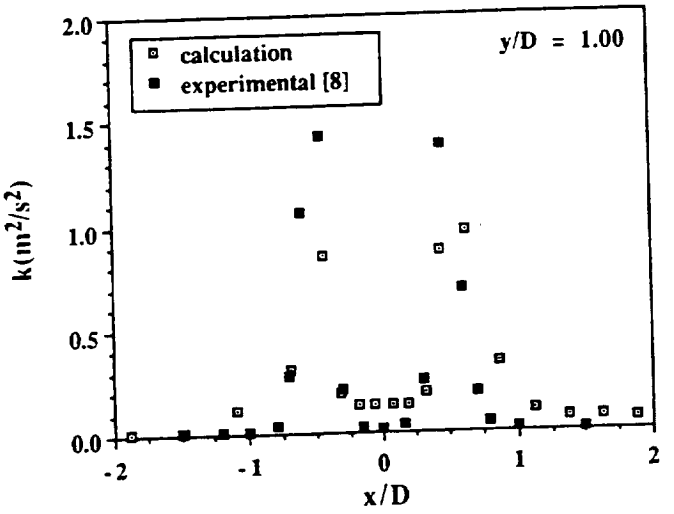

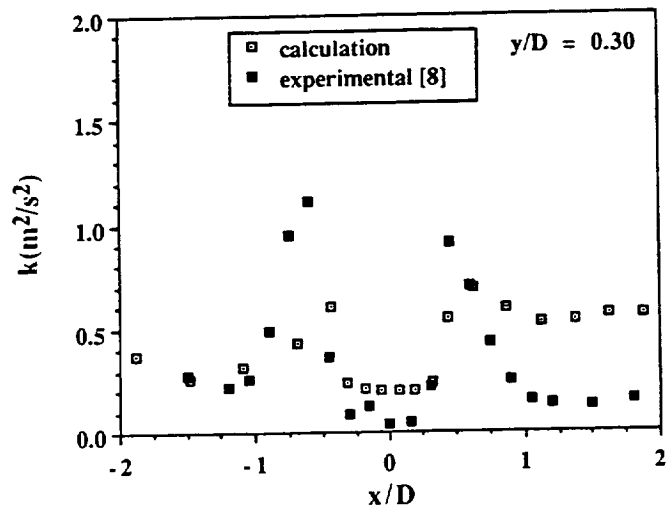

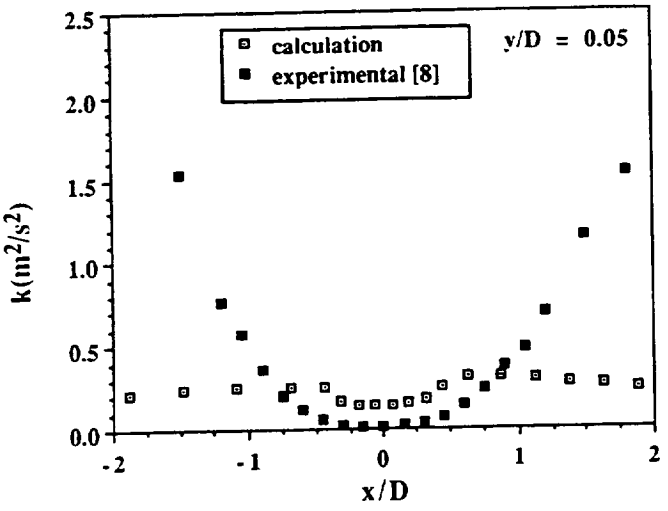

Fig. 5 Turbulent Kinetic Energy Across the Impinging Jet

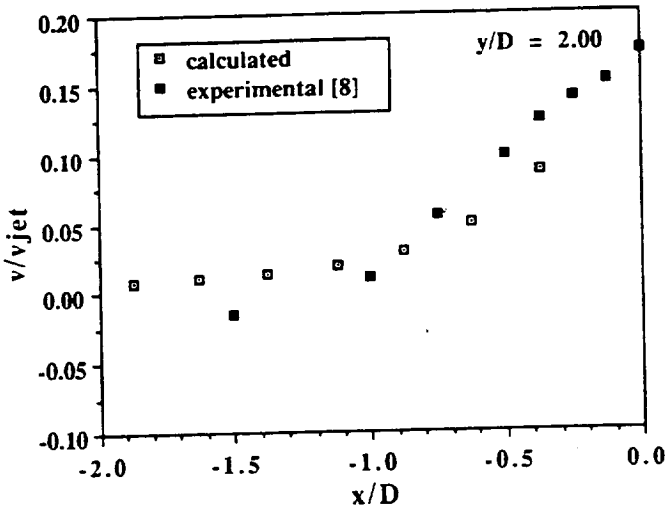

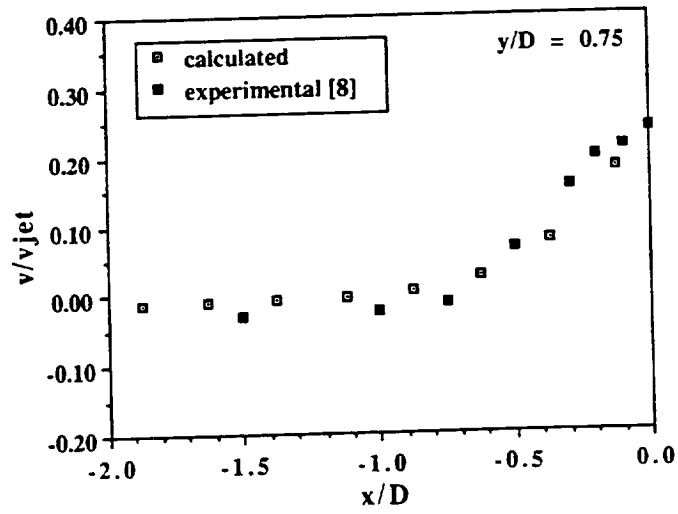

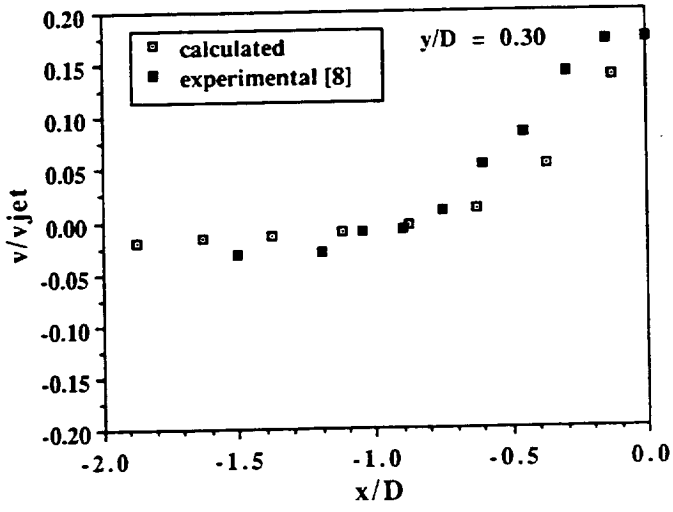

Fig. 6 Axial Velocity in the Fountain

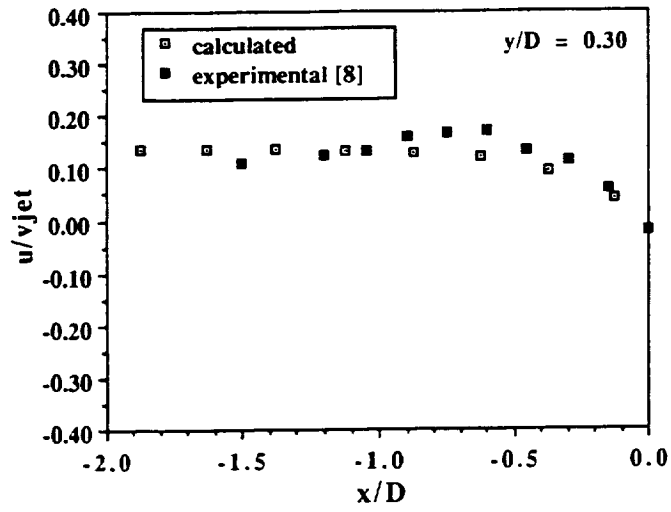

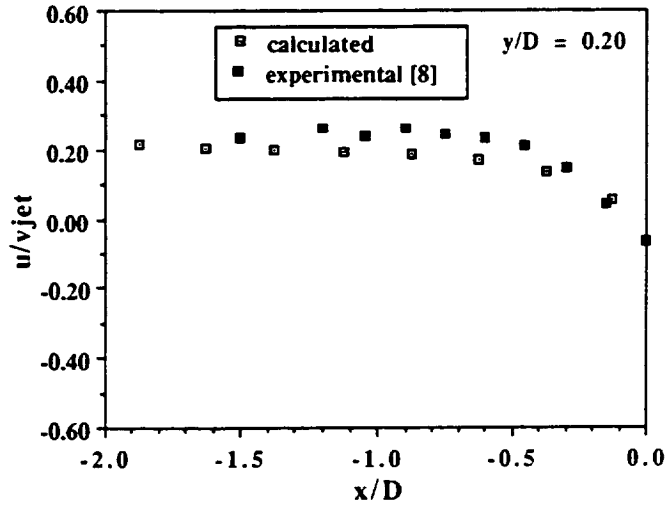

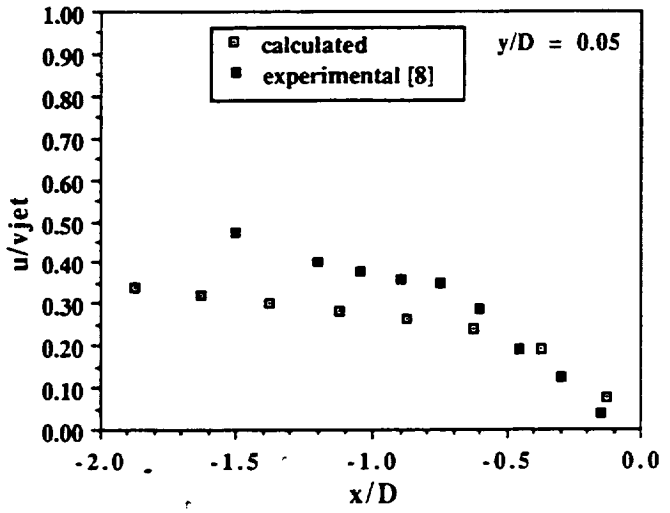

Fig. 7 Radial Velocity in the Fountain

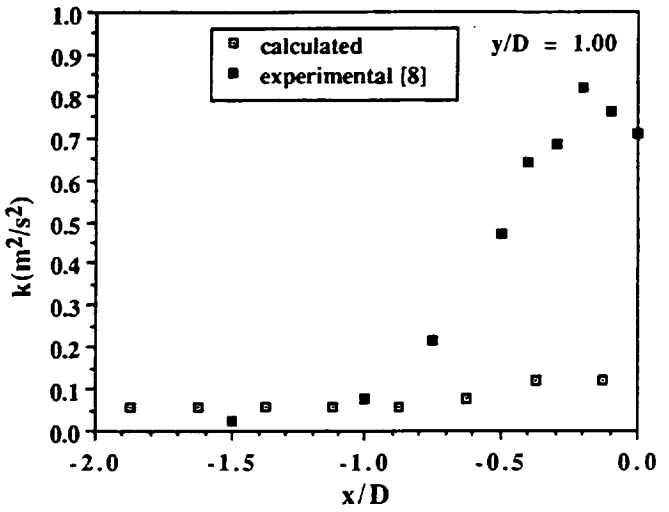

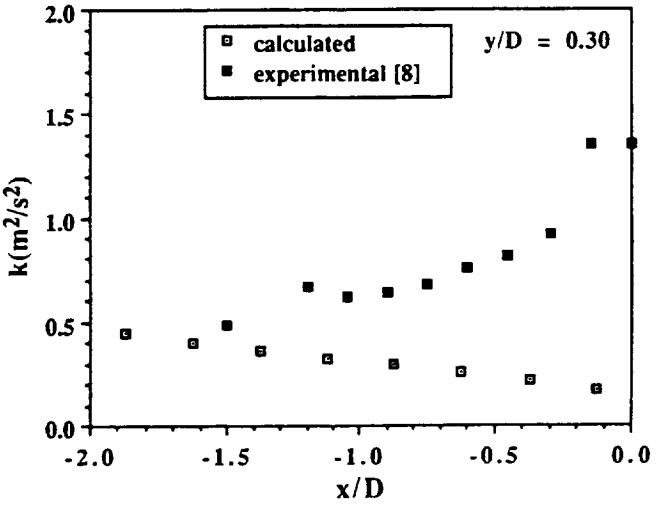

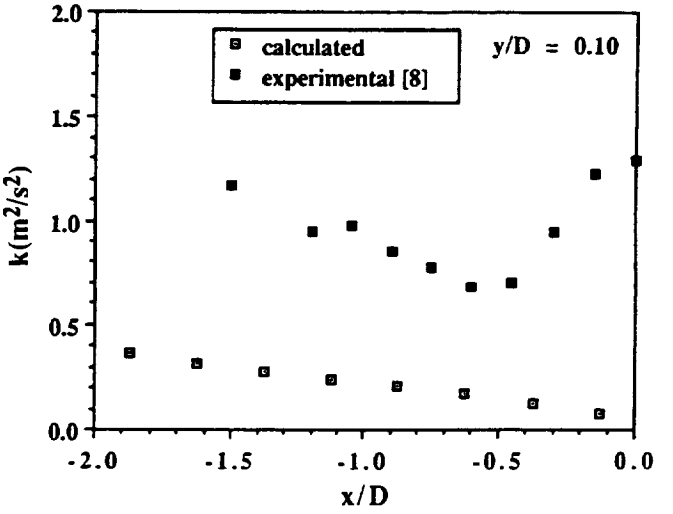

Fig. 8 Turbulent Kinetic Energy in the Fountain

APPENDIX B

HOT GAS ENVIRONMENT AROUND STOVL AIRCRAFT IN GROUND PROXIMITY, PART II: NUMERICAL STUDY

AIAA Paper 90-2270

Hot Gas Environment Around STOVL Aircraft in Ground Proximity: Part 2: Numerical Study

D. K. Tafti* and S. P. Vanka**
Department of Mechanical and Industrial Engineering,
University of Illinois, Urbana-Champaign
Urbana, IL 61801.

Abstract

Ingestion of hot exhaust gases by the engines of Short Take-off and Vertical Landing (STOVL) aircraft has been an important research problem for several years. The hot gas environment around STOVL aircraft is three-dimensional and turbulent. In this study, the Navier-Stokes equations governing the hot gas ingestion flow field are solved by an efficient finite-difference calculation procedure. The complete geometry including the head wind and the fuselage is simulated. Four demonstration calculations with variations in the height of the fuselage and the head wind velocity are presented. It is shown that the calculation procedure efficiently provides a solution to the governing equations and produces realistic descriptions of the flow and temperature fields.

1. Introduction

A number of interesting fluid dynamic effects have been identified when the lift jets of Short Take-off and Vertical Landing(STOVL) aircraft impinge on the ground surface (Kuhn [1], Kotansky [2], Kuhn and Eshelman [3], Agarwal [4]). First, as the lift jets expand, they entrain the surrounding fluid causing a negative pressure underneath the fuselage and a loss in lift. As the jets impinge on the ground and spread radially outwards, the wall jets further entrain external fluid and increase the loss in lift. In a multiple-jet configuration, these wall jets collide with each other and turn upwards to form an upwash fountain. This fountain flow has two main effects on the STOVL aircraft dynamics. First, an increase in lift force is caused when the fountain impinges on the aircraft fuselage. The recovery in lift is a positive effect of the upwash flow. However, this impinging fluid can also flow along the fuselage surface and eventually make its way into the engine inlets. Because the temperature of the fountain flow is much hotter than the ambient air, its ingestion by the engine can reduce the power and cause thermal stresses in the components. In addition to the fountain flow, another mechanism for hot gas ingestion results from the interaction of the forward moving wall jet with the headwind.When the headwind and the wall jet collide, a stagnation region is formed and the wall jet is turned into a ground vortex [3]. This ground vortex can subsequently be re-ingested by the engine, resulting in a further loss in power. However, the hot gas ingestion process depends on where and how the inlets to the engine are located with respect to the approach flow. For strong headwinds, the ground vortex can be pushed behind the engine inlets such that no hot gases are ingested. It can be recognized that the overall flow field governing these fluid dynamic interactions is strongly three-dimensional as well as turbulent.

In the last three decades, a number of studies addressing the above issues have been conducted(see [4,5] for good reviews). A majority of these studies were experimental in nature although some analytical studies of the individual processes, such as single jet impingement have also been conducted [6,7,8]. These studies have identified the fundamental processes and to a certain extent, quantified the effect of the parameters on hot gas ingestion and fountain flow. However, detailed measurements of the velocity and temperature fields in the fountain region and in the ground vortex in realistic operating conditions are not currently available. Recently, Saripalli [9,10] conducted some experiments in a water tunnel in which Laser-Doppler Velocimeter and Laser Imaging techniques were used to study the fountain region of the lift jets. These studies involved isothermal flows and were limited to the fountain formation.

With recent advances in the development of powerful digital computers, it has now become possible to numerically solve the equations that govern the transport of mass, momentum and enthalpy. However, because the flow is turbulent, such studies must necessarily make assumptions on the macroscopic behavior of turbulence. Despite the inherent limitations of such an approach in representing all the effects of turbulence with

*Research Associate

**Associate Professor, Member AIAA

precision, it has become a useful engineering tool. Numerical computation of the complete STOVL aircraft flow field requires the solution of nonlinear partial differential equations that govern the transport of mass, momentum and heat in three-dimensional space with boundary conditions that describe the lift jets, aircraft fuselage and the head wind. Because of the complexity of such solutions and limited computer capabilities, until recently most numerical studies were limited to two dimensions in which simplifications in the spanwise direction were made. Kotansky and Bower [11] were probably the first investigators to apply a Navier-Stokes analysis to the study of planar jet impingement of relevance to VTOL aircraft. In their analysis, a one equation model for turbulence kinetic energy was integrated with equations describing the stream function and transport of vorticity. A numerical solution of an impinging jet was obtained and compared with experimental data. This study was followed by Agarwal and Bower [12], who improved the turbulence model by considering an additional equation for the turbulence dissipation. Because the improved model explicitly calculated the local length scale of turbulence, the flowfields predicted by their model displayed better agreement with experimental data. Recently, other studies have appeared which also have numerically solved the equations for single and twin jet impingement flows using finite-difference techniques [e.g. 13,14,15]

Although the hot gas ingestion process results primarily from the impingment of the lift jets, the eventual ingestion is dictated by the complete flow dynamics including the formation of the fountain upwash and its interaction with the headwind. For stronger headwind speeds, it is possible to push the ground vortex downstream of the engine inlet and thus completely avoid its contribution to hot gas ingestion. Also, the collision of the wall jets and the fountain formation can be affected by the headwind and the geometry of the fuselage under surface. In addition, placement of Lift Increasing Devices (LIDs) [3] and other obstructions can divert the fountain flow from the engine inlets, thereby reducing the severity of the hot gas ingestion. In order to better understand all the flow processes, a complete Navier Stokes analysis including the far field condition of a prescribed headwind is necessary. Although such an analysis is computationally very intensive, the benefits are significant for evaluating the effects of geometric and flow parameters. Recently, an important contribution has been made in this direction by VanOverbeke and Holdeman [16]. In this study, the complete fuselage, headwind and multiple impinging jets were numerically simulated and the temperature fields close to the engine inlet face were studied. By varying the head wind and the impingement height, they were able to alter the ingestion pattern and quantify their effects. A finite-difference computer program [17] was used and the flow domain was discretized into a relatively large number of finite volumes.

A primary drawback of numerical computations of three dimensional elliptic fluid flows is that they can require substantial amounts of computer time to obtain a converged solution. These large computational costs often discourage systematic and thorough investigations of the effects of various parameters. However, with research into faster converging numerical algorithms, it is possible to substantially reduce these computer times. In this paper, we demonstrate the applicability of one such algorithm [18] which is based on the concept of using multiple levels of grids [19] to obtain faster convergence. In this study, the geometrical configuration studied by Van Overbeke and Holdeman [16] is considered and a set of four calculations have been performed. To compare our results with those of VanOverbeke and Holdeman [16], we have simulated exactly the same configurations, albeit with a finer grid, and compared the computer times and the flow fields. The four calculations in this study differ in the height of the jets from the ground and the ratio of the head wind to the jet velocity.

The following sections briefly describe the solution procedure and present the results of the calculations. In Part 1 of this study, a separate experimental investigation is presented by McLean et. al [20] in which the concentration of the exhaust jets is quantified through a Laser Imaging technique.

2. Governing Equations and Solution Algorithm

The flow and temperature fields around the STOVL aircarft are governed by the following set of elliptic partial-differential equations. In the present analysis, the flow is considered to be steady in the time-averaged sense, and the effects of turbulence are captured by a turbulence model [21]. The governing equations can be written as follows:

Mass continuity

$$\frac{\partial}{\partial x}(\rho u) + \frac{\partial}{\partial y}(\rho v) + \frac{\partial}{\partial z}(\rho w) = \dot{m} \qquad (1)$$

x-momentum

$$\frac{\partial(\rho uu)}{\partial x} + \frac{\partial(\rho uv)}{\partial y} + \frac{\partial(\rho uw)}{\partial z} = -\frac{\partial P}{\partial x} + \frac{\partial}{\partial x}\left(2\mu \frac{\partial u}{\partial x}\right) + \frac{\partial}{\partial y}\left[\mu\left(\frac{\partial u}{\partial y} + \frac{\partial v}{\partial x}\right)\right] + \frac{\partial}{\partial z}\left[\mu\left(\frac{\partial w}{\partial x} + \frac{\partial u}{\partial z}\right)\right] + \dot{m} u_{inj} \qquad (2)$$

y-momentum

$$\frac{\partial(\rho uv)}{\partial x}+\frac{\partial(\rho vv)}{\partial y}+\frac{\partial(\rho vw)}{\partial z}=-\frac{\partial P}{\partial y}$$

$$+\frac{\partial}{\partial x}\left[\mu\left(\frac{\partial u}{\partial y}+\frac{\partial v}{\partial x}\right)\right]+\frac{\partial}{\partial y}\left(2\mu\frac{\partial v}{\partial y}\right)$$

$$+\frac{\partial}{\partial z}\left[\mu\left(\frac{\partial w}{\partial y}+\frac{\partial v}{\partial z}\right)\right]+\dot{m}v_{inj} \qquad (3)$$

z-momentum

$$\frac{\partial(\rho uw)}{\partial x}+\frac{\partial(\rho vw)}{\partial y}+\frac{\partial(\rho ww)}{\partial z}=-\frac{\partial P}{\partial z}$$

$$+\frac{\partial}{\partial x}\left[\mu\left(\frac{\partial w}{\partial x}+\frac{\partial u}{\partial z}\right)\right]+\frac{\partial}{\partial y}\left[\mu\left(\frac{\partial v}{\partial z}+\frac{\partial w}{\partial y}\right)\right]$$

$$+\frac{\partial}{\partial z}\left(2\mu\frac{\partial w}{\partial z}\right)+\dot{m}w_{inj} \qquad (4)$$

Turbulence energy

$$\frac{\partial}{\partial x}(\rho uk)+\frac{\partial}{\partial y}(\rho vk)+\frac{\partial}{\partial z}(\rho wk)=$$

$$\frac{\partial}{\partial x}\left(\Gamma_k\frac{\partial k}{\partial x}\right)+\frac{\partial}{\partial y}\left(\Gamma_k\frac{\partial k}{\partial y}\right)+\frac{\partial}{\partial z}\left(\Gamma_k\frac{\partial k}{\partial z}\right)$$

$$+G-\rho\varepsilon+\dot{m}k_{inj} \qquad (5)$$

Dissipation of turbulence energy

$$\frac{\partial}{\partial x}(\rho u\varepsilon)+\frac{\partial}{\partial y}(\rho v\varepsilon)+\frac{\partial}{\partial z}(\rho w\varepsilon)=$$

$$\frac{\partial}{\partial x}\left(\Gamma_\varepsilon\frac{\partial \varepsilon}{\partial x}\right)+\frac{\partial}{\partial y}\left(\Gamma_\varepsilon\frac{\partial \varepsilon}{\partial y}\right)$$

$$+\frac{\partial}{\partial z}\left(\Gamma_\varepsilon\frac{\partial \varepsilon}{\partial z}\right)+C_1 G\frac{\varepsilon}{k}-C_2\rho\frac{\varepsilon^2}{k}+\dot{m}\varepsilon_{inj} \qquad (6)$$

Enthalpy

$$\frac{\partial}{\partial x}(\rho uH)+\frac{\partial}{\partial y}(\rho vH)+\frac{\partial}{\partial z}(\rho wH)=$$

$$\frac{\partial}{\partial x}\left(K\frac{\partial T}{\partial x}\right)+\frac{\partial}{\partial y}\left(K\frac{\partial T}{\partial y}\right)$$

$$+\frac{\partial}{\partial z}\left(K\frac{\partial T}{\partial z}\right)+\dot{m}H_{inj} \qquad (7)$$

Equation of state

$$\rho=\frac{P}{RT} \qquad (8)$$

u, v, w, are the velocities in the x, y and z directions,respectively. P is the pressure and R is the gas constant and G is the production of turbulent kinetic energy. In all the above equations, the diffusive coefficients contain the effects of laminar as well as turbulent diffusion. Standard values of the constants in the turbulence model [21] are used.

The above equations are solved on a rectangular domain that envelopes the aircraft fuselage and the exhaust jets. Because the current computer program is limited to the use of rectangular grids, the fuselage of the aircraft was modeled to be of rectangular shape. However, efforts are currently under way to extend the program to handle grids of arbitrary inclinations (boundary-fitted grids [22]) which will then permit a more realistic representation of the aircraft shape and angles of attack. The boundary conditions and solution domain considered in current calculations are described in section 3.1.

The above equations are finite-differenced by a hybrid scheme [23] that combines first and second order differencing for the total convective and diffusive operator. At high cell Peclet numbers, the finite-differencing scheme becomes first order accurate to preserve stability of the solution procedure. The multigrid solution technique [19] differs from the singe grid technique in the manner the finite-difference equations are solved to the required accuracy. It is well known that for elliptic equations, single grid techniques converge poorly when the finite-difference grid contains a large number of mesh points. This results from the low frequency errors that are slow to converge on a given fine grid. In the multigrid concept, a series of fine and coarse grids is used and the solution is switched between the coarse and fine grids such that errors of all frequencies converge at the same rate. This novel concept was originally proposed for model elliptic equations, but recently it has become popular in solving practical fluid flows [24].

The principle behind the multigrid procedure may be explained as follows. Consider an elliptic equation that is discretized by finite-difference or finite element methods. Generally, an iterative procedure that is designed to obtain a solution to the discrete equations will converge rapidly in the first few iterations but subsequently the convergence deteriorates. It can be shown through formal analyses that the cause for this poor convergence is the presence of low frequency errors that are not resolved well on any given grid. However, these errors can converge faster if the grid is coarse. Therefore, in the multigrid procedure, these errors are interpolated to a coarser grid and solved. The results of this coarse grid solution are then put back on the finer grid solution through extrapolation. In the case of a calculation with many mesh points, several layers of

coarse meshes can be used to obtain rapid convergence. However, the coarsest grid is often dictated by the constraints of geometry and boundary conditions.

In the present solution scheme, we have combined the multigrid technique with a coupled solution scheme for the momentum and continuity equations. The velocities and pressures are obtained by a block-implicit solution of the momentum and continuity equations. As this procedure is explained in previous works by one of the authors [18,25,26], it is not elaborated here. However, in order to simulate the fuselage and the lift jets, the procedure has been extended to handle internal obstacles and mass and momentum injections. These features have been incorporated in a manner that maintains consistency between the coarse and fine grids, a necessary feature for the algorithm to eventually converge to the correct solution. It must be pointed out that although the coarse grids are used, the final solution is obtained on the finest grid in the system. Thus the intermediate grids are used only for accelerating the convergence rate and they do not influence the final converged solution.

The next section describes the computational domain and a typical convergence history of the multigrid solution procedure. Simulated flow and temperature fields are presented along with a discussion on the mechanism of hot gas ingestion for a four jet configuration. These results compare qualitatively with the flow imaging data of McLean, Sullivan and Murthy [20], as well as with calculations presented by Van Overbeke and Holdeman [16].

3. Results

3.1 Computational details and Convergence Histories

In this study, four test cases have been considered, which are similar to those studied in ref. 16. The important flow and geometrical parameters are outlined in Table 1. The four cases differ in the height of the fuselage from the ground plane (h/d where d is the diameter of the lift jets) and the headwind to jet velocity ratio (U_∞/U_j). The solution domain is a three-dimensional wind tunnel with overall dimensions of 136d in the streamwise direction (x), 27 or 29d in the cross-stream direction (y) and 40d in the spanwise direction (z). These large dimensions are necessary to accurately resolve the flowfield around the jets and the fuselage without any interference from the simulated boundaries. Figure 1 shows the computational grid used and the flow geometry. The geometry simulates four

Table 1. Flow and Geometry Parameters.

CASE	U_∞/U_j	h/d	Ma_j	Re_∞ x10^{-4}	Re_j x10^{-5}
1	0.03	4.0	0.47	3.3	3.3
2	0.03	2.0	0.47	3.3	3.3
3	0.09	4.0	0.47	9.9	3.3
4	0.09	2.0	0.47	9.9	3.3

jets (due to symmetry, only half the domain is considered) issuing from the engine with the engine inlet located 10 jet diameters upstream of the fore jet axis. The distance between the fore and aft jet axis is 6 diameters while the spanwise distance between the jets is 3.2 diameters. The fuselage extends throughout the calculation domain and is 2.5 diameters in height and 2.2 diameters in width. The inlet, which is 67 jet diameters from the entrance of the test section, has a height of 2.5 diameters and a width of 1.4 diameters. It is adjacent to the fuselage in the spanwise direction and extends 9.5 jet diameters up to the fore jet after which it becomes part of the fuselage. The calculation domain is divided into 100 computational cells in the x direction, 44 in the y, and 48 in the z direction, giving a total of about 211,000 cells. The particular grid distribution was chosen to provide good resolution in the near field of the jets and at the same time keep the grid expansion ratio as small as possible. The grid distribution was also influenced by the necessity to accomodate internal obstacles and baffles such that grid lines bounded the surfaces of these structures.

At the inlet of the test section, uniform velocity and temperature conditions are prescribed for the incoming headwind and the turbulent kinetic energy was assumed to be one percent of the mean kinetic energy. At the exit, outflow boundary conditions are prescribed. In the y direction, wall boundary conditions are prescribed. The bottom wall is assumed to have zero heat loss while the top wall is assumed to be at a uniform temperature. In the spanwise direction, symmetry boundary conditions are applied on one side while an adiabatic wall is prescribed on the other side. Within the calculation domain, additional conditions are prescribed for the engine inlet and the jets. The inlet acts as a mass sink while the jets as mass sources. In prescribing these conditions it is important to conserve mass. The jet velocity profile is assumed to be uniform with the turbulent kinetic energy equal to one percent of the mean kinetic energy.

In the calculation procedure, the prescribed fine grid was coarsened to two additional levels. The calculation was started on the coarsest grid from prescribed initial conditions but on the finer grids, the starting solutions were obtained by successively extrapolating converged flow fields from the coarser grids. This Full Multigrid Cycle (FMG) provided realistic starting values for the calculations on the fine grids. Figure 2 shows a typical convergence history for the calculation of Case 1. The convergence is monitored by the normalized sum of the absolute mass and momentum residuals over the whole solution domain. It is seen that the solution converges to the required tolerance of one percent error in approximately 150 iterations. In the previous study of VanOverbeke and Holdeman [16], which used a single grid procedure, the number of iterations were approximately 2000 for a 134,000 grid. This represents a significant reduction in computational effort. The present calculation required approximately 35 minutes of CPU time on a CRAY-2; typically this translates to a few hours of interactive real clock time.

3.2 Calculated Velocity and Temperature Fields

Hot gas ingestion is a serious problem for STOVL aircraft in ground proximity. Two important factors which govern hot gas ingestion are the proximity of the lift jets to the ground (h/d ratio) and the ratio of the freestream velocity to the jet velocity (U_∞/U_j). Another important factor, which is not considered in the present study, is the location of the inlet with respect to the lift jets and the use of shields and baffles to deflect flow of hot gases away from the engine inlet. When the lift jets impinge on the ground they stagnate and form radially flowing wall jets. When two opposing wall jets meet they manifest themselves into a fountain flow. The flow field caused by a rectangular four jet configuration is governed by a strong fountain flow between the fore and aft jets (streamwise fountain) and also between the symmetrical spanwise jets (spanwise fountain). The streamwise fountain upwash when obstructed by the fuselage is forced to flow laterally outwards and up while the spanwise fountain upwash tends to flow under and along the length of the fuselage in the streamwise direction. Both these mechanisms contribute to the direct ingestion of hot gases into the inlet. The other mechanism of hot gas ingestion, which is not as severe, is due to the recirculating flow caused by the interaction of the outward flowing hot gases with the headwind. The outward flowing hot gases are forced to stagnate by the freestream flow and are deflected towards the engine inlet where they are reingested.

Figure 3 shows the velocity distribution in an x-y plane passing through the center of the fore and aft jets for the four cases (for the sake of clarity, different vector scales are used in different segments of the domain). The effect of headwind to jet velocity ratio (U_∞/U_j) on the flow field is clearly evident. In Case 1 and 2 (U_∞/U_j=0.03), the effect of the lift jets extends far upstream (35 jet diameters for Case 1 and 46 jet diameters for Case 2), while for Case 3 and 4 (U_∞/U_j=0.09) the stagnation region is much closer to the jets. For the low velocity ratio, hot gas from the lift jets flow under the fuselage towards the inlet, where part of it is ingested directly by the strong suction of the inlet, while the rest is carried by its streamwise momentum further upstream until it is forced to stagnate by the oncoming flow and recirculate back towards the inlet (ground vortex). The most striking difference between high and low U_∞/U_j is the complete absence of the recirculating ground vortex in Case 3 and 4. This is due to the high forward momentum of the headwind which prevents the hot gas from the jets from moving upstream. The effect of different h/d ratios is not as strong. For h/d of 2 (Case 2 and Case 4), a smaller area is available between the fuselage and the ground and consequently the radial momentum of the hot gas is larger than for h/d of 4. This enhances the spread of the jet, both in the lateral and streamwise direction. A comparison of Case 3 and Case 4 (just upstream of the fore jet and under the fuselage), suggests that for h/d of 2 the forward flow is stronger than for h/d of 4. This is also the case for Case 1 and 2, in which the recirculating zone for h/d of 2 extends about 11 jet diameters further upstream than for h/d of 4.

Figure 4 shows temperature contours corresponding to the velocity vector fields shown in Figure 3. In all cases, the temperature fields upstream of the lift jets are very similar to those implied by the velocity field. For Cases 1 and 2 (U_∞/U_j=0.03), the hot gases from the jets are transported much further upstream of the inlet. Although not clearly evident in Figure 4, the upstream transport and the subsequent recirculation of hot gases (although cooler) back to the inlet can be directly correlated with the velocity vector field. This effect can be clearly seen in Figure 5, which summarizes Figures 3 and 4. In Figure 5(a) and 5(b), the cooler recirculated gases (positive streamwise velocity) can be clearly distinguished from the hotter gases (negative streamwise velocity). This relation between the velocity field and the temperature field is also evident in Case 4 (U_∞/U_j=0.09, h/d = 2) between the inlet and the fore jet where hot gases are transported upstream along the bottom of the fuselage. However, for Case 3 (U_∞/U_j=0.09, h/d = 4), the temperature field extends further upstream than indicated by the velocity field; this indicates either a diffusive transport of heat or convective transport of heat from the sides. Another interesting feature is the difference in temperature between the fore half of the fountain and the aft half. In all

cases the fore half is cooler than the aft half, which must be due to the its greater interaction with the cooler freestream fluid. This effect was also observed in the simulations of [16]. Maclean et al. [20] compared the upstream distribution of temperature (along the jet center and along the axis of symmetry) obtained from their experiments with the present calculations for Case 3. In the region near the jets, the agreement between the two is good, but further upstream the experiments show a higher concentration of jet fluid.

Figure 6 shows the velocity distribution in the ground plane for Case 1 (U_∞/U_j=0.03, h/d = 4) and Case 3 (U_∞/U_j=0.09, h/d = 4). In the vicinity of the jets, the outward flowing radial wall jets are clearly visible. These wall jets interact with each other to form the streamwise and spanwise fountain flows. We can also see the effect of the headwind on the outward movement of the hot jet fluid; for the low velocity ratio the momentum of the jets carry the hot gases much further than with the higher headwind. This effect is more clearly seen in Figures 7 and 8, which show line and color contours of the temperature field in the ground plane. For the low headwind case, both the forward and lateral spread of the hot gases is much more than with the higher headwind. In addition, the height of the fuselage above the ground (h/d ratio) also has a effect on the forward and lateral spreading of the jets. As mentioned earlier, for h/d=2 the radial momentum of the jet is higher and this can be seen in the greater lateral spread of the jet fluid before it is pushed downstream by the headwind. Another interesting feature is the sharp temperature gradients observed between the jets in the fountain upwash region. This is due to the vertical movement of two jet streams at different temperatures with little transverse movement of fluid across this boundary. In fact, the locus of points across which these sharp gradients are seen in the lateral direction is the stagnation line which divides fluid from the fore and aft jets until finally they mix and smooth out the differences. These sharp gradients are also present in the simulations of [16] and in the experiments of [20], although the experimentally observed gradients are not as sharp.

Table 2 compares the upstream extent of the recirculating hot gas zone with the experiments of [20]. In the present study, the temperature distribution is used as a means to determine the upstream spread of the hot gases (Figures 4 and 5). It is seen that the calculated values agree well with the experimental values for Cases 1, 3 and 4, while for Case 2 the calculated value of x/d is much higher. Also, the trend indicated by the experiments (increased upstream penetration (x/d) with increased h/d ratio) is the opposite of what the numerical calculations indicate. This in effect would indicate that the jet fluid mixes more rapidly with the free stream flow and loses its

Table 2. Extent of Recirculating Hot Gas Zone Upstream of Foreward Lift Jets.

CASE	Present Calculations	Experiments Ref. [20]
1	35	31
2	46	22
3	10	12
4	12.5	14

identity earlier than the calculations predict. This discrepency could be due to the inability of the k-ε turbulence model to accurately capture the full extent of turbulence production caused by the stagnating jets. Recent numerical studies of the fountain region of twin jet impingement [28] indicate that the turbulent kinetic energy is severely under predicted, particularly in the region close to the ground plane. This in part also explains the sharp temperature gradients seen in the upwash region of the fountain flow. The authors suspect that for Case 2 this might be a critical factor in determining the dilution and spread of the jet fluid.

Figures 9-12 show velocity and temperature distributions in three z-y planes for each of the cases tested. Part (a) is the z-y plane passing through the fountain upwash between the jets, part (b) is the z-y plane between the fore jet and the inlet and part (c) is the plane at the inlet. In all four cases, the spanwise fountain flow which is responsible for the movement of hot gases upstream from the fore jets is clearly visible in (b). As the hot gases from the jets move upstream under the fuselage they are considerably diluted due to mixing with the cooler headwind. As this gas approaches the inlet, part of it is directly ingested into the inlet (c). It is interesting to see that for the low velocity ratio, ingestion occurs from the side, top and bottom of the fuselage while for the higher headwind most of the ingestion occurs from the bottom and side of the fuselage. Another interesting feature is the movement of hot gases; for the higher headwind, the hot gases show a lateral outward and upward movement while for the lower headwind the flow is laterally inward, i.e., cooler fluid is entrained into the fountain region. This phenomenon is also reflected in the ground plane temperatures (Figures 7 and 8), where the lateral spread of the jet fluid between the fore jet and the inlet is more with the higher headwind. This is due to the higher dynamic pressure of the oncoming free stream, which forces the hot gases out from

Table 3. Non-dimensional Mass Averaged Inlet Plane Temperatures. $(T_{avg} - T_\infty)/(T_j - T_\infty)$

CASE	Present Calculations	Caculations Ref. [16]
1	0.083	0.13
2	0.097	0.11
3	0.0	0.08
4	0.017	0.03

under the fuselage. Table 3 shows the mass averaged non-dimensional inlet plane temperatures calculated for the four cases and compares them to those obtained by the numerical simulations of [16]. There is some discrepancy between the two calculations. It is not possible to identify the reasons for this discrepancy, but the difference in the resolution of the flow field between the two methods could be one of the major contributing factors. The results of the present calculation follow the trends indicated by the velocity and the temperature profiles. The maximum average inlet temperature is for Case 2 (U_∞/U_j=0.03, h/d = 2) while Case 3 does not seem to ingest any hot gases.

4. Summary and Conclusions

In the present paper, a multigrid calculation procedure for three-dimensional flows is used to study the hot gas ingestion by STOVL aircraft. Calculations with a simulated fuselage and twin exhaust jets have been made for two ground positions and two head-wind ratios. The global features of the flowfield like the ground plane temperature distributions and the formation of the ground vortex for the four cases are according to expectations and agree well with the recent numerical study of ref. 16. A major contribution of the present study is the demonstration that the multigrid algorithm can significantly reduce the computational effort required to solve the governing equations compared to a conventional single grid procedure. The reduction in computational effort permits more parametric studies to be conducted.

In the present study, the Reynolds-averaged flow equations have been solved in conjunction with the k-ε turbulence model. The flow is considered to be steady in time, although, it has been observed [27] that the region of jet impingment is highly unsteady and the turbulence structures are very complex. Therefore, the accuracy of the current calculations is limited by the assumptions made in deriving the governing equations of the turbulence model. A study performed on the twin jet impingement flow in isolation [28] showed that the k-ε model is able to predict the velocity field reasonably well, but the turbulence kinetic energies are severely under-predicted. Although it is possible to incorporate more complex turbulence models into the current algorithm, at this time it is not certain that they improve the predictions over those of the k-ε model. Future extension of this study will be in the direction of representing the aircraft geometry more realistically through the use of curvilinear grids.

5. Acknowledgements

The present work was supported by a grant NAG-3-1026 from NASA Lewis Research Center, Cleveland, Ohio. The authors wish to thank Dr. J. D. Holdeman for his encouragement during this study. The calculations were performed on the NASA Ames NAS computer facility.

References

1. R. E. Kuhn, " Design Concepts for Minimizing Hot Gas Ingestion in V/STOL Aircraft," Journal of Aircraft, Vol. 19, No. 10, pp. 845-850, 1982.
2. D. R. Kotansky, "Multiple Jet Impingement Flowfields," Proceedings of the International Symposium on Recent Advances in Aeronautics and Acoustics, Stanford Univ., 1983.
3. R. E. Kuhn and J. Eshelman, "Ground Effects on V/STOL and STOL Aircraft--- A Survey," AIAA-85-4033, AIAA/AHS/ASEE Aircraft Design Systems and Operations Meeting,Colorado Springs Co., Oct., 1985.
4. R. K. Agarwal, "Recent Advances in Prediction Methods for Jet-Induced Effects on V/STOL Aircraft", Recent Advances in Aerodynamics, International Symposium held at Stanford University, Edited by A. Krothapalli and C. A. Smith, pp. 473-521, August 1983.
5. J. G. Skifstad, "Aerodynamics of Jets Pertinent to VTOL Aircraft, " Journal of Aircraft, Vol. 7, No. 3, pp. 193-203, 1970.
6. M. J. Siclari, W. G. Hill, Jr., R. C. Jenkins and D. Migdal, "VTOL In-GROUND Effect Flows for Closely Spaced Jets," AIAA-80-1880, AIAA Aircraft Systems Meeting, Anaheim, CA., Aug. 1980.
7. A. Rubel, "Computations of Jet Impingement on a Flat Surface," AIAA J., Vol. 18, 1980, pp. 168.

8. J. C. Wu, et. al, "Experimental and Analytical Investigation of Jets Exhausting Into a Deflecting Stream," J. Aircraft, Vol. 7, pp. 193-203, 1970.
9. K. R. Saripalli, "Visualization of Multi-Jet Impingement Flow," AIAA-81-1364, AIAA/SAE/ASME 17th Joint Propulsion Conference, Colorado Springs, Co., July 1981.
10. K. R. Saripalli, "Lase-Doppler Velocimeter Measurements in 3-D Impinging Twin-Jet Fountain Flows," Turbulent Shear Flows, 5, pp. 146-148, Springer Verlag, 1987.
11. D. R. Kotansky and W.W. Bower, " A Basic Study of the VTOL Ground Effect Problem for Planar Flow," J. Aircraft, Vol. 15, No. 4, pp. 214-220, 1978.
12. R. K. Agarwal and W. W. Bower," Navier-Stokes Computation of Turbulent Compressible Two-Dimensional Impinging Jet Flowfields," AIAA Journal, Vol. 20, No. 5, pp. 577-584, May 1982.
13. R. Childs, "Turbulence Modelling for Impinging Jets," AIAA-90-0022, 28th Aerospace Sciences Meeting, Reno, NV, Jan. 1990.
14. J. M. M. Barata, D. F. G. Durao and J. J. McGuirk, "Numerical Study of Single Impinging Jets Through a Crossflow, " AIAA-89-0449, 27th Aerospace Sciences Meeting, Reno, NV, 1989.
15. C. Hwang, S. Yang and J. Liu, "Numerical Investigations of Airfoil/Jet/Fuselage Undersurface Flowfields in Ground Effect, AIAA-90-0597, 28th Aerospace Sciences Meeting, Reno, NV, Jan. 1990.
16. T. J. VanOverbeke and J. D. Holdeman, "A Numerical Study of the Hot Gas Environment Around a STOVL Aircraft in Ground Proximity", AIAA-88-2882, 24th AIAA/ASME/SAE/ASEE Joint Propulsion Conference, Boston, 1988.
17. S. A. Syed and R. H. James, "User Manual for 3D-Teach With Rotation", NASA-CR-180886, 1980.
18. S. P. Vanka, "A Calculation Procedure for Three-Dimensional Recirculating Flows," Computer Methods in Applied Mechanics and Engineering, Vol. 55, pp. 321, 1986.
19. A. Brandt, "Multi-Level Adaptive Solutions to Boundary-Value Problems," Mathematics of Computations, Vol. 31, pp. 333-390, 1977.
20. R. McLean, J. Sullivan and S. Murthy, " Hot Gas Environment Around STOVL Aircraft in Ground Proximity, Part 2: Experimental Study," AIAA 90-2269, 26th AIAA/SAE/ASME/ASEE Joint Propulsion Conference, Orlando, Florida, 1990
21. B. E. Launder and D. B. Spalding, "The Numerical Computation of Turbulent Flows," Computer Methods in Applied Mechanics and Engineering, Vol. 3, pp. 269-289, 1974.
22. J. F. Thompson, W. V. A. Warsi and C. W. Mastin, Numerical Grid Generation, North Holland, Amsterdam, The Netherlands, 1985.
23. D. B. Spalding, "A Novel Finite-Difference Formulation for Differential Expressions Involving First and Second Derivatives," International Journal for Numerical Methods in Engineering, Vol. 4, pp. 551-559, 1972.
24. J. Linden, G. Lonsdale, B. Steckel and Klaus Stuben, " Multigrid for the Steady-State Incompressible Navier-Stokes Equations: A survey," GMD Report No. 322, July 1988.
25. S. P. Vanka, "Analytical Studies of Three-Dimensional Combustion Processes," Aero Propulsion Laboratory Report, AFWAL-TR-88-2140, 1989.
26. S. P. Vanka, et. al., "An Efficient Computational Tool for Ramjet Combustor Research," AIAA Journal of Propulsion and Power, Vol. 5, No. 4, pp 189-199, 1989.
27. V. Kibens, K. R. Saripalli, R. W. Wiezen and J. T. Kegelman, "Unsteady Features of Jets in Lift and Cruise Modes for VTOL Aircraft," SAE paper. 872359, International Power Lift Conference, Santa Clara, CA., 1987.
28. W. P. Pegues and S. P. Vanka, "Numerical Study of Twin-Jet Impingement Upwash Flow," ASME Forum on Turbulent Flows, Toronto, Canada, June, 1990.

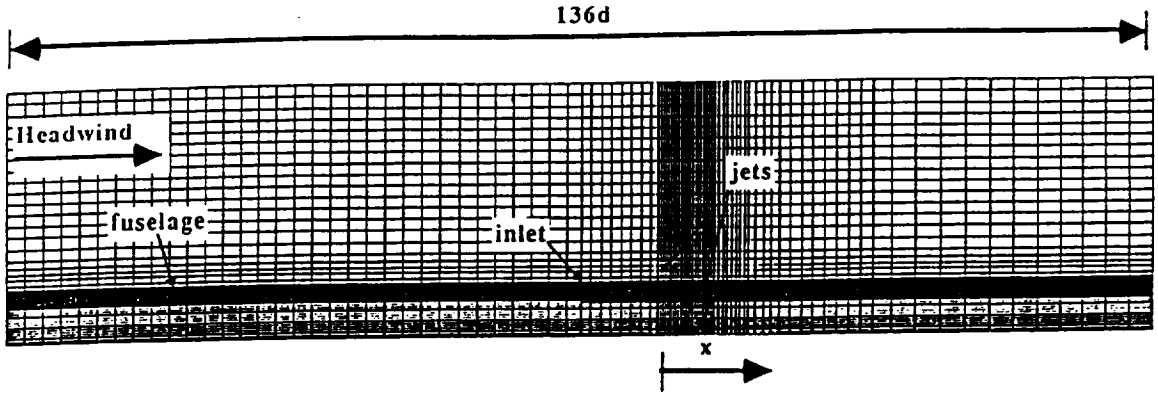

(a)

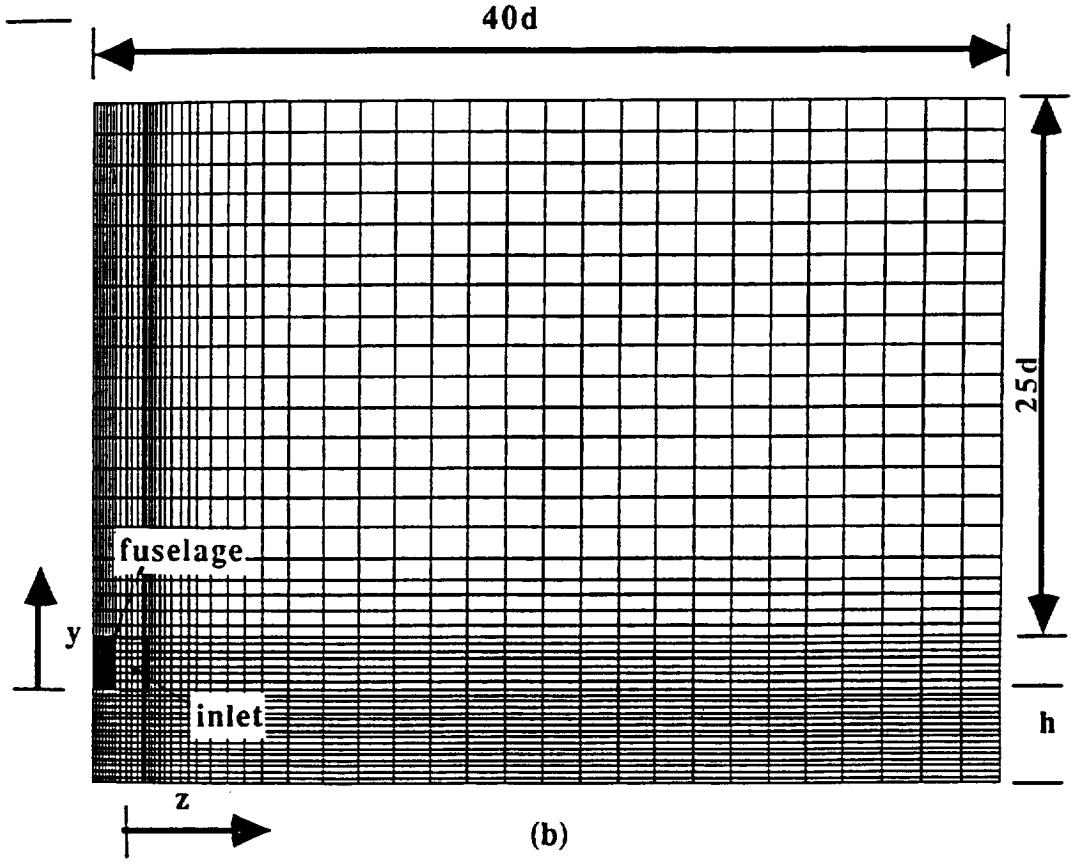

(b)

Figure 1: Computational domain and grid distribution. (a) side view; (b) front view (not to same scale as (a)).

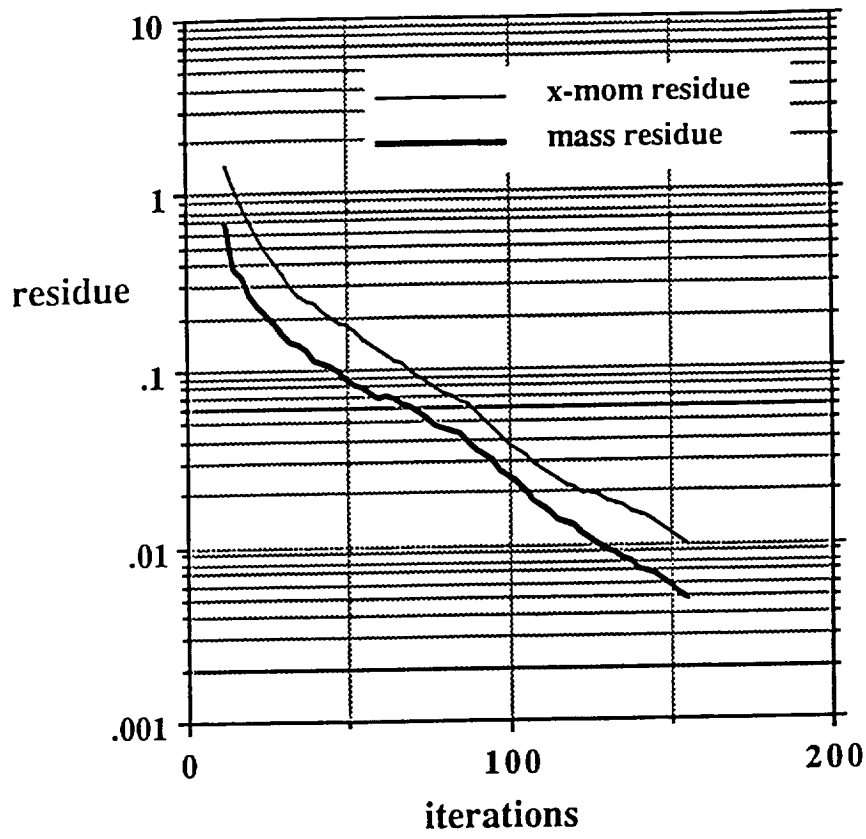

Figure 2: Typical convergence history for multigrid calculation procedure.100 x 44 x 48 cells with 2 coarse levels.

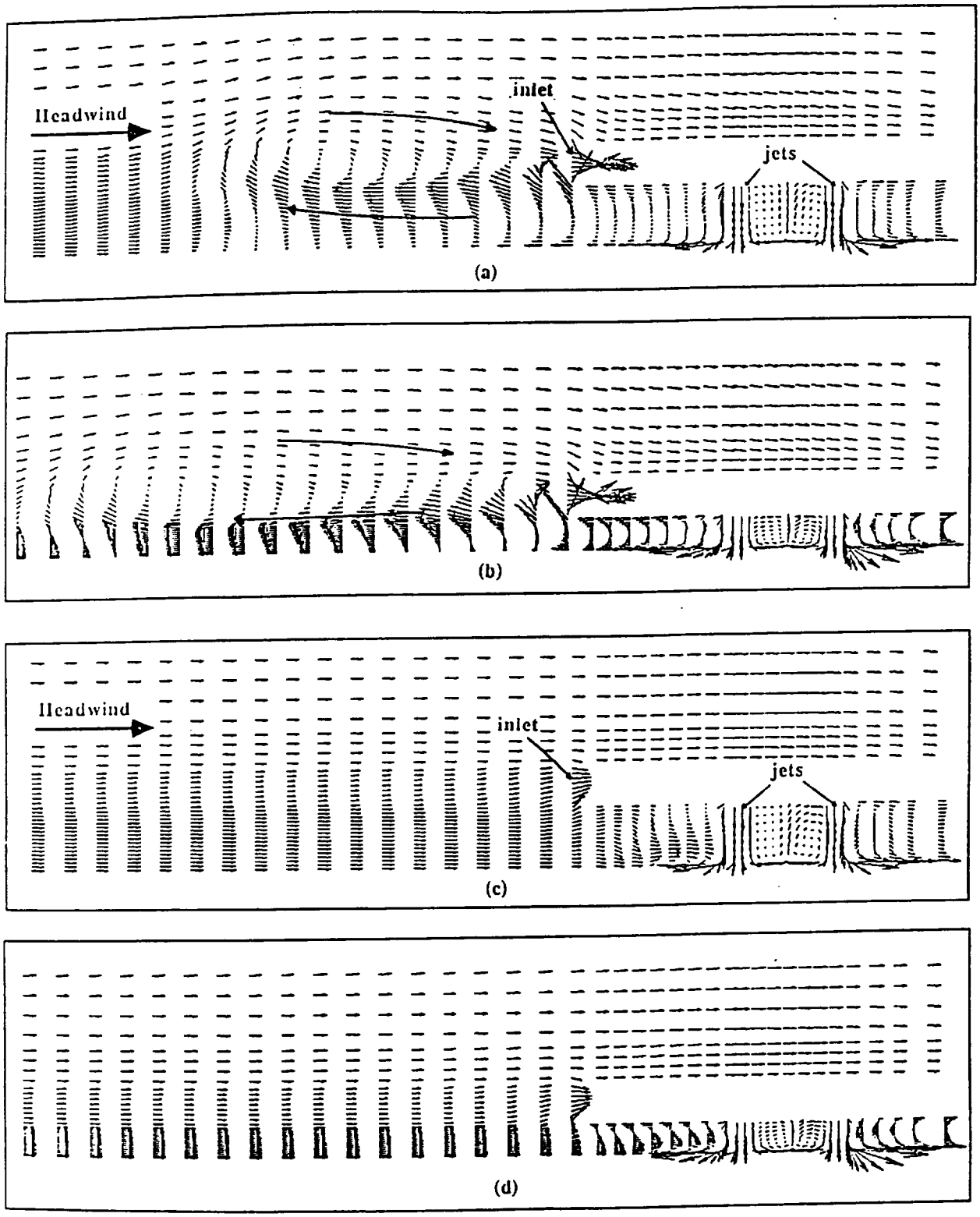

Figure 3: Velocity vectors in x-y plane passing through the jet centerline (z=0). Plot domain extends from -46 ≤x/d≤ 14 and from the ground plane to y/d = 20. Vector scales vary in different regions of the flow field.(a) Case 1 (h/d = 4, U_∞/U_j = 0.03); (b) Case 2 (h/d = 2, U_∞/U_j = 0.03); (c) Case 3 (h/d = 4, U_∞/U_j = 0.09); (d) Case 4 (h/d = 2, U_∞/U_j = 0.09).

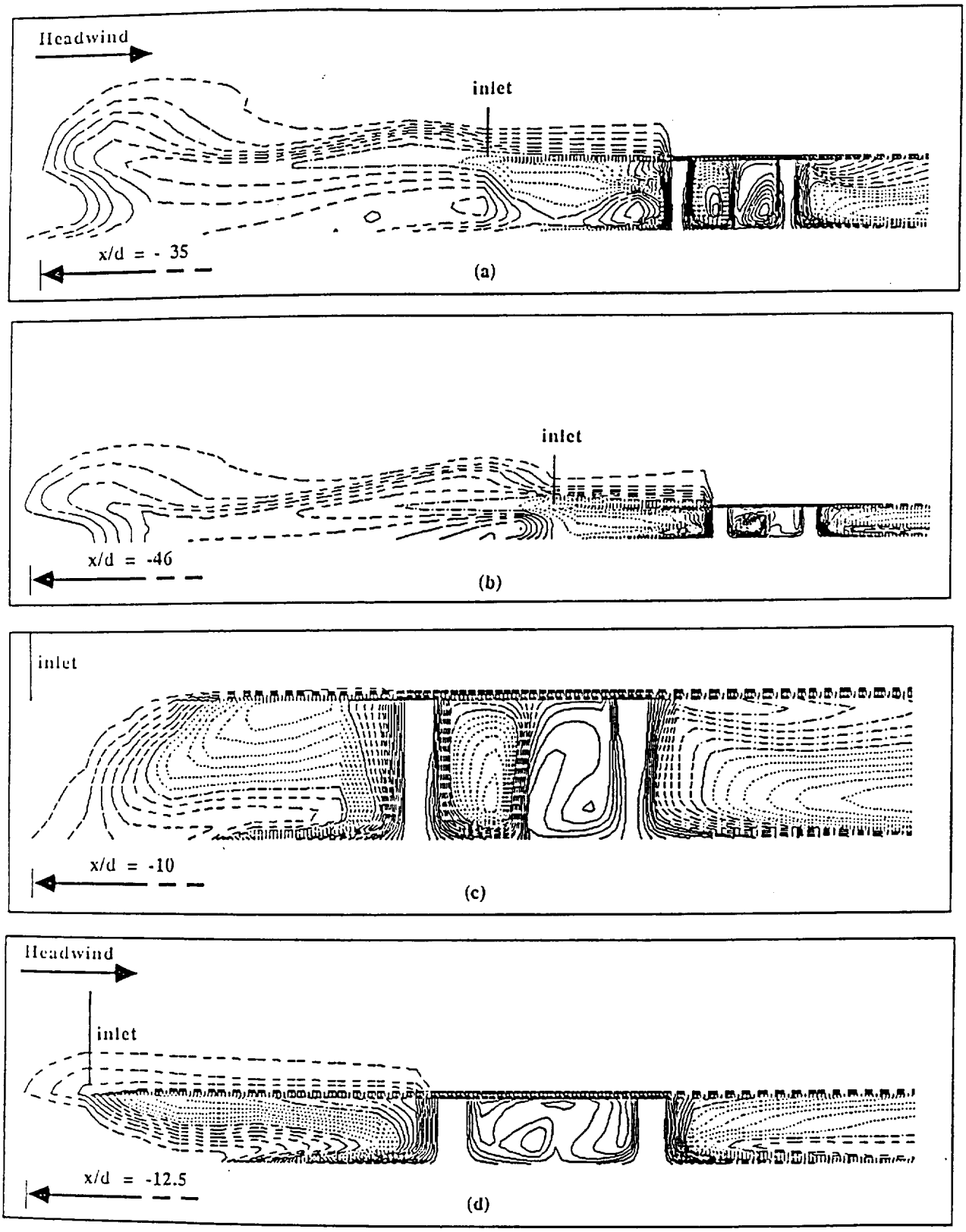

Figure 4: Temperature contours in x-y plane passing through the jet centerline (z=0). Contour levels: - - - 300-475 K; ..... 475-650 K; __ . __ 650-825 K; _____ 825-1000 K. (a) Case 1 (h/d = 4, $U_\infty/U_j = 0.03$); (b) Case 2 (h/d=2, $U_\infty/U_j =$ 0.03); (c) Case 3 (h/d = 4, $U_\infty/U_j = 0.09$); (d) Case 4 (h/d=2, $U_\infty/U_j = 0.09$).

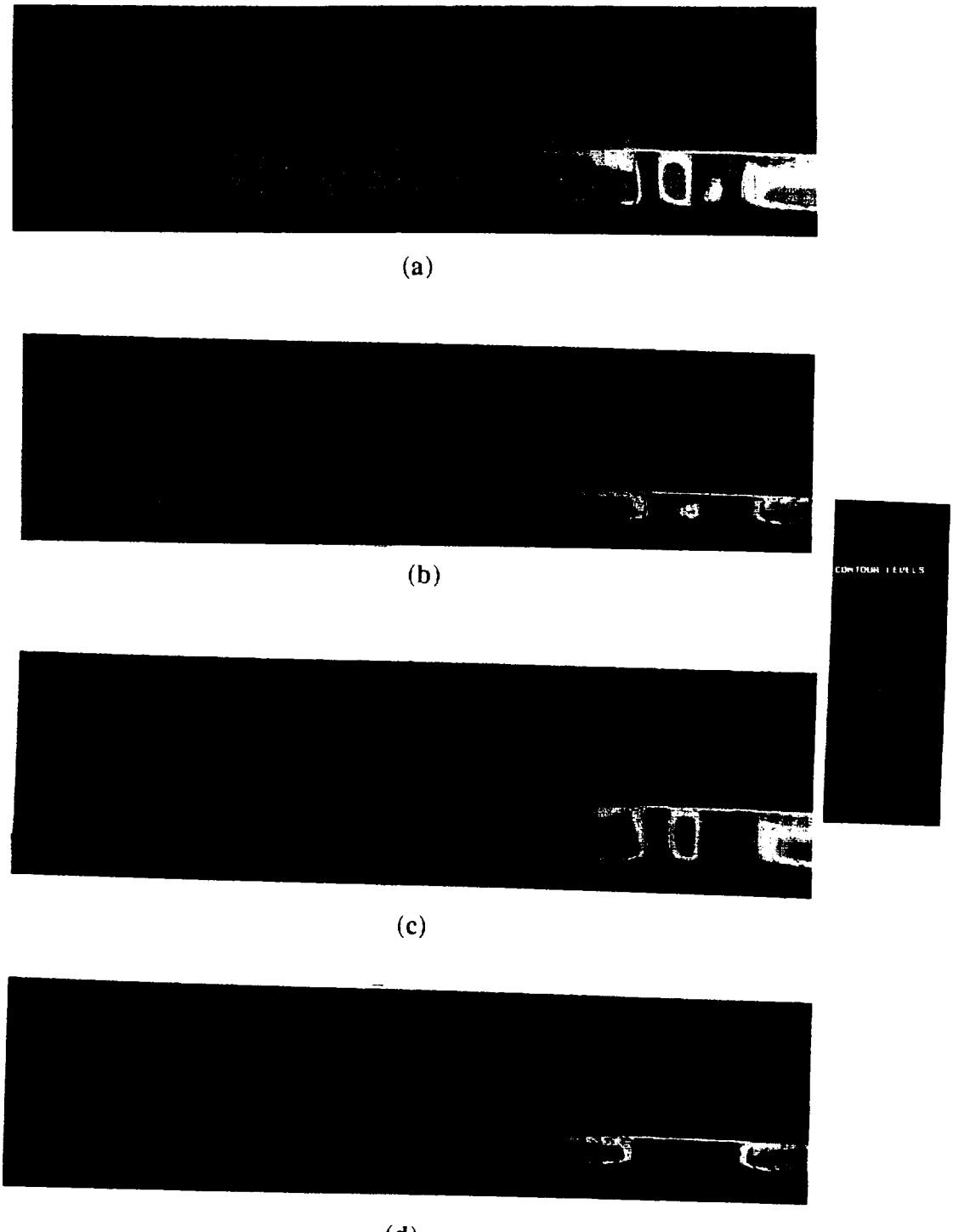

(a)

(b)

(c)

(d)

Figure 5: Superimposed velocity vectors and temperature color contours in x-y plane through the jet centerline (Figures 3 and 4). Plot domain extends from -46 ≤ x/d ≤ 14 and from the ground plane to y/d=20.(a) Case 1; (b) Case 2; (c) Case 3; (d) Case 4.

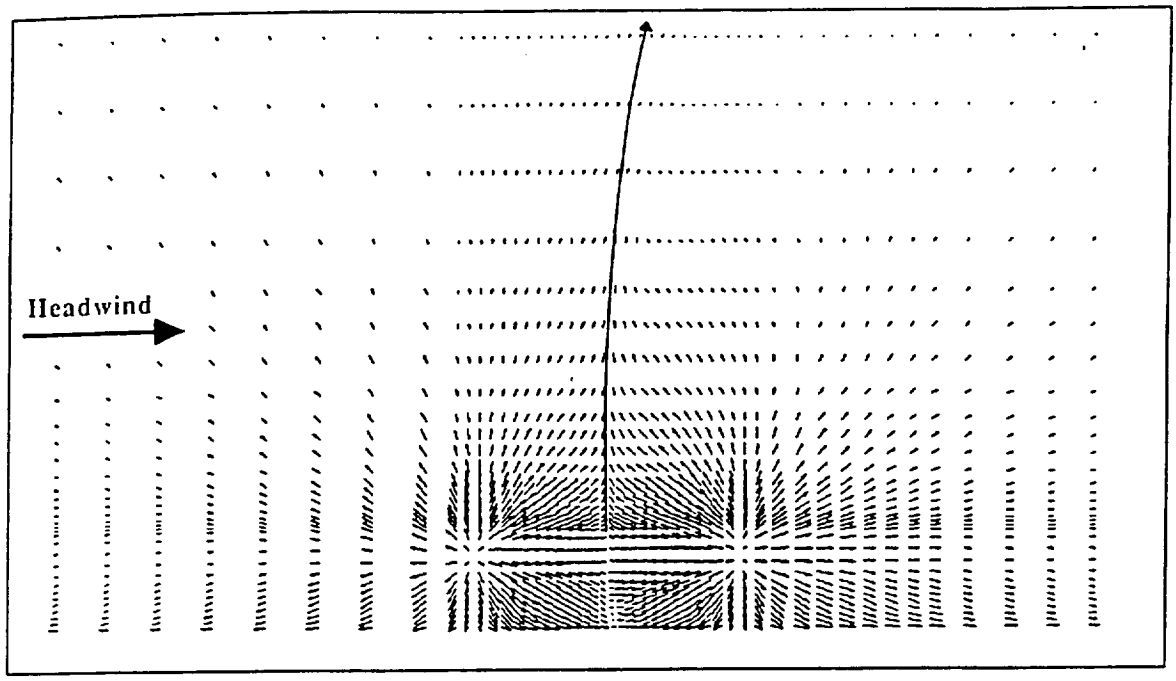

(a)

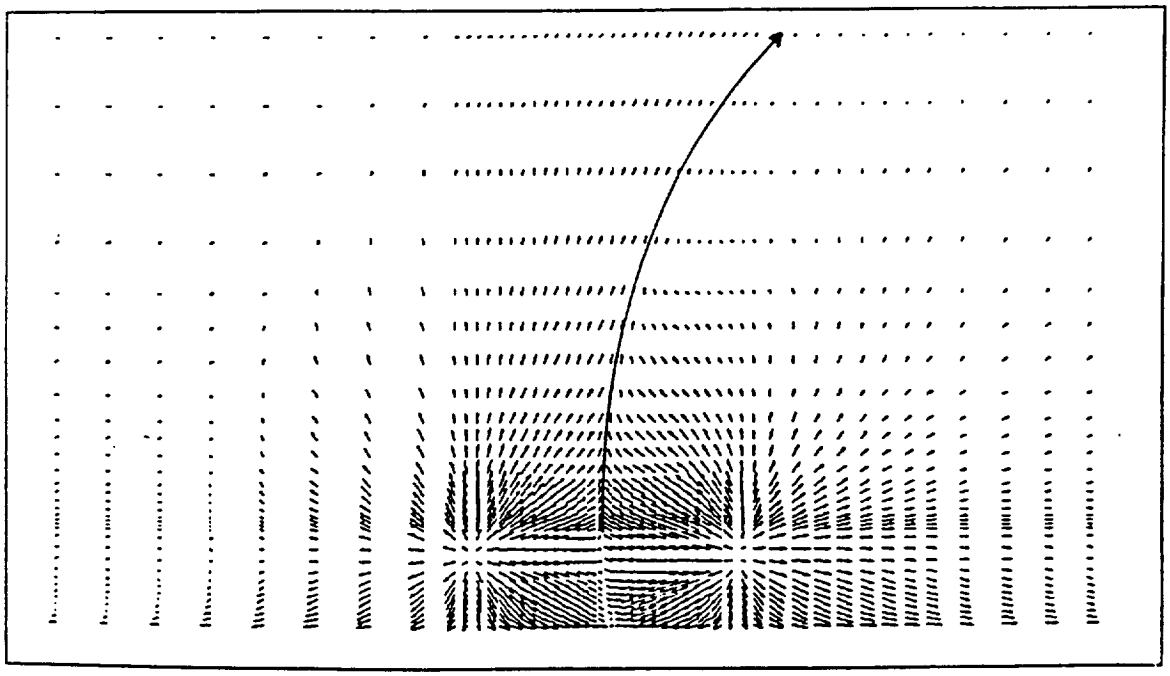

(b)

Figure 6: Velocity vectors in x-z ground plane. Plot domain extends from $-10 \leq x/d \leq 14$ and from symmetry plane to z/d=12.(a) Case 1 (h/d=4, $U_\infty/U_j = 0.03$); (b) Case 3 (h/d=4, $U_\infty/U_j = 0.09$).

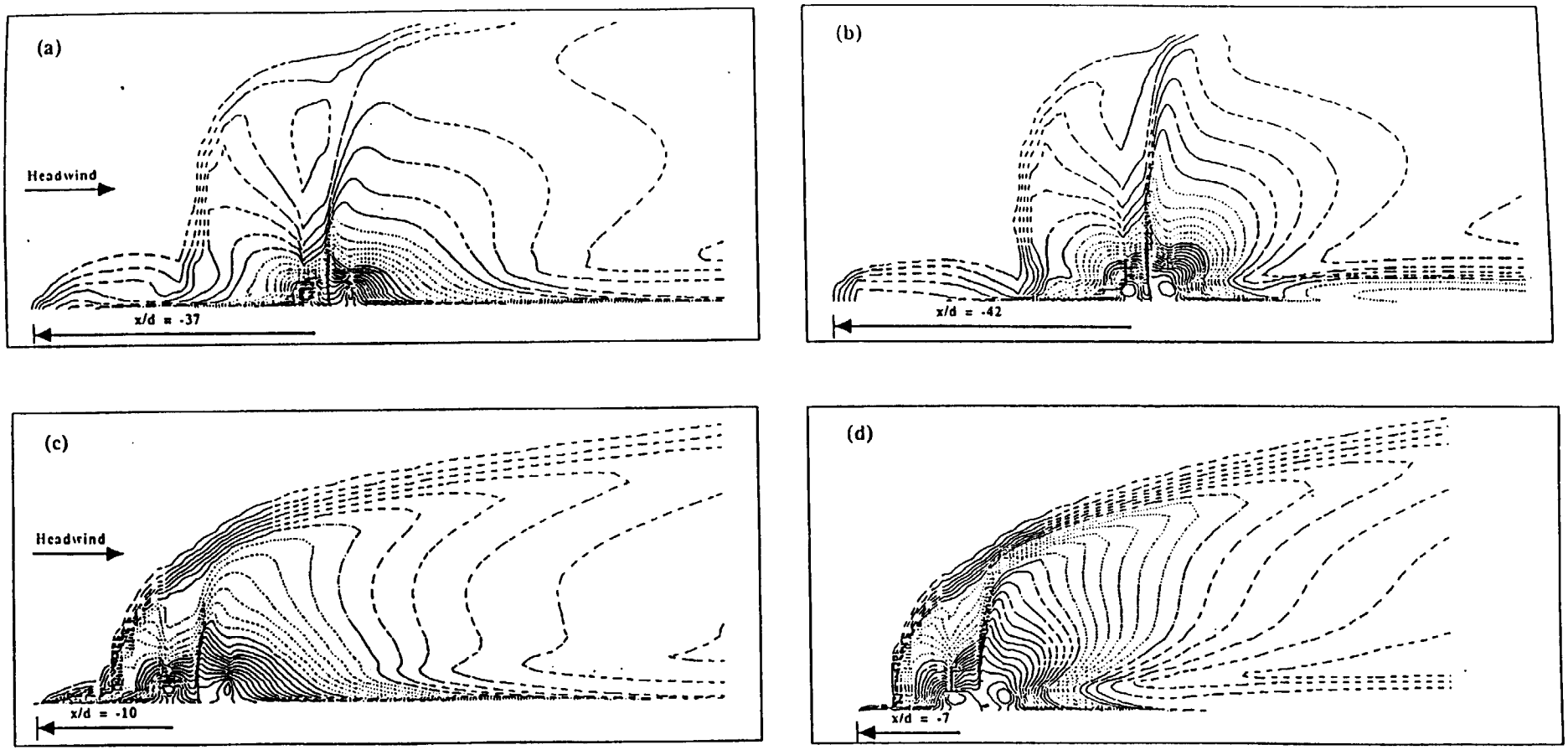

Figure 7: Temperature contours in x-z ground plane. Contour levels: - - - 300-475 K; ..... 475-650 K; ___ . ___ 650-825 K; _____ 825-1000 K. (a) Case 1 (h/d=4, $U_\infty/U_j = 0.03$); (b) Case 2 (h/d=2, $U_\infty/U_j=0.03$); (c) Case 3 (h/d=4, $U_\infty/U_j = 0.09$); (d) Case 4 (h/d=2, $U_\infty/U_j=0.09$).

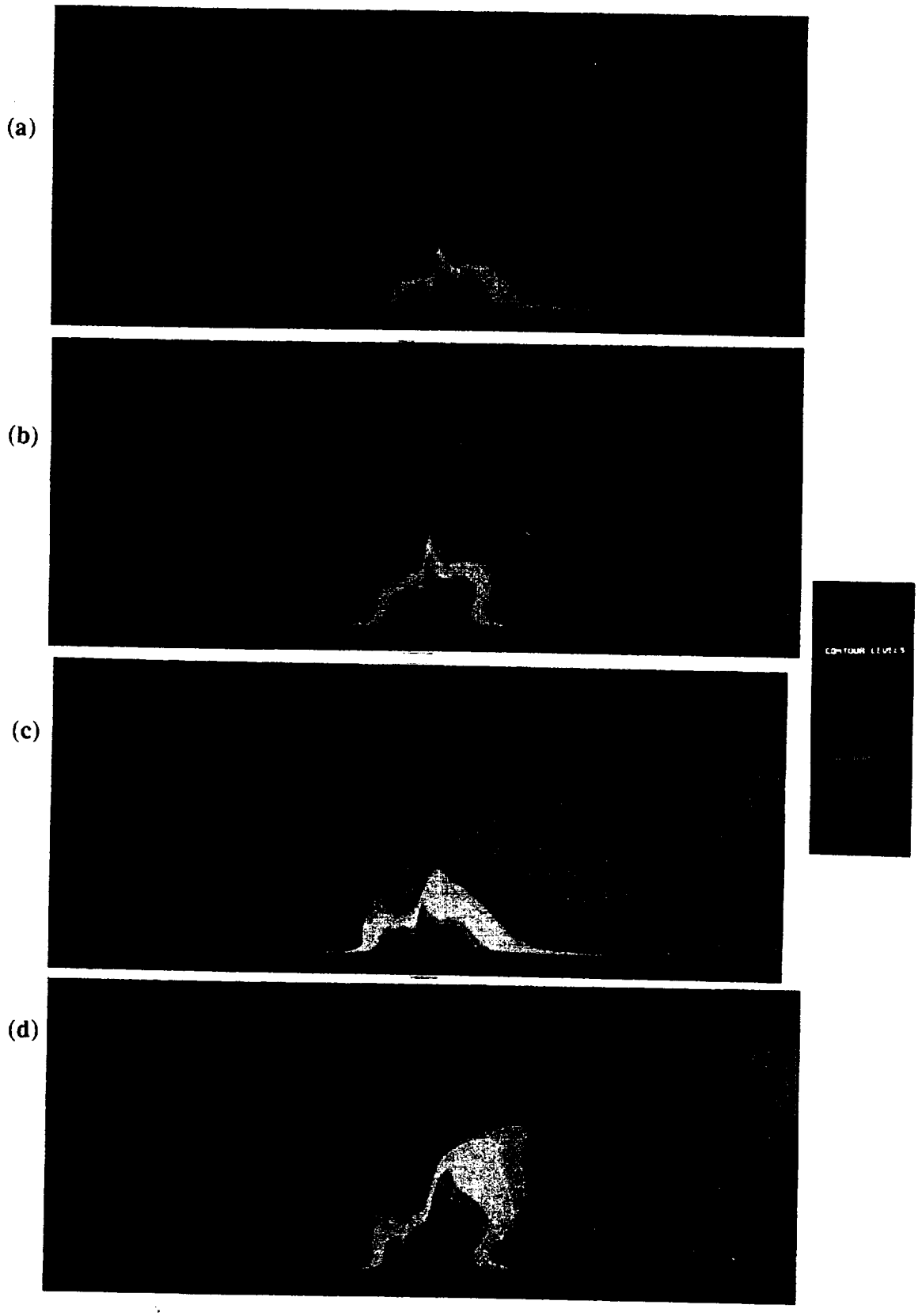

Figure 8: Temperature color contours in x-z ground plane (Figure7). (a) Case 1; (b) Case 2; (c) Case 3; (d) Case 4.

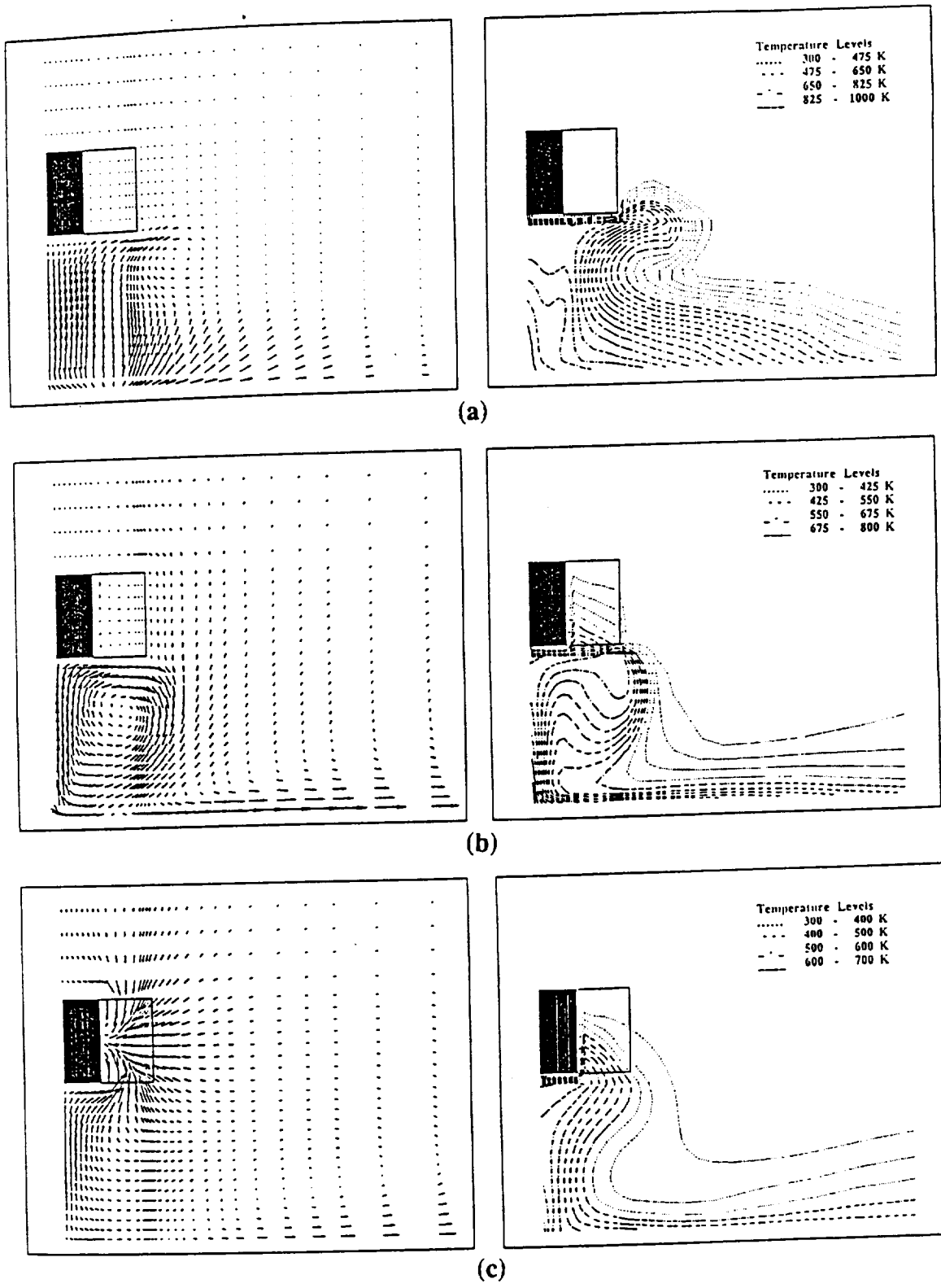

Figure 9: Velocity vector and temperature contours in different z-y planes for Case 1 (h/d = 4, $U_\infty/U_j = 0.03$). Plot domain extends from symmetry plane to z/d = 9 and from ground plane to y/d = 5. (a) x/d = 3 (between fore and aft jets in the fountain upwash region); (b) x/d = -5 (between inlet and fore jet); (c) x/d = -10 (at inlet).

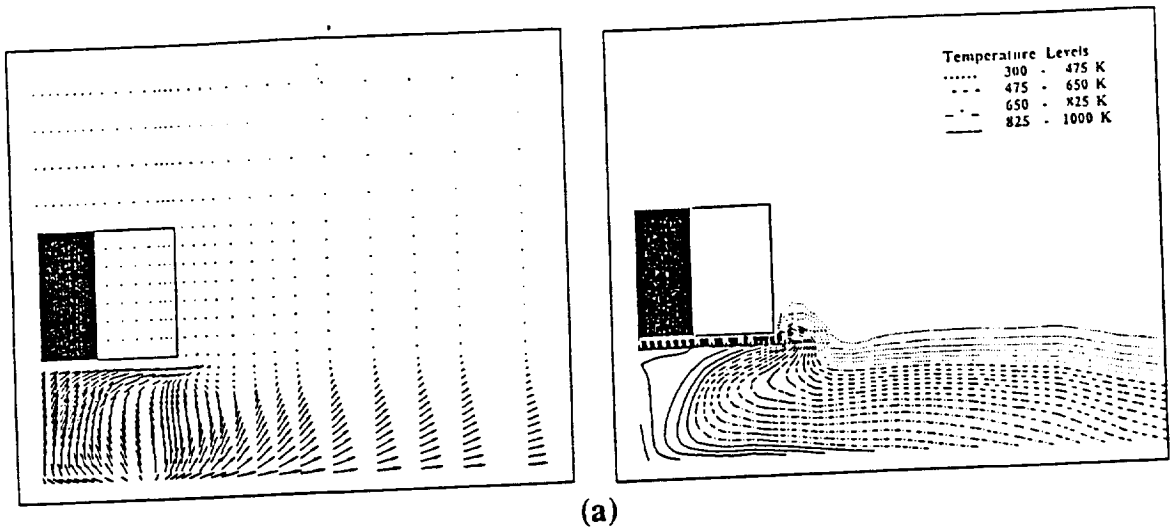

(a)

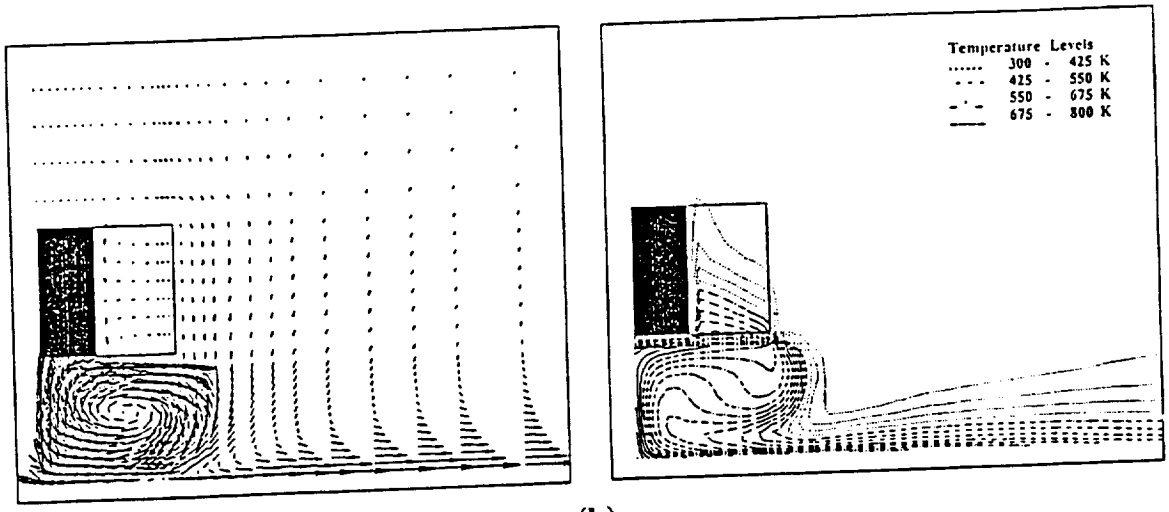

(b)

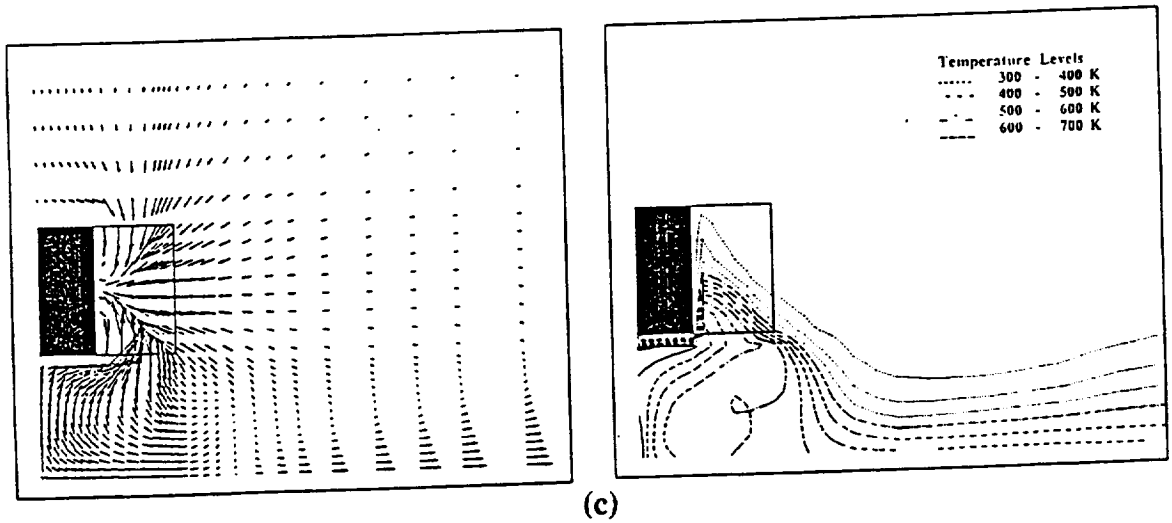

(c)

Figure 10: Velocity vector and temperature contours in different z-y planes for Case 2 (h/d = 2, $U_\infty/U_j = 0.03$). Plot domain extends from symmetry plane to z/d = 9 and from ground plane to y/d = 5.(a) x/d = 3 (between fore and aft jets in the fountain upwash region); (b) x/d = -5 (between inlet and fore jet); (c) x/d = -10 (at inlet).

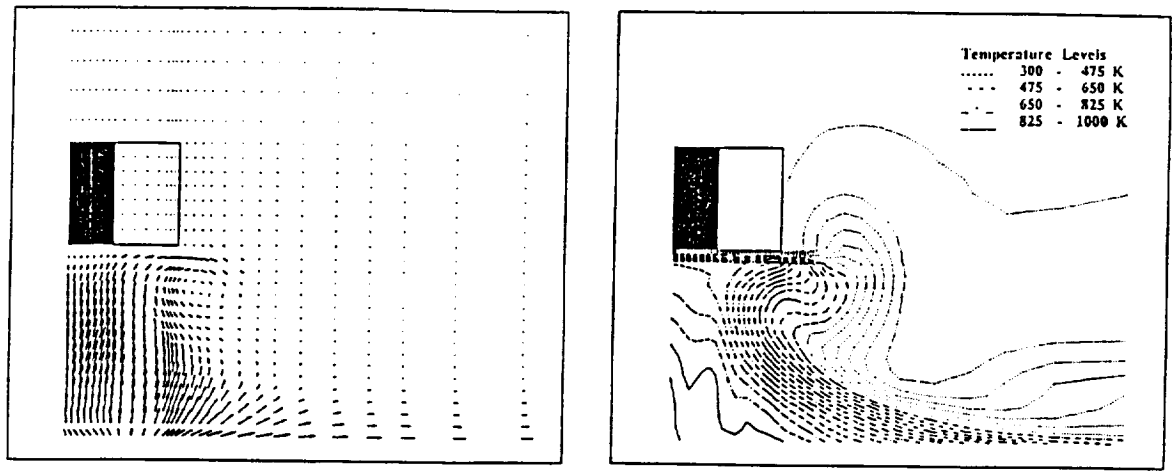

(a)

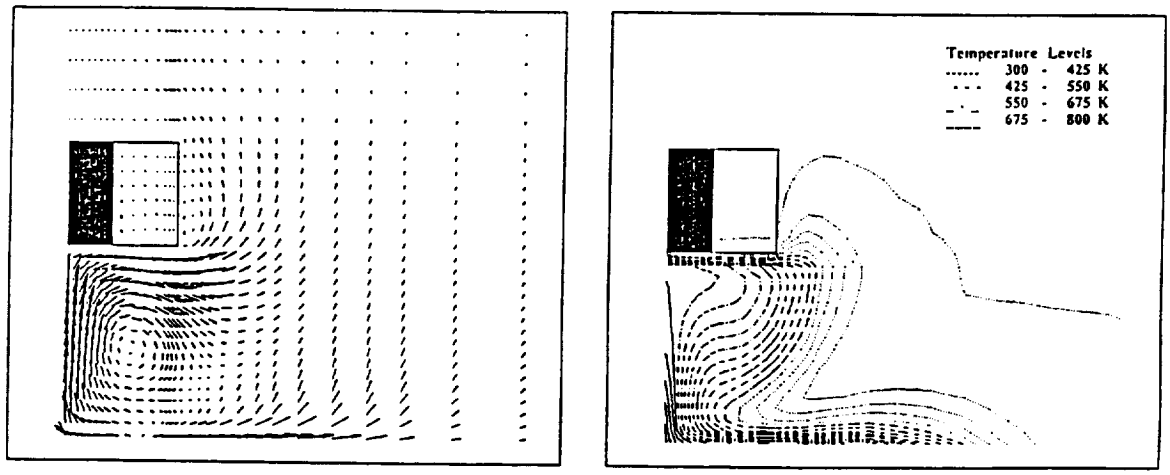

(b)

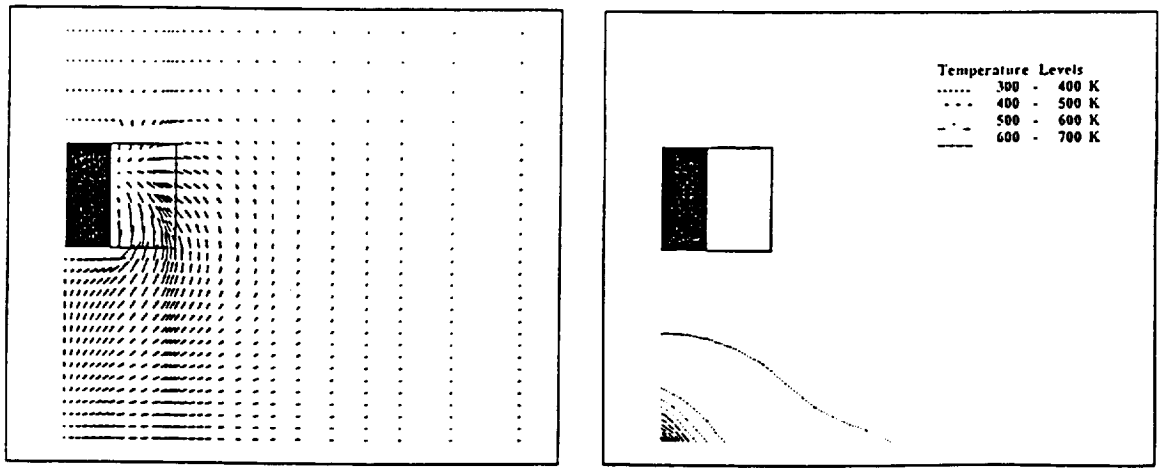

(c)

Figure 11: Velocity vector and temperature contours in different z-y planes for Case 3 (h/d = 4, $U_\infty/U_j = 0.09$). Plot domain extends from symmetry plane to z/d = 9 and from ground plane to y/d = 5. (a) x/d = 3 (between fore and aft jets in the fountain upwash region); (b) x/d = -5 (between inlet and fore jet); (c) x/d = -10 (at inlet).

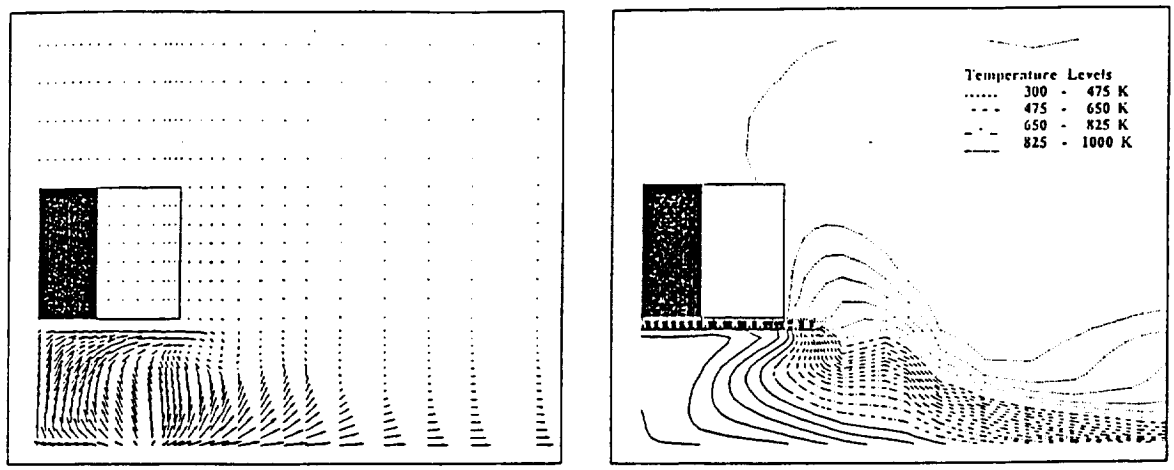

(a)

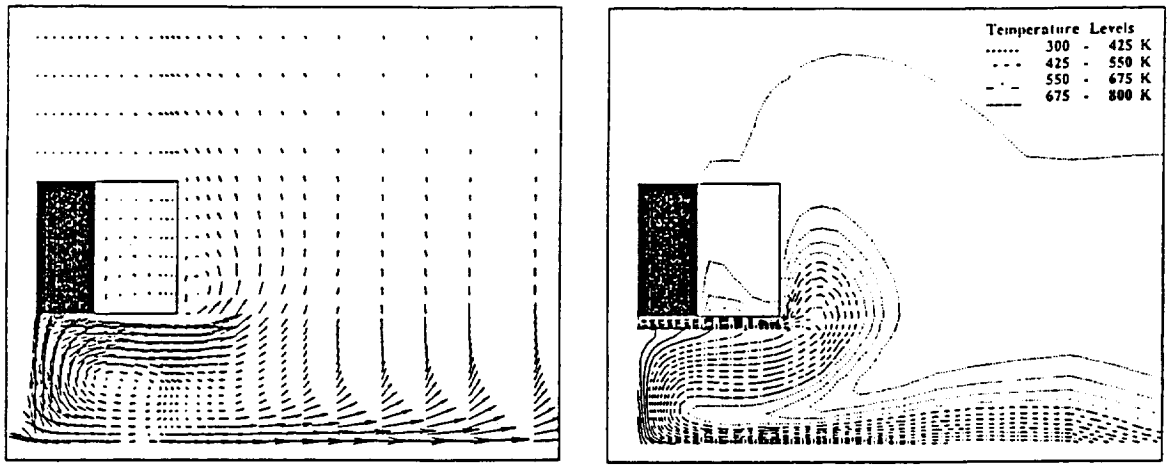

(b)

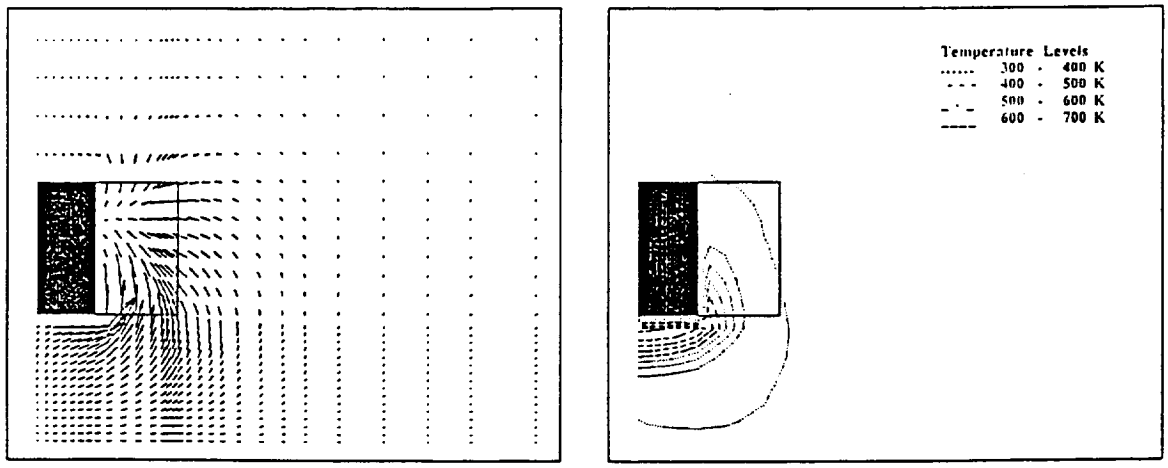

(c)

Figure 12: Velocity vector and temperature contours in different z-y planes for Case 4 (h/d = 2, U_∞/U_j = 0.09). Plot domain extends from symmetry plane to z/d = 9 and from ground plane to y/d = 5. (a) x/d = 3 (between fore and aft jets in the fountain upwash region); (b) x/d = -5 (between inlet and fore jet); (c) x/d = -10 (at inlet).

APPENDIX C

HOT GAS ENVIRONMENT AROUND STOVL AIRCRAFT IN GROUND PROXIMITY—PART 2: NUMERICAL STUDY

Hot Gas Environment Around STOVL Aircraft in Ground Proximity—Part 2: Numerical Study

D. K. Tafti* and S. P. Vanka†
University of Illinois, Urbana-Champaign, Urbana, Illinois 61801

Ingestion of hot exhaust gases by the engines of Short Take-off and Vertical Landing (STOVL) aircraft has been an important research problem for several years. The hot gas environment around STOVL aircraft is three-dimensional and turbulent. In this study, the Navier-Stokes equations governing the hot gas ingestion flowfield are solved by an efficient finite-difference calculation procedure. The complete geometry, including the head wind and the fuselage, is simulated. Four demonstration calculations with variations in the height of the fuselage and the head wind velocity are presented. It is shown that the calculation procedure efficiently provides a solution to the governing equations, and produces realistic descriptions of the flowfield and temperature field.

Introduction

A NUMBER of interesting fluid dynamic effects have been identified when the lift jets of Short Take-off and Vertical Landing (STOVL) aircraft impinge on the ground surface.[1-3] First, as the lift jets expand, they entrain the surrounding fluid, causing a negative pressure underneath the fuselage and a loss in lift. As the jets impinge on the ground and spread radially outwards, the wall jets further entrain external fluid and increase the loss in lift. In a multiple-jet configuration, these wall jets collide with each other and turn upwards to form an upwash fountain. This fountain flow has two main effects on the STOVL aircraft dynamics. First, an increase in lift force is caused when the fountain impinges on the aircraft fuselage. The recovery in lift is a positive effect of the upwash flow. However, this impinging fluid can also flow along the fuselage surface and eventually make its way into the engine inlets. Because the temperature of the fountain flow is much hotter than the ambient air, its ingestion by the engine can reduce the power and cause thermal stresses in the components. In addition to the fountain flow, another mechanism for hot gas ingestion results from the interaction of the forward-moving wall jet with the headwind. When the headwind and the wall jet collide, a stagnation region is formed, and the wall jet is turned into a ground vortex.[2] This ground vortex can subsequently be re-ingested by the engine, resulting in a further loss in power. However, the hot gas ingestion process depends on where and how the inlets to the engine are located with respect to the approach flow. For strong headwinds, the ground vortex can be pushed behind the engine inlets, such that no hot gases are ingested. It can be recognized that the overall flowfield governing these fluid dynamic interactions is strongly three-dimensional, as well as turbulent.

In the last three decades, a number of studies addressing these issues has been conducted (see Ref. 3 for good review). A majority of these studies were experimental in nature, although some analytical studies of the individual processes, such as single jet impingement, have also been conducted. These studies have identified the fundamental processes and, to a certain extent, quantified the effect of the parameters on hot gas ingestion and fountain flow. However, detailed measurements of the velocity and temperature fields in the fountain region and in the ground vortex in realistic operating conditions are not currently available. Recently, Saripalli[4] conducted some experiments in a water tunnel in which Laser-Doppler velocimeter and laser imaging techniques were used to study the fountain region of the lift jets. These studies involved isothermal flows, and were limited to the fountain formation.

With recent advances in the development of powerful digital computers, it has now become possible to numerically solve the equations that govern the transport of mass, momentum, and enthalpy. However, because the flow is turbulent, such studies must necessarily make assumptions on the macroscopic behavior of turbulence. Despite the inherent limitations of such an approach in representing all the effects of turbulence with precision, it has become a useful engineering tool. Numerical computation of the complete STOVL aircraft flowfield requires the solution of nonlinear partial-differential equations that govern the transport of mass, momentum, and heat in three-dimensional space with boundary conditions that describe the lift jets, aircraft fuselage, and the head wind. Because of the complexity of such solutions and limited computer capabilities, until recently most numerical studies were limited to two dimensions, in which simplifications in the spanwise direction were made. Kotansky and Bower[5] were probably the first investigators to apply a Navier-Stokes analysis to the study of planar jet impingement of relevance to Vertical Take-Off and Landing (VTOL) aircraft. In their analysis, a one-equation model for turbulence kinetic energy was integrated with equations describing the stream function and transport of vorticity. A numerical solution of an impinging jet was obtained and compared with experimental data. This study was followed by Agarwal and Bower,[6] who improved the turbulence model by considering an additional equation for the turbulence dissipation. Because the improved model explicitly calculated the local-length scale of turbulence, the flowfields predicted by their model displayed better agreement with experimental data.

Although the hot gas ingestion process results primarily from the impingement of the lift jets, the eventual ingestion is dictated by the complete flow dynamics, including the formation of the fountain upwash and its interaction with the headwind. For stronger headwind speeds, it is possible to push the ground vortex downstream of the engine inlet and, thus,

Presented as Paper 90-2270 at the AIAA/SAE/ASME/ASEE 26th Joint Propulsion Conference, Orlando, FL, July 16-18, 1990; received Aug. 16, 1990; revision received Dec. 3, 1990; accepted for publication Dec. 27, 1990.

*Research Associate, Department of Mechanical and Industrial Engineering; currently at NCSA-UIUC. Member AIAA.

†Associate Professor, Department of Mechanical and Industrial Engineering. Member AIAA.

completely avoid its contribution to hot gas ingestion. Also, the collision of the wall jets and the fountain formation can be affected by the headwind and the geometry of the fuselage under surface. In addition, placement of Lift Increasing Devices (LIDs)[2] and other obstructions can divert the fountain flow from the engine inlets, thereby reducing the severity of the hot gas ingestion. In order to better understand all the flow processes, a complete Navier-Stokes analysis, including the far-field condition of a prescribed headwind, is necessary. Although such an analysis is computationally very intensive, the benefits are significant for evaluating the effects of geometric and flow parameters. Recently, an important contribution has been made in this direction by VanOverbeke and Holdeman.[7] In this study, the complete fuselage, headwind, and multiple impinging jets were numerically simulated, and the temperature fields close to the engine inlet face were studied. By varying the head wind and the impingement height, they were able to alter the ingestion pattern and quantify their effects. A finite-difference computer program[8] was used, and the flow domain was discretized into a relatively large number of finite volumes.

A primary drawback of numerical computations of three-dimensional elliptic fluid flows is that they can require substantial amounts of computer time to obtain a converged solution. These large computational costs often discourage systematic and thorough investigations of the effects of various parameters. However, with research into faster converging numerical algorithms, it is possible to substantially reduce these computer times. In this paper, we demonstrate the applicability of one such algorithm,[9] which is based on the concept of using multiple levels of grids[10] to obtain faster convergence. In this study, the geometrical configuration studied by VanOverbeke and Holdeman[7] is considered, and a set of four calculations have been performed. To compare our results with those of VanOverbeke and Holdeman,[7] we have simulated exactly the same configurations, albeit with a finer grid, and compared the computer times and the flowfields. The four calculations in this study differ in the height of the jets from the ground and the ratio of the head wind to the jet velocity.

The following sections briefly describe the solution procedure and present the results of the calculations. In Part 1 of this study, a separate experimental investigation is presented by McLean et al.,[11] in which the concentration of the exhaust jets is quantified through a laser imaging technique.

Governing Equations and Solution Algorithm

The flowfield and temperature field around the STOVL aircraft are governed by the following set of elliptic partial-differential equations. In the present analysis, the flow is considered to be steady in the time-averaged sense, and the effects of turbulence are captured by a turbulence model.[12] The governing equations can be written as follows:

$$\text{mass continuity: } \frac{\partial}{\partial x}(\rho u) + \frac{\partial}{\partial y}(\rho v) + \frac{\partial}{\partial z}(\rho w) = \dot{m} \quad (1)$$

$$x\text{-momentum: } \frac{\partial(\rho u u)}{\partial x} + \frac{\partial(\rho u v)}{\partial y} + \frac{\partial(\rho u w)}{\partial z} = -\frac{\partial P}{\partial x} + \frac{\partial}{\partial x}\left(2\mu \frac{\partial u}{\partial x}\right) + \frac{\partial}{\partial y}\left[\mu\left(\frac{\partial u}{\partial y} + \frac{\partial v}{\partial x}\right)\right] + \frac{\partial}{\partial z}\left[\mu\left(\frac{\partial w}{\partial x} + \frac{\partial u}{\partial z}\right)\right] + \dot{m} u_{in_j} \quad (2)$$

$$y\text{-momentum: } \frac{\partial(\rho u v)}{\partial x} + \frac{\partial(\rho v v)}{\partial y} + \frac{\partial(\rho v w)}{\partial z} = -\frac{\partial P}{\partial y} + \frac{\partial}{\partial x}\left[\mu\left(\frac{\partial u}{\partial y} + \frac{\partial v}{\partial x}\right)\right] + \frac{\partial}{\partial y}\left(2\mu \frac{\partial v}{\partial y}\right) + \frac{\partial}{\partial z}\left[\mu\left(\frac{\partial w}{\partial y} + \frac{\partial v}{\partial z}\right)\right] + \dot{m} v_{in_j} \quad (3)$$

$$z\text{-momentum: } \frac{\partial(\rho u w)}{\partial x} + \frac{\partial(\rho v w)}{\partial y} + \frac{\partial(\rho w w)}{\partial z} = -\frac{\partial P}{\partial z} + \frac{\partial}{\partial x}\left[\mu\left(\frac{\partial w}{\partial x} + \frac{\partial u}{\partial z}\right)\right] + \frac{\partial}{\partial y}\left[\mu\left(\frac{\partial v}{\partial z} + \frac{\partial w}{\partial y}\right)\right] + \frac{\partial}{\partial z}\left(2\mu \frac{\partial w}{\partial z}\right) + \dot{m} w_{in_j} \quad (4)$$

$$\text{turbulence energy: } \frac{\partial}{\partial x}(\rho u k) + \frac{\partial}{\partial y}(\rho v k) + \frac{\partial}{\partial z}(\rho w k) = \frac{\partial}{\partial x}\left(\Gamma_k \frac{\partial k}{\partial x}\right) + \frac{\partial}{\partial y}\left(\Gamma_k \frac{\partial k}{\partial y}\right) + \frac{\partial}{\partial z}\left(\Gamma_k \frac{\partial k}{\partial z}\right) + G - \rho\varepsilon + \dot{m} k_{in_j} \quad (5)$$

$$\text{dissipation of turbulence energy: } \frac{\partial}{\partial x}(\rho u \varepsilon) + \frac{\partial}{\partial y}(\rho v \varepsilon) + \frac{\partial}{\partial z}(\rho w \varepsilon) = \frac{\partial}{\partial x}\left(\Gamma_\varepsilon \frac{\partial \varepsilon}{\partial x}\right) + \frac{\partial}{\partial y}\left(\Gamma_\varepsilon \frac{\partial \varepsilon}{\partial y}\right) + \frac{\partial}{\partial z}\left(\Gamma_\varepsilon \frac{\partial \varepsilon}{\partial z}\right) + C_1 G \frac{\varepsilon}{k} - C_2 \rho \frac{\varepsilon^2}{k} + \dot{m} \varepsilon_{in_j} \quad (6)$$

$$\text{enthalpy: } \frac{\partial}{\partial x}(\rho u H) + \frac{\partial}{\partial y}(\rho v H) + \frac{\partial}{\partial z}(\rho w H) = \frac{\partial}{\partial x}\left(K \frac{\partial T}{\partial x}\right) + \frac{\partial}{\partial y}\left(K \frac{\partial T}{\partial y}\right) + \frac{\partial}{\partial z}\left(K \frac{\partial T}{\partial z}\right) + \dot{m} H_{in_j} \quad (7)$$

$$\text{equation of state: } \rho = P/RT \quad (8)$$

where u, v, w, are the velocities in the x, y, and z directions, respectively; P is the pressure, R is the gas constant, and G is the production of turbulent kinetic energy. In all these equations, the diffusive coefficients contain the effects of laminar as well as turbulent diffusion. Standard values of the constants in the turbulence model[12] are used.

These equations are solved on a rectangular domain that envelopes the aircraft fuselage and the exhaust jets. Because the current computer program is limited to the use of rectangular grids, the fuselage of the aircraft was modeled to be of rectangular shape. However, efforts are currently under way to extend the program to handle grids of arbitrary inclinations (boundary-fitted grids), which will then permit a more realistic representation of the aircraft shape and angles of attack. The boundary conditions and solution domain considered in current calculations will be described in a later section.

The above equations are finite-differenced by a hybrid scheme[9] combining first- and second-order differencing for the total convective and diffusive operator. At high-cell Peclet numbers, the finite-differencing scheme becomes first-order accurate to preserve stability of the solution procedure. The multigrid solution technique[10] differs from the single grid technique in the manner the finite-difference equations are solved to the required accuracy. It is well-known that, for elliptic equations, single grid techniques converge poorly when the

finite-difference grid contains a large number of mesh points. This results from the low-frequency errors that are slow to converge on a given fine grid. In the multigrid concept, a series of fine and coarse grids are used, and the solution is switched between the coarse and fine grids such that errors of all frequencies converge at the same rate. This novel concept was originally proposed for model elliptic equations, but recently it has become popular in solving practical fluid flows.

The principle behind the multigrid procedure may be explained as follows. Consider an elliptic equation that is discretized by finite-difference or finite element methods. Generally, an iterative procedure that is designed to obtain a solution to the discrete equations will converge rapidly in the first few iterations, but subsequently the convergence deteriorates. It can be shown through formal analyses that the cause for this poor convergence is the presence of low-frequency errors that are not resolved well on any given grid. However, these errors can converge faster if the grid is coarse; therefore, in the multigrid procedure, these errors are interpolated to a coarser grid and solved. The results of this coarse grid solution are then put back on the finer grid solution through extrapolation. In the case of a calculation with many mesh points, several layers of coarse meshes can be used to obtain rapid convergence. However, the coarsest grid is often dictated by the constraints of geometry and boundary conditions.

In the present solution scheme, we have combined the multigrid technique with a coupled solution scheme for the momentum and continuity equations. The velocities and pressures are obtained by a block-implicit solution of the momentum and continuity equations. Because this procedure is explained in previous works by one of the authors,[9] it is not elaborated on here. However, in order to simulate the fuselage and the lift jets, the procedure has been extended to handle internal obstacles and mass and momentum injections. These features have been incorporated in a manner that maintains consistency between the coarse and fine grids—a necessary feature for the algorithm to eventually converge to the correct solution. It must be pointed out that, although the coarse grids are used, the final solution is obtained on the finest grid in the system. Thus the intermediate grids are used only for accelerating the convergence rate, and do not influence the final converged solution.

The present computer program was initially validated in model laminar flow problems prior to being used for more complex flows. Recently, the computer program was applied to calculate the interaction of a transverse jet with a cross-stream flow.[13] Also, the program was validated by applying it to studying the twin-jet upwash flow in isolation and comparing[14] the resulting solutions with the experimental data of Saripalli.[4] These two studies, as well as a calculation of a single jet impingement (unpublished), provide confidence in the use of the present computer program to the complete STOVL configuration.

The next section describes the computational domain and a typical convergence history of the multigrid solution procedure. Simulated flowfields and temperature fields are presented, along with a discussion on the mechanism of hot gas ingestion for a four-jet configuration. These results compare qualitatively with the flow imaging data of McLean, Sullivan, and Murthy,[11] as well as with calculations presented by Van Overbeke and Holdeman.[7]

Results

Computational Details and Convergence Histories

In this study, four test cases have been considered, which are similar to those studied in Ref. 7. The important flow and geometrical parameters are outlined in Table 1. The four cases differ in the height of the fuselage from the ground plane (h/d, where d is the diameter of the lift jets) and the headwind to jet velocity ratio (U_∞/U_j). The solution domain is a three-dimensional wind tunnel with overall dimensions of 136d in the streamwise direction (x), 27 or 29d in the cross-stream direction (y), and 40d in the spanwise direction (z). These large dimensions are necessary to accurately resolve the flowfield around the jets and the fuselage without any interference from the simulated boundaries. Figure 1 shows the computational grid used and the flow geometry. The geometry simulates four jets (due to symmetry, only half the domain is considered) issuing from the engine with the engine inlet located 10 jet diameters upstream of the fore jet axis. The distance between the fore and aft jet axis is 6 diameters; the spanwise distance between the jets is 3.2 diameters. The fuselage extends throughout the calculation domain, and is 2.5 diameters in height and 2.2 diameters in width. The inlet, which is 67 jet diameters from the entrance of the test section, has a height of 2.5 diameters and a width of 1.4 diameters. It is adjacent to the fuselage in the spanwise direction and extends 9.5 jet diameters up to the fore jet, after which it becomes part of the fuselage. The calculation domain is divided into 100 computational cells in the x direction, 44 in the y, and 48 in the z direction, giving a total of about 211,000 cells. The particular grid distribution was chosen to provide good resolution in the near field of the jets and, at the same time, keep the grid expansion ratio as small as possible. The grid distribution was also influenced by the necessity to accommodate internal obstacles and baffles, such that grid lines bounded the surfaces of these structures.

At the inlet of the test section, uniform velocity and temperature conditions are prescribed for the incoming headwind; the turbulent kinetic energy was assumed to be 1% of the mean kinetic energy. At the exit, outflow boundary con-

Table 1 Flow and geometry parameters

Case	U_∞/U_j	h/d	Ma_j	$Re_\infty \times 10^{-4}$	$Re_j \times 10^{-5}$
1	0.03	4.0	0.47	3.3	3.3
2	0.03	2.0	0.47	3.3	3.3
3	0.09	4.0	0.47	9.9	3.3
4	0.09	2.0	0.47	9.9	3.3

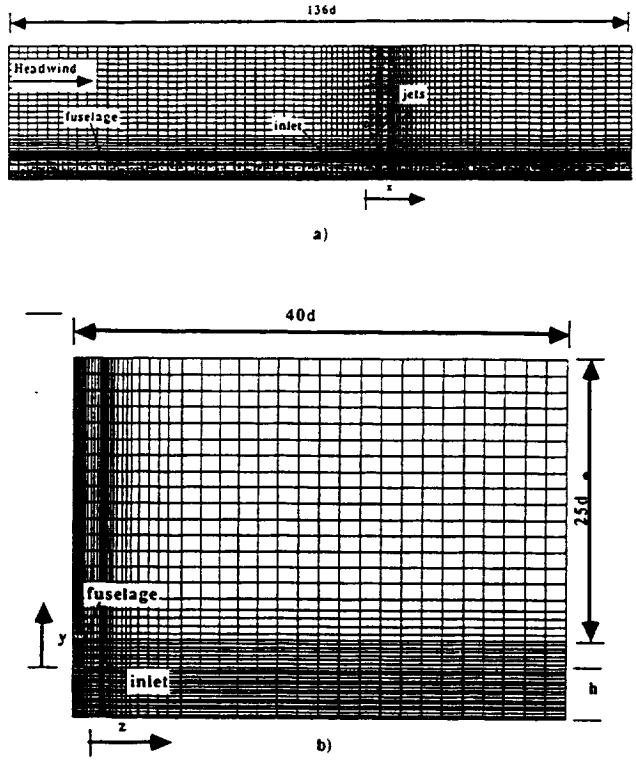

Fig. 1 Computational domain and grid distribution: a) side view; b) front view (not to same scale as a)).

ditions are prescribed. In the y direction, wall boundary conditions are prescribed. The bottom wall is assumed to have zero heat loss, whereas the top wall is assumed to be at a uniform temperature. In the spanwise direction, symmetry boundary conditions are applied on one side, whereas an adiabatic wall is prescribed on the other side. Within the calculation domain, additional conditions are prescribed for the engine inlet and the jets. The inlet acts as a mass sink, the jets as mass sources. In prescribing these conditions, it is important to conserve mass. The jet velocity profile is assumed to be uniform, with the turbulent kinetic energy equal to 1% of the mean kinetic energy.

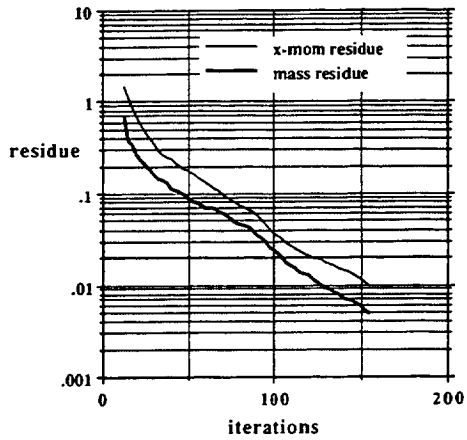

Fig. 2 Typical convergence history for multigrid calculation procedure, 100 × 44 × 48 cells with two coarse levels.

In the calculation procedure, the prescribed fine grid was coarsened to two additional levels. The calculation was started on the coarsest grid from prescribed initial conditions, but, on the finer grids, the starting solutions were obtained by successively extrapolating converged flowfields from the coarser grids. This Full Multigrid Cycle (FMG) provided realistic starting values for the calculations on the fine grids. Figure 2 shows a typical convergence history for the calculation of case 1. The convergence is monitored by the normalized sum of the absolute mass and momentum residuals over the whole solution domain. It is seen that the solution converges to the required tolerance of 1% error in approximately 150 iterations. In the previous study of VanOverbeke and Holdeman,[7] which used a single grid procedure, the number of iterations were approximately 2000 for a 134,000 grid. This represents a significant reduction in computational effort. The present calculation required approximately 35 min of CPU time on a CRAY-2; typically, this translates to a few hours of interactive real clock time.

Calculated Velocity and Temperature Fields

Hot gas ingestion is a serious problem for STOVL aircraft in ground proximity. Two important factors governing hot gas

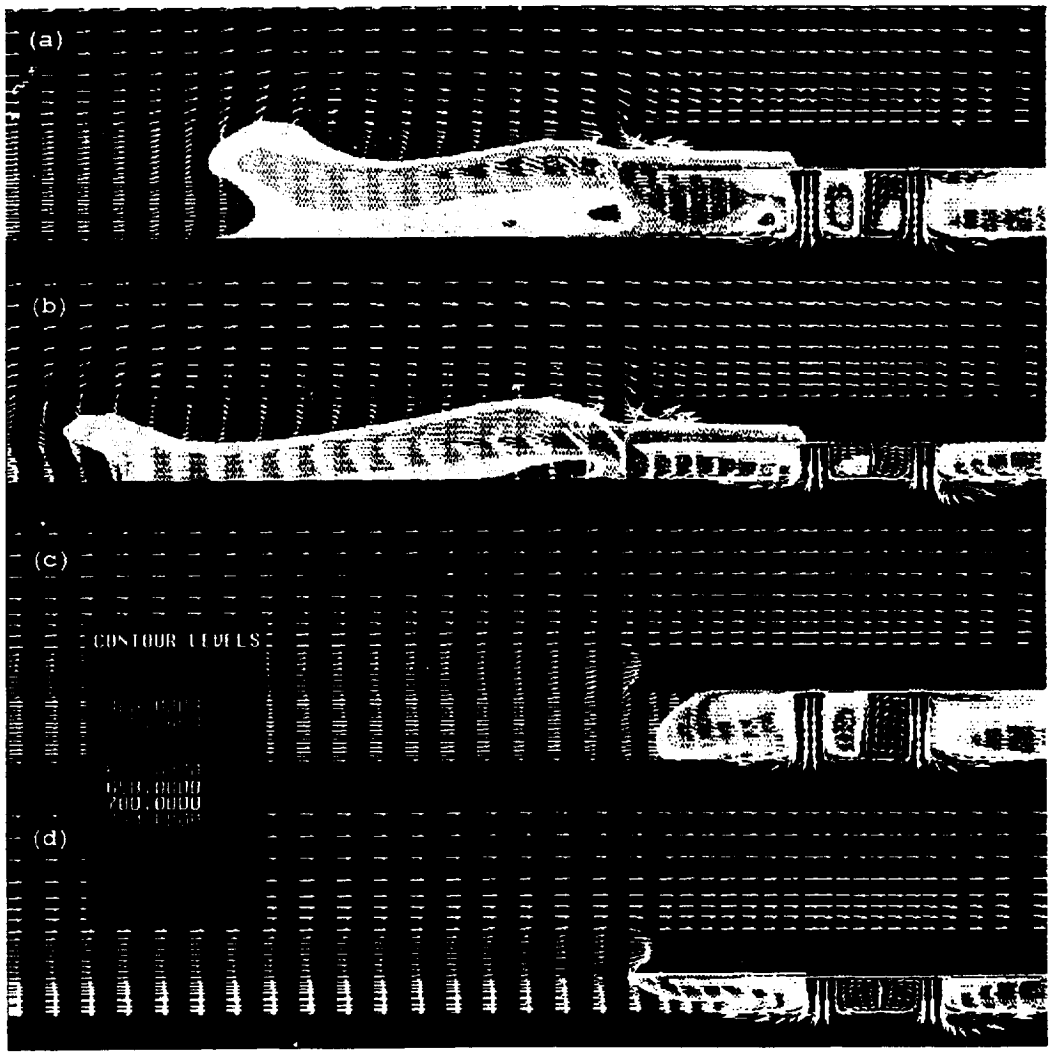

Fig. 3 Superimposed velocity vectors and temperature gray scale contours in x-y plane through the jet centerline (z = 0). Plot domain extends from $-46 \leq x/d \leq 14$ and from the ground plane to y/d = 20: a) case 1; b) case 2; c) case 3; d) case 4; headwind from left to right.

ingestion are the proximity of the lift jets to the ground (h/d ratio) and the ratio of the freestream velocity to the jet velocity (U_∞/U_j). Two other important factors, not considered in the present study are the location of the inlet with respect to the life jets and the use of shields and baffles to deflect the flow of hot gases away from the engine inlet. When the lift jets impinge on the ground, they stagnate and form radially flowing wall jets. When two opposing wall jets meet, they manifest themselves into a fountain flow. The flowfield caused by a rectangular four-jet configuration is governed by a strong fountain flow between the fore and aft jets (streamwise fountain) and also between the symmetrical spanwise jets (spanwise fountain). The streamwise fountain upwash, when obstructed by the fuselage, is forced to flow laterally outwards and up, whereas the spanwise fountain upwash tends to flow under and along the length of the fuselage in the streamwise direction. Both these mechanisms contribute to the direct ingestion of hot gases into the inlet. The other mechanism of hot gas ingestion, which is not as severe, is due to the recirculating flow caused by the interaction of the outward flowing hot gases with the headwind. The outward flowing hot gases are forced to stagnate by the freestream flow, and are deflected towards the engine inlet where they are reingested.

Figure 3 shows velocity vectors superimposed on gray scale temperature contours in the x-y plane passing through the center of the fore and aft jets for the four cases. (For the sake of clarity, different vector scales are used in different segments of the domain.) The effect of headwind to jet velocity ratio (U_∞/U_j) on the flowfield is clearly evident. In cases 1 and 2 ($U_\infty/U_j = 0.03$), the effect of the lift jets extends far upstream (35 jet diameters for case 1 and 46 jet diameters for case 2), whereas for cases 3 and 4 ($U_\infty/U_j = 0.09$), the stagnation region is much closer to the jets. For the low-velocity ratio, hot gas from the lift jets flows under the fuselage towards the inlet, where part of it is ingested directly by the strong suction of the inlet, while the rest is carried by its streamwise momentum further upstream until it is forced to stagnate by the oncoming flow and recirculate back towards the inlet (ground vortex). The most striking difference between high and low U_∞/U_j is the complete absence of the recirculating ground vortex in cases 3 and 4. This is due to the high forward momentum of the headwind, which prevents the hot gas from the jets from moving upstream. The effect of different h/d ratios is not as strong. For h/d of 2 (cases 2 and 4), a smaller area is available between the fuselage and the ground and, consequently, the radial momentum of the hot gas is larger than for h/d of 4. This enhances the spread of the jet, both in the lateral and streamwise direction. A comparison of cases 3 and 4 (just upstream of the fore jet and under the fuselage) suggests that for h/d of 2 the forward flow is stronger than for h/d of 4. This is also the case for cases 1 and 2, in which the recirculating zone for h/d of 2 extends about 11 jet diameters further upstream than for h/d of 4.

In all cases, the temperature fields upstream of the lift jets are very similar to those implied by the velocity field. For cases 1 and 2 ($U_\infty/U_j = 0.03$), the hot gases from the jets are transported much further upstream of the inlet. The upstream transport and the subsequent recirculation of hot gases (although cooler) back to the inlet can be directly correlated with the velocity vector field. In Figs. 3a and 3b, the cooler recirculated gases (positive streamwise velocity) can be clearly distinguished from the hotter gases (negative streamwise velocity). This relation between the velocity field and the temperature field is also evident in case 4 ($U_\infty/U_j = 0.09$, h/d = 2) between the inlet and the fore jet, where hot gases are transported upstream along the bottom of the fuselage. However, for case 3 ($U_\infty/U_j = 0.09$, h/d = 4), the temperature field extends further upstream than indicated by the velocity field. This indicates either a diffusive transport of heat or convective transport of heat from the sides. Another interesting feature is the difference in temperature between the fore half of the fountain and the aft half. In all cases, the fore half is cooler than the aft half, which must be due to its greater interaction with the cooler freestream fluid. This effect was also observed in the simulations in Ref. 7. Maclean et al.[11] compared the upstream distribution of temperature (along the jet center and along the axis of symmetry) obtained from their experiments with the present calculations for case 3. In the region near the jets, the agreement between the two is good, but further upstream the experiments show a higher concentration of jet fluid.

Figure 4 shows gray scale contours of the temperature field in the ground plane. For the low headwind case, there is much more forward and lateral spread of the hot gases than with the higher headwind. In addition, the height of the fuselage above the ground (h/d ratio) also has an effect on the forward and lateral spreading of the jets. As mentioned earlier, for h/d = 2, the radial momentum of the jet is higher, as can be seen in the greater lateral spread of the jet fluid before it is pushed downstream by the headwind. Another interesting feature is the sharp temperature gradients observed between the jets in the fountain upwash region. This is due to the vertical movement of two jet streams at different temperatures, with little transverse movement of fluid across this boundary. In fact, the locus of points across which these sharp gradients are seen in the lateral direction is the stagnation line that divides fluid from the fore and aft jets, until finally

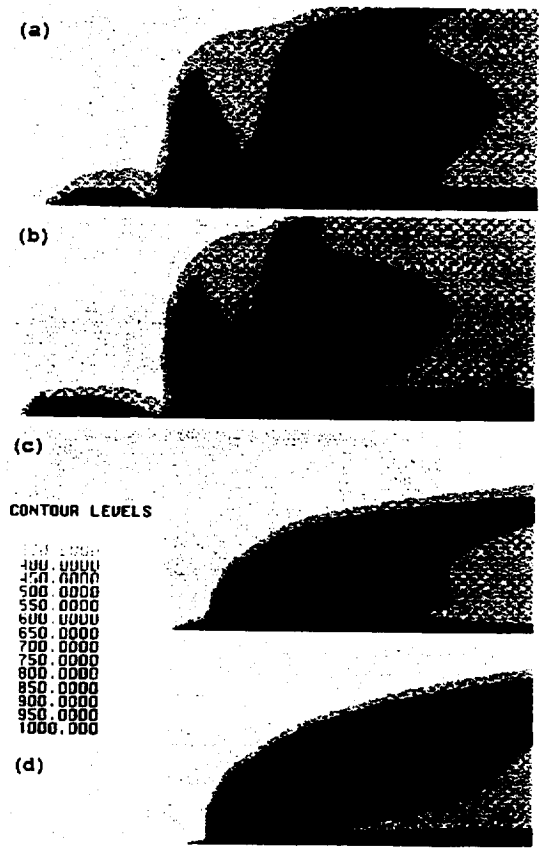

Fig. 4 Temperature contours in x-z ground plane: a) case 1; b) case 2; c) case 3; d) case 4; headwind from left to right.

Table 2 Extent of recirculating hot gas zone upstream of foreword lift jets

Case	Present Calculation	Experiments, Ref. 11
1	35	31
2	46	22
3	10	12
4	12.5	14

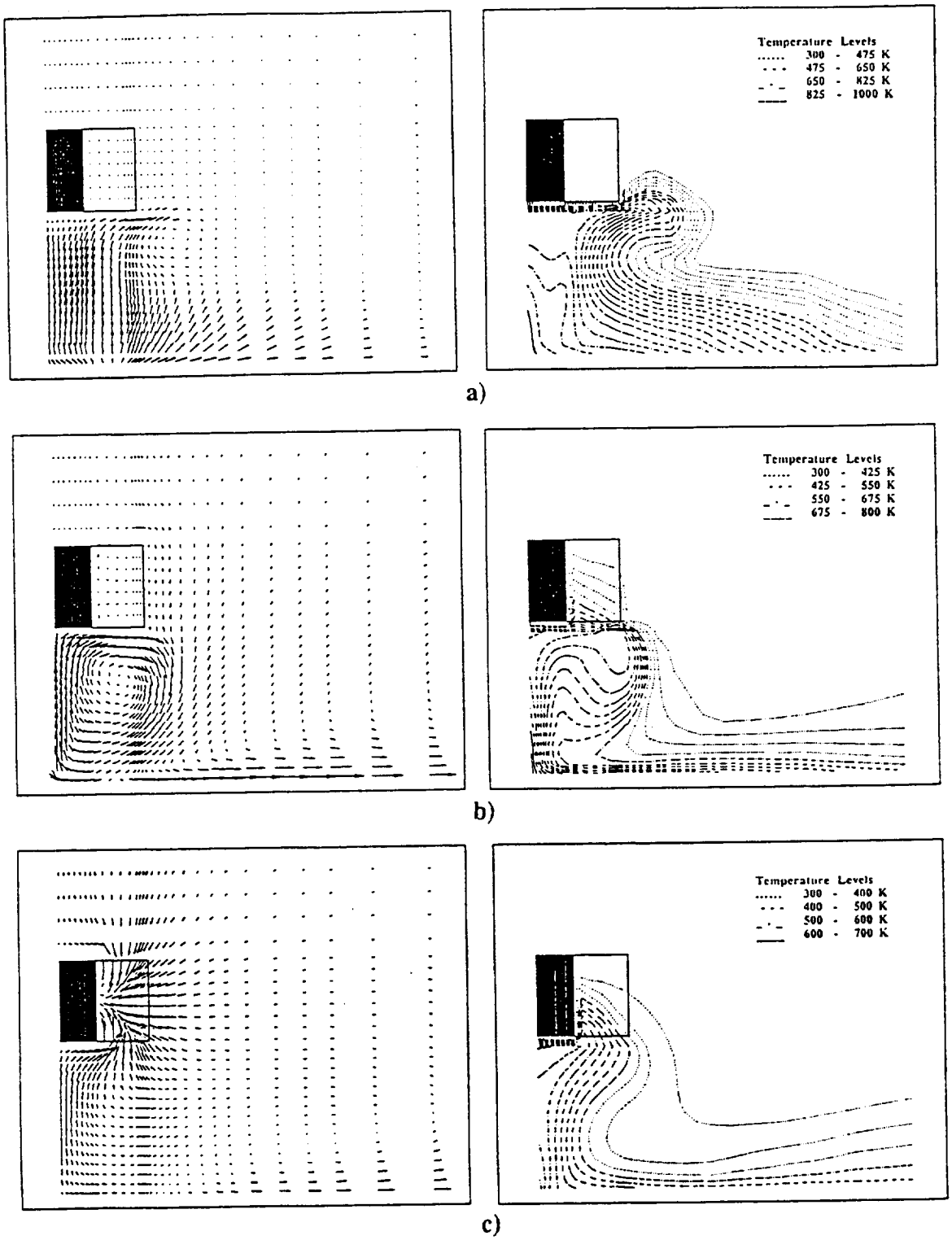

Fig. 5 Velocity vector and temperature contours in different z-y planes for case 1. Plot domain extends from symmetry plane to $z/d = 9$, and from ground plane to $y/d = 5$: a) $x/d = 3$; b) $x/d = -5$; c) $x/d = -10$.

they mix and smooth out the differences. These sharp gradients are also present in the simulations in Ref. 7 and in the experiments in Ref. 11, although the experimentally observed gradients are not as sharp.

Table 2 compares the upstream extent of the recirculating hot gas zone with the experiments in Ref. 11. In the present study, the temperature distribution is used as a means to determine the upstream spread of the hot gases (Fig. 3). It is seen that the calculated values agree well with the experimental values for cases 1, 3, and 4, whereas for case 2 the calculated value of x/d is much higher. Also, the trend indicated by the experiments [increased upstream penetration (x/d) with increased h/d ratio] is the opposite of what the numerical calculations indicate. This, in effect, would indicate that the jet fluid mixes more rapidly with the freestream flow and loses its identity earlier than the calculations predict. This discrepancy could be due to the inability of the k-ε turbulence model to accurately capture the full extent of turbulence production caused by the stagnating jets. Recent numerical studies of the fountain region of twin jet impingement[14] indicate that the turbulent kinetic energy is severely underpredicted, particularly in the region close to the ground plane. This, in

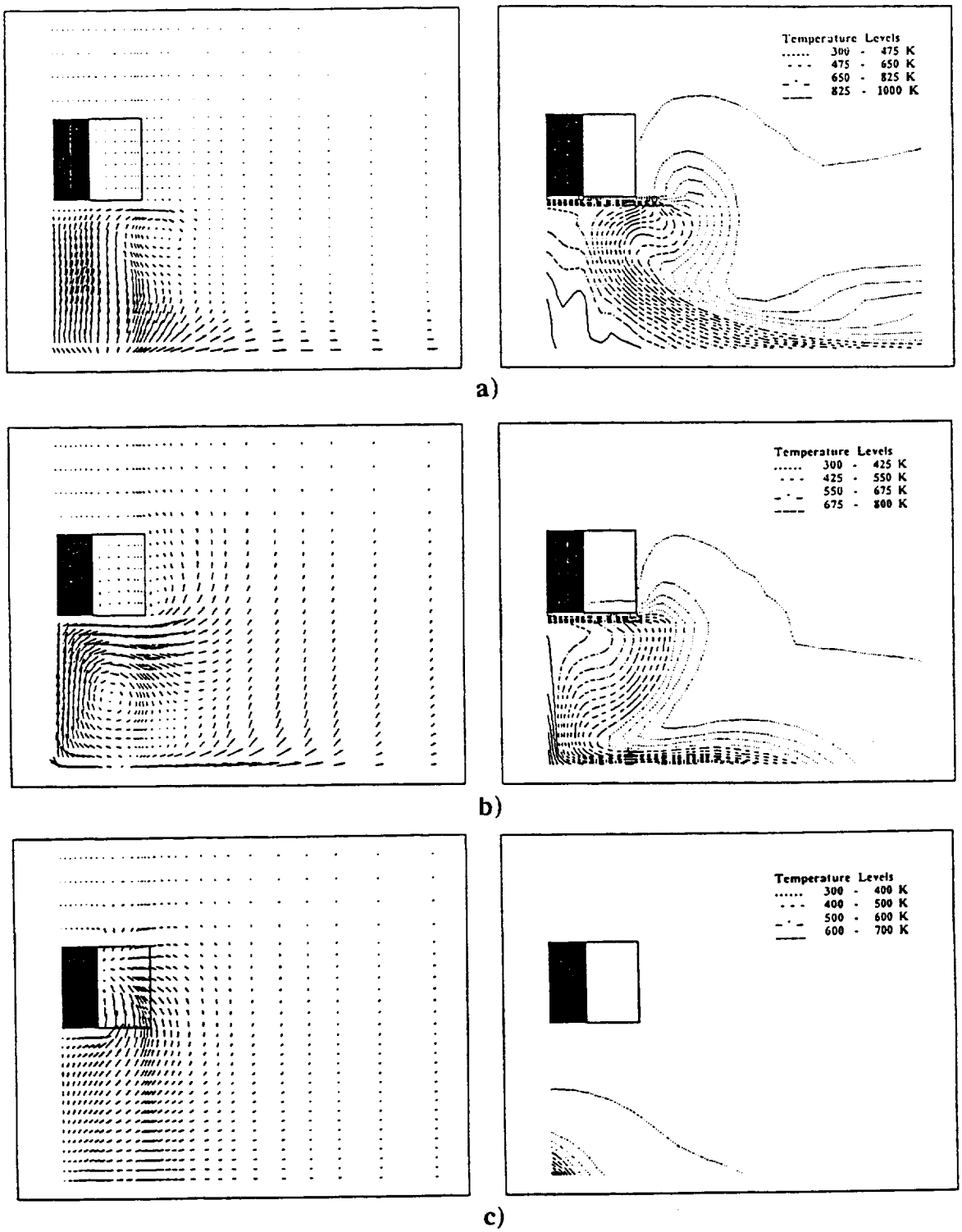

Fig. 6 Velocity vector and temperature contours in different z-y planes for case 3. Plot domain extends from symmetry plane to $z/d = 9$, and from ground plane to $y/d = 5$: a) $x/d = 3$; b) $x/d = -5$; c) $x/d = -10$.

part, also explains the sharp temperature gradients seen in the upwash region of the fountain flow. The authors suspect that, for case 2, this might be a critical factor in determining the dilution and spread of the jet fluid. More comparisons between the present simulations and experiments can be found in Ref. 11.

Figures 5 and 6 show velocity and temperature distributions in three z-y planes for cases 1 and 3. Part a) is the z-y plane passing through the fountain upwash between the jets, part b), the z-y plane between the fore jet and the inlet, and part c), the plane at the inlet. In both cases, the spanwise fountain flow responsible for the movement of hot gases upstream from the fore jets is clearly visible in b). As the hot gases from the jets move upstream under the fuselage, they are considerably diluted, due to mixing with the cooler headwind. As this gas approaches the inlet, part of it is directly ingested into the inlet c). It is interesting to see that, for the low-velocity ratio, ingestion occurs from the side, top, and bottom of the fuselage, whereas, for the higher headwind, most of the ingestion occurs from the bottom and side of the fuselage. Another interesting feature is the movement of hot gases: for the higher headwind, the hot gases show a lateral outward and upward

Table 3 Nondimensional mass averaged inlet plane temperatures $(T_{avg} - T_\infty)/(T_j - T_\infty)$

Case	Present Calculation	Calculation, Ref. 7
1	0.083	0.13
2	0.097	0.11
3	0.0	0.08
4	0.017	0.03

movement whereas for the lower headwind the flow is laterally inward, i.e., cooler fluid is entrained into the fountain region. This phenomenon is also reflected in the ground plane temperatures (Fig. 4), where the lateral spread of the jet fluid between the fore jet and the inlet is greater with the higher headwind. This is due to the higher dynamic pressure of the oncoming freestream, which forces the hot gases out from under the fuselage. Table 3 shows the mass averaged nondimensional inlet plane temperatures calculated for the four cases, and compares them to those obtained by the numerical simulations in Ref. 7. There is some discrepancy between the two calculations. It is not possible to identify the reasons for this discrepancy, but the difference in the resolution of the flowfield between the two methods could be one of the major contributing factors. The results of the present calculation follow the trends indicated by the velocity and the temperature profiles. The maximum average inlet temperature is for case 2 (U_∞/U_j = 0.03, h/d = 2); case 3 does not seem to ingest any hot gases.

Summary and Conclusions

In the present paper, a multigrid calculation procedure for three-dimensional flows is used to study the hot gas ingestion by STOVL aircraft. Calculations with a simulated fuselage and twin exhaust jets have been made for two ground positions and two head-wind ratios. The global features of the flowfield (e.g., the ground plane temperature distributions and the formation of the ground vortex) for the four cases are according to expectations and agree well with the recent numerical study of Ref. 7. A major contribution of the present study is the demonstration that the multigrid algorithm can significantly reduce the computational effort required to solve the governing equations, compared to a conventional single grid procedure. The reduction in computational effort permits more parametric studies to be conducted.

In the present study, the Reynolds-averaged flow equations have been solved in conjunction with the k-ε turbulence model. The flow is considered to be steady in time, although, it has been observed[11] that the region of jet impingement is highly unsteady and the turbulence structures are very complex. Therefore, the accuracy of the current calculations is limited by the assumptions made in deriving the governing equations of the turbulence model. A study performed on the twin jet impingement flow in isolation[14] showed that the k-ε model is able to predict the velocity field reasonably well, but the turbulence kinetic energies are severely underpredicted. Although it is possible to incorporate more complex turbulence models into the current algorithm, it is not certain at this time that they improve the predictions over those of the k-ε model. Future extension of this study will be in the direction of representing the aircraft geometry more realistically through the use of curvilinear grids.

Acknowledgments

The present work was supported by Grant NAG-3-1026 from the NASA Lewis Research Center, Cleveland, Ohio. The authors wish to thank J. D. Holdeman for his encouragement during this study. The calculations were performed on the NASA Ames NAS computer facility.

References

[1]Kuhn, R. E., "Design Concepts for Minimizing Hot Gas Ingestion in V/STOL Aircraft," *Journal of Aircraft*, Vol. 19, No. 10, 1982, pp. 845–850.

[2]Kuhn, R. E., and Eshelman, J., "Ground Effects on V/STOL and STOL Aircraft—A Survey," AIAA-85-4033, AIAA/AHS/ASEE Aircraft Design Systems and Operations Meeting, Colorado Springs, CO, Oct. 1985.

[3]Agarwal, R. K., "Recent Advances in Prediction Methods for Jet-Induced Effects on V/STOL Aircraft," *International Symposium on Recent Advances in Aerodynamics*, Stanford Univ., Stanford, CA, Edited by A. Krothapalli and C. A. Smith, Springer-Verlag, New York, August 1983, pp. 471–521.

[4]Saripalli, K. R., "Lase-Doppler Velocimeter Measurements in 3-D Impinging Twin-Jet Fountain Flows," *Turbulent Shear Flows*, Vol. 5, Springer Verlag, New York, 1987, pp. 146–148.

[5]Kotansky, D. R., and Bower, W. W., "A Basic Study of the VTOL Ground Effect Problem for Planar Flow," *Journal of Aircraft*, Vol. 15, No. 4, 1978, pp. 214–220.

[6]Agarwal, R. K., and Bower, W. W., "Navier-Stokes Computation of Turbulent Compressible Two-Dimensional Impinging Jet Flowfields," *AIAA Journal*, Vol. 20, No. 5, May 1982, pp. 577–584.

[7]VanOverbeke, T. J., and Holdeman, J. D., "Three-Dimensional Turbulent Flow Code Calculations of Hot Gas Injection," *Journal of Aircraft*, Vol. 27, No. 7, July 1990, pp. 577–582.

[8]Syed, S. A., and James, R. H., "User Manual for 3D-Teach With Rotation," NASA-CR-180886, 1980.

[9]Vanka, S. P., "A Calculation Procedure for Three-Dimensional Recirculating Flows," *Computer Methods in Applied Mechanics and Engineering*, Vol. 55, 1986, pp. 321.

[10]Brandt, A., "Multi-Level Adaptive Solutions to Boundary-Value Problems," *Mathematics of Computations*, Vol. 31, 1977, pp. 333–390.

[11]McLean, R., Sullivan, J., and Murthy, S., "Hot Gas Environment Around STOVL Aircraft in Ground Proximity, Part 2: Experimental Study," AIAA 90-2269, 26th AIAA/SAE/ASME/ASEE Joint Propulsion Conference, Orlando, FL, July 1990.

[12]Launder, B. E., and Spalding, D. B., "The Numerical Computation of Turbulent Flows," *Computer Methods in Applied Mechanics and Engineering*, Vol. 3, 1974, pp. 269–289.

[13]Claus, R. W., and Vanka, S. P., "Multigrid Calculations of a Jet in Crossflow," AIAA-90-0444, 28th Aerospace Sciences Meeting, Reno, NV, Jan. 1990, *Journal of Propulsion and Power* (to be published).

[14]Pegues, W. P., and Vanka, S. P., "Numerical Study of Twin-Jet Impingement Upwash Flow," Fluids Engineering Division, Vol. 94, ASME Forum on Turbulent Flows, Toronto, Canada, June 1990, pp. 97–103.

APPENDIX D

CALCULATIONS OF HOT GAS INGESTION FOR A STOVL AIRCRAFT MODEL

AIAA Paper 92-0385

CALCULATIONS OF HOT GAS INGESTION FOR A STOVL AIRCRAFT MODEL

D.M. Fricker*
Propulsion Directorate
U.S. Army Aviation Systems Command
Lewis Research Center
Cleveland, Ohio 44135

J.D. Holdeman†
National Aeronautics and Space Administration
Lewis Research Center
Cleveland, Ohio 44135

and

S.P. Vanka‡
University of Illinois
Urbana, Illinois 61801

ABSTRACT

Hot gas ingestion problems for STOVL (Short Take-Off, Vertical Landing) aircraft are typically approached with empirical methods and experience. In this study, the hot gas environment around a STOVL aircraft was modeled as multiple jets in crossflow with inlet suction. The flow field was calculated with a Navier-Stokes, Reynolds-averaged, turbulent, 3D CFD code using a multi-grid technique. A simple model of a STOVL aircraft with four choked jets at 1000 K was studied at various heights, headwind speeds, and thrust splay angles in a modest parametric study. Scientific visualization of the computed flow field shows a pair of vortices in front of the inlet. This and other qualitative aspects of the flow field agree well with experimental data.

NOMENCLATURE

D_j = characteristic length of jet nozzles, 0.0366 m (1.44 in)
H = distance from ground to bottom of the aircraft (aircraft altitude or height)
U_∞ = headwind velocity
V_j = jet nozzle exit velocity, 633 m/s (2080 ft/sec)
δ = thrust splay angle measured from the downward vertical toward symmetry plane
k = turbulent kinetic energy
ε = turbulent energy dissipation
x = axial Cartesian coordinate, zero at upstream boundary
x-y = vertical plane aligned in axial direction
x-z = horizontal plane
y = vertical Cartesian coordinate, zero at ground plane
y-z = vertical plane aligned in spanwise direction
z = spanwise Cartesian coordinate, zero at aircraft centerline plane

INTRODUCTION

Hot gas ingestion can cause significant problems for a STOVL (Short Take-Off, Vertical Landing) aircraft including reduced thrust and compressor stalls. These problems involve many hazards for the pilots including very hard landings. During the design of a STOVL aircraft, hot gas ingestion problems are typically approached with empirical methods and experience[1,2]. Given the power of today's supercomputers and workstations, numerical methods employing efficient algorithms are becoming a viable engineering tool for analysis and design. In a previous endeavor, VanOverbeke & Holdeman[3,4] proved the feasibility of CFD analysis for hot gas ingestion. This study is a follow-on effort exploring the practicality of using an efficient numerical method for the problem of hot gas ingestion.

FLOW FIELD DESCRIPTION

Ingestion of hot gases generates problems in two ways: an average temperature rise results in a loss of engine thrust, and a temperature distortion may cause the engine to stall. Engine exhaust gases may be ingested by far-field and/or near-field mechanisms. A schematic of these mechanisms is shown in Fig. 1.

The far-field mechanism results from the exhaust gases impinging on the ground and forming radial wall jets which flow forward, separate, and mix with the headwind. Near-field ingestion occurs with multiple jet configurations. Wall jets flowing out from the lift jets meet and create an upflow or

*Aerospace Engineer, Propulsion Directorate, Member AIAA.
†Senior Research Engineer, Internal Fluid Mechanics Division, Member AIAA.
‡Associate Professor, Dept. of Mechanical & Industrial Engineering, Member AIAA.

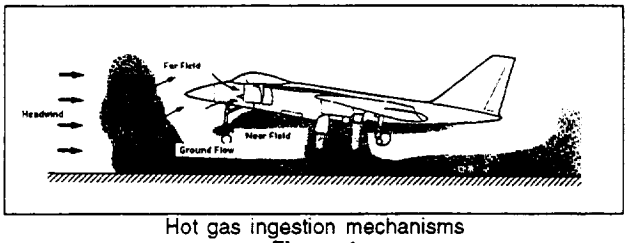

Hot gas ingestion mechanisms
Figure 1

fountain. This fountain flow can impinge on the aircraft's underside, flow along the fuselage to the engine inlets, and be ingested. The gases ingested by this near-field mechanism tend to be hotter, giving greater temperature distortion than those ingested by the far-field mechanism.

As stated earlier, the hot gas environment around a STOVL aircraft was modeled as multiple jets in crossflow with inlet suction. Mass sources represent the nozzle exits, and a mass sink at the end of the inlet provides the suction. The mass injected by the nozzles balances the mass removed by the inlet suction. This configuration derives from the previous study by VanOverbeke & Holdeman[3,4]. To meet the requirements of the CFD code, the aircraft model is placed in a confined flow, i.e., a 'wind tunnel'. Also, the aircraft model has no angle of attack due to the use of a cartesian grid based flow solver.

The STOVL aircraft model (see Fig. 2) is composed of rectangular solids for the fuselage and engine. For computational simplicity, the nose and

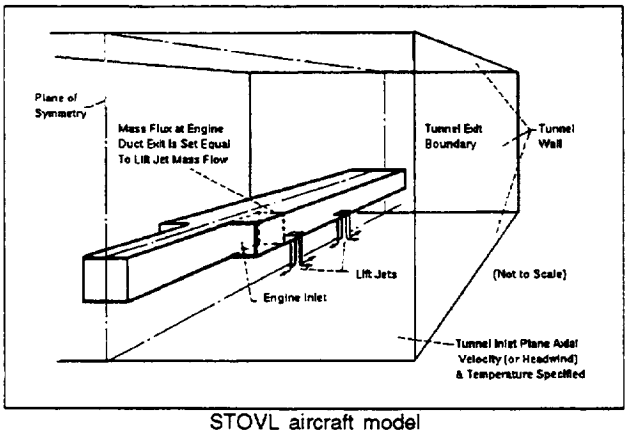

STOVL aircraft model
Figure 2

the tail of the aircraft reach to infinity, and the model lacks wings. Baffles on the sides of the fuselage comprise the walls of the inlet. The nozzles are square in cross-section and are flush with the bottom of the aircraft. The square cross-section of the jets and the rectangular aircraft body result from the use of the cartesian grid.

The four choked nozzles inject air at 1000 K (1340°F) straight down into the flowfield with a velocity of 633 m/s (2080 ft/sec). Each lift jet issues from the nozzle exit in a uniform flow. The headwind is also a uniform flow, but at a temperature of 300 K (81°F). This approximates an aircraft landing with a forward speed or an aircraft facing into a wind which lacks a boundary layer. In the baseline case, the headwind (U_∞) flows at 3% of the jet velocity (V_j), or about 19 m/s (37 kts), and the distance from the ground to the bottom of the aircraft model (H) is four times the characteristic length of the nozzles (4 D_j). The parametric studies include: various altitudes (H = 2 to 32 D_j) at a constant headwind (U_∞ = 0.03 V_j); various headwind speeds (U_∞ = 0.01 to 0.09 V_j) for a constant aircraft altitude (H = 4 D_j); and various thrust splay angles (δ = 0° to 45°) for a constant height (H = 4 D_j) and headwind speed (U_∞ = 0.03 V_j).

The physical dimensions of the aircraft model are given in Table I. Note that the forward and aft nozzles have the same side-to-side separation, i.e., they are in-line, not offset.

Table I
STOVL aircraft model dimensions

Fuselage:		
width (nose)	=	2.25 D_j
width (tail)	=	5.05 D_j
height	=	2.5 D_j
length	=	∞
Inlet:		
width	=	1.4 D_j
height	=	2.5 D_j
length	=	9.5 D_j
Jets separation:		
(center-to-center)		
side-to-side	=	3.25 D_j
fore & aft	=	6.0 D_j

NUMERICAL DESCRIPTION

Calculation domain

The grid geometry used for the baseline case is shown in Fig. 3. Exhibited are the centerline plane, the ground plane, and a vertical spanwise plane at the end of the domain as well as the aircraft model. The grid shows the high density of the calculation nodes in the region of the jets. For all calculations, symmetry assumptions allowed calculating only half of the physical domain.

The other boundary conditions for the calculation domain include an inflow simulating the headwind for the domain face in front of the aircraft model and an outflow condition for the domain face behind the model. All flow properties are defined for the inflow condition. The outflow condition, in contrast, merely assumes the properties of the

axially nearest cells. The top, bottom, and remaining side of the domain are no-slip, stationary walls as are the aircraft surfaces. All the walls assume adiabatic conditions for the energy equation. The symmetry plane also has a symmetry condition for the energy equation.

For the height variation, the grid contains 211,200 cells arranged as follows: 100 cells in the x direction, 44 cells in the y direction, and 48 cells in the z direction. The physical dimensions of the baseline grid are about 135 D_j long, 29 D_j high, and 40 D_j wide. The aircraft to ground distance was varied by elongating the cells underneath the aircraft. This facilitated the comparative analysis.

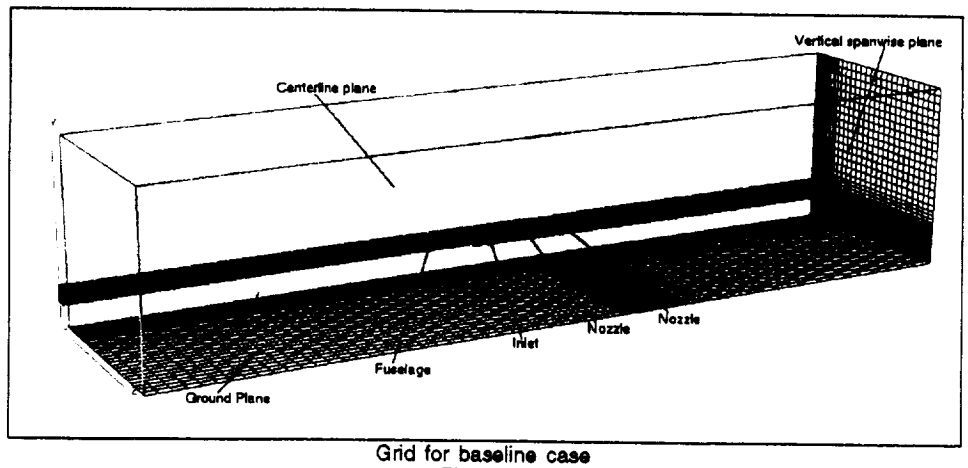

Grid for baseline case
Figure 3

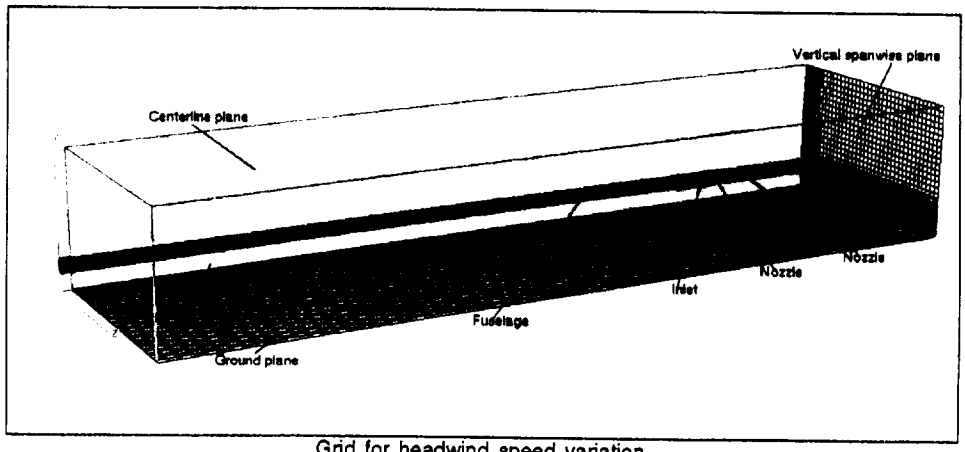

Grid for headwind speed variation
Figure 4

The headwind speed variation used a slightly modified grid; 100 cells in x, 44 cells in y, and 60 cells in z yielding 264,000 total cells. (See Fig. 4.) This grid has a greater length (177 D_j) and greater width (59 D_j) than the baseline grid. Also, the distance in front of the forward pair of jets is greater (152 D_j versus 76 D_j for the baseline grid) to accommodate the long region of hot gas in front of the inlet in the U_∞ = 0.01 V_j case. No grid modification was needed to vary the headwind speed.

Flow solver

The flow field in this domain was calculated with a Navier-Stokes, Reynolds-averaged CFD code. References 5-7 describe this steady-state CFD code (and its techniques) for the three-dimensional analysis of turbulent elliptic flows in a Cartesian coordinate system.

The CFD code (CART3D) solves the time-averaged Navier-Stokes or Reynolds equations. The k-ε turbulence model provides closure. The governing equations include continuity, x-, y-, and z-momenta, energy, turbulent kinetic energy, and turbulent energy dissipation. These equations are solved using a block-implicit multigrid algorithm developed by Vanka.

CART3D uses a hybrid differencing scheme on a staggered grid. This means that the code uses central differencing or upwind differencing depending upon the cell's Reynolds number. Also, the scalar properties (density, pressure, etc.) are calculated at the cell volume centers while the velocities are solved at the centers of the cell faces.

The multi-grid technique speeds convergence by solving the equations on sequential grids of different cell densities. The flow is initialized on the coarsest grid which gets refined by the multi-gridding. Dividing each cell on a grid into eight equal cells refines the grid for the next grid level. A V-cycle of sweeps on the various grid levels is performed until the solution converges on the finest grid. This technique speeds convergence by dampening out errors with the various levels of grid refinement.

To determine convergence, the residuals are non-dimensionalized by an appropriate number, and then the maximum of all the residuals is compared to the tolerance criterion. The tolerance criterion used by this study is 1% for the finest grid. All test cases used the third grid level for the finest grid.

FLOW FIELD FEATURES

A short study of the features in the baseline case will help bring out the differences caused by varying the aircraft altitude.

Fig. 5 displays the temperature contours in an x-z plane near the ground. These contours show the locations of the forward vortex pair and the two ground vortices generated by the interaction of the jets and the crossflow. The axis for the forward vortex pair is perpendicular to the plane shown in Fig. 5 while the axes for the ground vortices are parallel to the plane. The forward vortex pair is smeared by the steady-state calculations but still agrees well with the time-averaged experimental data[8-10].

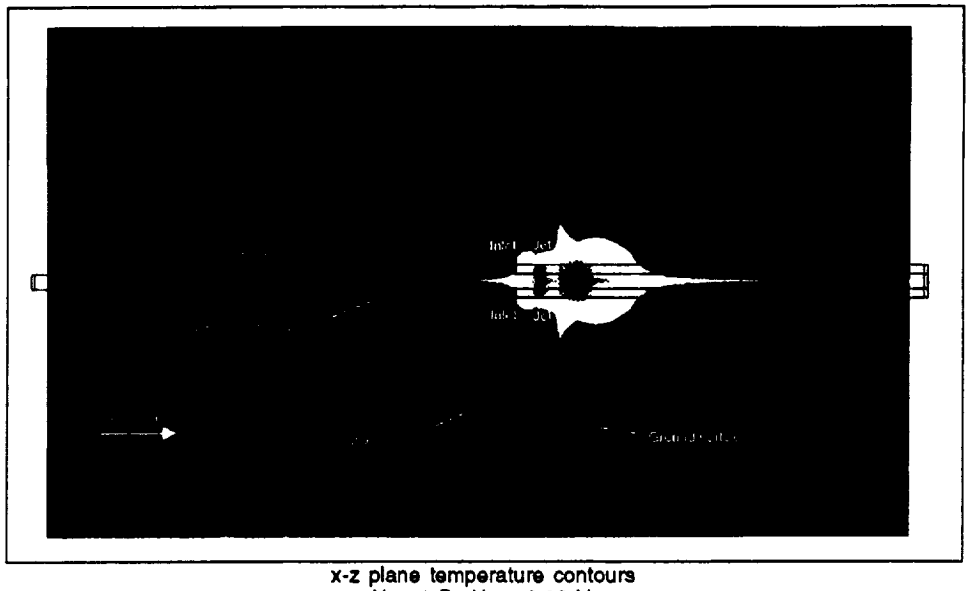

x-z plane temperature contours
$H = 4\ D_j$, $U_\infty = 0.03\ V_j$
Figure 5

The particle traces in Fig. 6 reveal ingestion of exhaust gases. The particle traces from the jet region show the forward vortex and ingestion into the inlet. The particle traces starting at the inflow boundary show the headwind's deflection around the forward vortex. Temperature contours along the ground plane are also shown for clarity of position.

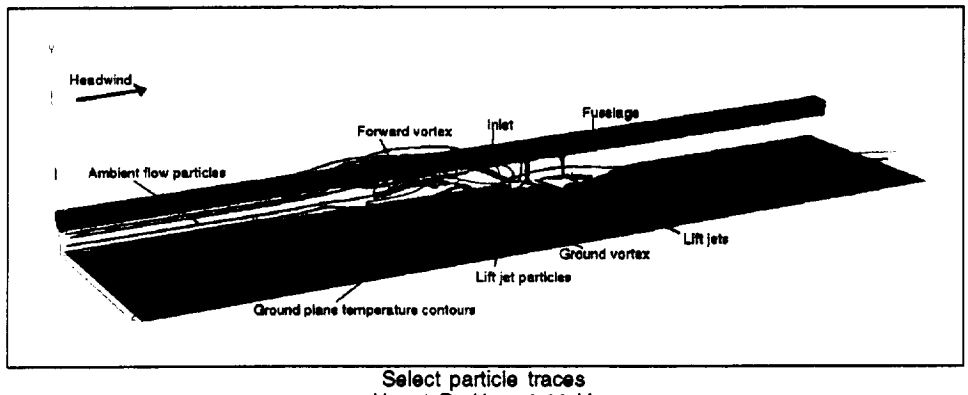

Select particle traces
$H = 4\ D_j$, $U_\infty = 0.03\ V_j$
Figure 6

Fig. 7 shows a three-dimensional temperature contour for the baseline case. This isotherm is for 325 K (125°F), a reasonable upper limit on the temperature of the air reaching the engine. With the ambient flow at 300 K (81°F), this represents a temperature rise of more than 25 K (45°F) for the fluid inside the isotherm. The inlet is almost completely obscured by the contour. Clearly, the engine is exposed to a considerable amount of hot gas from the engine exhaust. The bubble in front of the inlet reveals the location of the forward vortex. Note that the clipping of the isotherm in the right side of Fig. 7 is due to wall effects which have no consequence on the hot gas ingestion.

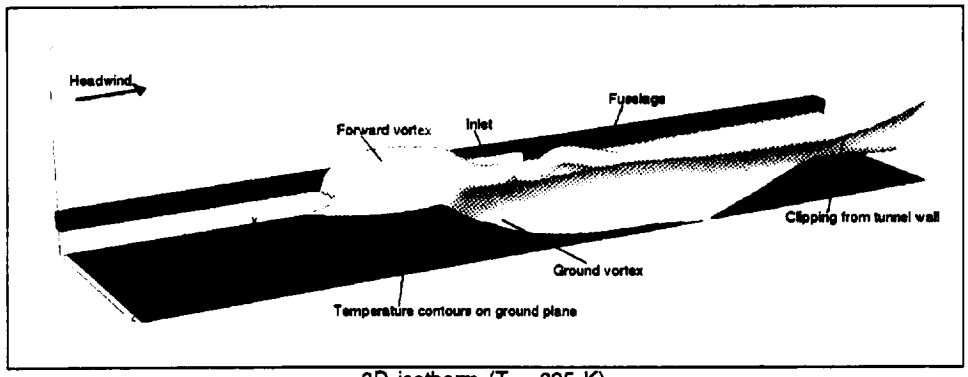

3D isotherm ($T = 325$ K)
$H = 4\ D_j$, $U_\infty = 0.03\ V_j$, $T_\infty = 300$ K, $T_j = 1000$ K
Figure 7

AIRCRAFT ALTITUDE PARAMETER VARIATION

The aircraft altitude varied from 2 D_j to 32 D_j. The cases actually computed over this range (H = 2, 3, 4, 5, 6, 8, 12, 16, 24, and 32 D_j) were carefully chosen to capture the changes in the flow field features. Fig. 8 shows temperature contours for select aircraft altitudes (2 D_j, 4 D_j, 8 D_j, 12 D_j, and 32 D_j) in two planes: the ground plane and a vertical plane passing through the jets near the jet centers. These cases show the changes in the flow field affecting hot gas ingestion over the range of variation. In each case, the fuselage is mostly hidden by the vertical plane of temperature contours. The major effects of aircraft altitude can be seen in this figure: the forward vortex changes in character, the amount of hot gas ingested is reduced, and the ground vortices decrease in size.

In Fig. 9, the temperatures at the cells in front of the mass sink or 'engine face' are plotted against the aircraft altitude. The temperatures shown are the minimum, the maximum, and a weighted average based on the cell volumes. The spread of the minimum temperature and the maximum temperature shows the temperature distortion at the engine face. This and the average temperature rise above ambient is plotted in Fig. 10. At low altitudes, the distortion is obviously

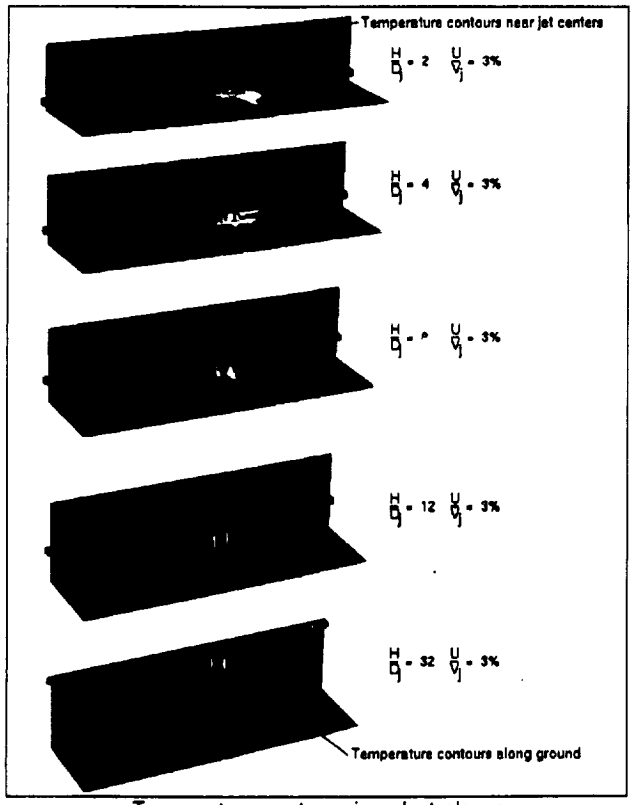

Temperature contours in select planes
(U_∞ = 0.03 V_j)
Figure 8

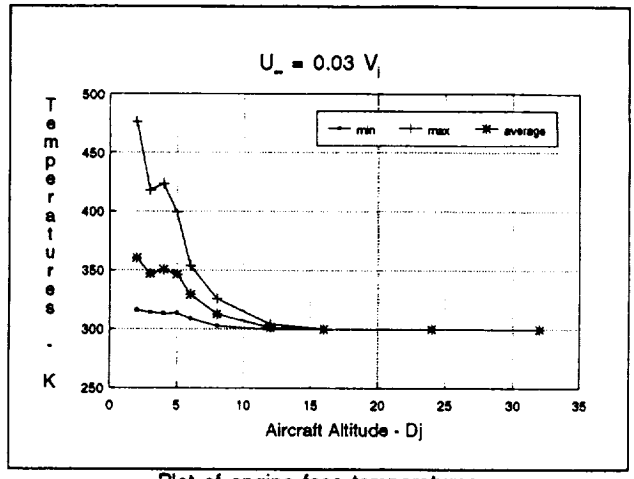

Plot of engine face temperatures
vs. aircraft altitude
Figure 9

extreme; and it quickly diminishes with increasing altitude. The average temperature shows a similar behavior. The non-monotonic behavior at H = 3 D_j in all of these curves appears to be physical. Other calculations on different grids exhibit the same trends.

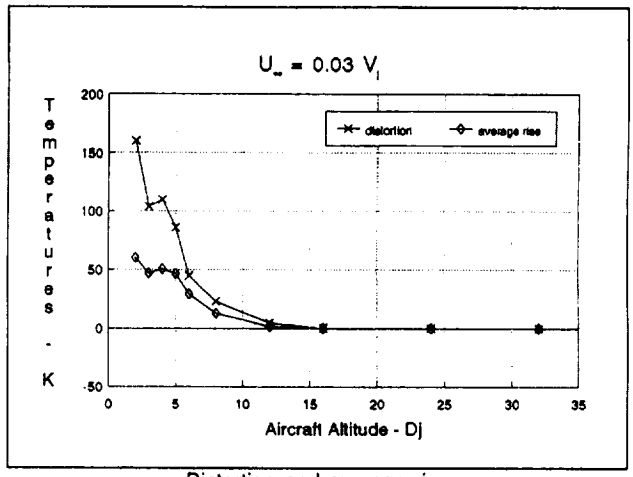

Distortion and average rise
vs. aircraft altitude
Figure 10

HEADWIND SPEED PARAMETER VARIATION

The headwind speed was varied from 1% to 9% of the jet velocity (U_∞ = 0.01 to 0.09 V_j) in 1% increments for a constant altitude (H = 4 D_j). Fig. 11 displays temperature contours in the same two planes as in Fig. 8: the ground plane and a vertical plane passing through the jets near the jet centers. Selected headwind speeds (1%, 3%, 5%, 7%, and 9%) show the changes in the flow field for the varying headwind speed. Again, the fuselage is mostly hidden by the vertical plane of temperature contours. In Fig. 11 the calculated domain includes

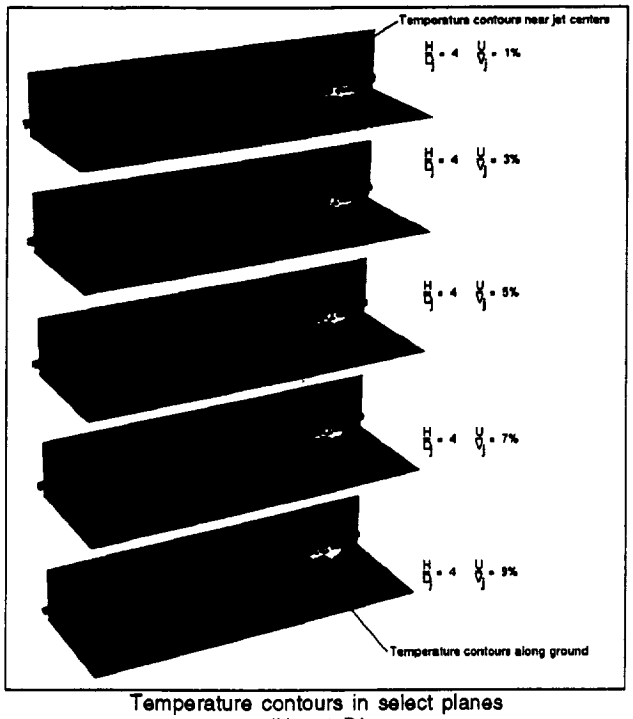

Temperature contours in select planes
(H = 4 D_j)
Figure 11

a much larger region in front of the inlet in comparison with Fig. 8. This is due to a very long region of exhaust gas which extends in front of the inlet along the ground in the U_∞ = 0.01 V_j case.

The effect of headwind speed on the engine face temperatures can be seen in Fig. 12. Note that the minimum temperature declines rather steadily with increasing headwind speed. The temperature distortion at the engine face varies weakly with headwind speed at the low speeds and is greatest for the 7% case as shown in Fig. 13. One should note that these high velocity ratios are

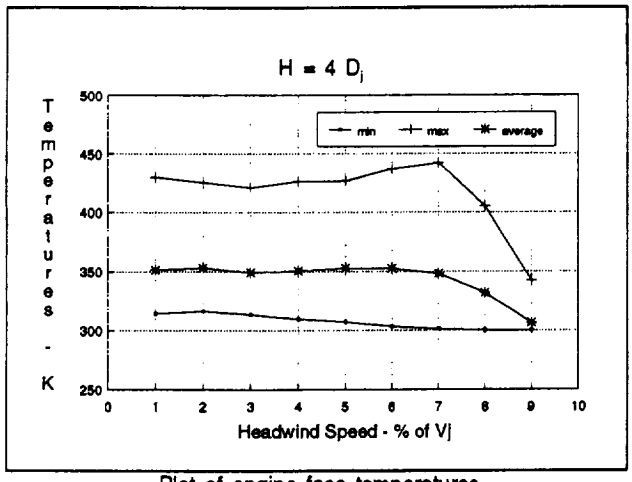

Plot of engine face temperatures
vs. headwind speed
Figure 12

unrealistically representing a windy vertical landing, but they might be relevant for a low speed landing. For choked jets, the 9% headwind represents about a 110 knot headwind which would either be a hurricane or a slower than normal landing speed for a conventional fighter aircraft.

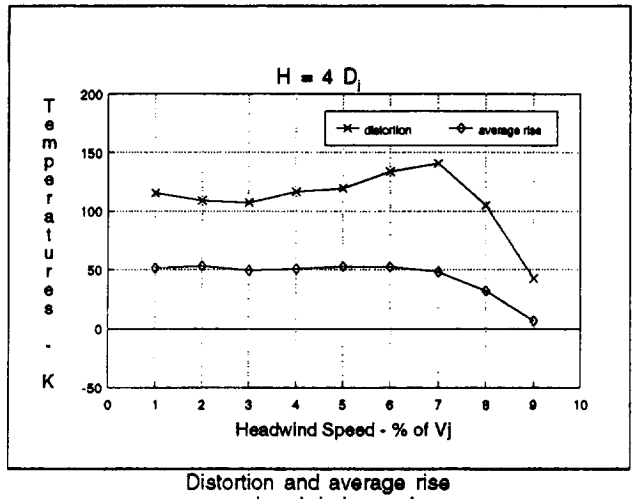

Distortion and average rise
vs. headwind speed
Figure 13

THRUST SPLAY ANGLE PARAMETER VARIATION

A technique used to help control hot gas ingestion is to splay the jets. By angling the lift jets, the relative strengths of the fountain, upwash, and vortices are changed thus changing the flow structures affecting ingestion. In this study, the splay angle (δ) of the thrust is measured from the downward vertical inward to the centerline plane of the aircraft model. To vary the thrust splay angle, the component velocities on the jets changed to provide the required angle while keeping the speed of the jet constant. Thus the direction of the lift jets changed while the geometry of the aircraft model did not change.

Splaying all jets

For the first variation of the thrust splay angle, all four jets were splayed the same amount. The splay angle varied from 0° to 45° (δ = 0° to 45°) in 5° increments for a constant height (H = 4 D_j) and constant headwind speed (U_∞ = 0.03 V_j). Fig. 14 shows temperature contours in two planes similar to those displayed in Fig. 8 & Fig. 11: the ground plane and a vertical plane that is now on the inner side of the lift jets (instead of near the center). Selected splay angles (0°, 5°, 10°, 20°, 25°, and 30°) show the changes in the flow structures due to varying the angle of all the jets. The most noticeable change occurs in the length of the hot gas region in front of the inlet. A less noticeable change is the increase of hot gas directly

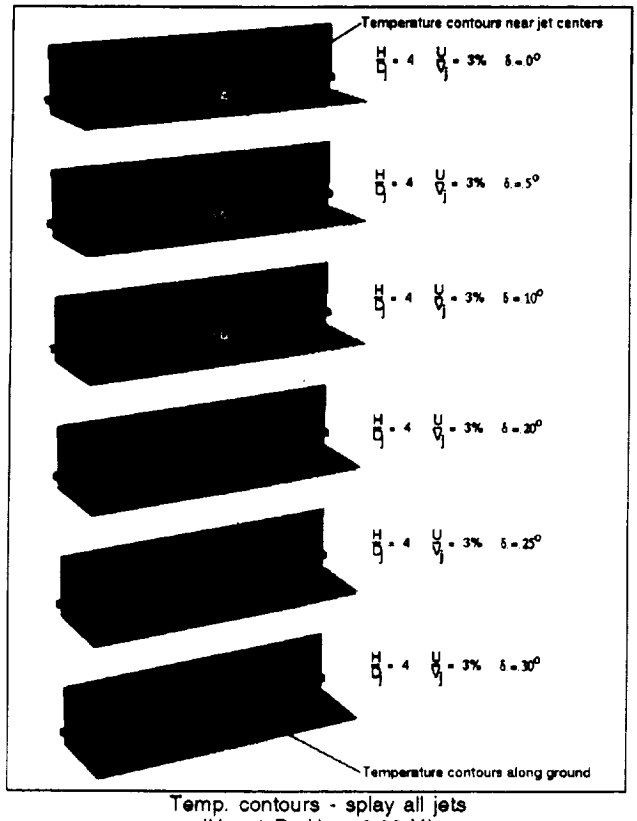

Temp. contours - splay all jets
($H = 4\ D_j$, $U_\infty = 0.03\ V_j$)
Figure 14

in front of the inlet for the 5° case. This actually causes an increase in hot gas ingestion over the 0° case, instead of reducing it.

This and other effects of thrust splay angle for all the jets can be seen in Fig. 15 and Fig. 16. In Fig. 15, the average temperature first rises and then drops until a splay angle of about 20° where it starts rising again. A local maximum exists at the 25° point before the average temperature flattens out at its lowest value. Both the minimum and maximum temperatures follow the same behavior. The distortion and average temperature rise displayed in Fig. 16 show the same patterns. Note that for this configuration of model and altitude, the jets will converge at the ground for a thrust splay angle of 22°.

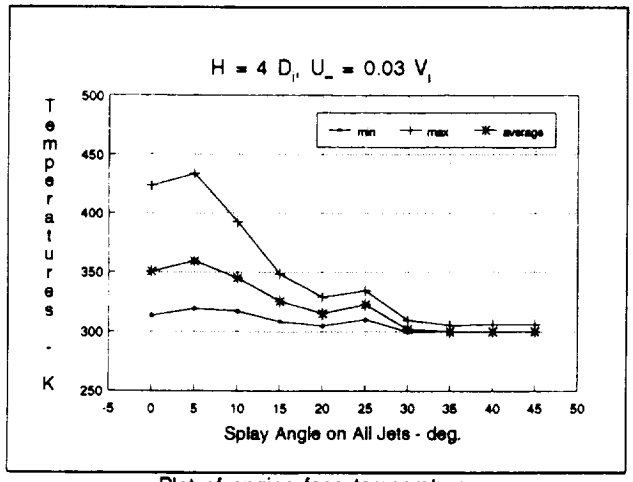

Plot of engine face temperatures
vs. splay angle on all jets
Figure 15

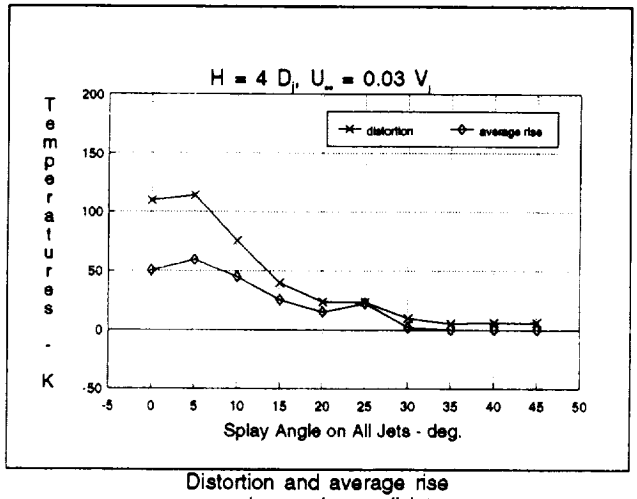

Distortion and average rise
vs. splay angle on all jets
Figure 16

Splaying forward jets only

In the second variation, only the forward jets varied in thrust splay angle. The rear lift jets maintained a 0° splay angle. Again, the thrust splay angle varied from 0° to 45° (δ = 0° to 45°) in 5° increments at the same altitude ($H = 4\ D_j$) and headwind speed ($U_\infty = 0.03\ V_j$) just as in the all jets splayed variation. Fig. 17 shows the temperature contours in the same two planes as in Fig. 14: the ground plane and a vertical plane on the inner side of the lift jets. Again, the selected splay angles (0°, 5°, 10°, 20°, 25°, and 30°) show the changes in the flow structures due to varying the angle of the forward jets alone. The flow field changes are basically the same as in the cases with all the jets splayed.

The ingestion effects of thrust splay angle for the forward jets can be seen in Fig. 18. The average temperature first rises and then drops until a splay angle of about 20° where it rises very slightly. A local maximum exists at 25° splay angle before the average temperature drops and flattens out at its lowest value. Both the minimum and maximum temperatures follow a similar behavior. The distortion and average temperature rise displayed in Fig. 19 show the same patterns, just as when all the jets are splayed. Overall, splaying the forward jets alone gives the same effects on hot gas ingestion as splaying all the jets.

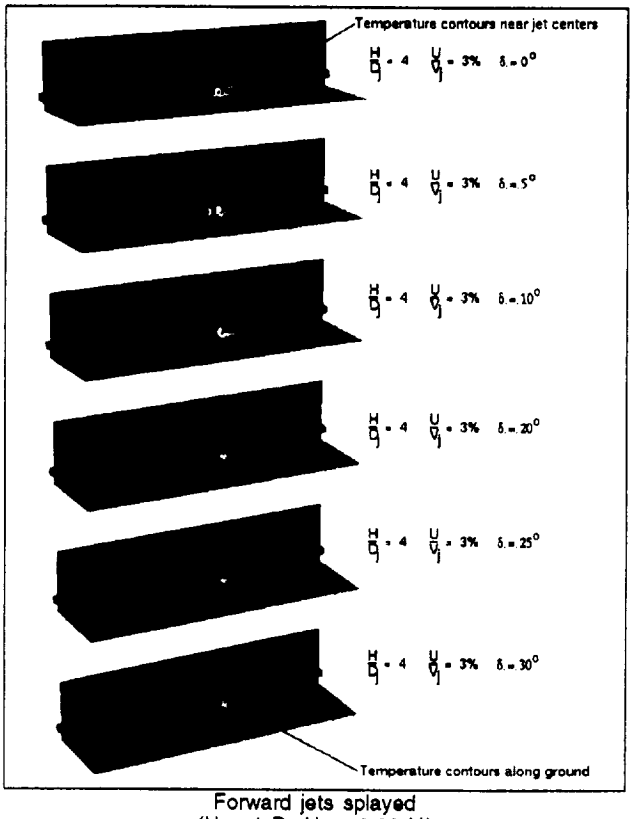

Forward jets splayed
($H = 4\ D_j$, $U_\infty = 0.03\ V_j$)
Figure 17

CONCLUSIONS/REMARKS

In summary, the average of the engine face temperatures decreases with increasing height but is relatively unaffected by headwind speed. Engine face temperature distortion also decreases with increasing height, but unexpectedly increases with headwind speed until the forward vortex is behind the inlet face. The headwind speed variation reveals that (for a constant height) the engine face temperature is dominated by near field ingestion effects.

As for the thrust splay angle variation, splaying the jets inward (for a constant height and headwind speed) first causes a rise and then a rapid decrease in hot gas ingestion, although a local maximum exists when the jets converge at the ground plane. Also, splaying the forward jets alone instead of all the jets gives almost the same reduction in hot gas ingestion without as large a thrust penalty.

A comparison of the $H = 4\ D_j$, $U = 0.03\ V_j$ cases in the height parameter variation and the headwind speed parameter variation show the effects of the calculation domain on the flow field. The vertical walls of the narrower calculation domain definitely affect the ground vortices, but no differences exist in the temperatures reaching the

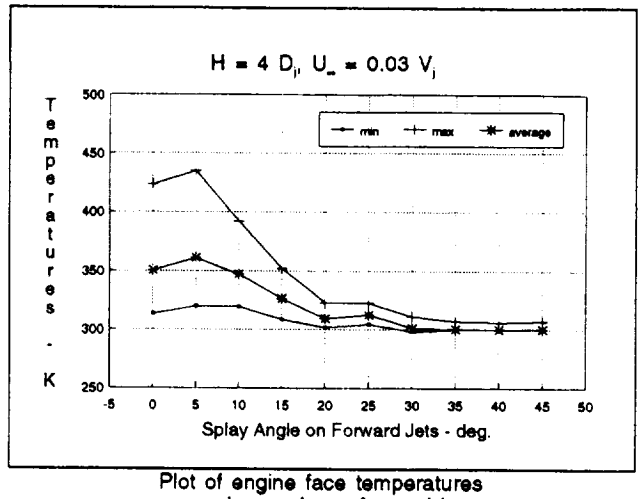

Plot of engine face temperatures
vs. splay angle on forward jets
Figure 18

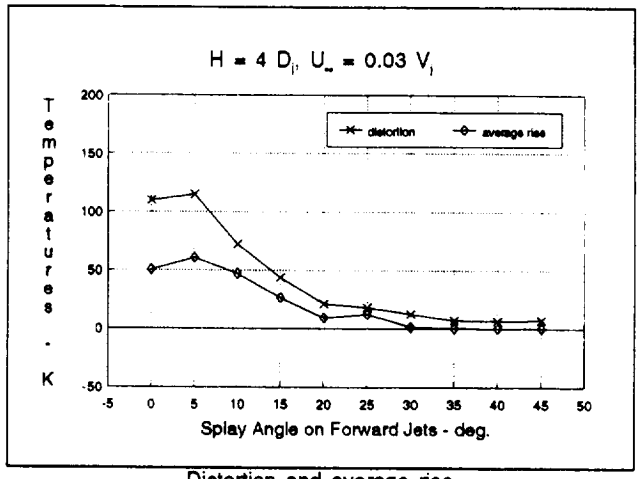

Distortion and average rise
vs. splay angle on forward jets
Figure 19

engine. Essentially, the tunnel walls in the calculation domain used for the height parameter variation are sufficiently far from the aircraft model so as to not affect the desired quantities (engine face temperatures). If the overall flow field is of primary interest, then the tunnel walls would have to be farther from the aircraft model.

This study did not address the importance of the aircraft geometry (fuselage, wings, tails, etc.) in relation to the flow field. Only one aircraft model was used, and it was quite simplistic.

The last conclusion from this study concerns the practicality of using an efficient CFD code for parameter variation studies. The turn-around time on a Cray-2 supercomputer and state-of-the-art workstations allows quick parameter changes. Typically, a Cray-2 supercomputer solved the flow field in about an hour with a turn-around time of a day. A dedicated IBM RS-6000 workstation can

solve the flow field in about 6 hours and can actually give shorter turn-around than the shared supercomputer.

REFERENCES

1. Kuhn, R.E., "Design Concepts for Minimizing Hot-Gas Ingestion in V/STOL Aircraft," Journal of Aircraft, Vol. 19, No. 10, Oct. 1982, pp. 845-850.

2. Kuhn, R.E., and Eshelman, J., "Ground Effects on V/STOL and STOL Aircraft--A Survey," AIAA Paper 85-4033, Oct. 1985. (NASA TM-86825).

3. VanOverbeke, T.J., and Holdeman, J.D., "A Numerical Study of the Hot Gas Environment Around a STOVL Aircraft in Ground Proximity," AIAA Paper 88-2882, July 1988. (NASA TM 100895).

4. VanOverbeke, T.J., and Holdeman, J.D., "Three-Dimensional Turbulent Flow Code Calculations of Hot Gas Ingestion," Journal of Aircraft, Vol. 27, No. 7, July 1990, pp 577-582.

5. Vanka, S.P., "Block-implicit Multigrid Solution of Navier-Stokes Equations in Primitive Variables," Journal of Computational Physics, Vol. 65, July 1986, pp. 138-158.

6. Vanka, S.P., "Efficient Computation of Viscous Internal Flows, SBIR Phase I Report (NAS3-25573)," August 1989.

7. Tafti, D., and Vanka, S.P., "Hot Gas Environment Around STOVL Aircraft in Ground Proximity, Part II: Numerical Study," AIAA Paper 90-2270, July 1990.

8. McLean, R., Sullivan, J., and Murthy, S.N.B., "Hot Gas Environment Around STOVL Aircraft in Ground Proximity--Part I: Experimental Study," AIAA Paper 90-2269, July 1990.

9. McLean, R.J, "The Flowfield Around a STOVL Aircraft Model in Ground Effect," May 1991, NASA CR187091.

10 . Johns, A.L., Neiner, G., and Bencic, T.J., "Hot Gas Ingestion Test Results of a Two-Poster Vectored Thrust Concept With Flow Visualization in the NASA Lewis 9- by 15-Foot Low Speed Wind Tunnel," AIAA Paper 90-2268. (NASA TM 103258).

APPENDIX E

CALCULATIONS OF HOT GAS INGESTION FOR A STOVL AIRCRAFT MODEL

JOURNAL OF AIRCRAFT
Vol. 31, No. 1, Jan.–Feb. 1994

Calculations of Hot Gas Ingestion for a STOVL Aircraft Model

D. M. Fricker* and J. D. Holdeman†
NASA Lewis Research Center, Cleveland, Ohio 44135
and
S. P. Vanka‡
University of Illinois at Urbana—Champaign, Urbana, Illinois 61801

Hot gas ingestion problems for STOVL (short take-off, vertical landing) aircraft are typically approached with empirical methods and experience. In this study, the hot gas environment around a STOVL aircraft was modeled as multiple jets in crossflow with inlet suction. The flowfield was calculated with a Navier-Stokes, Reynolds-averaged, turbulent, three-dimensional CFD code using a multigrid technique. A simple model of a STOVL aircraft with four choked jets at 1000 K was studied at various heights, head wind speeds, and thrust splay angles in a modest parametric study. Scientific visualization of the computed flowfield shows a pair of vortices in front of the inlet.

Nomenclature

D_j = characteristic length of jet nozzles, 0.0366 m (1.44 in.)
H = distance from ground to bottom of the aircraft (aircraft altitude or height)
k = turbulent kinetic energy
U_∞ = head wind velocity
V_j = jet nozzle exit velocity, 633 m/s (2080 ft/s)
x = axial Cartesian coordinate, zero at upstream boundary
x-y = vertical plane aligned in axial direction
x-z = horizontal plane
y = vertical Cartesian coordinate, zero at ground plane
y-z = vertical plane aligned in spanwise direction
z = spanwise Cartesian coordinate, zero at aircraft centerline plane
δ = thrust splay angle measured from the downward vertical toward symmetry plane
ε = turbulent energy dissipation

Introduction

HOT gas ingestion can cause significant problems for a STOVL (short take-off, vertical landing) aircraft, including reduced thrust and compressor stalls. These problems involve many hazards for the pilots, including very hard landings. During the design of a STOVL aircraft, hot gas ingestion problems are typically approached with empirical methods and experience.[1,2] Given the power of today's supercomputers and workstations, numerical methods employing efficient algorithms are becoming a viable engineering tool for analysis and design. In a previous endeavor, VanOverbeke and Holdeman[3,4] demonstrated the feasibility of CFD analysis for hot gas ingestion. This study is a follow-on effort exploring the practicality of using an efficient numerical method for the problem of hot gas ingestion.

Presented as Paper 92-0385 at the AIAA 30th Aerospace Sciences Meeting and Exhibit, Reno, NV, Jan. 6–9, 1992; received March 27, 1992; revision received Sept. 30, 1992; accepted for publication Oct. 25, 1992.

*Aerospace Engineer, Vehicle Propulsion Directorate, Army Research Laboratory (AMSRL-VP), M/S 5-11. Member AIAA.
†Senior Research Engineer, Internal Fluid Mechanics Division, MC 244. Associate Fellow AIAA.
‡Associate Professor, Department of Mechanical and Industrial Engineering. Member AIAA.

Flowfield Description

Ingestion of hot gases generates problems in two ways: 1) an average temperature rise results in a loss of engine thrust, and 2) a temperature distortion may cause the engine to stall. Engine exhaust gases may be ingested by far-field and/or near-field mechanisms. A schematic of these mechanisms is shown in Fig. 1.

The far-field mechanism results from the exhaust gases impinging on the ground and forming radial wall jets which flow forward, separate, and mix with the head wind. Near-field ingestion occurs with multiple jet configurations. Wall jets flowing out from the lift jets meet and create an upflow or fountain. This fountain flow can impinge on the aircraft's underside, flow along the fuselage to the engine inlets, and be ingested. The gases ingested by this near-field mechanism tend to be hotter, giving greater temperature distortion than those ingested by the far-field mechanism.

As stated earlier, the hot gas environment around a STOVL aircraft was modeled as multiple jets in crossflow with inlet suction. Mass sources represent the nozzle exits, and a mass

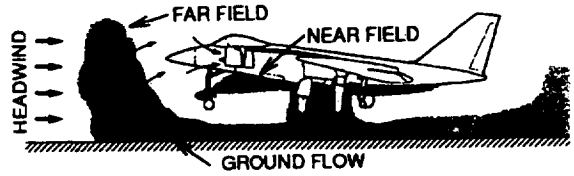

Fig. 1 Hot gas ingestion mechanisms.

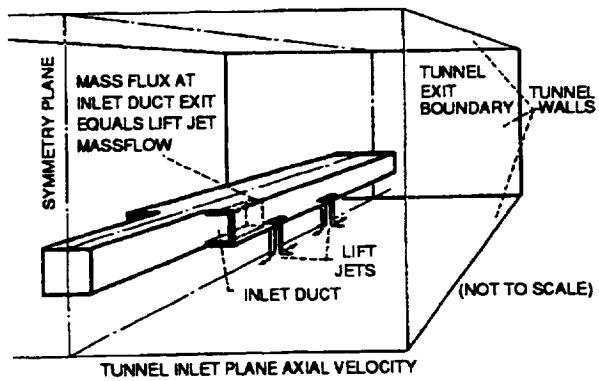

Fig. 2 STOVL Aircraft model.

sink at the end of the inlet provides the suction. The mass injected by the nozzles balances the mass removed by the inlet suction. This configuration is derived from the previous study by VanOverbeke and Holdeman.[3,4] To meet the requirements of the CFD code, the aircraft model is placed in a confined flow, i.e., a "wind tunnel." (It should be noted that changes in the width of the confinement did not significantly affect the flowfield in the vicinity of the jets and inlet for the same inflow and jet conditions. Thus, the wind-tunnel walls had minimal effect on the desired results.) Also, the aircraft model has no angle of attack due to the use of a Cartesian grid-based flow solver.

The STOVL aircraft model (see Fig. 2) is composed of rectangular solids for the fuselage and engine. For computational simplicity, the nose and the tail of the aircraft reach to infinity, and the model lacks wings. Baffles on the sides of the fuselage comprise the walls of the inlet. The nozzles are square in cross section and are flush with the bottom of the aircraft. The square cross section of the jets and the rectangular aircraft body result from the use of the Cartesian grid.

The four choked nozzles inject air at 1000 K (1340°F) straight down into the flowfield with a velocity of 633 m/s (2080 ft/s). Each lift jet issues from the nozzle exit in a uniform flow. The head wind is also a uniform flow, but at a temperature of 300 K (81°F). This approximates an aircraft landing with a forward speed, or an aircraft facing into a wind which lacks a boundary layer. In the baseline case, the head wind (U_∞) flows at 3% of the jet velocity (V_j), or about 19 m/s (37 kt), and the distance from the ground to the bottom of the aircraft model (H) is four times the characteristic length of the nozzles ($4D_j$). The parametric studies include: various altitudes ($H = 2-32D_j$) at a constant head wind ($U_\infty = 0.03V_j$); various head wind speeds ($U_\infty = 0.01-0.09V_j$) for a constant aircraft altitude ($H = 4D_j$); and various thrust splay angles ($\delta = 0-45$ deg) for a constant height ($H = 4D_j$) and head wind speed ($U_\infty = 0.03V_j$).

The physical dimensions of the aircraft model are given in Table 1. Note that the forward and aft nozzles have the same side-to-side separation, i.e., they are in-line, not offset.

Table 1 STOVL Aircraft model dimensions

Fuselage	
Width (nose)	$2.25D_j$
Width (tail)	$5.05D_j$
Height	$2.5D_j$
Length	∞
Inlet	
Width	$1.4D_j$
Height	$2.5D_j$
Length	$9.5D_j$
Jets separation	
Center-to-center	
Side-to-side	$3.25D_j$
Fore and aft	$6.0D_j$

Numerical Description

Calculation Domain

The grid geometry used for the baseline case is shown in Fig. 3. Exhibited are the centerline plane, the ground plane, and a vertical spanwise plane at the end of the domain as well as the aircraft model. The grid shows the high density of the calculation nodes in the region of the jets. For all calculations, symmetry assumptions allowed calculating only half of the physical domain.

The other boundary conditions for the calculation domain include an inflow simulating the head wind for the domain face in front of the aircraft model and an outflow condition for the domain face behind the model. All flow properties are defined for the inflow condition. The outflow condition, in contrast, merely assumes the properties of the axially nearest cells. The top, bottom, and remaining side of the domain are no-slip, stationary walls, as are the aircraft surfaces. All the walls assume adiabatic conditions for the energy equation. The symmetry plane also has a symmetry condition for the energy equation.

For the height variation, the grid contains 211,200 cells arranged as follows: 100 cells in the x (longitudinal) direction, 44 cells in the y (vertical) direction, and 48 cells in the z (horizontal) direction. The physical dimensions of the baseline grid are about $135D_j$ long, $29D_j$ high, and $40D_j$ wide. The

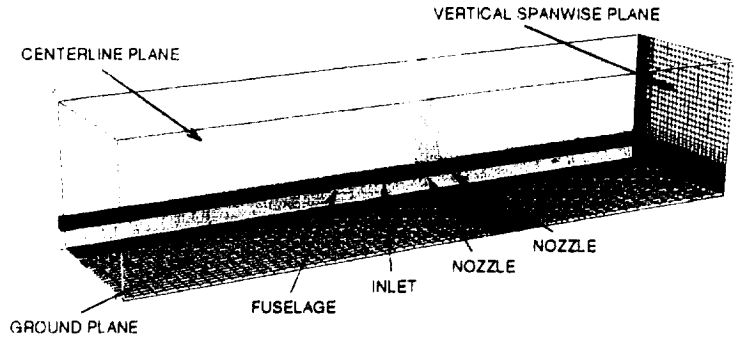

Fig. 3 Grid for baseline case.

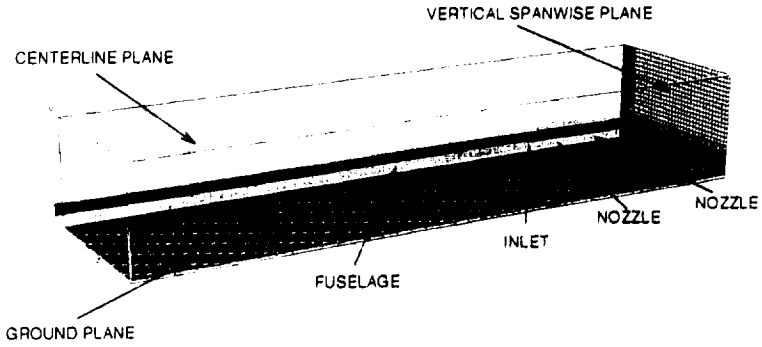

Fig. 4 Grid for head wind speed variation.

aircraft to ground distance was varied by elongating the cells underneath the aircraft. This facilitated the comparative analysis.

The head wind speed variation used a slightly modified grid; 100 cells in x, 44 cells in y, and 60 cells in z, yielding 264,000 total cells (see Fig. 4). This grid has a greater length ($177D_j$) and greater width ($59D_j$) than the baseline grid. Also, the distance in front of the forward pair of jets is greater ($152D_j$ vs $76D_j$ for the baseline grid) to accommodate the long region of hot gas in front of the inlet in the $U_\infty = 0.01V_j$ case. (In each of the grids, the inflow boundary condition is far enough from the stagnation point of the hot ground flow to prevent interference with the fluid mechanics. Also, the tunnel wall boundaries are sufficiently far from the aircraft model to minimize effects on the flowfield.) No grid modification was needed to vary the head wind speed.

Flow Solver

The flowfield in this domain was calculated with a Navier-Stokes, Reynolds-averaged CFD code. References 5–7 describe this steady-state CFD code (and its techniques) for the three-dimensional analysis of turbulent elliptic flows in a Cartesian coordinate system.

The CFD code (CART3D) solves the time-averaged Navier-Stokes or Reynolds equations. The k-ε turbulence model provides closure. The governing equations include continuity, x-, y-, and z-momenta, energy, turbulent kinetic energy, and turbulent energy dissipation. These equations are solved using a block-implicit multigrid algorithm developed by Vanka.[5]

CART3D uses a hybrid-differencing scheme on a staggered grid. This means that the code uses central differencing or upwind differencing, depending upon the cell's Reynolds number. Also, the scalar properties (density, pressure, etc.) are calculated at the cell volume centers, while the velocities are solved at the centers of the cell faces.

The multigrid technique speeds convergence by solving the equations on sequential grids of different cell densities. The flow is initialized on the coarsest grid which gets refined by the multigridding. Dividing each cell on a grid into eight equal cells refines the grid for the next grid level. A V cycle of sweeps on the various grid levels is performed until the solution converges on the finest grid. This technique speeds convergence by dampening out errors with the various levels of grid refinement.

To determine convergence, the residuals are nondimensionalized by an appropriate number, and then the maximum of all the residuals is compared to the tolerance criterion. The tolerance criterion used by this study is 1% for the finest grid. All test cases used the third grid level for the finest grid.

Flowfield Features

A short study of the features in the baseline case will help bring out the differences caused by varying the aircraft altitude, the head wind speed, and the thrust splay angle.

Figure 5 displays the temperature contours in an x-z plane near the ground. These contours show the locations of the forward vortex pair and the two ground vortices generated by the interaction of the jets and the crossflow. The axis for the forward vortex pair is perpendicular to the plane shown in Fig. 5, while the axes for the ground vortices are parallel to the plane. The forward vortex pair is smeared by the steady-state calculations, but still agrees well with the time-averaged experimental data.[8–10]

The particle traces in Fig. 6 reveal ingestion of exhaust gases. The particle traces from the jet region show the forward vortex and ingestion into the inlet. The particle traces starting at the inflow boundary show the head wind's deflection around the forward vortex. Temperature contours along the ground plane are also shown for clarity of position.

Figure 7 shows a three-dimensional temperature contour for the baseline case. This isotherm is for 325 K (125°F), a reasonable upper limit on the temperature of the air reaching the engine. With the ambient flow at 300 K (81°F), this represents a temperature rise of more than 25 K (45°F) for the fluid inside the isotherm. The inlet is almost completely obscured by the contour. Clearly, the engine is exposed to a considerable amount of hot gas from the engine exhaust. The

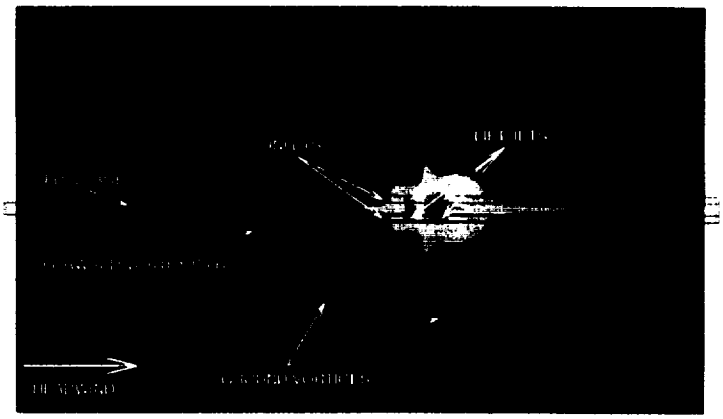

Fig. 5 x-z plane temperature contours $H = 4D_j$, $U_\infty = 0.03V_j$.

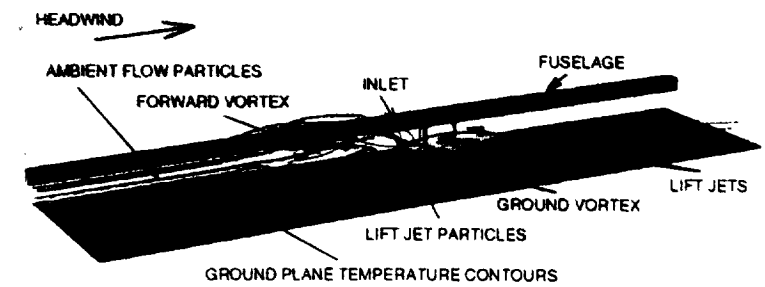

Fig. 6 Select particle traces $H = 4D_j$, $U_\infty = 0.03V_j$.

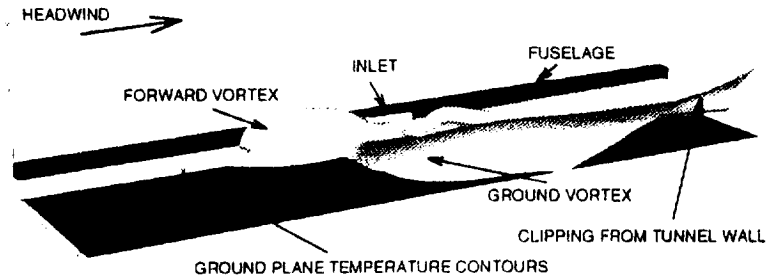

Fig. 7 Three-dimensional isotherm (T = 325 K) $H = 4D_j$, $U_\infty = 0.03V_j$, T_∞ = 300 K, T_j = 1000 K.

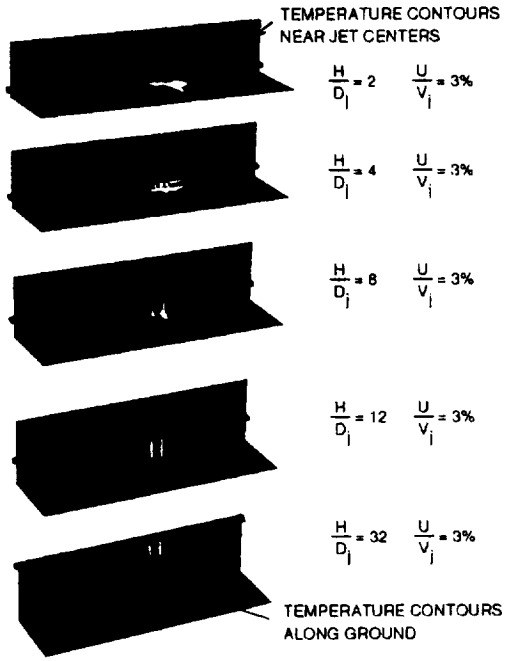

Fig. 8 Temperature contours in select planes ($U_\infty = 0.03V_j$).

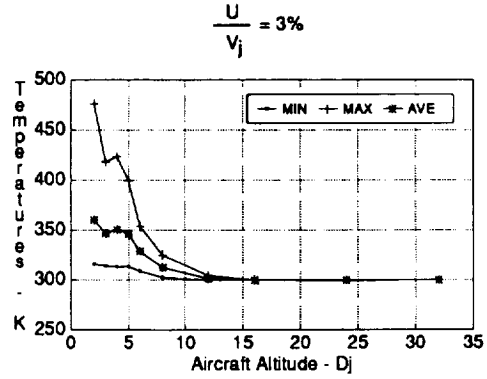

Fig. 9 Plot of engine face temperatures vs aircraft altitude.

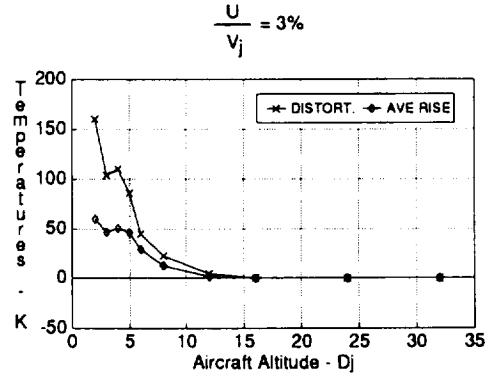

Fig. 10 Distortion and average rise vs aircraft altitude.

bubble in front of the inlet reveals the location of the forward vortex. Note that the clipping of the isotherm in the right side of Fig. 7 is due to wall effects which have no consequence on the hot gas ingestion.

Aircraft Altitude Parameter Variation

The aircraft altitude varied from 2 to $32D_j$. The cases actually computed over this range (H = 2, 3, 4, 5, 6, 8, 12, 16, 24, and $32D_j$) were carefully chosen to capture the changes in the flowfield features. Figure 8 shows temperature contours for select aircraft altitudes (2, 4, 8, 12, and $32D_j$) in two planes: 1) the ground plane and 2) a vertical plane passing through the jets near the jet centers. These cases show the changes in the flowfield affecting hot gas ingestion over the range of variation. In each case, the fuselage is mostly hidden by the vertical plane of temperature contours. The major effects of aircraft altitude can be seen in this figure: the forward vortex changes in character, the amount of hot gas ingested is reduced, and the ground vortices decrease in size.

In Fig. 9, the temperatures at the cells in front of the mass sink or "engine face" are plotted against the aircraft altitude. The temperatures shown are the minimum, the maximum, and a weighted average based on the cell volumes. The spread of the minimum and maximum temperature shows the temperature distortion at the engine face. This, and the average temperature rise above ambient, is plotted in Fig. 10. At low altitudes, the distortion is obviously extreme, and it quickly diminishes with increasing altitude. The average temperature shows a similar behavior. The nonmonotonic behavior at $H = 3D_j$ in all of these curves appears to be physical. At this time, the physical mechanism creating the local increase at $H = 3D_j$ is unknown. In tests for grid dependencies, other calculations on different grids exhibited the same trends, including the nonmonotonicity.

Head Wind Speed Parameter Variation

The head wind speed was varied from 1 to 9% of the jet velocity ($U_\infty = 0.01$–$0.09V_j$) in 1% increments for a constant altitude ($H = 4D_j$). Figure 11 displays temperature contours in the same two planes as in Fig. 8; the ground plane and a vertical plane passing through the jets near the jet centers. Selected head wind speeds (1, 3, 5, 7, and 9%) show the changes in the flowfield for the varying head wind speed. Again, the fuselage is mostly hidden by the vertical plane of temperature contours. In Fig. 11 the calculated domain includes a much larger region in front of the inlet in comparison with Fig. 8. This is due to a very long region of exhaust gas which extends in front of the inlet along the ground in the $U_\infty = 0.01V_j$ case.

The effect of head wind speed on the engine face temperatures can be seen in Fig. 12. Note that the minimum temperature declines rather steadily with increasing head wind speed. The general flatness of the average temperature would indicate that near-field ingestion dominates over most of the speed range. The temperature distortion at the engine face varies weakly with head wind speed at the low speeds, and is

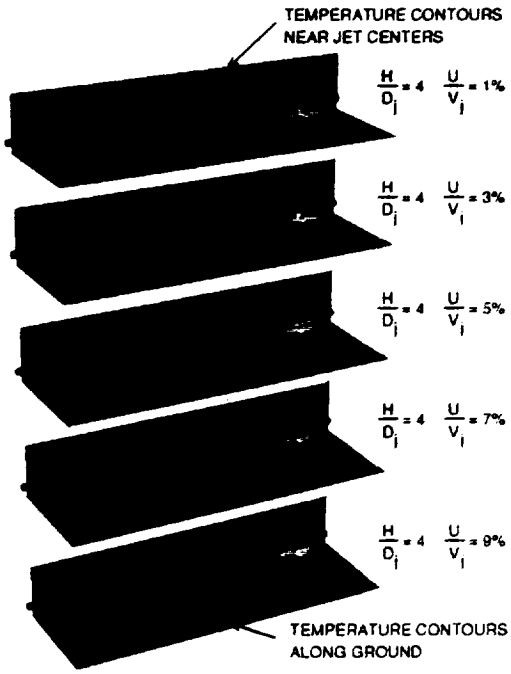

Fig. 11 Temperature contours in select planes ($H = 4D_j$).

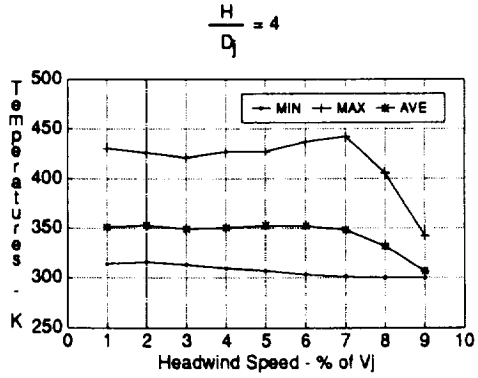

Fig. 12 Plot of engine face temperatures vs head wind speed.

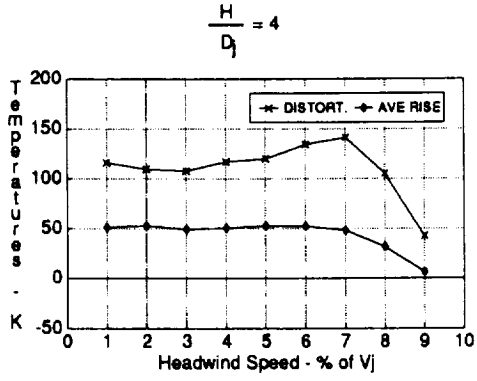

Fig. 13 Distortion and average rise vs head wind speed.

greatest for the 7% case as shown in Fig. 13. One should note that these high-velocity ratios are unrealistically representing a windy vertical landing, but they might be relevant for a low-speed runway landing. For choked jets, the 9% head wind represents about a 110-kt head wind which would either be a hurricane, or a slower than normal landing speed for a conventional fighter aircraft.

Thrust Splay Angle Parameter Variation

A technique used to help control hot gas ingestion is to splay the jets. By angling the lift jets, the relative strengths

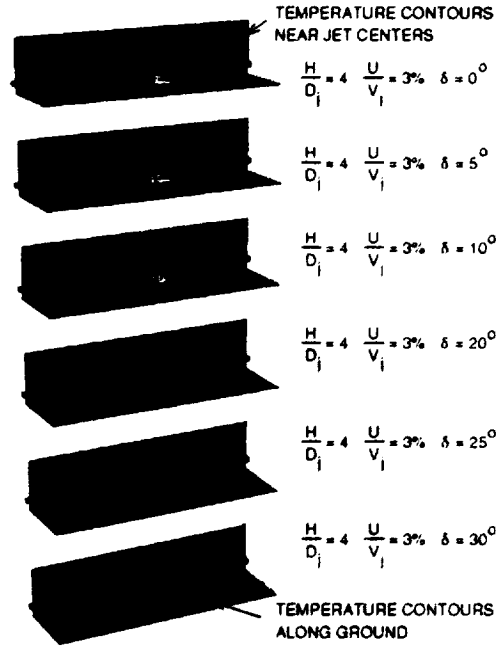

Fig. 14 Temperature contours in select planes—splaying all jets ($H = 4D_j$, $U_\infty = 0.03V_j$).

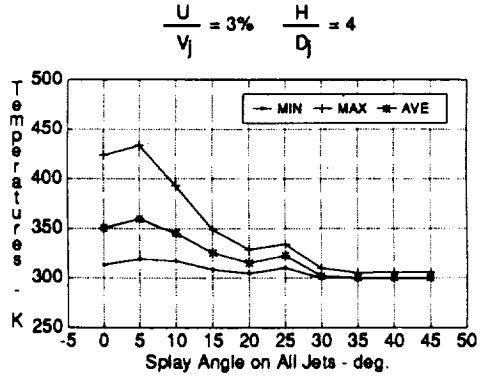

Fig. 15 Plot of engine face temperatures vs splay angle on all jets.

of the fountain, upwash, and vortices are changed, therefore changing the flow structures affecting ingestion. In this study, the splay angle (δ) of the thrust is measured from the downward vertical inward to the centerline plane of the aircraft model. To vary the thrust splay angle, the component velocities on the jets changed to provide the required angle while keeping the speed of the jet constant. Thus, the direction of the lift jets changed while the geometry of the aircraft model did not.

Splaying All Jets

For the first variation of the thrust splay angle, all four jets were splayed the same amount. The splay angle varied from 0 to 45 deg (δ = 0–45 deg) in 5-deg increments for a constant height ($H = 4D_j$) and constant head wind speed ($U_\infty = 0.03V_j$). Figure 14 shows temperature contours in two planes similar to those displayed in Figs. 8 and 11; the ground plane and a vertical plane that is now on the inner side of the lift jets (instead of near the center). Selected splay angles (0, 5, 10, 20, 25, and 30 deg) show the changes in the flow structures due to varying the angle of all the jets. The most noticeable change occurs in the length of the hot gas region in front of the inlet. A less noticeable change is the increase of hot gas directly in front of the inlet for the 5-deg case. This actually causes an increase in hot gas ingestion over the 0-deg case, instead of reducing it.

This and other effects of thrust splay angle for all the jets can be seen in Figs. 15 and 16. In Fig. 15, the average tem-

perature first rises and then drops until a splay angle of about 20 deg, where it starts rising again. A local maximum exists at the 25-deg point before the average temperature flattens out at its lowest value. Both the minimum and maximum temperatures follow the same behavior. The distortion and average temperature rise displayed in Fig. 16 show the same patterns. Note that for this configuration of model and altitude, the jets will converge at the ground for a thrust splay angle of 22 deg.

Splaying Forward Jets Only

In the second variation, only the forward jets varied in thrust splay angle. The rear lift jets maintained a 0-deg splay angle. Again, the thrust splay angle varied from 0 to 45 deg (δ = 0–45 deg) in 5-deg increments at the same altitude ($H = 4D_j$) and head wind speed ($U_\infty = 0.03V_j$), just as in the all jets splayed variation. The calculated results are extremely similar to the results from splaying all the jets. As a matter of fact, a plot of the temperature contours in the same two planes as in Fig. 14 would appear almost identical to Fig. 14

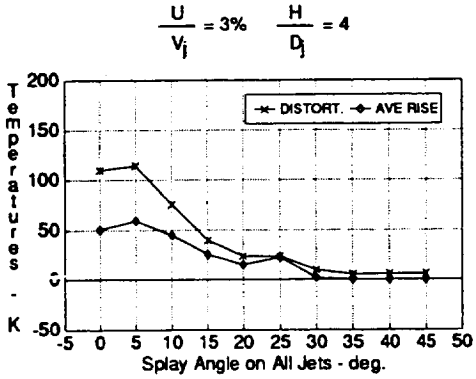

Fig. 16 Distortion and average rise vs splay angle on all jets.

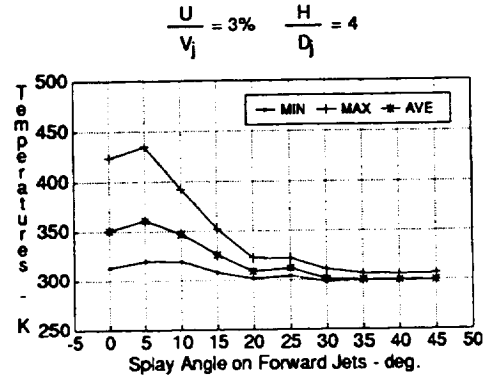

Fig. 17 Plot of engine face temperatures vs splay angle on forward jets.

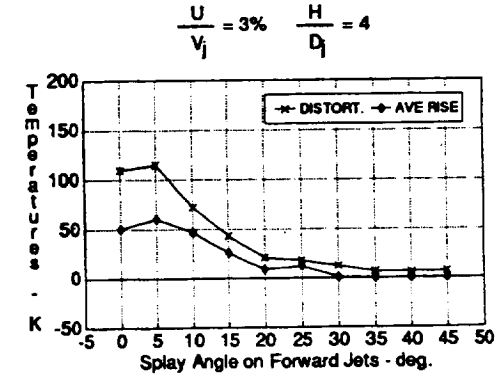

Fig. 18 Distortion and average rise vs splay angle on forward jets.

forward of the jets. (Such a plot does exist in the paper, but it is not here for brevity.)

The ingestion effects of thrust splay angle for the forward jets can be seen in Fig. 17. The average temperature first rises and then drops until a splay angle of about 20 deg, where it rises very slightly. A local maximum exists at 25-deg splay angle before the average temperature drops and flattens out at its lowest value. Both the minimum and maximum temperatures follow a similar behavior. The distortion and average temperature rise displayed in Fig. 18 show the same patterns, just as when all the jets are splayed. Overall, splaying the forward jets alone gives the same effects on hot gas ingestion as splaying all the jets.

Conclusions and Remarks

In summary, the average of the engine face temperatures decreases with increasing height, but is relatively unaffected by head wind speed. Engine face temperature distortion also decreases with increasing height, but increases with head wind speed until the forward vortex is behind the inlet face. The head wind speed variation reveals that (for a constant height) the engine face temperature is dominated by near-field ingestion effects.

As for the thrust splay angle variation, splaying the jets inward (for a constant height and head wind speed) first causes a rise and then a rapid decrease in hot gas ingestion, although a local maximum exists when the jets converge at the ground plane. Also, splaying the forward jets alone, instead of all the jets, gives almost the same reduction in hot gas ingestion without as large a thrust penalty.

A comparison of the $H = 4D_j$, $U = 0.03V_j$ cases in the height parameter variation and the head wind speed parameter variation show the effects of the calculation domain on the flowfield. The vertical walls of the narrower calculation domain definitely affect the ground vortices, but no differences exist in the temperatures reaching the engine. If the overall flowfield is of primary interest, then the tunnel walls would have to be farther from the aircraft model.

This study did not address the importance of the aircraft geometry (fuselage, wings, tails, etc.) in relation to the flowfield. Only one aircraft model was used, and it was quite simplistic.

The last conclusion from this study concerns the practicality of using an efficient CFD code for parameter variation studies. The turnaround time on a Cray-2 supercomputer and state-of-the-art workstations allows quick parameter changes. Typically, a Cray-2 supercomputer solved the flowfield in about an hour with a turnaround time of a day. A dedicated IBM RS-6000 workstation can solve the flowfield in about 6 h and can actually give shorter turnaround than the shared supercomputer.

References

[1]Kuhn, R. E., "Design Concepts for Minimizing Hot-Gas Ingestion in V/STOL Aircraft," *Journal of Aircraft*, Vol. 19, No. 10, 1982, pp. 845–850.

[2]Kuhn, R. E., and Eshelman, J., "Ground Effects on V/STOL and STOL Aircraft—A Survey," AIAA Paper 85-4033, Oct. 1985; see also NASA TM-86825, Nov. 1985.

[3]VanOverbeke, T. J., and Holdeman, J. D., "A Numerical Study of the Hot Gas Environment Around a STOVL Aircraft in Ground Proximity," AIAA Paper 88-2882, July 1988; see also NASA TM-100895, July 1988.

[4]VanOverbeke, T. J., and Holdeman, J. D., "Three-Dimensional Turbulent Flow Code Calculations of Hot Gas Ingestion," *Journal of Aircraft*, Vol. 27, No. 7, 1990, pp. 577–582.

[5]Vanka, S. P., "Block-Implicit Multigrid Solution of Navier-Stokes Equations in Primitive Variables," *Journal of Computational Physics*, Vol. 65, July 1986, pp. 138–158.

[6]Claus, R. W., and Vanka, S. P., "Multigrid Calculations of a Jet in Crossflow," *Journal of Propulsion and Power*, Vol. 8, No. 2, 1992,

pp. 425–431.

[7]Tafti, D. K., and Vanka, S. P., "Hot Gas Environment Around STOVL Aircraft in Ground Proximity—Part 2: Numerical Study," *Journal of Aircraft*, Vol. 29, No. 1, 1992, pp. 20–27; see also AIAA Paper 90-2270, July 1990.

[8]McLean, R., Sullivan, J., and Murthy, S. N. B., "Hot Gas Environment Around STOVL Aircraft in Ground Proximity—Part 1: Experimental Study," *Journal of Aircraft*, Vol. 29, No. 1, 1992, pp. 67–72; see also AIAA Paper 90-2269, July 1990.

[9]McLean, R. J., "The Flowfield Around a STOVL Aircraft Model in Ground Effect," NASA CR-187091, May 1991.

[10]Johns, A. L., Neiner, G., and Bencic, T. J., "Hot Gas Ingestion Test Results of a Two-Poster Vectored Thrust Concept with Flow Visualization in the NASA Lewis 9- by 15-Foot Low Speed Wind Tunnel," AIAA Paper 90-2268, July 1990; see also NASA TM-103258, July 1990.

APPENDIX F

MULTIGRID CALCULATIONS OF INTERNAL FLOWS IN COMPLEX GEOMETRIES

AIAA Paper 92-0096

Multigrid Calculation of Internal Flows in Complex Geometries

K. M. Smith* and S. P. Vanka**
Department of Mechanical and Industrial Engineering
University of Illinois at Urbana-Champaign
Urbana, Illinois 61801

Abstract

The development, validation, and application of a general purpose multigrid solution algorithm and computer program for the computation of elliptic flows in complex geometries is presented. This computer program combines several desirable features including a curvilinear coordinate system, collocated arrangement of the variables, and Full Multi-Grid / Full Approximation Scheme (FMG/FAS). Provisions are made for the inclusion of embedded obstacles and baffles inside the flow domain. The momentum and continuity equations are solved in a decoupled manner and a pressure correction equation is used to update the pressures such that the fluxes at the cell faces satisfy local mass continuity. Despite the computational overhead required in the restriction and prolongation phases of the multigrid cycling, the superior convergence results in reduced overall CPU time. The numerical scheme and selected results of several validation flows are presented. Finally, the procedure is applied to study the flowfields in a side-inlet dump combustor and twin jet impingement from a simulated aircraft fuselage.

Introduction

In recent years, multigrid methods have been shown to effectively improve the speed of many internal and external fluid flow calculations[1-4]. Multigrid methods have been applied to both incompressible and compressible flows and unstructured grids[5]. Despite these advances, there have not been many applications of multigrid methods to complex practical internal flows that include features such as embedded obstacles, mass injections, combustion and complex geometries.

In the present paper, we describe our recent work towards the development of a finite volume multigrid algorithm as well as a computer program that can address several practical flows encountered in the propulsion industry. The solution algorithm is based on a collocated arrangement of pressures and velocities and uses multigrid cycling to efficiently converge the low frequency errors. A combined first/second order difference scheme is used to discretize the equations. The steady-state mean flow equations along with a two-equation k-ε model of turbulence are solved for analyzing turbulent flows. Further, provisions are made to include any arbitrary number of obstacles and baffles to simulate internal flow obstructions.

The concept of multigrid methods is to use a sequence of coarse and fine finite-difference grids on which the solution is cycled continuously to remove the low frequency content of the solution error. The current multigrid cycling uses a V-cycle for transferring the residuals and prolongating the corrections from the coarse grids. In the collocated arrangement, the velocities and pressure are located at the cell centers, but the fluxes are evaluated at the cell faces. For incompressible flows, this evaluation of fluxes must be done carefully in order to avoid a checker-board split of the pressure field. The present scheme uses a momentum interpolation scheme similar to the practices of Rhie and Chow[6], Peric et al.[7], and Barcus et al.[4]

In the following sections, a description of the governing equations, the numerical procedure, the systematic validation of the code, and its application to two problems of interest to the aero-propulsion community are presented.

Governing Fluid Flow Equations

All the relevant partial-differential equations can be represented by a single equation for the transport of a general scalar variable ϕ. The governing equation for ϕ in an arbitrary coordinate system (ξ,η,ζ) can be written in strong conservative form as

$$\frac{\partial}{\partial\xi}(\rho U\phi)+\frac{\partial}{\partial\eta}(\rho V\phi)+\frac{\partial}{\partial\zeta}(\rho W\phi)=$$

$$\frac{\partial}{\partial\xi}\left[\frac{\Gamma}{J}(q_{11}\,\phi_\xi+q_{12}\,\phi_\eta+q_{13}\,\phi_\zeta)\right]+$$

$$\frac{\partial}{\partial\eta}\left[\frac{\Gamma}{J}(q_{21}\,\phi_\xi+q_{22}\,\phi_\eta+q_{23}\,\phi_\zeta)\right]+$$

$$\frac{\partial}{\partial\zeta}\left[\frac{\Gamma}{J}(q_{31}\,\phi_\xi+q_{32}\,\phi_\eta+q_{33}\,\phi_\zeta)\right]+$$

$$S(\xi,\eta,\zeta)\cdot J \tag{1}$$

where U, V and W are the contravariant components of the velocity vector. These components are related to the Cartesian velocities by the relations

$$[\underline{U}^T]=J[A][\underline{u}^T] \tag{2}$$

$$[A]=\begin{bmatrix}\xi_x & \xi_y & \xi_z\\ \eta_x & \eta_y & \eta_z\\ \zeta_x & \zeta_y & \zeta_z\end{bmatrix} \tag{3}$$

where

$$\underline{u}^T=(u,v,w) \tag{4}$$

The metrics in these expressions are given by

$$\xi_x=\frac{y_\eta z_\zeta - y_\zeta z_\eta}{J} \tag{5}$$

$$\xi_y=\frac{x_\zeta z_\eta - x_\eta z_\zeta}{J} \tag{6}$$

$$q_{11}=(\xi_x^2+\xi_y^2+\xi_z^2)\,J^2 \tag{7}$$

* Graduate Research Assistant
** Associate Professor, Member AIAA

$$q_{22} = (\eta_x^2 + \eta_y^2 + \eta_z^2) \; J^2 \tag{8}$$

etc.

For the turbulence transport equations, additional production and dissipation source terms in the equations for k and ε are to be included. These terms are transformed to the curvilinear coordinate system by the chain rule of differentiation.

Numerical Procedure

For a collocated scheme, the mass fluxes at the cell faces and the velocities at the cell centers are separately calculated and stored. The algorithm currently employs the popular hybrid differencing for evaluating the interface values. The discrete equation can be written in the conventional form

$$a_P \phi_P = \sum_{nb} a_{nb} \phi_{nb} + S^{\phi} \tag{9}$$

where ϕ_{nb} are the neighbor values of ϕ_P on a seven point stencil. S^{ϕ} is the corresponding total source term.

The key feature in collocated schemes for incompressible flows is the momentum interpolation of two cell-centered Cartesian velocities. The central idea of momentum interpolation[6] is to alter the expression for the net $\partial p/\partial \xi$ at the (i+1/2) cell face with a staggered pressure difference. For the V and W fluxes, the effective $\partial p/\partial \eta$ and $\partial p/\partial \zeta$ are similarly modified by staggered pressure differences. Such a momentum interpolation then provides a well-connected pressure field.

Consistent evaluation of the volume fluxes (U, V, W) on a coarse grid and prolongation of the associated corrections to the finer grids are observed to be the most important issues in the present collocated multigrid procedure. An inconsistent procedure resulting in limit cycling of the mass residuals is observed if the coarse grid fluxes at the cell faces are not properly updated after the momentum equations are solved. Let

$$\underline{\tilde{U}}^H = I_h^H \, \underline{U}^h \tag{10}$$

$$\underline{\tilde{u}}^H = I_h^H \, \underline{u}^h \tag{11}$$

be the restriction of the fluxes and the Cartesian velocities from a fine grid h to a coarse grid H, respectively, during the multigrid cycle. The solution of the coarse grid momentum equations gives a velocity field that satisfies

$$L^H \underline{u}^H = F^H + \tilde{R}^H \tag{12}$$

where $\tilde{R}^H$ is the residual of the coarse grid equation given by

$$\tilde{R}^H = I_h^H \, R^h \tag{13}$$

Let

$$\delta \underline{u}^H = \underline{u}^H - \underline{\tilde{u}}^H \tag{14}$$

A consistent update of the coarse grid flux is obtained by evaluating $\underline{U}^H$ as

$$\underline{U}^H = \underline{\tilde{U}}^H + J \cdot [A] [\delta \underline{u}^H]^T \tag{15}$$

where [A] is the matrix of coordinate transformation on the coarse grid. This coarse grid flux, however, does not satisfy the local mass continuity equation, thus requiring the restricted pressure field

$$\tilde{p}^H = I_h^H \, p^h \tag{16}$$

to be corrected by a pressure-correction equation. The coarse grid pressure-correction equation is derived in an identical manner to the fine grid equation by implying a staggered location of the cell face fluxes.

It is necessary to point out that the direct evaluation of the coarse grid fluxes from the newly computed Cartesian velocities leads to an inconsistent formulation with the residual mass source reaching a fixed non-zero value. Thus, the seemingly straight-forward update procedure

$$\underline{U}^H = J \cdot [A] [\underline{u}^H]^T \tag{17}$$

on a coarse grid during restriction phase does not lead to a consistent formulation. The derivation of the pressure correction equation follows the perturbation concept introduced by Patankar and Spalding[8] and used widely. The complete details of the solution algorithm are given in Smith and Vanka[9].

Results

The solution algorithm and its multigrid efficiency have been tested in a number of model problems. A detailed description of the systematic validation is precluded by space limitations; therefore, only three selected calculations are presented.

Laminar Lid-Driven Cube

To demonstrate the efficacy of using multigrid methods on elliptic problems, the laminar flow in a lid-driven cube was simulated for a Reynolds number of 100 based on lid velocity and side dimension. A 32^3 cell solution was selected. This problem was solved using identical initial guesses, relaxation factors, convergence criteria, and other numerical parameters in both a single-grid mode and in a three-grid mode. Figure 1 presents the convergence history for both a single grid solution

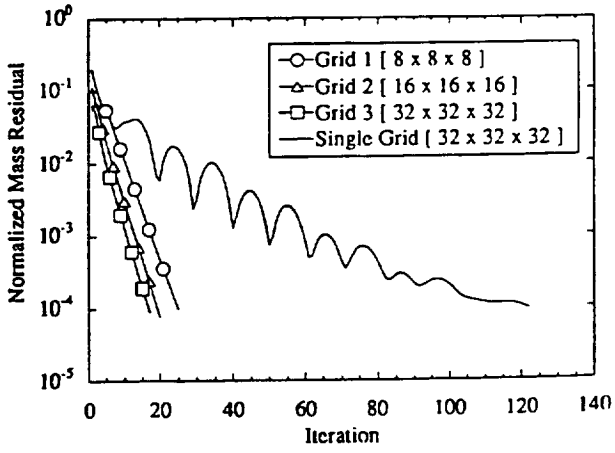

Fig. 1 Convergence history for laminar lid-driven cube calculation.

and a multigrid solution using a standard (1,1,1) three-level V-cycle. The multigrid solution converges at a log-linear rate on all three grid levels, while, in comparison, the single grid solution has an oscillatory and sluggish rate of convergence. The multigrid solution required only 20 equivalent iterations to converge to a mass residual of 10^{-5}; however, the single-grid

solution required 122 iterations to reach the same convergence level. The multigrid solution represents a speedup of 3.75 (based on CPU timings) over the single-grid solution. Further speedup can be expected when finer grids are considered.

Laminar Pipe Bend

As a stringent test to the coordinate transformations, the laminar flow in a 90 degree strongly curved pipe was analyzed. The flow in strongly curved ducts is elliptic because of the strong radial pressure variations and possible axial flow recirculation[10]. The circular pipe was transformed to a square through an elliptic grid generation procedure[11]. The curvature of the duct is also represented by a grid transformation to a straight duct. This flow has been previously computed by other researchers but on coarser grids and using single grid techniques.

The calculation was performed for the geometry described by Enayet et al.[12] In these experiments, the radius ratio of the bend was 5.6 and the Reynolds number was 500, corresponding to a Dean number of 211. The computational domain consisted of a short upstream tangent, the bend itself, and a downstream tangent. A representative computational grid is shown in figure 2. The advantage of the present coordinate system versus the conventional (r, θ, ϕ) system used in earlier works is that the current system distributes the mesh points more uniformly in the cross-section and avoids numerical difficulties caused by large cell aspect ratios at the center. The finest grid used in the present study consisted of 120 x 64 x 32 cells in the streamwise and cross-sectional directions, respectively. In order to accurately prescribe the thick inlet boundary layer, a fourth-order polynomial was fitted to the experimental streamwise velocity data at 0.58 diameters upstream of the bend inlet plane and prescribed as the inlet velocity to the computations. The remaining boundary conditions were no-slip at the walls, symmetry conditions at the center plane, and a zero-derivative condition at the exit.

Figure 3 shows the rate of convergence for a three-level 120 x 64 x 32 computation. The coarsest grid converges slowly due to the poor initial guess and is not shown. However, the two finer grids converge to a good accuracy at essentially the same rate. Approximately 5 minutes were required on a CRAY-Y/MP computer to complete the computation. Sequential grid refinement demonstrated that 120 x 64 x 32 cells provide an adequate grid-independent solution. Figure 4 presents a comparison of calculated values over a range of grid distributions and the experimental data of Enayet et al.[12] at the 60 degree plane. The agreement is very good with the high peaks being extremely well predicted. Agreement at other bend angles is observed to be also equally good. Figure 5 shows cross-stream flow patterns at 60 degrees indicating the production of streamwise vorticity by the bend.

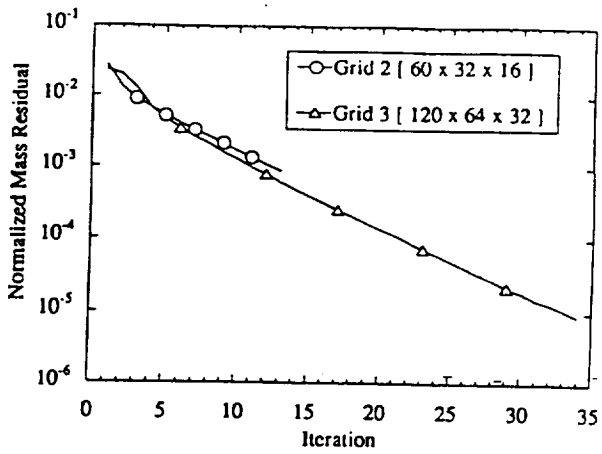

Fig. 3 Convergence history for laminar curved pipe calculation.

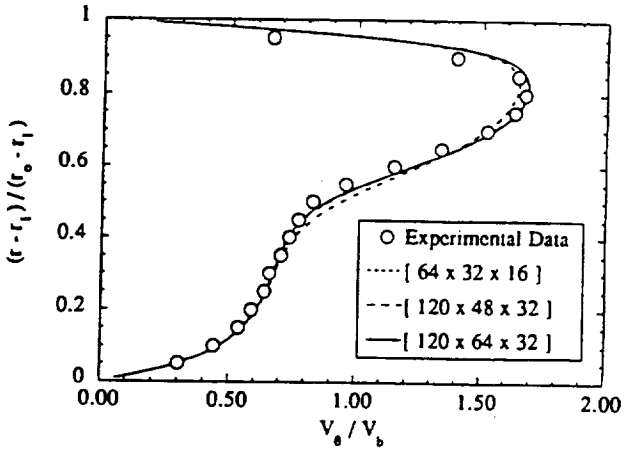

Fig. 4 Calculated and experimental streamwise velocity profiles at the 60° plane in the laminar curved pipe (radial coordinate versus non-dimensional streamwise velocity).

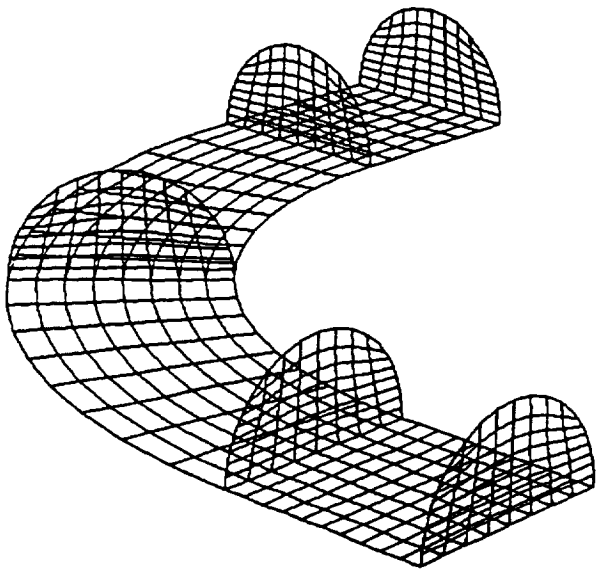

Fig. 2 Representative computational grid for curved circular pipe calculation.

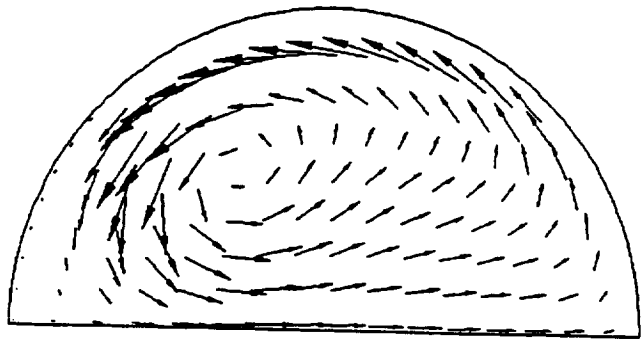

Fig. 5 Calculated secondary flow at the 60° plane in laminar curved pipe calculation.

Turbulent Flow in a Curved Square Duct

As a final validation case, calculations of the turbulent flow in a strongly curved square duct were performed. The computations were performed for the geometry described by Taylor et al.[13] including a 2.3 radius ratio at a Reynolds number of 40,000. Again, upstream and downstream tangent sections were included in the computational domain. The turbulence modeling is based on the standard k-ε model[14] without modifications to account for the curvature-induced anisotropy effects. Admittedly, this will result in some discrepancies between measurements and calculations. The solution of the k-ε equations in conjunction with the momentum equations is carried out in a sequential manner, but the k-ε equations are solved only on the locally finest grid in the Full Multigrid cycle and the turbulence viscosity field is restricted from the fine to coarse grids. Wall functions[14] are imposed on the finest grid and the implied wall viscosity is restricted for use in the coarse grid momentum equations. The finest grid in the present study utilized 120 x 64 x 32 cells in the streamwise, spanwise, and transverse directions, respectively.

Figure 6 shows the convergence of the algorithm on the two finest grids. It is seen that the convergence is not as fast as for the laminar case; however, the number of iterations required is still small and independent of the grid density. The solution required approximately 20 minutes on a CRAY-Y/MP computer. The slower convergence for turbulent flows in comparison with laminar flows is due to the coupling between the momentum and turbulence equations. It may be possible to accelerate this convergence slightly by better optimization of the relaxation factors.

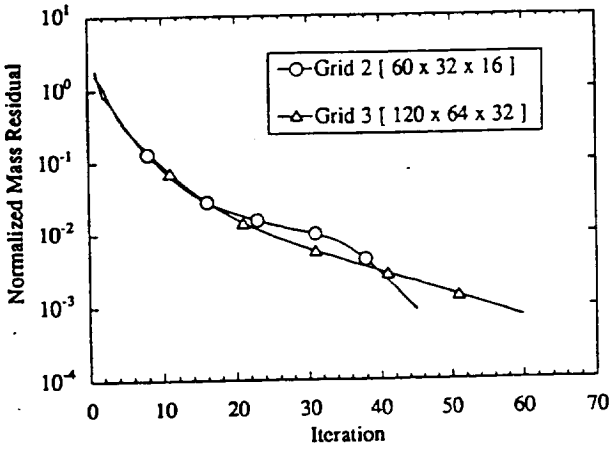

Fig. 6 Convergence history for the turbulent curved square duct calculation.

Figure 7 shows comparisons between calculated and experimental streamwise velocity profiles at angular positions of 30 degrees and 77.5 degrees in the bend. The calculations show satisfactory agreement with measured values and are also in good agreement with the calculations of Kreskovsky et al.[15] who used a similar model for the turbulent closure. However, the agreement with experimental data can be improved with more advanced turbulence models such as those based on the solution of the Reynolds stress equations.

Side-Inlet Ducted Rocket

As a demonstration of the computer program, the flowfield in a side-inlet ducted rocket was studied. The investigation was limited to an isothermal water tunnel simulation as reported by Stull et al.[16] This turbulent flowfield possesses several complex features including a streamwise recirculation region within the dome, impinging jets within the inlet region, and a pair of cross-stream vortices downstream of the inlet.

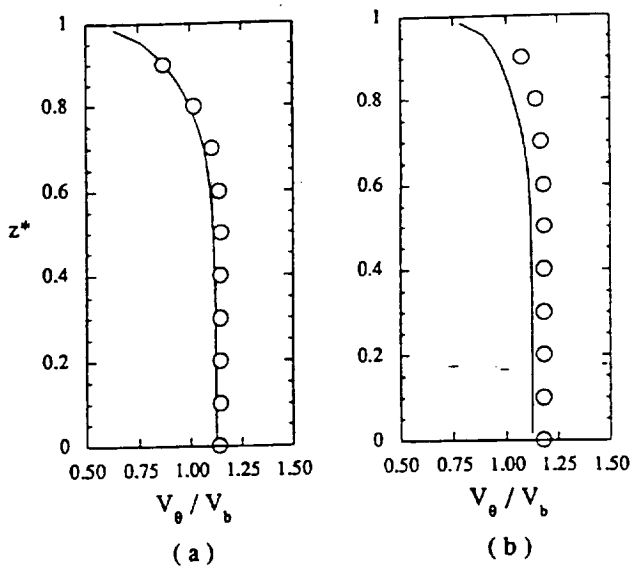

Fig. 7 Calculated and experimental streamwise velocity profiles along a mid-span line in turbulent curved square duct at a) 30 degrees and b) 77.5 degrees (transverse coordinate versus non-dimensional streamwise velocity).

The computations were carried out over a grid of 96 x 48 x 24 cells in the streamwise, transverse, and spanwise directions, respectively. Figure 8 illustrates a representative computational grid in the cross-sectional plane. Boundary conditions included no-slip walls for the combustor lining and dome plate, symmetry for the mid-span plane, inflow segment for the inlet duct, and zero-derivative outflow for the exit plane. The side-inlet arms were modelled as an inlet boundary condition with a plug velocity of 2.67 m/s corresponding to a inlet duct Reynolds number of 2.0×10^5. Three grid levels were used and the solution was iterated until a normalized mass residual of 1.0×10^{-3} was obtained. Figure 9 illustrates the good convergence rate on all grids. The slow convergence towards the end on the third grid is believed to be a result of the coupling between the turbulence and flow equations as described previously. Approximately 20 minutes on a CRAY-Y/MP computer were required to complete the computation.

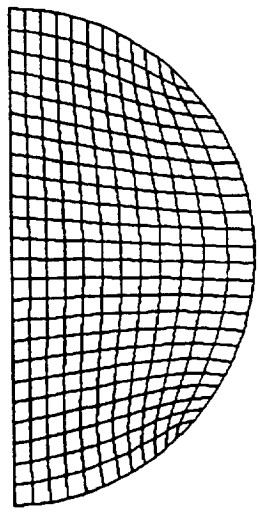

Fig. 8 Representative cross-sectional computational grid for ducted rocket calculation.

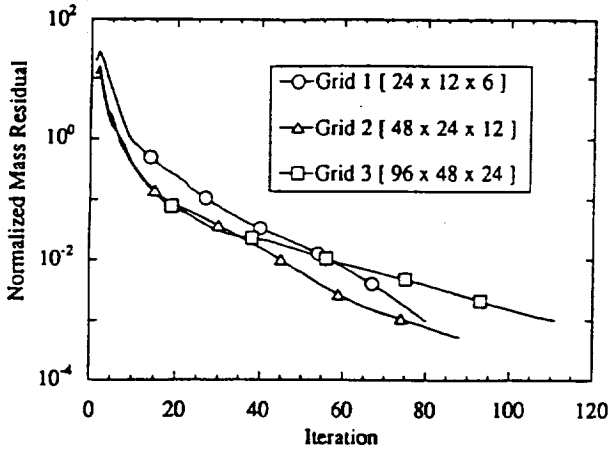

Fig. 9 Convergence history for ducted rocket calculation.

Figure 10 presents the computed velocity vectors in the symmetry plane of the ducted rocket. The entrainment by the inlet jets is responsible for driving the dome recirculation pattern shown. Figure 11 shows computed cross-stream flow patterns at two axial locations. Downstream of the inlet region, the flow is seen to possess a cross-stream vortex which results in helical pathlines.

The authors are not aware of any existing quantitative experimental data to which the present calculations can be directly compared; therefore, only qualitative observations are reported. The computed flow patterns agree well with flow visualization tests[16] except in the dome region where the flow was observed to be unsteady. The present calculations solve the steady-flow equations and, therefore, are not expected to give good agreement in this region. The flowfield downstream of the inlet is well characterized by the computations.

STOVL Hot Gas Ingestion Study

The eventual application of this computer program is intended to be the study of ingestion of hot gases by the inlets of Short Take-off and Vertical Landing (STOVL) aircraft in ground proximity. A number of interesting fluid dynamic effects have been identified when the lift jets of STOVL aircraft impinge on the ground surface[17,18]. First, as the lift jets expand, they entrain the surrounding fluid causing a negative pressure underneath the fuselage and a loss in lift. As the jets impinge on the ground and spread radially outwards, the wall jets

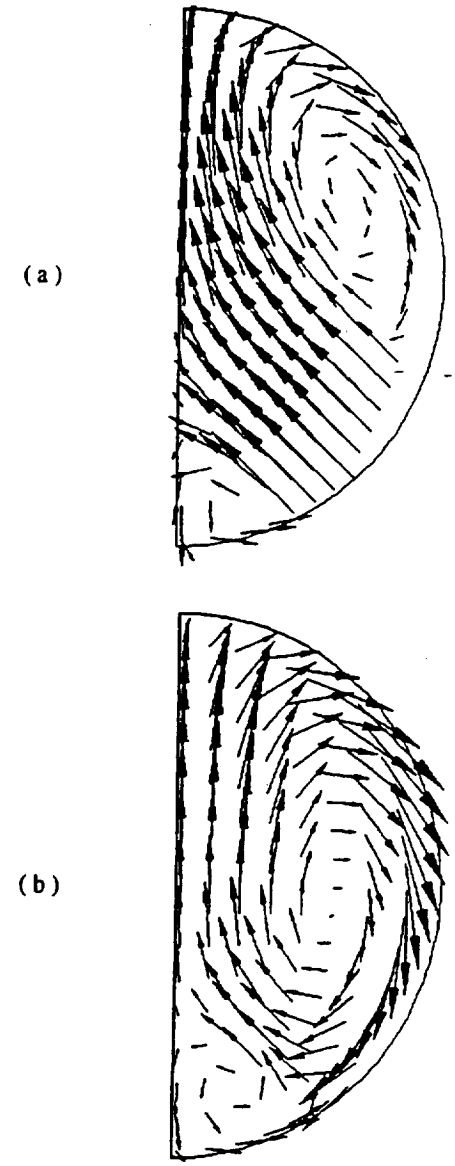

Fig. 11 Computed cross-sectional velocity vectors in the ducted rocket a) immediately downstream of inlet and b) at 1.0 diameter downstream of inlet.

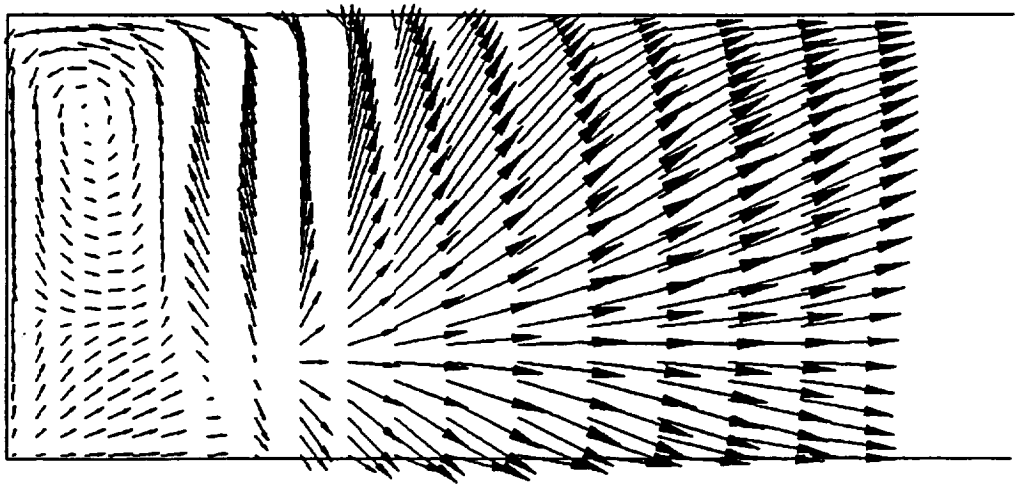

Fig. 10 Computed velocity vectors in the symmetry plane of the ducted rocket.

further entrain external fluid and increase the loss in lift. In a multiple-jet configuration, these wall jets collide with each other and turn upwards to form an upwash fountain. This fountain flow has two main effects on the STOVL aircraft dynamics. First, an increase in lift force is caused when the fountain impinges on the aircraft fuselage. The recovery in lift is a positive effect of the upwash flow. However, this impinging fluid can also flow along the fuselage surface and eventually make its way into the engine inlets. Because the temperature of the fountain flow is much hotter than the ambient air, its ingestion by the engine can reduce the power and cause thermal stresses in the components. In addition to the fountain flow, another mechanism for the hot gas ingestion results from the interaction of the forward moving wall jet with the headwind. When the headwind and the wall jet collide, a stagnation region is formed and the wall jet is turned into a ground vortex. This ground vortex can subsequently be ingested by the engine resulting in a further loss in power.

Several numerical studies of twin- and single-jet impingement have been previously reported[18,19]. Recently VanOverbeke and Holdeman[20] studied the hot gas ingestion process in a simulated geometrical configuration of the STOVL aircraft. The study was restricted to Cartesian geometries but demonstrated the potential of computational fluid dynamics to this practical flow problem. This study was followed by Tafti and Vanka[21] who applied a multigrid solution procedure and demonstrated significant reductions in computer times over a single grid procedure such as that used by VanOverbeke and Holdeman. In this section, we present results of a preliminary calculation of the impingement of twin jets from a simulated fuselage represented by a curvilinear grid.

The simulated aircraft fuselage was a truncated NACA 0012 airfoil at 10 degrees angle-of-attack embedded within the computational domain. Figure 12 shows the grid in the impingement region. The calculation domain extended far upstream but is not shown in this figure. The lift jets were specified as 300 m/s at 1000 K and the headwind was prescribed as 3% of the jet velocity at an ambient temperature of 300 K. The flowfield was considered to be turbulent. A 104 x 32 x 32 grid distribution with two grid levels were used in this calculation requiring approximately 150 iterations to converge to a normalized mass residual of one percent. The above calculation required approximately one hour on the CRAY-2 at NAS of NASA-Ames Facility.

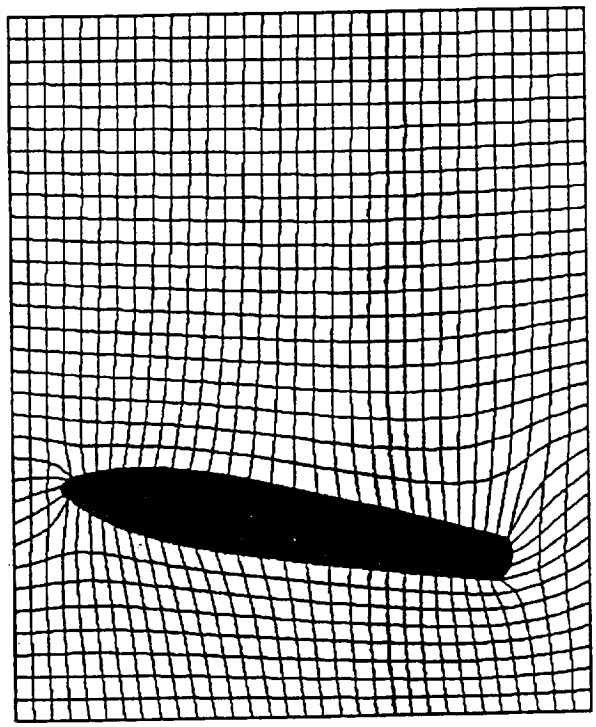

Fig. 12 Grid system for the twin-jet impingement flow.

Figure 13 shows a selected velocity field in a plane through the jet centers. The impingement of the jets on the ground and the formation of the wall jets is evident in this plot. The headwind is seen to create a stagnant zone ahead of the fuselage and the jet flow is turned back by the headwind. The interaction of the hot jets with the cooler ambient is illustrated in Figure 14 in two different planes. In figure 14-a, the temperature distribution in a plane through the jet centers is shown. In the present calculation, engine suction was not considered; therefore, the temperatures at the engine face could not be estimated. This feature will be exercised in future calculations. Figure 14-b shows the temperature footprint of the lift jets on the ground plane. The interaction of the wall jets with the headwind can also be seen in this figure.

Summary

A multigrid based computational algorithm and code have been developed and validated for elliptic complex flows. The algorithm solves the momentum equations for the Cartesian velocities as the dependent variables and stores all the variables at the cell centers. A consistent multigrid formulation in curvilinear geometries has been developed and tested. The rapid convergence of the algorithm has been demonstrated in a variety of complex flows.

Acknowledgements

The work reported here was supported by the Internal Fluid Mechanics Division at NASA Lewis Research Center, Cleveland, Ohio, under a grant (NAG 3-1026) to the University of Illinois. The computer code development and simulations were performed at NSF's National Center for Supercomputing Applications (NCSA) at the University of Illinois, Urbana-Champaign and the NAS facilities at NASA-Ames, California. The support of these organizations and of the NASA technical monitor, Dr. J. D. Holdeman, are gratefully acknowledged.

References

1. Brandt, A., "Multigrid Techniques: 1984 Guide with Applications to Fluid Dynamics," Monograph, GMD-Studien, 85, 1984.

2. Linden, J., Lonsdale, G., Steckel, B., and Stuben, K., "Multigrid for the Steady-State Incompressible Navier-Stokes Equations: A Survey," Arbeitspapiere der GMD 322, Gessellschaft fur Mathematik und Datenverarbeitung mbH, pp. 1-16, July 1988.

3. Solchenbach, K., and Steckel, B., "Numerical Simulation of the Flow in 3D-Cylindrical Combustion Chambers using Multigrid Methods," Arbeitspapiere der GMD 216, Gessellschaft fur Mathematik und Datenverarbeitung mbH, pp. 1-30, July 1986.

4. Barcus, M., Peric, M., and Scheuerer, G., "A Control Volume Based Full Multigrid Procedure for the Prediction of Two-Dimensional, Laminar, Incompressible Flows," In *Notes on Numerical Fluid Mechanics* (Deville, M., ed.), Vol. 20, pp. 9-16, 1988.

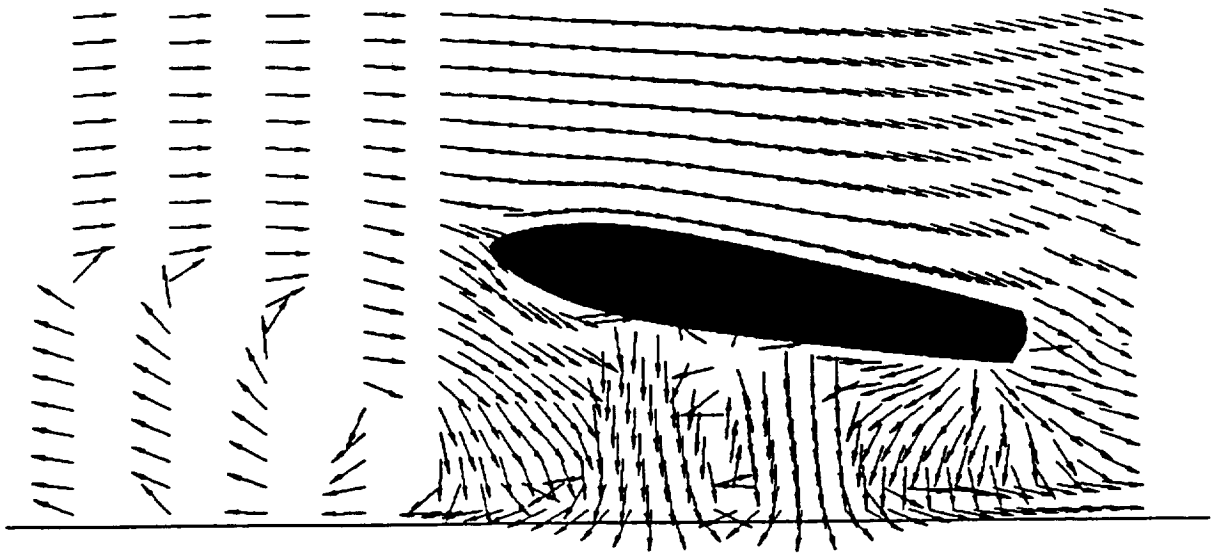

Fig. 13 Velocity vectors in a plane through the jet center for twin-jet impingement flow. Vectors are not to scale.

5. Mavriplis, D. J., Jameson, A., and Martinelli, L., "Multigrid Solution of the Navier-Stokes Equations on Triangular Meshes," AIAA paper 89-0120, 27th Aerospace Sciences Meeting, Reno, Nevada, January 9-12, 1989.

6. Rhie, C. M., and Chow, W. L., "Numerical Study of the Turbulent Flow Past an Airfoil with Trailing Edge Separation," AIAA Journal, Vol. 21, pp. 1525-1532, 1983.

7. Peric, M., Kessler, R., and Scheuerer, G., "Comparison of Finite-Volume Numerical Methods with Staggered and Collocated Grids," Computers and Fluids, Vol. 16, pp. 389-403, 1988.

8. Patankar, S. V., and Spalding, D. B.,"A Calculation Procedure for Heat, Mass and Momentum Transfer in Three-Dimensional Parabolic Flows," International Journal of Heat and Mass Transfer, Vol. 15, pp. 1787-1806, 1972.

9. Smith, K. M. and Vanka, S.P., "Computation of Flow in Strongly Curved Ducts with a Collocated Multigrid Algorithm," Department of Mechanical and Industrial Engineering, Internal Report, CFD-91-05, 1991.

10. Humphrey, J. A. C., Taylor, A. M. K., and Whitelaw, J. H., "Laminar Flow in a Square Duct of Strong Curvature," Journal of Fluid Mechanics, Vol. 83, part 3, pp. 509-527, 1977.

11. Thompson, J. F., "Elliptic Grid Generation," In *Numerical Grid Generation*, (Thompson, J. F., ed.), North-Holland, Amsterdam, pp. 79-105, 1982.

12. Enayet, M. M., Gibson, M. M., Taylor, A. M. K. P., and Yianneskis, M., "Laser Doppler Measurements of Laminar and Turbulent Flow in a Pipe Bend," NASA Contractor Report 3551, 1982.

13. Taylor, A. M. K. P., Whitelaw, J. H., and Yianneskis, M., "Measurements of Laminar and Turbulent Flow in a Curved Duct with Thin Inlet Boundary Layers," NASA Contractor Report 3367, 1981.

14. Launder, B. E., and Spalding, D. B., "The Numerical Calculation of Turbulent Flows," Computational Methods in Applied Mechanics and Engineering, Vol. 3, No. 2, pp. 269-289, 1974.

15. Kreskovsky, J. P., Briley, W. R., and McDonald, H. "Prediction of Laminar and Turbulent Primary and Secondary Flows in Strongly Curved Ducts," NASA Contractor Report 3388, 1981.

16. Stull, F. D., Craig, R. R., Streby, G. D., and Vanka, S. P., "Investigation of a Dual Inlet Side Dump Combustor Using Liquid Fuel Injection," Journal of Propulsion, Vol. 1, No. 1, pp. 83-88, 1985.

17. Kuhn, R. E., "Design Concepts for Minimizing Hot Gas Ingestion in V/STOL Aircraft," Journal of Aircraft, Vol. 19, No. 10, pp. 845-850, 1982.

18. Kotansky, D. R., "Multiple Jet Impingement Flowfields," Proceedings of the International Symposium on Recent Advances in Aeronautics and Acoustics, Stanford Univ., 1983.

19. Agrawal, R. K., "Recent Advances in Prediction Methods for Jet-Induced Effects on V/STOL Aircraft," Proceedings of the International Symposium on Recent Advances in Aeronautics and Acoustics, Stanford Univ., 1983.

20. VanOverbeke, T. J. and Holdeman, J. D., "A Numerical Study of Hot Gas Environment Around a STOVL Aircraft in Ground Proximity," AIAA-88-2882, 24th AIAA/ASME/SAE/ASEE Joint Propulsion Conference, 1988.

21. Tafti, D. K. and Vanka, S. P., "Numerical Study of Hot Gas Environment Around STOVL Aircraft in Ground Proximity," AIAA-90-2270, 26th Joint Propulsion Conference, Orlando, FL, July 16-18, 1990.

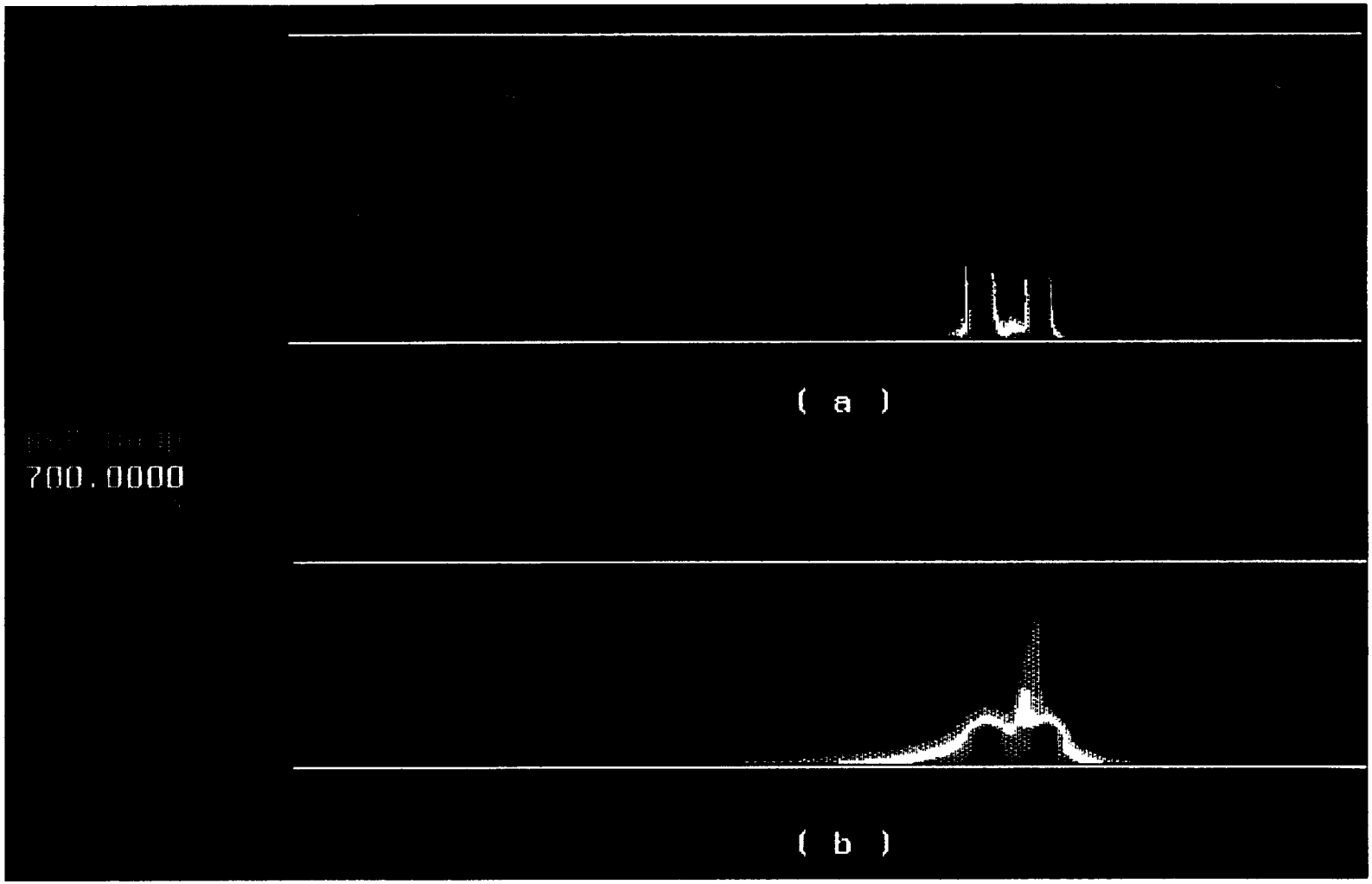

Fig. 14 Contours of temperature in a) the jet central plane and b) ground plane for twin-jet impingement flow.

APPENDIX G

A STAGGERED GRID MULTILEVEL METHOD FOR THE SIMULATION OF FLUID FLOW IN 3-D COMPLEX GEOMETRIES

AIAA Paper 94-0778

A STAGGERED GRID MULTILEVEL METHOD FOR THE SIMULATION OF FLUID FLOW IN 3-D COMPLEX GEOMETRIES

Wm. Kevin Cope*, Gang Wang**, and S. P. Vanka***

Department of Mechanical and Industrial Engineering
University of Illinois at Urbana-Champaign
1206 West Green Street
Urbana, Illinois 61801

Abstract

A multigrid method for internal flows in complex geometries based on multiple velocity grid staggering has been described. The numerical method has been tested for laminar flow in a curved pipe and for laminar and turbulent flow in the dilution zone of a gas turbine combustion chamber. The convergence characteristics for the method have been compared to the convergence obtained for use of traditional grid staggering. It has been observed that the use of the multiple velocity grid staggering arrangement is superior to traditional grid staggering only when a ninety degree bend exists in the problem geometry. For the simulation of flow in the dilution zone of a gas turbine combustion chamber, it was observed that both grid staggering arrangements required approximately the same number of iterations for convergence. In this case, the traditional grid staggering is to be favored due to its lower work count per iteration.

I. Introduction

Multigrid methods have long been advocated for accelerating the convergence of iterative schemes used for the numerical solution of elliptic partial-differential equations (Brandt, 1977; Brandt, 1980). Multigrid methods rely on the simultaneous use of several grid levels on which the governing equations are discretized and iteratively solved. The principal argument for multiple grid levels is that the various frequencies in the error spectrum are efficiently resolved at the corresponding high frequency rate of the iterative scheme. Thus, a strict O(n) rate of work increase can be achieved. The theory of multigrid methods is well established for model linear elliptic partial-differential equations (Brandt, 1980). Also, multigrid methods have been applied to a large number of linear and nonlinear partial-differential equations including the Navier-Stokes equations.

The application of the multigrid technique to accelerate the calculation of practical engineering fluid flows is not well established. Although a number of earlier works (Vanka, 1986a; Rayner, 1991; Rubini et al., 1992; Shyy et al., 1993; etc.) have solved the Navier-Stokes equations for model flow geometries, the application of multigrids to practical flows that necessitate the solution of a much larger set of coupled equations in complex geometries has not been fully investigated. Currently, computational fluid dynamics plays an important role in industry in the evaluation of proposed as well as existing designs of engineering components. Today, commercial software packages are in the position of providing answers to several questions arising out of new designs. Therefore development of efficient computational algorithms utilising the multigrid concept for practical engineering flows is of much significance.

In several of our previous works (Vanka, 1986b; Joshi and Vanka, 1991), we had developed multigrid based algorithms for flows in complex geometries with inclusion of models for turbulence and combustion. While these works were satisfactory in their own respect, the issue of the treatment of complex geometries still remains to be properly resolved. Our interest is primarily with methods involving structured grids such as those generated from the solution of elliptic partial differential equations (Thompson et al., 1985), rather than unstructured grids such as those used in the finite-element methodology. The key issues in our previous works have always been the selection of the proper set of dependent variables for the momentum equations and the layout of the velocities with respect to the locations of the pressures (Joshi and Vanka, 1991; Smith et al., 1993). This issue is of much more significance to incompressible flows as it is possible to generate a checker-board split in the pressure field, if the pressure gradient terms in the momentum equations are not properly discretized. The various schemes have ranged from those using the Cartesian velocities located on the cell faces and pressures at the cell centers (Vanka et al., 1989) to the use of a collocated arrangement of velocities and pressures at the cell centers (Smith et al., 1993). While these practices have had adequate success in solving complex flows, they have also resulted in certain difficulties.

The location of single Cartesian velocity components on appropriate cell faces has been pursued by Vanka et al. (1989) and Shyy and Vu (1991). Its multigrid performance has been discussed in Vanka (1987) in the context of a block-implicit solution algorithm. This algorithm however has been observed to have convergence difficulties when the angle between the grid lines is beyond a certain value (~ 40 degrees). In cases when the flow geometry turns ninety degrees or more, the layout can result in a staggered arrangement that is contrary to the desired objective. The use of collocated Cartesian velocities at the cell centers resolves the difficulty arising from arbitrary grid skewness and can be incorporated into a multigrid procedure with sequential solution of the momentum and continuity equations (Miller and Schmidt, 1988; Hortmann et al., 1990; Smith et al., 1993). However, in selected problems, we have observed that this procedure can result in inconsistencies during the multigrid restriction and prolongation operations. This causes the overall algorithm to converge to a limit residual (~1%). Further, the restriction and prolongation operators must always be consistent with the momentum interpolation that is used to avoid the checker-board decoupling of the pressure. The use of cell face mass fluxes or grid aligned velocities (Karki and Patankar, 1988; Joshi and Vanka, 1991) as dependent variables can be another alternative, but both practices lead to complex forms of curvature terms which again are difficult to treat in a multigrid context.

In the present work, we have considered an extension of a practice originally proposed by Maliska and Raithby (1984). The proposed scheme locates all components of the Cartesian velocity vector on each cell face and solves the respective momentum equations. Thus in a two-dimensional problem, two Cartesian velocities are located on each cell face. Four momentum equations are solved for the components of velocity on the ξ and η cell faces and are directly used in the continuity equation. This arrangement avoids the difficulties associated with grid turning and does not require momentum interpolation as used in the collocated scheme. However, its disadvantage is the additional work and storage for the multiple momentum equations. This work at first appears to be twice (two dimensional problems) or three times (three dimensional problems) the work of a

* Teaching Assistant, Member AIAA
** Research Assistant
*** Professor, Dept. of Mech. and Ind. Eng.
Senior Member, AIAA

traditional single component algorithm. However, if we consider the fact that a common set of finite-difference equations can be assembled for all equations on a given cell face and that the momentum equations require fewer sweeps (in the context of the SIMPLE algorithm (Patankar and Spalding, 1972)) than the pressure and k-ε equations, it can be shown that the overall increase in work is at most a factor of *two* in three dimensional problems and less in two dimensional problems. Similarly, the storage increase is also not large in a relative sense.

In the present paper, we describe our work relating to the development and assessment of a multigrid algorithm for complex internal flows that solves multiple Cartesian velocity components on the cell faces. The algorithm uses a segregated iterative scheme for resolving the pressure-velocity coupling. The multigrid procedure uses a FAS-FMG strategy and a V-cycle for restricting and prolongating between grids. The discretization uses either the traditional hybrid differencing or a third-order flux limited scheme (Leonard and Mokhtari, 1990). The algorithm has been incorporated such that with one index it is possible to retrieve the single component algorithm appropriate for simple geometries. We have applied the procedure to two model flows: a) laminar flow in a curved pipe and b) the flow in a model annular combustor. We have solved the two problems in both single grid and multigrid modes and with single and multiple Cartesian velocity procedures. As expected, the multigrid algorithm converges faster than the single grid algorithm, although the benefits are not as great as would be desired due to the relatively coarse demonstration grids considered. A two equation turbulence model (k-ε) has also been included in the solution procedure but currently the performance of the overall algorithm for turbulent flows is in the preliminary stage.

In what follows, the discretization procedures and the governing equations are described in section 2. The solution procedure is treated in section 3. Sections 4 and 5 present the results for the two problems considered in this study.

II. Governing Equations and Discretization

Governing Equations and Boundary Conditions

The conservation laws can be written in terms of a general equation containing convection, diffusion, and source terms. For a general variable ϕ we solve the following equation:

$$\begin{aligned}
&\frac{\partial}{\partial\xi}(\rho U\phi)+\frac{\partial}{\partial\eta}(\rho V\phi)+\frac{\partial}{\partial\varsigma}(\rho W\phi)=\\
&\frac{\partial}{\partial\xi}\left[\frac{\Gamma^{\phi}}{J}\left(q_{11}\phi_{\xi}+q_{12}\phi_{\eta}+q_{13}\phi_{\varsigma}\right)\right]+\\
&\frac{\partial}{\partial\eta}\left[\frac{\Gamma^{\phi}}{J}\left(q_{21}\phi_{\xi}+q_{22}\phi_{\eta}+q_{23}\phi_{\varsigma}\right)\right]+\\
&\frac{\partial}{\partial\varsigma}\left[\frac{\Gamma^{\phi}}{J}\left(q_{31}\phi_{\xi}+q_{32}\phi_{\eta}+q_{33}\phi_{\varsigma}\right)\right]+S^{\phi}(\xi,\eta,\varsigma)\cdot J
\end{aligned} \tag{1}$$

where the metrics of the coordinate transformation and contravariant velocities are given by the following expressions:

$$J=x_{\xi}y_{\eta}z_{\varsigma}+x_{\varsigma}y_{\xi}z_{\eta}+x_{\eta}y_{\varsigma}z_{\xi}-x_{\xi}y_{\varsigma}z_{\eta}-x_{\varsigma}y_{\eta}z_{\xi}-x_{\eta}y_{\xi}z_{\varsigma}$$

$$U=\left(y_{\eta}z_{\varsigma}-y_{\varsigma}z_{\eta}\right)u+\left(x_{\varsigma}z_{\eta}-x_{\eta}z_{\varsigma}\right)v+\left(x_{\eta}y_{\varsigma}-x_{\varsigma}y_{\eta}\right)w$$

$$V=\left(y_{\varsigma}z_{\xi}-y_{\xi}z_{\varsigma}\right)u+\left(x_{\xi}z_{\varsigma}-x_{\varsigma}z_{\xi}\right)v+\left(x_{\varsigma}y_{\xi}-x_{\xi}y_{\varsigma}\right)w$$

$$W=\left(y_{\xi}z_{\eta}-y_{\eta}z_{\xi}\right)u+\left(x_{\eta}z_{\xi}-x_{\xi}z_{\eta}\right)v+\left(x_{\xi}y_{\eta}-x_{\eta}y_{\xi}\right)w$$

$$q_{11}=\left(y_{\eta}z_{\varsigma}-y_{\varsigma}z_{\eta}\right)^2+\left(x_{\varsigma}z_{\eta}-x_{\eta}z_{\varsigma}\right)^2+\left(x_{\eta}y_{\varsigma}-x_{\varsigma}y_{\eta}\right)^2$$

$$q_{22}=\left(y_{\varsigma}z_{\xi}-y_{\xi}z_{\varsigma}\right)^2+\left(x_{\xi}z_{\varsigma}-x_{\varsigma}z_{\xi}\right)^2+\left(x_{\varsigma}y_{\xi}-x_{\xi}y_{\varsigma}\right)^2$$

$$q_{33}=\left(y_{\xi}z_{\eta}-y_{\eta}z_{\xi}\right)^2+\left(x_{\eta}z_{\xi}-x_{\xi}z_{\eta}\right)^2+\left(x_{\xi}y_{\eta}-x_{\eta}y_{\xi}\right)^2$$

$$\begin{aligned}
q_{12}=q_{21}&=\left(y_{\varsigma}z_{\xi}-y_{\xi}z_{\varsigma}\right)\left(y_{\eta}z_{\varsigma}-y_{\varsigma}z_{\eta}\right)\\
&+\left(x_{\xi}z_{\varsigma}-x_{\varsigma}z_{\xi}\right)\left(x_{\varsigma}z_{\eta}-x_{\eta}z_{\varsigma}\right)\\
&+\left(x_{\varsigma}y_{\xi}-x_{\xi}y_{\varsigma}\right)\left(x_{\eta}y_{\varsigma}-x_{\varsigma}y_{\eta}\right)
\end{aligned}$$

$$\begin{aligned}
q_{13}=q_{31}&=\left(y_{\xi}z_{\eta}-y_{\eta}z_{\xi}\right)\left(y_{\eta}z_{\varsigma}-y_{\varsigma}z_{\eta}\right)\\
&+\left(x_{\varsigma}z_{\eta}-x_{\eta}z_{\varsigma}\right)\left(x_{\eta}z_{\xi}-x_{\xi}z_{\eta}\right)\\
&+\left(x_{\xi}y_{\eta}-x_{\eta}y_{\xi}\right)\left(x_{\eta}y_{\varsigma}-x_{\varsigma}y_{\eta}\right)
\end{aligned}$$

$$\begin{aligned}
q_{23}=q_{32}&=\left(y_{\xi}z_{\eta}-y_{\eta}z_{\xi}\right)\left(y_{\varsigma}z_{\xi}-y_{\xi}z_{\varsigma}\right)\\
&+\left(x_{\eta}z_{\xi}-x_{\xi}z_{\eta}\right)\left(x_{\xi}z_{\varsigma}-x_{\varsigma}z_{\xi}\right)\\
&+\left(x_{\xi}y_{\eta}-x_{\eta}y_{\xi}\right)\left(x_{\varsigma}y_{\xi}-x_{\xi}y_{\varsigma}\right)
\end{aligned} \tag{2}$$

In the present investigation, turbulence closure has been accomplished by using the k-ε model proposed by Launder and Spalding (1974).

The numerical method can accommodate a variety of boundary conditions including Dirichlet, Neumann, and outflow boundary conditions. For the problems addressed in this study, the values of velocity, temperature, density, and turbulence variables are specified at inlet boundaries. A Neumann boundary condition at the outflow plane requires that the normal derivative of all velocity components, temperature, k, and ε be equal to zero. Wall boundaries are treated as no slip, no penetration surfaces. The wall boundaries are treated as either constant temperature or adiabatic surfaces for the solution of the energy equation. For the simulation of turbulent flow, the wall functions proposed by Launder and Spalding (1974) have been used for the three velocity components and temperature. The wall functions have been implemented by writing the effective viscosity in terms of the wall shear stress, where the wall shear stress is obtained from the turbulence equilibrium assumption.

Discretization

A multiple velocity grid staggering scheme has been used in discretizing the governing equations. All three Cartesian velocity components are stored on the cell faces of a given control volume (see Figure 1). The pressure, density, and other scalar variables are located at the cell centers. The grid staggering is an extension of the scheme proposed by Maliska and Raithby (1984). For a given cell, nine Cartesian velocity components are solved. The multiple velocity grid staggering has been utilized because it does not exhibit pressure-velocity decoupling when ninety degree bends occur in the geometry. Furthermore, the velocities which are solved in the momentum equations are the same velocities updated in the pressure correction equation, unlike the situation for collocated grids. Thus, the same velocities will satisfy both the momentum and continuity equations.

The governing equations are discretized by a finite volume method. The integration of the partial differential

equation over a control volume results in the following equation:

$$\begin{aligned}
&\left[(\rho U\phi)_{\xi^+} - (\rho U\phi)_{\xi^-}\right] + \left[(\rho V\phi)_{\eta^+} - (\rho V\phi)_{\eta^-}\right] \\
&+\left[(\rho W\phi)_{\varsigma^+} - (\rho W\phi)_{\varsigma^-}\right] = \\
&\left[\left(\Gamma J^{-1} q_{11}\phi_\xi\right)_{\xi^+} - \left(\Gamma J^{-1} q_{11}\phi_\xi\right)_{\xi^-}\right] + \\
&\left[\left(\Gamma J^{-1} q_{22}\phi_\eta\right)_{\eta^+} - \left(\Gamma J^{-1} q_{22}\phi_\eta\right)_{\eta^-}\right] + \\
&\left[\left(\Gamma J^{-1} q_{33}\phi_\varsigma\right)_{\varsigma^+} - \left(\Gamma J^{-1} q_{33}\phi_\varsigma\right)_{\varsigma^-}\right] \\
&+S^\phi(\xi,\eta,\varsigma)\cdot J + S^\phi_{MD}
\end{aligned} \tag{3}$$

where S^ϕ_{MD} refers to the mixed derivative terms in curvilinear coordinates. This equation is discretized by specifying the relationship between convective and diffusive cell face fluxes and the surrounding volume averaged quantities. The above equation is first linearized by treating the cell face mass fluxes and exchange coefficients explicitly. These cell face quantities are approximated by using linear interpolation. The cell face values of the dependent variables and diffusive fluxes are then discretized and treated implicitly. The diffusive flux at a control volume face is discretized by a second order central difference approximation:

$$\left.\frac{\partial\phi}{\partial\xi}\right|_{\xi^+} = \frac{\phi_E - \phi_P}{\Delta\xi} \tag{4}$$

The dependent variable at a cell face is described by the hybrid differencing procedure (Spalding, 1972). As the discretized equations using this differencing are well known and thoroughly documented they will not be repeated. The results of calculations using a higher order discretization are also given and the discretized equations using the higher order flux function will be presented.

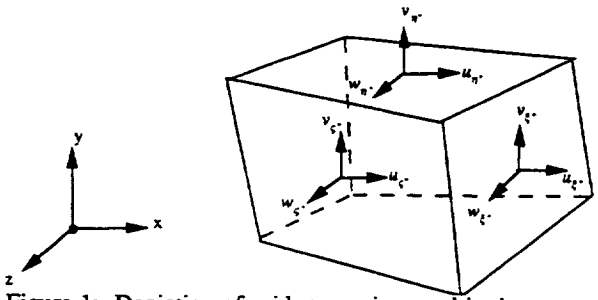

Figure 1: Depiction of grid staggering used in the present numerical method. All scalar variables are located at the center of the cell.

In the higher order differencing scheme, the cell face value of a given dependent variable is related to the surrounding volume averaged quantities by a flux limited form of quadratic interpolation for convective kinematics, QUICK (Leonard, 1979). In order to rigorously treat a cell face quantity using this method, a multi-dimensional interpolation operator should be used (Leonard, 1988). In the present study, the one dimensional form of quadratic interpolation has been implemented. For the cell face value of a variable ϕ, the following expression is used:

$$\phi_f = \frac{3}{8}\phi_D + \frac{3}{4}\phi_C - \frac{1}{8}\phi_U \tag{5}$$

Where ϕ_D, ϕ_U, and ϕ_C are the downstream, upstream, and central values of the dependent variable. The cell face flux is limited through use of normalized variables, where a normalized variable is defined by the following:

$$\tilde{\phi} \equiv \frac{\phi - \phi_U}{\phi_D - \phi_U} \tag{6}$$

At a given cell face, the downstream, upstream, and central values of the dependent variable are identified. The normalized variable associated with the center quantity, $\tilde{\phi}_C$, is used to assess the local behaviour of the solution of ϕ. Depending on the local variation, the value of the cell face normalized variable, $\tilde{\phi}_f$, is determined. In this study, the universal limiter of Leonard and Mokhtari (Leonard and Mokhtari, 1990) has been utilized. The value taken by $\tilde{\phi}_f$ is determined from $\tilde{\phi}_C$ in the following manner:

$$\tilde{\phi}_f = 1 + \frac{1}{2}\left(\tilde{\phi}_C - 1\right) \text{ if } \tilde{\phi}_C > 1 \tag{7}$$

$$\tilde{\phi}_f = \frac{3}{2}\cdot\tilde{\phi}_C \text{ if } \tilde{\phi}_C \le 0 \tag{8}$$

$$\tilde{\phi}_f = 100\cdot\tilde{\phi}_C \text{ if } 0 < \tilde{\phi}_C \le \frac{3}{794} \tag{9}$$

$$\tilde{\phi}_f = \frac{3}{8} + \frac{3}{4}\cdot\tilde{\phi}_C \text{ if } \frac{3}{794} < \tilde{\phi}_C \le \frac{5}{6} \tag{10}$$

$$\tilde{\phi}_f = 1 \text{ if } \frac{5}{6} < \tilde{\phi}_C \le 1 \tag{11}$$

The functional dependance of $\tilde{\phi}_f$ on $\tilde{\phi}_C$ is depicted in Figure 2. In order to implement the flux limited interpolation implicitly, the downwind weighting factor is defined:

$$DWF \equiv \frac{\phi_f - \phi_C}{\phi_D - \phi_C} = \frac{\tilde{\phi}_f - \tilde{\phi}_C}{1 - \tilde{\phi}_C} \tag{12}$$

Having determined $\tilde{\phi}_f$ at a given cell face from equations 7-11, the downwind weighting factor can be calculated and the cell face value of the dependent variable written as follows:

$$\phi_f = DWF\cdot\phi_D + (1 - DWF)\cdot\phi_C \tag{13}$$

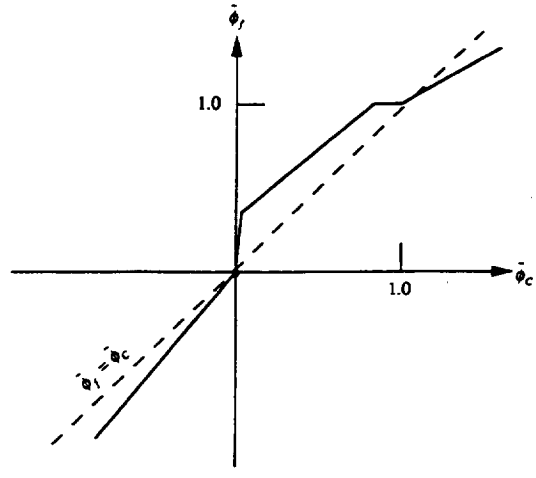

Figure 2: The Universal limiter constraints imposed on a cell face variable as shown on the Normalized Variable Diagram (NVD).

A deferred correction procedure has been used to implement the flux limited QUICK formulation. The convective cell face flux is written in terms of the first order upwind value plus the difference between the higher order

and first order approximations. For a ξ-plus cell face flux, the following expression is obtained:

$$(\rho U\phi)_{\xi^+} = \left\{\phi_P \cdot \max\left[(\rho U)_{\xi^+},0\right] - \phi_E \cdot \max\left[-(\rho U)_{\xi^+},0\right]\right\}$$
$$+\left\{\begin{array}{l}\left[DWF_{\xi^+}\cdot\phi_E + \left(1-DWF_{\xi^+}\right)\phi_P\right]\cdot\max\left[(\rho U)_{\xi^+},0\right] - \\ \left[DWF_{\xi^+}\cdot\phi_P + \left(1-DWF_{\xi^+}\right)\phi_E\right]\cdot\max\left[-(\rho U)_{\xi^+},0\right]\end{array}\right\}$$
$$-\left\{\phi_P \cdot \max\left[(\rho U)_{\xi^+},0\right] - \phi_E \cdot \max\left[-(\rho U)_{\xi^+},0\right]\right\} \quad (14)$$

The first order upwind term is treated implicitly and the difference term is treated explicitly as a source. Such a procedure maintains diagonal dominance in the system of linear algebraic equations and ensures that the coefficients are always positive (Hayase et al., 1992). The final form of the discretized equation for the variable ϕ is thus given by the following:

$$a_P\phi_P = a_E\phi_E + a_W\phi_W + a_N\phi_N + a_S\phi_S + a_H\phi_H + a_L\phi_L$$
$$+S^*(\xi,\eta,\varsigma)\cdot J + S^*_{MD} + S^*_{DC} + \frac{(1-\alpha)\sum a_{nb}}{\alpha}\phi_P^{old}$$

$$a_E = \left\{\max\left[-(\rho U)_{\xi^+},0\right] + \left(\Gamma J^{-1}q_{11}\right)_{\xi^+}\right\}$$
$$a_W = \left\{\max\left[(\rho U)_{\xi^-},0\right] + \left(\Gamma J^{-1}q_{11}\right)_{\xi^-}\right\}$$
$$a_N = \left\{\max\left[-(\rho V)_{\eta^+},0\right] + \left(\Gamma J^{-1}q_{22}\right)_{\eta^+}\right\}$$
$$a_S = \left\{\max\left[(\rho V)_{\eta^-},0\right] + \left(\Gamma J^{-1}q_{22}\right)_{\eta^-}\right\}$$
$$a_H = \left\{\max\left[-(\rho W)_{\varsigma^+},0\right] + \left(\Gamma J^{-1}q_{33}\right)_{\varsigma^+}\right\} \quad (15)$$
$$a_L = \left\{\max\left[(\rho W)_{\varsigma^-},0\right] + \left(\Gamma J^{-1}q_{33}\right)_{\varsigma^-}\right\}$$
$$a_P = \left(a_E + a_W + a_N + a_S + a_H + a_L\right)/\alpha$$

III. Solution Procedure

The coupled set of nonlinear algebraic equations which results from discretization is solved using a multigrid solution procedure. The relaxation on any given grid is accomplished by using a segregated solution technique (Patankar and Spalding, 1972). A FMG-FAS multigrid procedure is used to accelerate the rate of convergence of the basic relaxation operator.

Relaxation Operator

In the segregated relaxation method, each equation is solved in a sequential fashion. On a given grid, the following procedure is used:

1) Solve for all Cartesian velocities at ξ faces.
2) Solve for all Cartesian velocities at η faces.
3) Solve for all Cartesian velocities at ς faces.
4) Solve for the pressure correction, P'.
5) Update Cartesian velocities and P based on the solution for P'.
6) If on the locally finest grid, solve for scalar variables (T, k, ε)

The iterative process for any particular flow variable is not carried to convergence since subsequent iterations on the other flow variables will change the coefficients of the discrete equation. In general, three to five iterations of an alternating line Gauss-Seidel procedure were performed for each velocity and scalar variable while ten iterations were performed on the pressure correction equation. The six steps given above constitute one "outer" iteration, i.e. iterative update of all flow variables. A numerical method employing only a single grid would simply continue these outer iterations until the residuals in the governing equations were reduced below a prescribed level. In the present multigrid method, the outer iterations are performed on a given grid prior to restriction or prolongation to another grid. It is important to note that during the execution of a V-cycle, the scalar equations are only solved on the *locally finest grid*. The values of T, k, and ε on the finest grid are held fixed on the coarse grids during the V-cycle. The details pertaining to the pressure correction equation are described below.

Pressure Correction Equation

The pressure correction equation used in the present study is obtained by writing expressions for the mass fluxes associated with a given cell in terms of an initial estimate plus a correction. The integral form of the conservation of mass for a control volume is given by the following:

$$\left[(\rho U)_{\xi^+} - (\rho U)_{\xi^-}\right] +$$
$$\left[(\rho V)_{\eta^+} - (\rho V)_{\eta^-}\right] + \quad (16)$$
$$\left[(\rho W)_{\varsigma^+} - (\rho W)_{\varsigma^-}\right] = 0$$

The relation between flux corrections and pressure corrections is obtained from the momentum equations. Consider the mass flux at the ξ-plus cell face. The correction to the mass flux is written in terms of velocity corrections

$$\rho U_{\xi^+} = \rho\left(y_\eta z_\varsigma - y_\varsigma z_\eta\right)_{\xi^+}\cdot\left(u^*_{\xi^+} + u'_{\xi^+}\right)$$
$$+\rho\left(x_\varsigma z_\eta - x_\eta z_\varsigma\right)_{\xi^+}\cdot\left(v^*_{\xi^+} + v'_{\xi^+}\right) \quad (17)$$
$$+\rho\left(x_\eta y_\varsigma - x_\varsigma y_\eta\right)_{\xi^+}\cdot\left(w^*_{\xi^+} + w'_{\xi^+}\right)$$

Since all three Cartesian velocities are stored at any cell face, the relations for u', v', and w' at the ξ-plus cell face are obtained from the momentum equations for the velocites u, v, and w at that cell face. The following expression for U_{ξ^+} is thus obtained:

$$U_{\xi^+} = \left(y_\eta z_\varsigma - y_\varsigma z_\eta\right)_{\xi^+}u^*_{\xi^+}$$
$$+\left(x_\varsigma z_\eta - x_\eta z_\varsigma\right)_{\xi^+}v^*_{\xi^+} \quad (18)$$
$$+\left(x_\eta y_\varsigma - x_\varsigma y_\eta\right)_{\xi^+}w^*_{\xi^+}$$
$$+\left[\frac{\left(y_\eta z_\varsigma - y_\varsigma z_\eta\right)^2 + \left(x_\varsigma z_\eta - x_\eta z_\varsigma\right)^2 + \left(x_\eta y_\varsigma - x_\varsigma y_\eta\right)^2}{a_P^\xi}\right]_{\xi^+}\cdot\left(P'_P - P'_E\right)$$

It should be noted that for simplicity, the cross derivative terms in pressure $(\partial P'/\partial\eta,\ \partial P'/\partial\varsigma)$ are neglected. However, when the included angle between any two grid lines is less than thirty degrees, the use of the cross derivative terms may be needed to accelerate the convergence (Peric, 1990). The expressions for V' and W' are obtained using a similar logic. The final pressure correction equation resulting from the perturbed continuity equation can be

written as follows:

$$a_p P'_p = a_E P'_E + a_W P'_W + a_N P'_N + a_S P'_S + a_H P'_H + a_L P'_L - \dot{m}_{error}$$

where,

$$a_E = \rho\left(\frac{\left(y_\eta z_\varsigma - y_\varsigma z_\eta\right)^2 + \left(x_\varsigma z_\eta - x_\eta z_\varsigma\right)^2 + \left(x_\eta y_\varsigma - x_\varsigma y_\eta\right)^2}{a_p^\xi}\right)_{\xi^+}$$

$$a_W = \rho\left(\frac{\left(y_\eta z_\varsigma - y_\varsigma z_\eta\right)^2 + \left(x_\varsigma z_\eta - x_\eta z_\varsigma\right)^2 + \left(x_\eta y_\varsigma - x_\varsigma y_\eta\right)^2}{a_p^\xi}\right)_{\xi^-}$$

$$a_N = \rho\left(\frac{\left(y_\varsigma z_\xi - y_\xi z_\varsigma\right)^2 + \left(x_\xi z_\varsigma - x_\varsigma z_\xi\right)^2 + \left(x_\varsigma y_\xi - x_\xi y_\varsigma\right)^2}{a_p^\eta}\right)_{\eta^+}$$

$$a_S = \rho\left(\frac{\left(y_\varsigma z_\xi - y_\xi z_\varsigma\right)^2 + \left(x_\xi z_\varsigma - x_\varsigma z_\xi\right)^2 + \left(x_\varsigma y_\xi - x_\xi y_\varsigma\right)^2}{a_p^\eta}\right)_{\eta^-}$$

$$a_H = \rho\left(\frac{\left(y_\xi z_\eta - y_\eta z_\xi\right)^2 + \left(x_\eta z_\xi - x_\xi z_\eta\right)^2 + \left(x_\xi y_\eta - x_\eta y_\xi\right)^2}{a_p^\varsigma}\right)_{\varsigma^+}$$

$$a_L = \rho\left(\frac{\left(y_\xi z_\eta - y_\eta z_\xi\right)^2 + \left(x_\eta z_\xi - x_\xi z_\eta\right)^2 + \left(x_\xi y_\eta - x_\eta y_\xi\right)^2}{a_p^\varsigma}\right)_{\varsigma^-}$$

$$\begin{aligned} a_p &= a_E + a_W + a_N + a_S + a_H + a_L \\ \dot{m}_{error} &= \left[(\rho U)_{\xi^+} - (\rho U)_{\xi^-}\right] \\ &\quad + \left[(\rho V)_{\eta^+} - (\rho V)_{\eta^-}\right] \\ &\quad + \left[(\rho W)_{\varsigma^+} - (\rho W)_{\varsigma^-}\right] \end{aligned} \tag{19}$$

After the pressure correction equation is solved, the cell face Cartesian velocities are corrected along with the cell centered pressure. The mass fluxes at the cell faces are then calculated from the corrected Cartesian velocities.

Multigrid Acceleration

The segregated procedure described has been incorporated within a multigrid acceleration technique. A full multigrid-full approximation scheme (FMG-FAS) using a (1,1) V-cycle has been used. Various multigrid schemes and cycles have been proposed and tested in the literature (Brandt, 1977; Ghia et al., 1982; Hortmann et al., 1990, etc.). The correction scheme (CS) is the most simple for linear problems from the conceptual and algorithmic standpoint but is less efficient when used for nonlinear problems. The FAS scheme has therefore been utilized. The full multigrid procedure involves obtaining an approximate solution to the problem on coarse grids and subsequently prolongating the approximation to finer grids so as to provide a good initial estimate.

The equation set on the finest grid (k) can be written as

$$L^k \phi^k = F^k \tag{20}$$

Here, L is the nonlinear operator consisting of convection and diffusion terms, ϕ is the solution vector, and F represents the source terms. In the FAS procedure, the values calculated on a coarser grid (k-1) are not simple corrections to the values on grid (k), instead they are approximations on grid (k-1) to the correct values on grid (k). Therefore, the equations solved on grid (k-1) are

$$\begin{aligned} L^{k-1}\phi^{k-1} &= F^{k-1} + I_k^{k-1}\left(F^k - L^k\phi^k\right) \\ &\quad + \left(L^{k-1} I_k^{k-1}\phi^k - F^{k-1}\right) \end{aligned} \tag{21}$$

where I_k^{k-1} is the restriction operator. Alternatively, I_{k-1}^k is the prolongation operator. ϕ^k is then updated as

$$\phi^k_{new} = \phi^k_{old} + I_{k-1}^k\left(\phi^{k-1} - I_k^{k-1}\phi^k_{old}\right) \tag{22}$$

Note that only the change from the previous value $\left(\phi^{k-1} - I_k^{k-1}\phi^k_{old}\right)$ is prolongated to grid k and not the value ϕ^{k-1} itself. The advantage of using FAS over the Correction Scheme is that the solution vector from the fine grid, and not just the residuals are transferred to the coarser grids. If multiple iterations are performed on a coarse grid, the nonlinear operator and the source terms are continuously updated.

The grid iterations can be arranged in a variety of ways which affect the overall rate of convergence. The fixed cycle is preferred here over an adaptive cycling strategy since it is not always possible to assign an optimal smoothing rate as is required in an adaptive strategy. The present study employs a fixed (1,1) V-cycle with one iteration performed on u, v, w, and P per grid during the downward leg and one iteration during the upward leg.

Consistent transfer of residuals and solutions is a major aspect of any multigrid-based algorithm. In the present algorithm, cell-center quantities have been restricted using full weighting of neighbor values. Restriction of the momentum residuals has been performed via summation. Corrections have been prolongated by use of trilinear interpolation. These restriction and prolongation operators are much more straightforward than those used in a collocated procedure because of the absence of the momentum interpolation. The operators are essentially the same as those for a single component staggered mesh procedure (Vanka, 1986a).

IV. Results

In the present study, three problems have been considered in assessing the performance of the numerical method: laminar flow in a curved pipe, laminar flow in a combustion chamber, and turbulent flow in a combustion chamber. The simulations have been performed with multiple velocity grid staggering and with traditional grid staggering for purposes of comparison. The results obtained using the flux limited quadratic interpolation are also discussed.

Laminar flow in a curved pipe

The laminar flow in a curved pipe has been considered because of the pressure-velocity decoupling which occurs in the downstream section of the pipe when conventional grid staggering is used. The flow at a Reynolds number of 500 and radius ratio of 0.217 has been simulated. The inlet plane was specified as fully developed pipe flow. The geometry used in the simulations is given in Figure 3. A downstream pipe section of two diameters was used so as to ensure that no flow separation would be present at the fluid outlet.

The simulations performed using the multiple velocity grid staggering were observed to yield a grid independent rate of convergence (Figure 4). The solution was obtained to a normalized mass residual $\left(\dot{m}_{error}/\dot{m}_{in}\right)$ of 0.01% in

approximately 50 fine grid iterations. It is apparent from the convergence depicted in Figure 5 that the single grid method requires many more iterations for convergence than does the multigrid method.

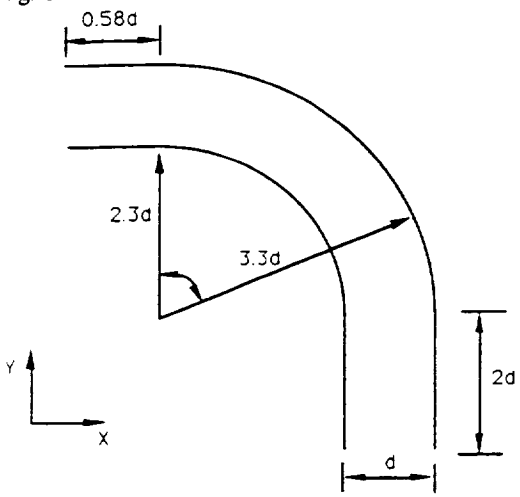

Figure 3: Schematic of curved pipe geometry.

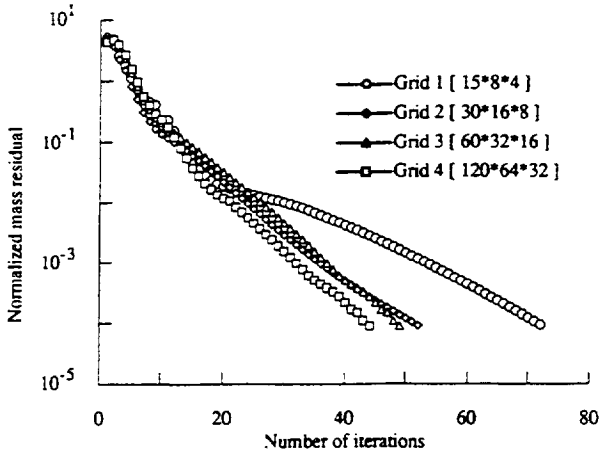

Figure 4: Multigrid convergence for calculations of laminar flow in a curved pipe.

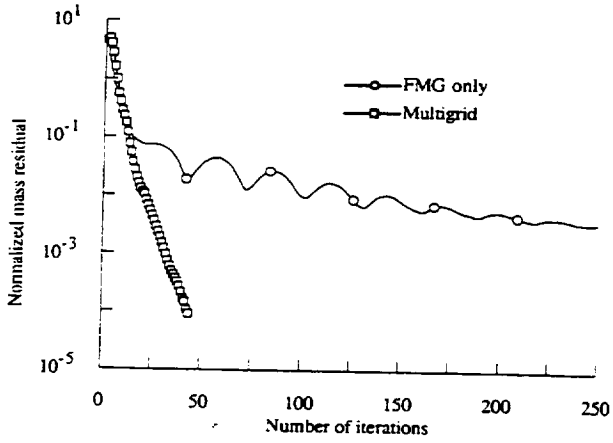

Figure 5: Comparison of multigrid and single grid rates of convergence for curved pipe calculations.

The single grid convergence histories for the calculations using traditional grid staggering are given in Figure 6 for different grids. It can be observed that the rate of convergence is inferior to that associated with use of multiple velocity grid staggering. Table 1 gives the CPU times and number of iterations required in obtaining converged solutions. All CPU times are for the Cray YMP at the NASA Lewis Research Center. It is apparent that although the multiple velocity staggering involves the solution of more quantities, its CPU time is *less* than that associated with traditional grid staggering. This is because the multiple velocity grid staggering is not plagued by pressure-velocity decoupling in the downstream section of the pipe.

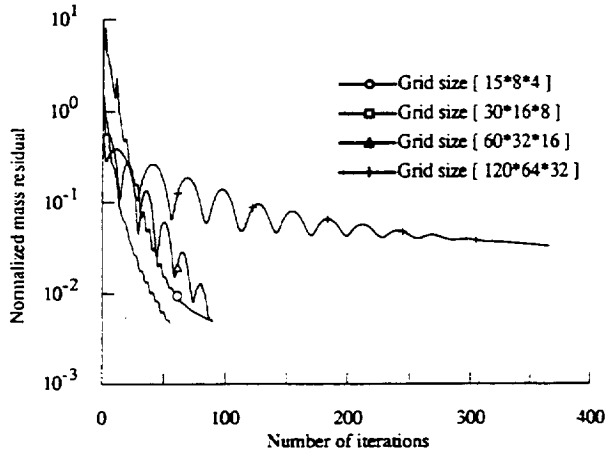

Figure 6: Single grid convergence histories when traditional grid staggering is used in the calculation of flow in a curved pipe.

The solution of the curved pipe flow has been compared with the experimental results of Enayet et al. (1982). In the tests reported in this section, hybrid differencing has been used. It can be seen from Figures 7 and 8 that a small difference does exist between experiment and predictions. The solutions do however indicate that the numerical method correctly predicts the flow in this benchmark problem. Improved solutions may be obtained by further grid resolution or the incorporation of higher order differencing.

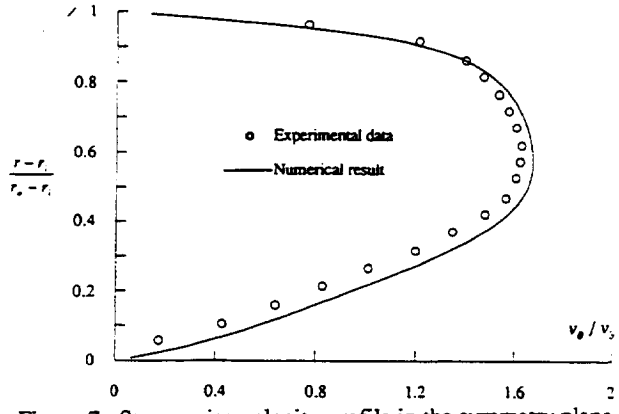

Figure 7: Streamwise velocity profile in the symmetry plane at Θ=30 degrees.

	Multiple Velocity Grid Staggering		Traditional Grid Staggering	
	Iterations	CPU time (s)	Iterations	CPU time (s)
Multigrid	47	507.4	-----	-----
Single Grid	507	2277.4	1073	3040.2

Table 1: Convergence times and total number of iterations required for laminar flow in a curved pipe at Re=500.

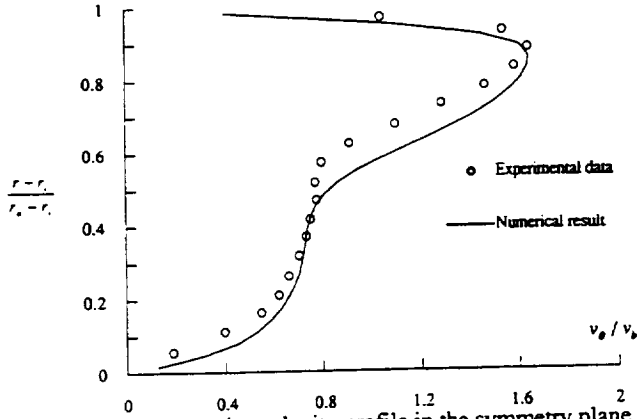

Figure 8: Streamwise velocity profile in the symmetry plane at Θ=60 degrees.

Laminar flow in the dilution zone of a gas turbine combustion chamber

Laminar flow in the dilution zone of a gas turbine combustion chamber was calculated as a test of the numerical method. For laminar flow, two cases have been considered: isothermal flow and laminar mixing of hot and cold flowing streams. The geometry considered is the same as that used by McGuirk and Palma (1992) and is depicted in Figure 9. For the isothermal flow, the inlet Reynolds number was equal to 27 with the top jet issuing into the chamber at a Reynolds number of 39 and the bottom jet issuing at a Reynolds number of 23. The laminar mixing problem considered an inlet Reynolds number of 27, a top jet at Reynolds number of 117, and a bottom jet at Reynolds number of 69. The inlet temperature for the mixing problem was 900 K while both jets were maintained at a uniform temperature of 300 K. The isothermal flow will be considered first.

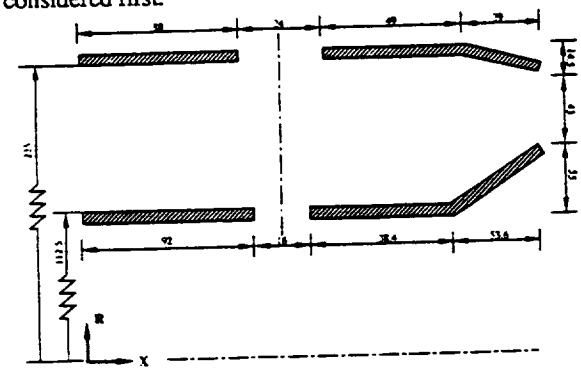

Figure 9: Schematic of the dilution zone of a gas turbine combustion chamber.

From Figure 10 it is apparent that the numerical method exhibits a grid independent rate of convergence. A solution to 0.1% normalized mass residual is obtained in approximately 50 fine grid iterations. Comparison of the multiple velocity scheme with the traditional grid staggering scheme reveals that both methods converge at the same rate for both the single grid (Figures 11 and 12) and the multigrid formulations (Figures 10 and 13). However, the CPU times required for the two methods are different. From Tables 2 and 3 it is seen that the time required by traditional grid staggering is approximately 2/3 of the multiple velocity scheme. Thus, in order for the multiple velocity grid staggering to be beneficial to this problem, it must converge in fewer than 2/3 the number of iterations required by the traditional grid staggering scheme. This is not seen to be the case. Tables 2 and 3 indicate that when using the multiple velocity grid staggering or the traditional grid staggering, the multigrid convergence is faster than the corresponding single grid convergence by a factor of 2.5.

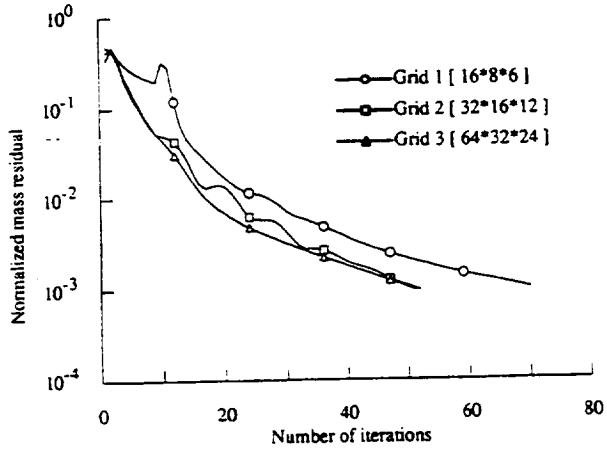

Figure 10: Multigrid convergence for laminar, isothermal flow in a combustor when multiple velocity grid staggering is used.

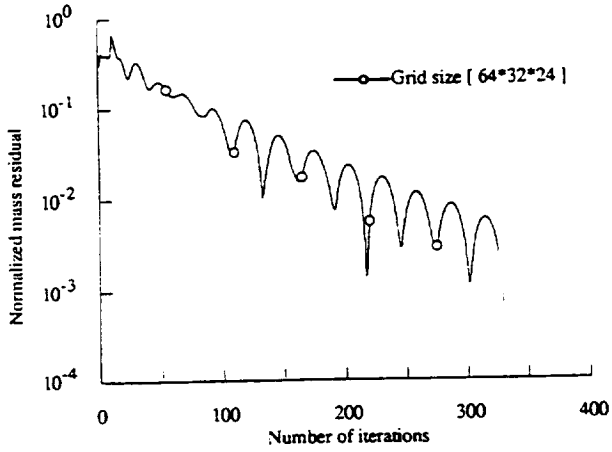

Figure 11: Single grid convergence for laminar, isothermal flow in a combustor when multiple velocity grid staggering is used.

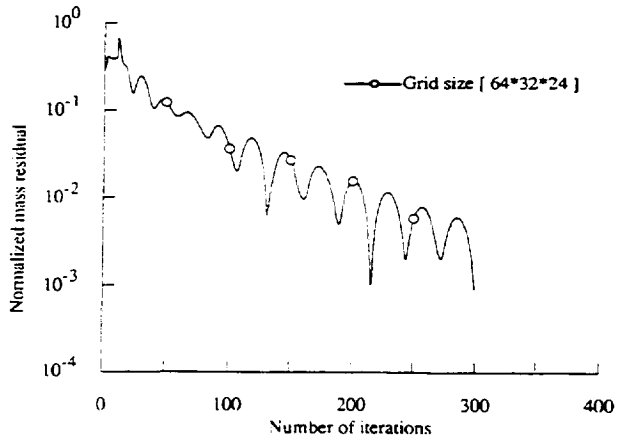

Figure 12: Single grid convergence for laminar, isothermal flow in a combustor when traditional grid staggering is used.

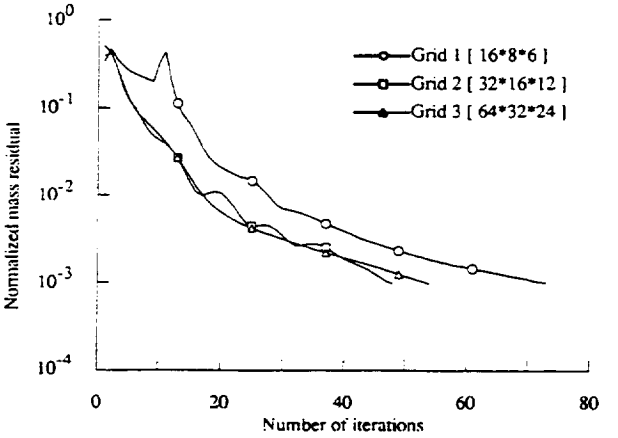

Figure 13: Multigrid convergence for laminar, isothermal flow in a combustor when traditional grid staggering is used.

The mixing problem also reveals that both grid staggering schemes have the same rate of convergence (Figure 14 and 15). Therefore, the traditional grid staggering requires less work as seen in Table 2. The CPU time required by the multiple velocity grid staggering scheme is larger by a factor of 1.6. In the multigrid mode, a strict grid independent rate of convergence was not obtained as evidenced by Figures 16 and 17. The observed behavior is due to the fact that the energy equation has not been incorporated into the V-cycle and thus its convergence is not accelerated. In order to obtain a strictly grid independent rate of convergence all equations should be contained in the V cycle.

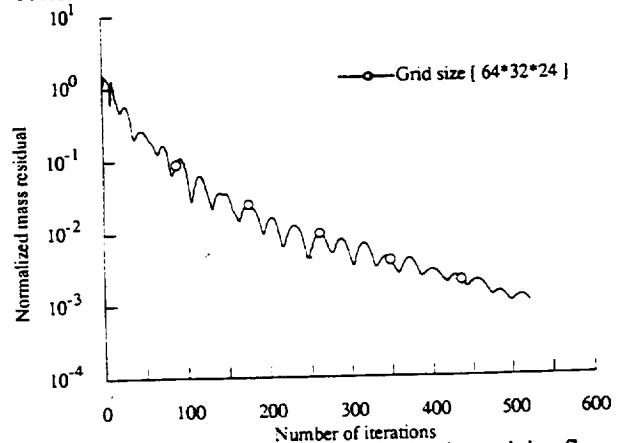

Figure 14: Single grid convergence for laminar mixing flow in a combustor when multiple velocity grid staggering is used.

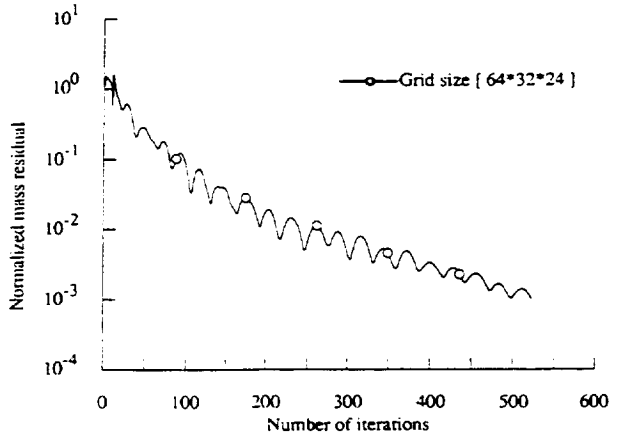

Figure 15: Single grid convergence for laminar mixing flow in a combustor when traditional grid staggering is used.

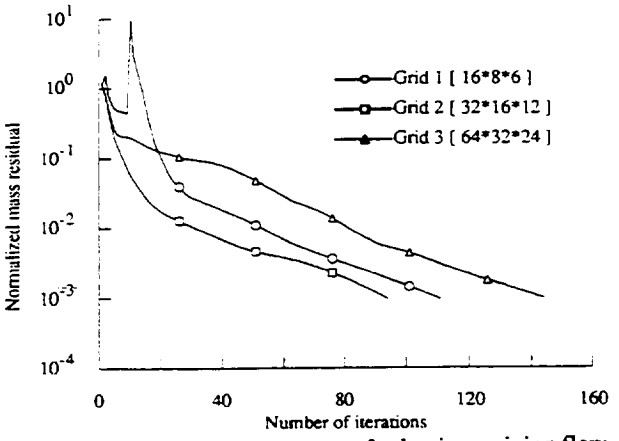

Figure 16: Multigrid convergence for laminar mixing flow in a combustor when multiple velocity grid staggering is used.

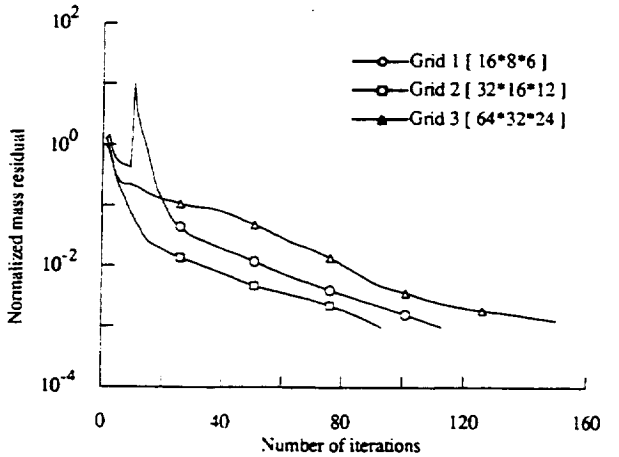

Figure 17: Multigrid convergence for laminar mixing flow in a combustor when traditional grid staggering is used.

	Multiple Velocity Grid Staggering		Traditional Grid Staggering	
	Iterations	CPU time (s)	Iterations	CPU time (s)
Isothermal	51	129.4	54	82.5
Cold mixing	144	403.5	150	249.5

Table 2: Multigrid convergence characteristics for laminar flow in the dilution zone of a gas turbine combustion chamber.

	Multiple Velocity Grid Staggering		Traditional Grid Staggering	
	Iterations	CPU time (s)	Iterations	CPU time (s)
Isothermal	329	343.8	299	177.9
Cold mixing	522	670.1	523	405.2

Table 3: Single grid convergence characteristics for laminar flow in the dilution zone of a gas turbine combustion chamber.

The solutions obtained are shown in Figures 18-22. It is apparent that the opposed jets merge for the case of a cold jet mixed with a hot fluid. The isothermal flow does not exhibit this jet merging. This is to be expected since the cold jets which issue into the chamber in the mixing flow case have a much larger momentum. The maximum momentum ratio for the isothermal case is 6.9, whereas the maximum momentum ratio in the mixing flow problem is 20.8. Also, in the mixing flow case a forward recirculation zone forms in the region where the opposed jets merge. This is not observed in the case of isothermal flow where the jets do not merge. Selected temperature distributions at various planes in the combustor are shown in Figure 20. The temperature distribution in the symmetry plane (Figure 20a) indicates that the high temperature flow from the inlet experiences more cooling along the bottom boundary than along the top. Figure 20b reveals that the fluid in the injection plane is advected toward the upper wall. These observations are further verified by Figure 20c which shows the temperature distribution in the exit plane of the combustor. The fluid at the top wall of the outflow nozzle is at a higher temperature than at the bottom wall.

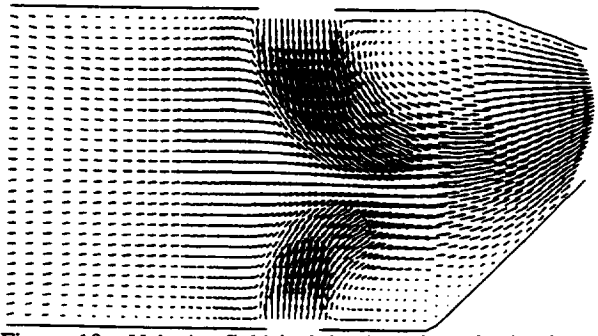

Figure 18: Velocity field in injection plane for laminar, isothermal flow in a combustor.

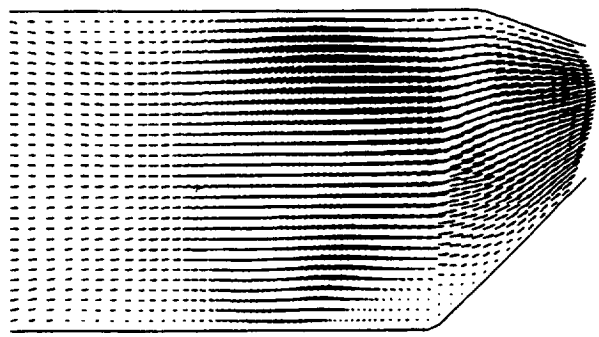

Figure 19: Velocity field in the symmetry plane for laminar, isothermal flow in a combustor.

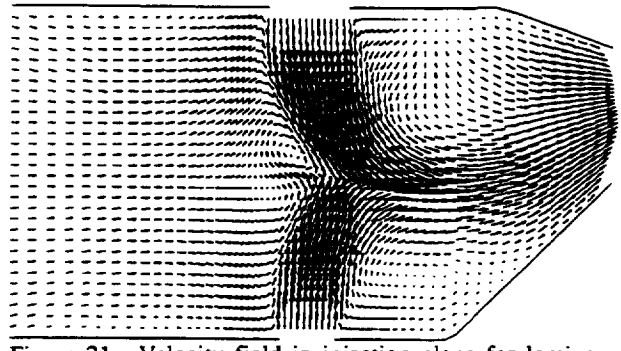

Figure 21: Velocity field in injection plane for laminar mixing flow in a combustor.

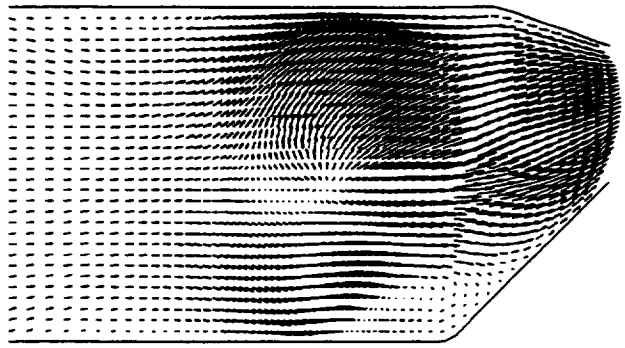

Figure 22: Velocity field in the symmetry plane for laminar mixing flow in a combustor.

Turbulent flow in the dilution zone of a gas turbine combustion chamber

The third case considered is the isothermal turbulent flow in the dilution zone of a gas turbine combustion chamber for an inlet Reynolds number of 12,000. The maximum jet-to-inlet momentum ratio is 6.9. The multigrid solution of this problem indicates that some deterioration in the rate of convergence occurs with grid refinement. As in the case of the laminar mixing, the k and ε equations have not been incorporated into the multigrid V-cycle. Several researchers have dealt with the issue of incorporating the k-ε turbulence model into a multigrid solution procedure (Vanka, 1987; Rubini et al., 1992; Shyy et al., 1993), but the rates of convergence for turbulent flow have still not been shown to be equivalent to that which is observed for laminar flows. The solution to 0.2% normalized mass residual was accomplished in approximately 150 fine grid iterations using both the multiple velocity grid staggering scheme as well as traditional grid staggering (Figures 23 and 24). The single grid convergence was obtained in approximately 555

	Multiple Velocity Grid Staggering		Traditional Grid Staggering	
	Iterations	CPU time (s)	Iterations	CPU time (s)
Multigrid	150	504.9	150	383.2
Single Grid	559	1214.3	555	930.3

Table 4: Convergence times and total number of iterations required for calculation of isothermal turbulent flow in the dilution zone of a gas turbine combustor.

iterations using both grid staggering schemes. Here also the traditional grid staggering requires a smaller CPU time (see Table 4).

The solution of the isothermal turbulent flow reveals that the opposed jets do impinge for this case. A small recirculation zone forms in front of the impingement region just as in the laminar mixing case (Figure 25). The recirculation region aft of the bottom jet which was present for laminar flow (Figure 18) is no longer present for turbulent flow. The flow in the symmetry plane between combustion chambers (Figure 26) indicates that the fluid from either side of the chamber impinges at this plane and advects outward toward the walls.

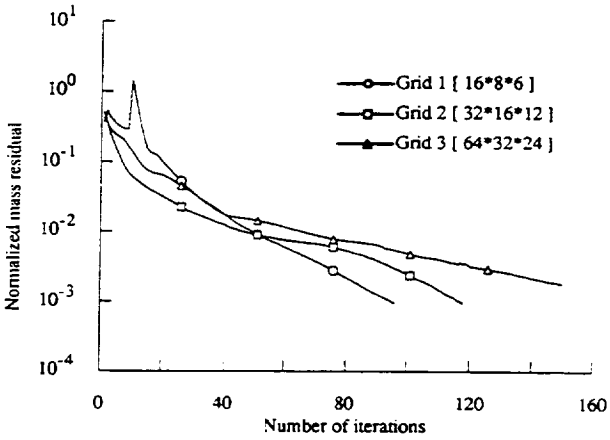

Figure 23: Multigrid convergence for calculation of turbulent flow in a combustor when multiple velocity grid staggering is used.

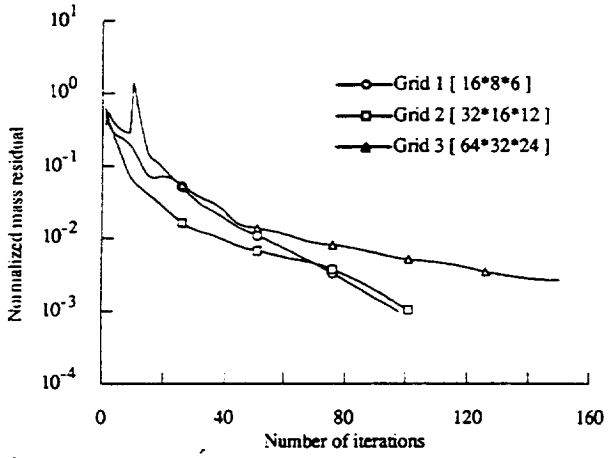

Figure 24: Multigrid convergence for calculation of turbulent flow in a combustor when traditional grid staggering is used.

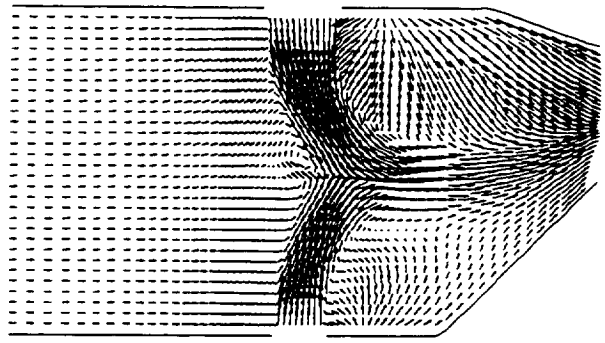

Figure 25: Velocity field in injection plane for turbulent flow in a combustor.

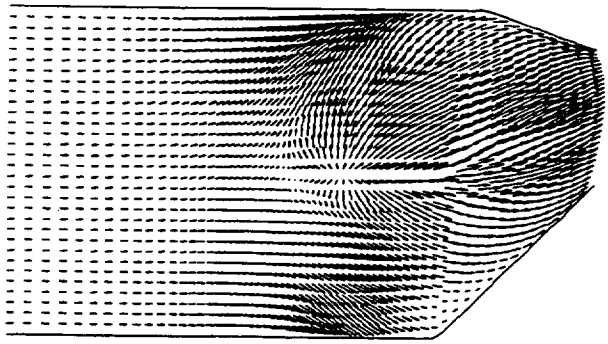

Figure 26: Velocity field in the symmetry plane for turbulent flow in a combustor.

Results obtained with flux limited quadratic interpolation

The laminar flow in a curved pipe of Reynolds number 500 and radius ratio 0.217 has also been calculated with a flux limited form of QUICK. The calculations have been made with the multiple velocity grid staggering scheme. The convergence history on a 60x32x16 grid using three levels in a (1,1) V-cycle is shown in Figure 27. The convergence is compared with that of the first order upwind scheme. It is observed that the higher order discretization converges only to 0.1% after which a high frequency oscillation is exhibited. This behavior was also seen in the single grid mode as well as when the multigrid cycling was switched off at 1% residual. A similar behavior was also observed for flow in a cube with a moving top wall. For this case, the limiting residual decreased as finer grids were considered. For a 10x10x10 grid the limit residual was approximately 0.1% while for a 40x40x40 grid, the method converged to 0.01% normalized mass residual. The flux limited quadratic interpolation is a nonlinear discretization which changes with the local solution. It is speculated that the limit residual may be the result of oscillation in the deferred correction source term arising from the flux limiting process.

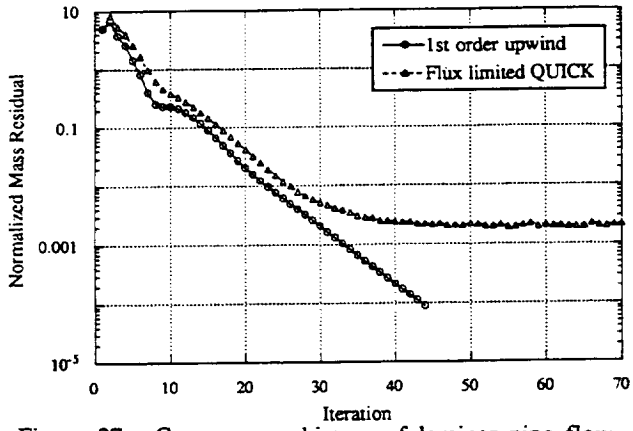

Figure 27: Convergence history of laminar pipe flow calculation on a 60x32x16 grid using two different discretizations.

V. Conclusions

A multigrid method for internal flows in complex geometries based on multiple velocity grid staggering has been described. The numerical method has been tested for laminar flow in a curved pipe and for laminar and turbulent flow in the dilution zone of a gas turbine combustion chamber. The convergence characteristics for the method have been compared to the convergence obtained for use of traditional grid staggering. It has been observed that the use of the multiple velocity grid staggering arrangement is superior to traditional grid staggering only when a ninety degree bend exists in the problem geometry. In this case, the multiple velocity arrangement avoids the pressure-velocity decoupling phenomena which occurs when traditional grid staggering is used for such problems. For the simulation of flow in the dilution zone of a gas turbine combustion chamber, it was observed that both grid staggering arrangements required approximately the same number of iterations for convergence. In this case, the traditional grid staggering is to be favored due to its lower work count per iteration. One potential advantage of the multiple velocity grid staggering arrangement involves the use of coupled solvers for the solution of the momentum and continuity equations. The multiple velocity grid staggering arrangement facilitates use of a symmetrical coupled Gauss-Seidel operator (Vanka, 1986c). It is not feasible to use such a coupled solver if only one Cartesian velocity component is stored at each cell face. The potential benefit arises from the lower work count of the SCGS operator in comparison to the SIMPLE algorithm used in this study. The SIMPLE algorithm requires approximately 30% more work than one sweep of SCGS (Sockol, 1993). If it is possible to obtain a converged solution with the SCGS operator in the same number of iterations as the SIMPLE algorithm when a multiple velocity staggered grid is used, the cost incurred by having more Cartesian velocity components may be alleviated.

Acknowledgements

This work has been supported by the NASA Lewis Research Center, Internal Fluid Mechanics Division with Dr. J. D. Holdeman as the program monitor. All computations have been performed on the Cray Y-MP at the NASA Lewis Research Center. The Air Force Office of Scientific Research has supported Wm. Kevin Cope during the period of this study. The support of these organizations is gratefully acknowledged.

References

Brandt, A., (1977) "Multi-Level Adaptive Solutions to Boundary-Value Problems", Mathematics of Computation, vol. 31, no. 138, pp. 333-390.

Brandt, A., (1980) "Multilevel Adaptive Computations in Fluid Dynamics", AIAA Journal, vol. 18, no. 10, pp. 1165-1172.

Enayet, M. M., Gibson, M. M., and Yianneskis, M., (1982) "Laser Doppler Measurements for Laminar and Turbulent Flow in a Pipe Bend", International Journal of Heat and Fluid Flow, vol. 3, pp. 213-220.

Ghia, U., Ghia, K. N., and Shin, C. T., (1982) "High-Re Solutions for Incompressible Flow Using the Navier-Stokes Equations and a Multigrid Method", Journal of Computational Physics, vol. 48, pp. 387-411.

Hayase, T., Humphrey, J. A. C., and Greif, R., (1992) "A Consistently Formulated QUICK Scheme for Fast and Stable Convergence Using Finite-Volume Iterative Calculation Procedures", Journal of Computational Physics, vol. 98, pp. 108-118.

Hortmann, M., Peric, M., and Scheuerer, G., (1990) "Finite Volume Multigrid Prediction of Laminar Natural Convection: Benchmark Solutions", International Journal for Numerical Methods in Fluids, vol. 11, pp. 189-207.

Joshi, D. S. and Vanka, S. P., (1991) "Multigrid Calculation Procedure for Internal Flows in Complex Geometries", Numerical Heat Transfer, Part B, vol. 20. pp. 61-80.

Karki, K. C. and Patankar, S. V., (1988) "Calculation Procedure for Viscous Incompressible Flows in Complex Geometries", Numerical Heat Transfer, vol. 14, pp. 295-307.

Launder, B. E., and Spalding, D. B., (1974) "The Numerical Computation of Turbulent Flows", Computer Methods in Applied Mechanics and Engineering, vol. 3, pp. 269-289.

Leonard, B. P. (1979) "A Stable and Accurate Convective Modelling Procedure Based on Quadratic Upstream Interpolation", Computer Methods in Applied Mechanics and Engineering, vol. 19, pp. 59-98.

Leonard, B. P. (1988) "Elliptic Systems: Finite Difference Method IV", Handbook of Numerical Heat Transfer, pp. 347-378, John Wiley and Sons, Inc., New York.

Leonard, B. P. and Mokhtari, Simin, (1990) "Beyond First-Order Upwinding: The Ultra-Sharp Alternative for Non-oscillatory Steady State Simulation of Convection", International Journal for Numerical Methods in Engineering, vol. 30. pp. 729-766.

Maliska, C. R. and Raithby, G. D., (1984) "A Method for Computing Three Dimensional Flows using Non-orthogonal Boundary Fitted Coordinates", International Journal for Numerical Methods in Fluids, vol. 4, pp. 519-537.

McGuirk, J. J. and Palma, J. M. L. M., (1992) "Calculations of the Dilution System in an Annular Gas Turbine Combustor", AIAA Journal, vol. 30, no. 4, pp. 963-972.

Miller, T. F. and Schmidt, F. W., (1988) "Use of a Pressure-Weighted Interpolation Method for the Solution of the Incompressible Navier-Stokes Equations on a Nonstaggered Grid System", Numerical Heat Transfer, vol. 14, pp. 213-233.

Patankar, S. V., (1980) Numerical Heat Transfer and Fluid Flow, Hemisphere Publishing Corporation, New York.

Patankar, S. V., and Spalding, D. B., (1972) "A Calculation Procedure for Heat, Mass and Momentum Transfer in Three-Dimensional Parabolic Flows", International Journal of Heat and Mass Transfer, vol. 15, pp. 1787-1806.

Peric, M., (1990) "Analysis of Pressure-Velocity Coupling on Nonorthogonal Grids", Numerical Heat Transfer, Part B, vol. 17, pp. 63-82.

Rayner, D., (1991) "Multigrid Flow Solutions in Complex Two-Dimensional Geometries", International Journal for Numerical Methods in Fluids, vol. 13, pp. 507-518.

Rubini, P. A., Becker, H. A., Grandmaison, E. W., Pollard, A., Sobiesiak, A., and Thurgood, C., (1992) "Multigrid Acceleration of Three-Dimensional, Turbulent, Variable-Density Flows", Numerical Heat Transfer, Part B, vol. 22, pp. 163-177.

Shyy, Wei and Vu, Thi C., (1991) "On the Adoption of Velocity Variable and Grid System for Fluid Flow Computation in Curvilinear Coordinates", Journal of Computational Physics, vol. 92, pp. 82-105.

Shyy, Wei, Sun, Chia-Sheng, Chen, Ming-Hsiung, and Chang, K. C. (1993) "Multigrid Computation for Turbulent Recirculating Flows in Complex Geometries", Numerical Heat Transfer, Part A, vol. 23, pp. 79-98.

Smith, K. M., Cope, W. K., and Vanka, S. P., (1993) "A Multigrid Procedure for Three-Dimensional Flows on Non-Orthogonal Collocated Grids", International Journal for Numerical Methods in Fluids, vol. 17, pp. 887-904.

Sockol, P. M., (1993) "Multigrid Solution of the Navier-Stokes Equations on Highly Stretched Grids", International Journal for Numerical Methods in Fluids, vol. 17, pp. 543-566.

Spalding, D. B., (1972) "A Novel Finite Difference Formulation for Differential Expressions Involving both First and Second Derivatives", International Journal for Numerical Methods in Engineering, vol. 4, pp. 551-559.

Thompson, Joe F., Warsi, Z. U. A., and Mastin, C. Wayne, (1985) Numerical Grid Generation: Foundations and Applications, Elsevier Science Publishing Co., Inc., New York.

Vanka, S. P., (1986a) "Performance of a Multigrid Calculation Procedure in Three-Dimensional Sudden Expansion Flows", International Journal for Numerical Methods in Fluids, vol. 6, pp. 459-477.

Vanka, S. P., (1986b) "Calculation of Axisymmetric, Turbulent, Confined Diffusion Flames", AIAA Journal, vol. 24, no. 3, pp. 462-469.

Vanka, S. P., (1986c) "Block Implicit Multigrid Solution of Navier Stokes Equations in Primitive Variables", Journal of Computational Physics, vol. 65, pp. 138-158.

Vanka, S. P., (1987) "Block Implicit Computation of Viscous Internal Flows-Recent Results", AIAA-87-0058, January 12-15, 1987, Reno, NV.

Vanka, S. P., Krazinski, J. L., and Nejad, A. S., (1989) "Efficient Computational Tool for Ramjet Combustor Research", Journal of Propulsion and Power, vol. 5, no. 4, pp. 431-437.

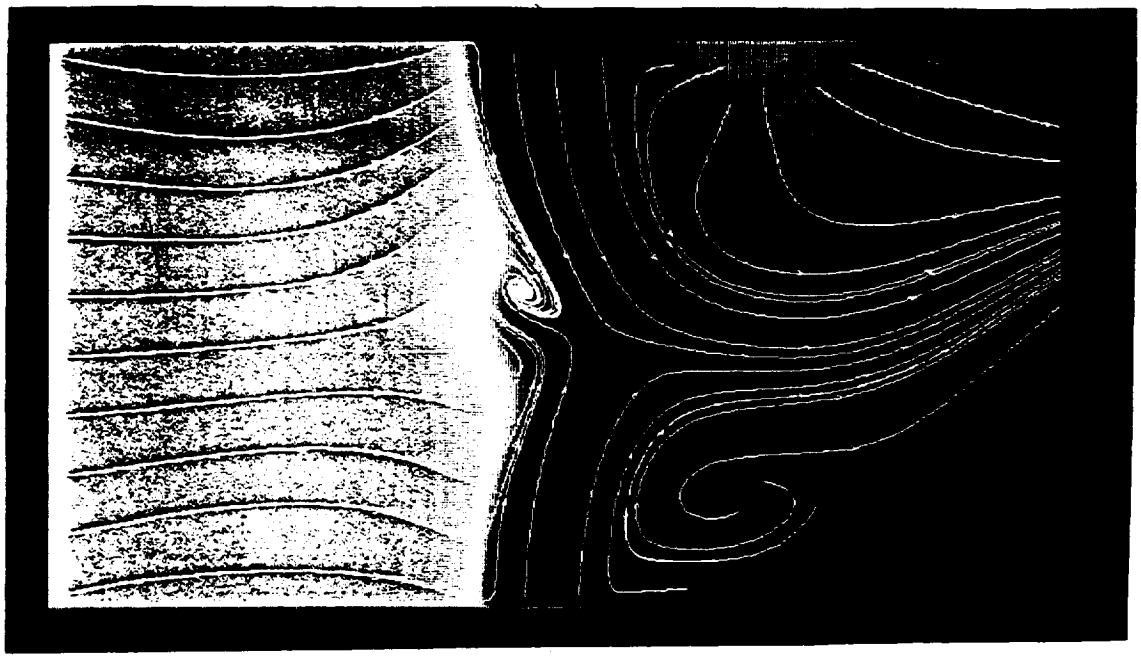

(a)

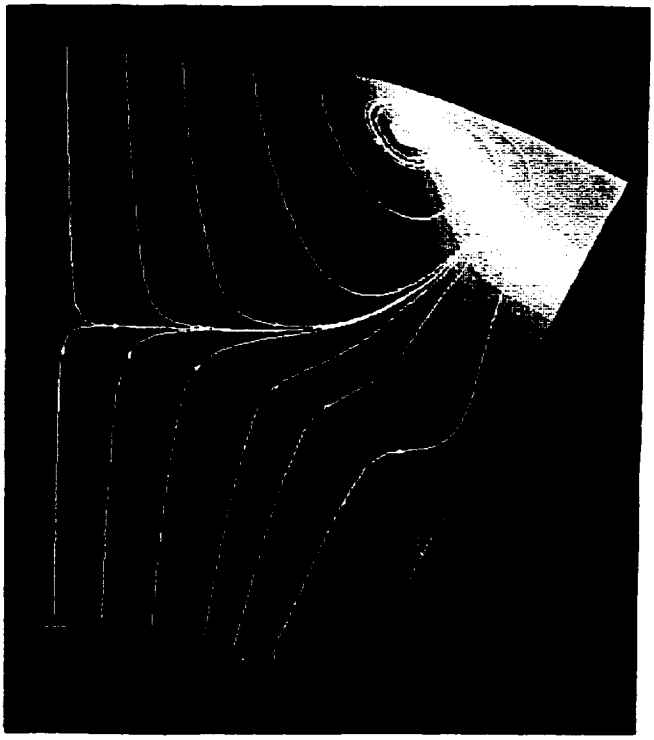

(b)

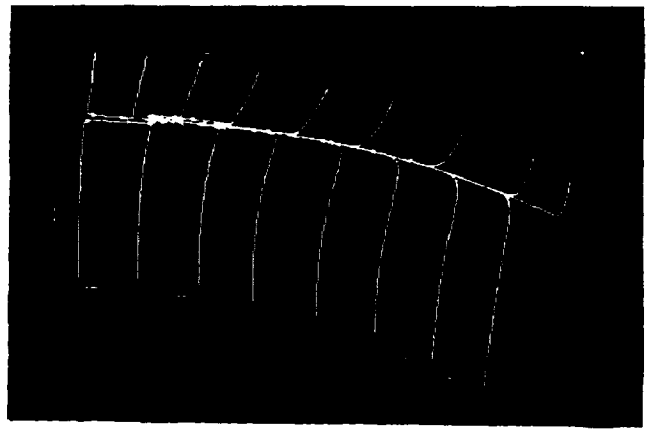

(c)

Figure 20: Temperature distributions for laminar mixing flow in a combustion chamber: (a) lengthwise plane at Θ=0 degrees (b) cross-stream plane at injectors (c) exit plane.

APPENDIX H

MULTIGRID CALCULATIONS OF TWIN JET IMPINGEMENT WITH CROSSFLOW: COMPARISON OF SEGREGATED AND COUPLED RELAXATION STRATEGIES

MULTIGRID CALCULATIONS OF TWIN JET IMPINGEMENT WITH CROSSFLOW: COMPARISON OF SEGREGATED AND COUPLED RELAXATION STRATEGIES

Gang Wang, Wm. Kevin Cope, and S. P. Vanka
Department of Mechanical and Industrial Engineering
University of Illinois at Urbana-Champaign
Urbana, Illinois

ABSTRACT

The present study compares coupled and segregated relaxation operators with multigrid acceleration for the calculation of jet impingement flow fields. The symmetrical coupled Gauss-Seidel (SCGS) scheme and the SIMPLE algorithm have been used as relaxation operators. The coupled operator is observed to require less work for convergence than the segregated method. When additional scalar equations were solved, the segregated method exhibited a definite deterioration in convergence rate. The coupled method revealed similar behavior as regards the solution of turbulence equations. Unlike the segregated operator, the convergence of the coupled operator did not deteriorate with the addition of the energy equation for high temperature flow calculations. The calculations performed in these tests required cell aspect ratios as large as sixteen in order to resolve important flow features. The SCGS operator provided rapid convergence even when these aspect ratios were used.

INTRODUCTION

In recent years, the multigrid technique has been shown to significantly improve the performance of iterative computational algorithms for the solution of the discretized fluid flow equations (Brandt, 1980; Demuren, 1989; Vanka, 1986; Shyy et al., 1993). In the multigrid technique, a number of coarse grids are used in conjunction with a given fine grid in order to accelerate the rate of convergence of the iterative procedure. Residuals that are slow to converge on a given grid are interpolated and solved on progressively coarser grids. The corrections implied by the solutions on the coarser grids are then applied to the fine grid solution. The primary advantage of the multigrid method is that the rate of convergence can be made independent of the number of discrete nodes in the computational domain and the work count can be made to vary as O(n). In contrast, the convergence of single grid algorithms deteriorates as the number of grid nodes is increased. The cause of such a behavior is attributed to the slow convergence of the low frequency errors that are present in any partially converged solution. By restricting such errors to coarser grids where they appear as high frequency errors, their rate of convergence can be improved. Beginning with the pioneering works of Brandt (1977), the multigrid method has been demonstrated to work well in a variety of applications including the computation of viscous internal fluid flows.

In any multigrid scheme, the relaxation procedure used to resolve the errors on a given grid plays an important role in the success of the overall numerical method. For viscous internal fluid flows, several relaxation procedures can be designed. Several computational parameters play an important role in the relative behavior of the relaxation scheme. These include the geometrical configuration, the aspect ratio of the grid cells, the speed of the flow (supersonic vs. subsonic), the presence of interior flow obstructions and the flow Reynolds number. It is not possible to provide *a priori* information on the best relaxation procedure for a given flow because of the complex nonlinear nature of the equations. As a result, much of the information must be gained through the testing of their performance in actual implementations.

For viscous internal flows dominated by the strong coupling between the pressure and the velocity fields, two main relaxation strategies have been advocated. In one of these, the momentum and continuity equations are solved in a coupled manner, thus preserving the strong pressure-velocity coupling. In the other, the momentum and continuity equations are solved in a segregated manner, wherein the momentum equations are first solved with an approximate

pressure field. The pressure field is then corrected using the local imbalances in the mass continuity equation. A pressure-correction equation is derived by substituting approximate forms of the discrete momentum equations into the continuity equation. Several pressure update strategies have been proposed in the past, having built on the original concept of the SIMPLE algorithm of Patankar and Spalding (1972).

Recent progress in the development of coupled operators has resulted in several procedures which have been observed to be more computationally efficient than segregated operators on certain problems. Galpin et al. (1985) developed the coupled equation line solver (CELS) which simultaneously solves for the velocities and pressures along a given grid line. In tests with two improved versions of the SIMPLE algorithm (SIMPLEC and SIMPLER), it was observed that CELS was not as sensitive to the choice of relaxation factor as was SIMPLEC and SIMPLER. The observation was a significant one since the optimal relaxation factor is not known *a priori*. The symmetrical coupled Gauss-Seidel (SCGS) operator proposed by Vanka (1986) is a point solver in that velocities and pressures for only one cell are coupled. One advantage which is observed for point solvers as compared to line solvers is a lower work count per iteration. Demuren (1989) extended the SCGS operator to solve implicitly all the pressures along a line (CLSOR) or a plane (SIM) with subsequent update of the velocities at each cell. The SCGS, coupled line successive over-relaxation (CLSOR), and strongly implicit (SIM) relaxation operators all involve *local* coupling between velocity and pressure. The extension of SCGS to CLSOR and SIM provided additional coupling for *pressures* along a line or plane. In comparisons of SCGS, CLSOR, SIM, and SIMPLE for a lid driven cavity flow, Demuren found that the SCGS operator gave the best performance of all methods in terms of CPU time and computer memory when implemented in the context of a multigrid method. The observation was made for nearly isotropic coefficients in the difference equations. The use of large cell aspect ratios ($\Delta x/\Delta y$) leads to anisotropy in the coefficients of the discrete equations. It was observed that SCGS did not yield the best performance when large aspect ratios were used. A similar observation was made by Rodi et al. (1987) as regards simulation of three-dimensional problems involving large aspect ratios. Recently, Sockol (1993) has compared SCGS, CLSOR, fully coupled line block Gauss Seidel (CLBGS), and SIMPLE relaxation procedures in the context of a multigrid method. The comparisons were made for three different flows: lid driven cavity flow, developing channel flow, and open cavity flow. In tests at various Reynolds number and cell aspect ratio, it was concluded that SCGS offered the best mix of robustness and computational speed. It was also observed that SCGS was less sensitive to the presence of corner singularities than were the other relaxation operators, but that the option of using CLBGS should be retained for regions of strongly aligned flow (e.g. flow in a straight pipe).

The present work is motivated by the desire to efficiently solve the flow fields created by the exhaust jets of a Short Take off and Vertical Landing (STOVL) Aircraft hovering in ground proximity. The determination of these flowfields is important to the estimation of the temperature of the hot gases ingested by the engine and to the determination of the loss of lift caused by vortices underneath the aircraft. Such flows provide several problems for any numerical method. Since jet impingement phenomena are inherently three-dimensional, a large number of cells must be used to cover the flow domain. As noted, convergence deteriorates with grid resolution for a single grid method, hence a multi-grid method is extremely important for such three-dimensional calculations. The use of fine grids in the jet impingement region to resolve sharp gradients, gives rise to large aspect ratios in the region of the freestream where no such resolution is needed. An additional problem, common to any turbulent flow, is that of equation coupling. The coupled methods which have been discussed involve coupling between velocities and pressures. The solution of scalar equations such as k and ε is usually accomplished in a segregated manner.

In the present study, a comparison of the segregated and coupled strategies has been made for the computation of the flow fields created by twin impinging jets in the presence of a head wind. The performance of the two relaxation operators is evaluated in terms of convergence and CPU time. A description of the governing equations and discretization is given first. The segregated and coupled procedures are then described followed by a discussion of the multigrid implementation of the two relaxation operators. The results obtained from the numerical experiments indicate that the coupled operator used in this study (SCGS) is computationally more efficient than the segregated procedure (SIMPLE) even when large cell aspect ratios are present.

GOVERNING EQUATIONS AND DISCRETIZATION

The continuity, momentum, energy, and turbulence equations may be conveniently written in terms of a general conservation equation which represents a balance of convection, diffusion, and source terms (Patankar, 1980):

$$\frac{\partial}{\partial x}(\rho u\phi)+\frac{\partial}{\partial y}(\rho v\phi)+\frac{\partial}{\partial z}(\rho w\phi)= \frac{\partial}{\partial x}\left[\Gamma^{\phi}\frac{\partial \phi}{\partial x}\right]+\frac{\partial}{\partial y}\left[\Gamma^{\phi}\frac{\partial \phi}{\partial y}\right]+\frac{\partial}{\partial z}\left[\Gamma^{\phi}\frac{\partial \phi}{\partial z}\right]+S^{\phi} \quad (1)$$

Γ^{ϕ} and S^{ϕ} are the diffusive exchange coefficient and source term respectively, for the general variable ϕ. The values of Γ^{ϕ} and S^{ϕ} associated with a given flow variable are given in Table 1. The strong conservation law form of the governing equations has been retained so as to facilitate use of a finite volume discretization.

For turbulent flows, the Reynolds averaged equations are closed by use of a k-ε turbulence model (Launder and Spalding,

1974). The model relates the Reynold's stresses to the mean velocity field through use of the Boussinesq approximation. The associated eddy viscosity is given by $\mu_T = \rho C_\mu k^2/\varepsilon$ where modeled equations for k and ε are solved. The turbulence model used in the present study incorporates the wall functions of Launder and Spalding (1974) to specify boundary conditions for the flow variables near a solid boundary.

The finite volume method is used to discretize the governing equations. In this method, the integral and not the differential form of the governing equations is approximated. In this method, the computational domain is divided into numerous control volumes. The integral form of the conservation laws is obtained for each control volume by integrating the governing equations (Eqn. 1) over the bounds of each control volume. The velocity and pressure cells have been staggered relative to one another so as to avoid the pressure-velocity split which occurs for simulations of incompressible flows (Harlow and Welch, 1965). The discrete expression for the combined convective/diffusive flux utilizes the hybrid differencing procedure of Spalding (1972). Having discretized the governing equations, the problem becomes one of solving for a set of coupled, nonlinear algebraic equations. The nonlinear algebraic equations are linearized by the procedure of lagged coefficients (Anderson et al., 1984) and solved through the process of iteration. The discrete equations are written in the following form:

$$A_p \phi_p = \sum A_{nb} \phi_{nb} + \left(\bar{S}^{\phi}\right) \Delta x \cdot \Delta y \cdot \Delta z \qquad (2)$$

In order to maintain numerical stability during the iterative process, it is necessary to dampen the successive changes of the flow variables. Under-relaxation has been implemented implicitly by changing the discrete equations as follows (Patankar, 1980):

$$A_p = \sum A_{nb}/\alpha \qquad (3)$$

$$S^{\phi} = S^{\phi} + \frac{\sum A_{nb}}{\alpha}(1-\alpha)\phi_{old} \qquad (4)$$

where α is the relaxation factor. The optimal relaxation factor varies with the problem solved and the characteristics of the finite-difference grid.

SOLUTION METHODOLOGY

The present study involves a comparison of the performance of multigrid based segregated and coupled solution procedures for the simulation of jet impingement flows. The segregated approach used in this investigation is the SIMPLE algorithm of Patankar and Spalding (1972). The coupled solution procedure used is the symmetrical coupled Gauss-Seidel (SCGS), proposed by Vanka (1986). The segregated and coupled solution procedures are embedded in a multigrid cycle which serves to accelerate their rates of convergence.

Segregated Method

In the segregated relaxation method, each equation is solved in a sequential fashion. On a given grid, the following procedure is used to iteratively solve for the flow variables:

1) Solve for the u component of velocity
2) Solve for the v component of velocity
3) Solve for the w component of velocity
4) Solve for the pressure correction, P'
5) Update u, v, w, and P based on the solution for P'
6) If on the locally finest grid, solve for scalar variables (T,k,ε)

where the pressure correction equation is written in a form analogous to the velocity and scalar equations:

$$A_p P'_p = \sum A_{nb} P'_{nb} + S^m \qquad (5)$$

The quantity S^m represents the mass imbalance for an individual cell. The iterative process for any particular flow variable is not carried to convergence since subsequent iterations on the other flow variables will change the coefficients of the discrete equation. In general, five iterations of an alternating line Gauss-Seidel procedure were performed for each velocity and scalar variable while fifteen iterations were performed on the pressure correction equation. The six steps given above constitute one "outer" iteration, i.e. iterative update of all flow variables. A numerical method employing only a single grid would simply continue these outer iterations until the residuals in the governing equations were reduced below a prescribed level. In the present multigrid method, the outer iterations are performed on a given grid prior to restriction or prolongation to another grid. It is important to note that during the execution of a V-cycle, the scalar equations are only solved on the locally finest grid. The values of T, k, and ε on the finest grid are held fixed on the coarse grids during the V-cycle. The details pertaining to the multigrid acceleration technique are described below.

The segregated solution procedure has been shown to be convergent for a wide range of flow problems although it can be very slow to converge on a single grid (Rayner, 1991). One potential shortcoming of the segregated method is the pressure-velocity coupling. The segregated method involves writing the continuity equation as a pressure correction equation. There are various means of deriving a pressure correction equation. The different pressure correction equations do not affect the final solution since all pressure corrections will be zero when the solution has converged. The rate of convergence however can be different for the various pressure correction practices. The coupled solution procedure seeks to improve on the coupling between pressure and velocity and it eliminates any ambiguity involving pressure correction equations simply because the primitive variable form of the continuity equation is retained.

Coupled Method

A coupled solution procedure solves for the velocities and pressures simultaneously. This is in contrast to the segregated procedure which solves these quantities in a sequential manner. The coupled solution seeks to attain a better coupling between velocities and pressures by retaining the primitive variable form of the continuity equation. A pressure correction equation is not needed in a coupled solution method. The coupled method used in the present investigation is the symmetrical coupled Gauss-Seidel (SCGS) proposed by Vanka (1986). The method was chosen because of the strong local pressure-velocity coupling as well as for its low work count. The SCGS operator also requires less storage than the coupled line or plane solvers. This can be a substantial benefit when very fine grids are required in 3-D calculations.

The SCGS operator considers a local coupling between pressure and velocities. For a 3-D geometry, the six momentum equations for a given finite volume, along with the continuity equation provide the seven equations necessary to find the six components of velocity located at the cell faces and the cell centered pressure. These equations are written in terms of current approximations for the unknowns plus a correction:

$$\begin{aligned} u &= u^{old} + u' \\ v &= v^{old} + v' \\ w &= w^{old} + w' \\ P &= P^{old} + P' \end{aligned} \tag{6}$$

The following 7x7 matrix can be analytically inverted to obtain the corrections to the local unknowns:

$$\begin{bmatrix} \left(A_P^u\right)_{i-1/2} & 0 & 0 & 0 & 0 & 0 & \delta y\delta z \\ 0 & \left(A_P^u\right)_{i+1/2} & 0 & 0 & 0 & 0 & -\delta y\delta z \\ 0 & 0 & \left(A_P^v\right)_{j-1/2} & 0 & 0 & 0 & \delta x\delta z \\ 0 & 0 & 0 & \left(A_P^v\right)_{j+1/2} & 0 & 0 & -\delta x\delta z \\ 0 & 0 & 0 & 0 & \left(A_P^w\right)_{k-1/2} & 0 & \delta x\delta y \\ 0 & 0 & 0 & 0 & 0 & \left(A_P^w\right)_{k+1/2} & -\delta x\delta y \\ -\delta y\delta z & \delta y\delta z & -\delta x\delta z & \delta x\delta z & -\delta x\delta y & \delta x\delta y & 0 \end{bmatrix} \times \begin{bmatrix} u'_{i-1/2} \\ u'_{i+1/2} \\ v'_{j-1/2} \\ v'_{j+1/2} \\ w'_{k-1/2} \\ w'_{k+1/2} \\ P'_{i,j,k} \end{bmatrix} = \begin{bmatrix} R^u_{i-1/2} \\ R^u_{i+1/2} \\ R^v_{j-1/2} \\ R^v_{j+1/2} \\ R^w_{k-1/2} \\ R^w_{k+1/2} \\ R^c_{i,j,k} \end{bmatrix} \tag{7}$$

where A_p^{ϕ} is the central coefficient in the discrete equation for the variable ϕ and R^{ϕ} is the residual (Vanka, 1986). The seven variables at each cell are solved for using algebraic relations. The computational domain is swept through in a lexicographic manner in order to update all velocities and pressures. When the entire domain has been swept through, each velocity will have been updated twice and each pressure once.

Multigrid Acceleration

The segregated and coupled solution procedures described have been incorporated within a multigrid acceleration technique. A full approximation scheme-full multigrid (FAS-FMG) algorithm using a (1,1) V-cycle has been used. Various multigrid schemes and cycles have been proposed and tested in the literature (Brandt, 1977; Ghia et al., 1982; Hortmann et al., 1990, etc.). The FAS method has been used since the problem is nonlinear. The correction scheme (CS) is conceptually and algorithmically more simple for linear problems, but is less efficient when used for nonlinear problems. The full multigrid procedure involves approximately solving the problem on coarse grids and subsequently prolongating the solution to the finer grids so as to provide a good initial estimate.

The equation set on the finest grid (k) can be written as

$$L^k \phi^k = F^k \tag{8}$$

Here, L is the nonlinear operator consisting of convection and diffusion terms, ϕ is the solution vector, and F represents the source terms. In the FAS procedure, the values calculated on a coarser grid (k-1) are not simple corrections to the values on grid (k); instead they are approximations on grid (k-1) to the correct values on grid (k). Therefore, the equations solved on grid (k-1) are

$$\begin{aligned} L^{k-1}\phi^{k-1} = F^{k-1} &+ I_k^{k-1}\left(F^k - L^k\phi^k\right) \\ &+ \left(L^{k-1}I_k^{k-1}\phi^k - F^{k-1}\right) \end{aligned} \tag{9}$$

where I_k^{k-1} is the restriction operator. Alternately, I_{k-1}^k is the prolongation operator. ϕ^k is then updated as

$$\phi^k_{new} = \phi^k_{old} + I^k_{k-1}\left(\phi^{k-1} - I_k^{k-1}\phi^k_{old}\right) \tag{10}$$

Note that only the change from the previous value $\left(\phi^{k-1} - I_k^{k-1}\phi_{old}^{k}\right)$ is prolongated to grid k and not the value ϕ^{k-1} itself. The advantage of using FAS over the Correction Scheme is that the solution vector from the fine grid, and not just the residuals are transferred to the coarser grids. Additionally, if multiple iterations are performed on a coarse grid, the nonlinear operator and the source terms are continuously updated.

The grid iterations can be arranged in a variety of ways which affect the overall rate of convergence. The fixed cycle is preferred here over an adaptive cycling strategy since it is not always possible to assign an optimal smoothing rate as is required in an adaptive strategy. The present study employs a fixed (1,1) V-cycle with one iteration performed on u, v, w, and P per grid during the downward leg and one iteration during the upward leg.

Consistent transfer of residuals and solutions is a major aspect of any multigrid-based algorithm. In the present algorithm, cell-center quantities are restricted using full weighting of neighbor values. Restriction of residuals is accomplished by requiring that the per unit volume residual on the fine grid is maintained on the coarse grid. Cell-face velocities are restricted so that mass conservation is maintained on both the fine and coarse grids. Corrections are prolongated by trilinear interpolation.

RESULTS

The simulation of jet impingement flows using coupled and segregated solution procedures has been accomplished for four test cases: laminar cold and hot impinging jets, turbulent cold and hot impinging jets. The basic flow fields observed for the turbulent flow cases will be briefly described as these are more relevant to the STOVL problem than the laminar flow cases. The convergence characteristics of the two methods are of primary importance in this investigation. The number of iterations required for convergence as well as the overall CPU time required for solution on a Cray Y-MP are considered in the analysis of the two methods.

Problem Definition

The geometry considered for all test cases is depicted in Figure 1. Two jets impinge normal to an infinite flat plate. The parallel plate is at a distance of five jet diameters from the jet exhaust and the two jets are placed six diameters apart. A cross flow is specified in a direction normal to the jets and has a magnitude of 3% relative to the jet velocity. Due to symmetry of the flow field in the z direction, only one half of the jet flow field is actually simulated. The computational domain was 69 jet diameters in the streamwise direction (x), 5 diameters in the cross stream direction (y), and 12.5 diameters in the spanwise direction (z). These dimensions were deemed necessary in order to accurately represent the flow characteristics present in an impinging jet flow without having interference from the simulated boundaries. The largest cell aspect ratio was sixteen for use of a fine grid of 120x20x36. Other details related to the geometry and flow variables used are given in Tables 2 and 3.

The simulation of any flow field requires that appropriate boundary conditions be specified. At the inlet of the domain, uniform velocity and temperature distributions have been specified. No slip, no penetration adiabatic walls have been specified at the solid surfaces. The outflow boundary was treated as fully developed flow in the present simulation, i.e.

$$\frac{\partial u}{\partial x} = \frac{\partial v}{\partial x} = \frac{\partial w}{\partial x} = \frac{\partial h}{\partial x} = 0. \qquad (11)$$

The z-minus boundary bisected the exhaust jets and therefore a symmetry boundary condition was specified. The z-plus boundary has been treated as a solid surface in the present calculations. The jets themselves were represented as mass, momentum, and energy sources and the profiles of velocity, density, temperature, k, and ε were specified as uniform.

Convergence and Execution Times

The simulations of impinging jet flow have been performed on a finest grid of 120x20x36 cells with a total of three (3) grids used in the solution. The relaxation factors and number of iteration sweeps used on the scalar equations for the four test cases are given in Table 4.

The convergence histories for the laminar, cold jet simulation using coupled and segregated operators are given in Figures 2 and 3. In Figure 2, the convergence history of the simulation as performed on all three grids using SCGS is presented. A similar convergence history is given in Figure 3 for the SIMPLE algorithm. It is observed from these figures that the multigrid rate of convergence is obtained with both relaxation operators. In other words, as the grid is refined from 30x5x9 out to 120x20x36, the convergence rate does not deteriorate. The number of iterations required for convergence on the coarse grid is essentially the same as the number of iterations required for convergence on the finest grid. This grid independent convergence is not achieved with single grid procedures and is the primary motivation for use of multigrid methods. It is also apparent that the coupled relaxation operator requires approximately 10-20 fewer iterations for convergence than does the segregated relaxation operator.

Table 5 reveals that the actual CPU time required for convergence is smaller for the coupled operator. This fact is not only the result of fewer iterations, but also due to the lower work count for the SCGS operator when compared to the SIMPLE method. The SCGS operator requires less computational work per iteration than SIMPLE. Sockol (1993) reports that SIMPLE requires approximately 30% more work per iteration than SCGS.

Comparison of convergence rates for the laminar and turbulent flow problems reveals that almost twice as many iterations (and hence work) is required for a turbulence simulation. This is understood when one considers that the scalar equations are not incorporated into the V-cycle of the

multigrid procedure. In particular, it is the turbulence equations which slow the rate of convergence since in the laminar, hot jet problem the energy equation is solved in single grid mode without a significant deterioration in the rate of convergence for use with the coupled operator (compare Figures 2 and 4). When the segregated relaxation procedure is used, solving the energy equation in single grid mode is sufficient to cause a deterioration in the rate of convergence (see Figures 3 and 4). These observations are also made for turbulent flow, where the solution of scalar equations seems to be more deterimental to the convergence rate when a segregated operator is used. Note from Table 5 that turbulent hot jet simulations performed with the segregated method required two more CPU minutes than did the turbulent cold jet simulations. In contrast, the turbulent hot jet simulations performed with the coupled operator actually required less time than the turbulent cold jet simulations.

From Figures 4 and 6 it is observed that the hot jet simulations required more work when the segregated relaxation operator was used. In this study, a work unit is defined as being an equivalent fine grid iteration. Table 5 reveals that almost twice as many work units were required for the segregated method as compared to the coupled method for hot jet calculations. In this case, not only does the coupled operator require less work per iteration, it also requires fewer iterations for these calculations.

Flow Field Description

The velocity fields in the symmetry and ground planes of both cold and hot turbulent flows are given in Figures 7-10. The exhaust jets impinge on the ground plane forming wall jets which flow radially in all directions from the point of impact. A ground vortex forms when the wall jets from the fore and aft exhaust jets are stagnated by one another (see Figures 7 and 9). It is apparent from Figures 7 and 9 that no upwash fountain forms as seen in actual STOVL flow fields (MacLean, et al., 1992). In other words, the stagnated wall jets do not turn upward and impinge on the underside of the exhaust plate. The ground vortex for the cold flowing jet is seen to be slightly larger than that of the hot flowing jet. Also, the stagnation point of the two wall jets is observed to be nearer the fore exhaust jet in the cold flow case. From Figure 9, one can observe that for the hot exhaust jet, the ground vortex partially blocks the aft exhaust jet. This behavior is not observed for the cold flow. The stagnation line is bent in the direction of the freestream flow for the hot exhaust jet case, while in the cold jet case it is almost perpendicular to the symmetry plane.

CONCLUSIONS

The present study has compared coupled and segregated relaxation operators with multigrid acceleration for the calculation of jet impingement flow fields. The symmetrical coupled Gauss-Seidel (SCGS) scheme and the SIMPLE algorithm have been used as relaxation operators. The coupled operator is seen to require less work for convergence than the segregated method. When additional scalar equations were required to be solved, the segregated method showed a definite deterioration in convergence rate. The coupled method revealed similar behavior as regards the solution of turbulence equations. Unlike the segregated operator however, the convergence of the coupled operator did not deteriorate with the addition of the energy equation for hot flow calculations. In test cases for which both methods required essentially the same number of iterations to converge, the lower work count per iteration for the SCGS operator led to a smaller execution time when compared to use of the SIMPLE algorithm. Finally, the calculations performed in these tests required cell aspect ratios as large as sixteen in order to resolve important flow features. The SCGS operator provided rapid convergence even when these aspect ratios were used. Our observations are consistent with the finding of Sockol (1993) and indicate that the SCGS operator can be used when large aspect ratios are required as in the case of impinging jet flows.

ACKNOWLEDGEMENTS

This work has been supported by the NASA Lewis Research Center, Internal Fluid Mechanics Division under the supervision of Dr. J. D. Holdeman. All computations have been performed on the Cray Y-MP at the NASA Lewis Research Center. The Air Force Office of Scientific Research has supported Wm. Kevin Cope during the period of this study. The support and encouragement from these individuals and organizations is gratefully acknowledged.

REFERENCES

Anderson, D. A., Tannehill, J. C., and Pletcher, R. H., 1984, *Computational Fluid Mechanics and Heat Transfer*, Hemisphere Pub. Corp.

Brandt, Achi, 1977, "Multi-Level Adaptive Solutions to Boundary-Value Problems", *Mathematics of Computation*, vol. 31, no. 138, pp. 333-390.

Brandt, Achi, 1980, "Multilevel Adaptive Computations in Fluid Dynamics", *AIAA Journal*, vol. 18, no. 10, pp. 1165-1172.

Demuren, A. O., 1989, "Application of Multi-grid Methods for Solving the Navier-Stokes Equations", *Proceedings of the Institute of Mechanical Engineers*, vol. 203, pp. 255-265.

Galpin, P. F., Van Doormaal, J. P., and Raithby, G. D., 1985, "Solution of the Incompressible Mass and Momentum Equations by Application of a Coupled Equation Line Solver", *International Journal for Numerical Methods in Fluids*, vol. 5, pp. 615-625.

Ghia, U., Ghia, K. N., and Shin, C. T., 1982, "High-Re Solutions for Incompressible Flow Using the Navier-Stokes Equations and a Multigrid Method", *Journal of Computational Physics*, vol. 48, pp. 387-411.

Harlow, F. H., and Welch, J. E., 1965, "Numerical Calculation of Time-Dependent Viscous Incompressible Flow

of Fluid with Free Surface", *Physics of Fluids*, vol. 8, no. 12, pp. 2182-2189.

Hortmann, M., Peric, M., and Scheuerer, G., 1990, "Finite Volume Multigrid Prediction of Laminar Natural Convection: Benchmark Solutions", *International Journal for Numerical Methods in Fluids*, vol. 11, pp. 189-207.

Launder, B. E. and Spalding, D. B., 1974, "The Numerical Computation of Turbulent Flows", *Computer Methods in Applied Mechanics and Engineering*, vol. 3, pp. 269-289.

MacLean, R., Sullivan, J., and Murthy, S. N. B. 1992, "Hot Gas Environment Around STOVL Aircraft in Ground Proximity-Part I: Experimental Study", *Journal of Aircraft*, vol. 29, no. 1, pp. 67-72.

Patankar, S. V., and Spalding, D. B., 1972, "A Calculation Procedure for Heat, Mass and Momentum Transfer in Three-Dimensional Parabolic Flows", *International Journal of Heat and Mass Transfer*, vol. 15, pp. 1787-1806.

Patankar, S. V., 1980, *Numerical Heat Transfer and Fluid Flow*, Hemisphere Pub. Corp.

Rayner, D., 1991, "Multigrid Flow Solutions in Complex Two-Dimensional Geometries", *International Journal for Numerical Methods in Fluids*, vol. 13, pp. 507-518.

Rodi, W., Majumdar, S., and Schönung, B, 1987, "Finite Volume Methods for Two-Dimensional Incompressible Flows with Complex Boundaries", Paper presented at 8th International Conference on Computing Methods in Applied Sciences and Engineering, Versailles, France, Dec. 14-18.

Sockol, Peter M., 1993, "Multigrid Solution of the Navier-Stokes Equations on Highly Stretched Grids", *International Journal for Numerical Methods in Fluids*, vol. 17, pp. 543-566.

Shyy, W., Sun, C. S., Chen, M. H., Chang, K. C. 1993, "Multigrid Computation for Turbulent Recirculating Flows in Complex Geometries", *Numerical Heat Transfer, Part A*, vol. 23, pp. 79-98.

Spalding, D. B., 1972, "A Novel Finite Difference Formulation for Differential Expressions Involving both First and Second Derivatives", *International Journal for Numerical Methods in Engineering*, vol. 4, pp. 551-559.

Vanka, S. P., 1986, "Block Implicit Multigrid Solution of Navier Stokes Equations in Primitive Variables", *Journal of Computational Physics*, vol. 65, pp. 138-158.

TABLE 1. EXCHANGE COEFFICIENTS AND SOURCE TERMS

ϕ	Γ^{ϕ}	S^{ϕ}
1	0	$\dot{m}_{inj}$
u	$\mu_l + \mu_t$	$-\partial P / \partial x + \dot{m}_{inj} u_{inj}$
v	$\mu_l + \mu_t$	$-\partial P / \partial y + \dot{m}_{inj} v_{inj}$
w	$\mu_l + \mu_t$	$-\partial P / \partial z + \dot{m}_{inj} w_{inj}$
H	$\frac{\mu_l}{\sigma_{h,l}} + \frac{\mu_t}{\sigma_{h,t}}$	$\dot{m}_{inj} h_{inj}$
k	$\mu_l + \frac{\mu_t}{\sigma_k}$	$G - \rho\varepsilon$ $G = \mu_t \left(\frac{\partial u_i}{\partial x_j} + \frac{\partial u_j}{\partial x_i} \right) \frac{\partial u_i}{\partial x_j}$
ε	$\mu_l + \frac{\mu_t}{\sigma_\varepsilon}$	$C_1 G \frac{\varepsilon}{k} - C_2 \rho \frac{\varepsilon^2}{k}$

TABLE 2. GEOMETRICAL AND FLOW PARAMETERS

Jet exit diameter, D	3.66 cm
Jet spacing, S	21.96 cm
Domain length, L	252.54 cm
Domain height, H	18.3 cm
Domain half width, W	45.75 cm
Jet exit velocity, V_{inj}	100.0 m / s
Cross stream velocity, V_{∞}	3.0 m / s

TABLE 3. JET TEMPERATURES AND REYNOLDS NUMBERS FOR THE VARIOUS TEST CASES CONSIDERED.

	T_{jet} (K)	Re
Laminar cold jet	300	238
Laminar hot jet	1000	71
Turbulent cold jet	300	238,000
Turbulent hot jet	1000	70,800

TABLE 4. SOLUTION PARAMETERS FOR MOMENTUM AND SCALAR EQUATIONS.

	Segregated Relaxation Procedure						Coupled Relaxation Procedure					
	α_u	α_p	α_T	$\alpha_{k,\varepsilon}$	α_μ	Iterations on scalar eqns.	α_u	α_p	α_T	$\alpha_{k,\varepsilon}$	α_μ	Iterations on scalar eqns.
Laminar cold	0.5	0.3	NA	NA	NA	NA	0.5	1.0	NA	NA	NA	NA
Laminar hot	0.5	0.3	0.9	NA	NA	3	0.5	1.0	0.9	NA	NA	3
Turbulent cold	0.5	0.3	NA	0.5	0.7	3	0.5	1.0	NA	0.5	0.5	3
Turbulent hot	0.5	0.3	0.9	0.5	0.5	3	0.5	1.0	0.9	0.5	0.5	3

TABLE 5. COMPARISON OF SEGREGATED AND COUPLED OPERATORS

	Work Unit		CPU time (sec)	
	Segregated	Coupled	Segregated	Coupled
Laminar cold jets	98.1	87.8	271.5	135.5
Laminar hot jets	118.4	57.4	362.1	143.0
Turbulent cold jets	242.5	219.5	975.3	719.4
Turbulent hot jets	287.1	150.0	1108.8	482.8

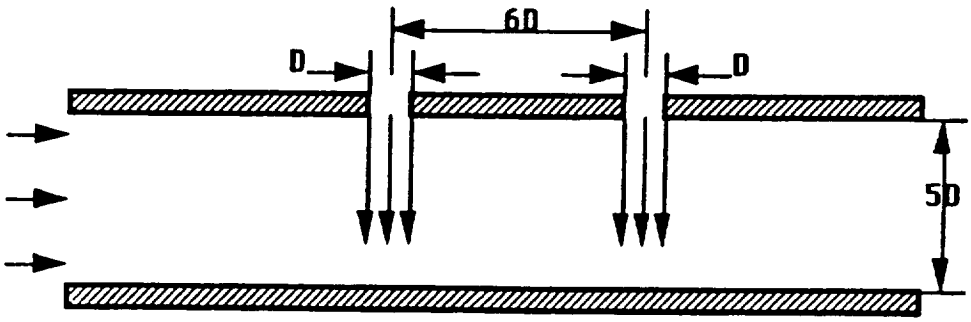

FIGURE 1. COMPUTATIONAL DOMAIN IN THE X-Y PLANE.

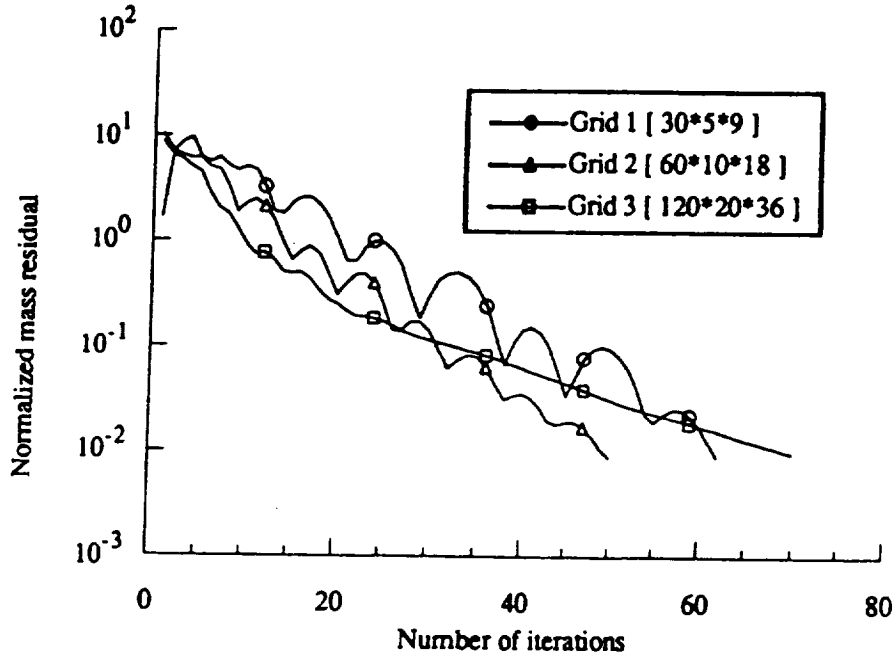

Figure 2 Convergence history for laminar twinjet impingement using a coupled relaxation operator. The jet exit temperature was 300 K.

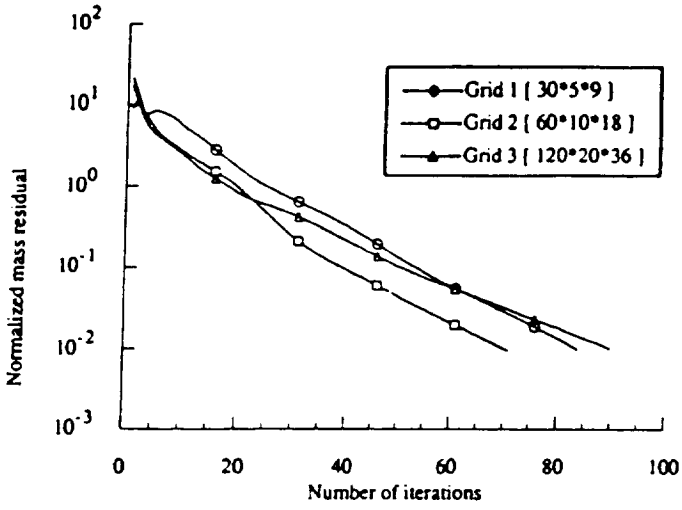

Figure 3 Convergence history for laminar twinjet impingement using a segregated relaxation operator. The jet exit temperature was 300 K.

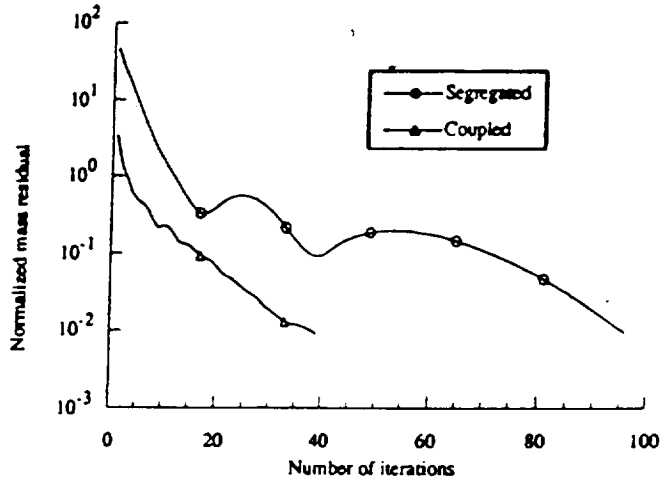

Figure 4 Comparison of convergence history for laminar twinjet impingement. The jet exit temperature was 1000 K.

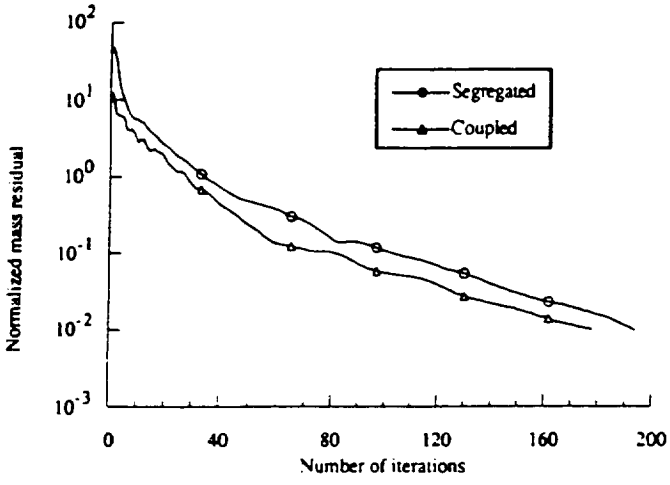

Figure 5 Comparison of convergence history for laminar twinjet impingement. The jet exit temperature was 300 K.

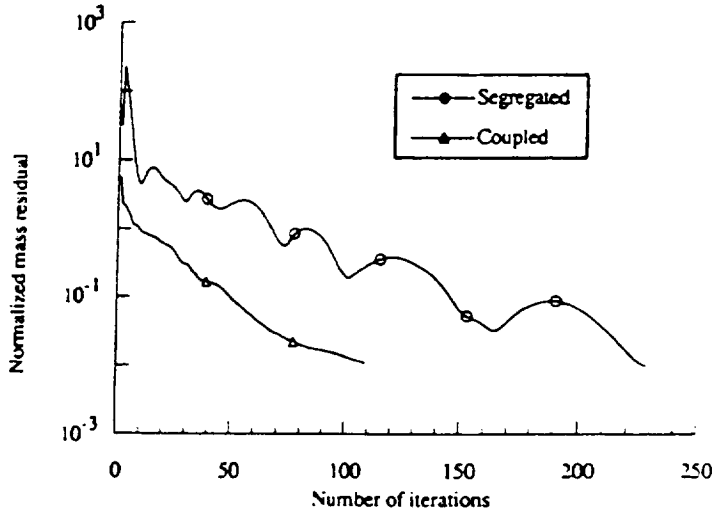

Figure 6 Comparison of convergence history for turbulent twinjet impingement. The jet exit temperature was 1000 K.

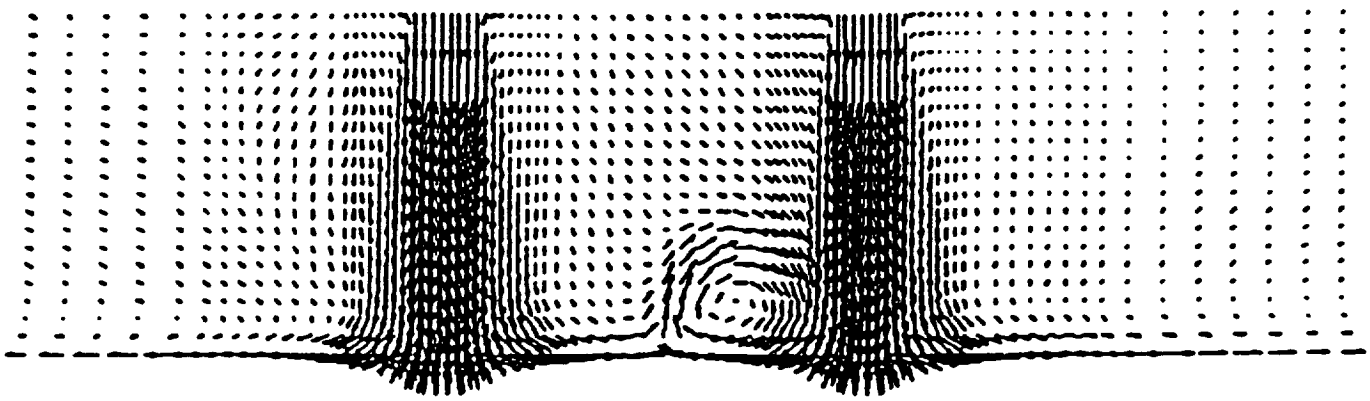

Figure 7. Velocity distribution in the plane of symmetry (x-y plane) for a turbulent impinging jet. The jet temperature is 300 K.

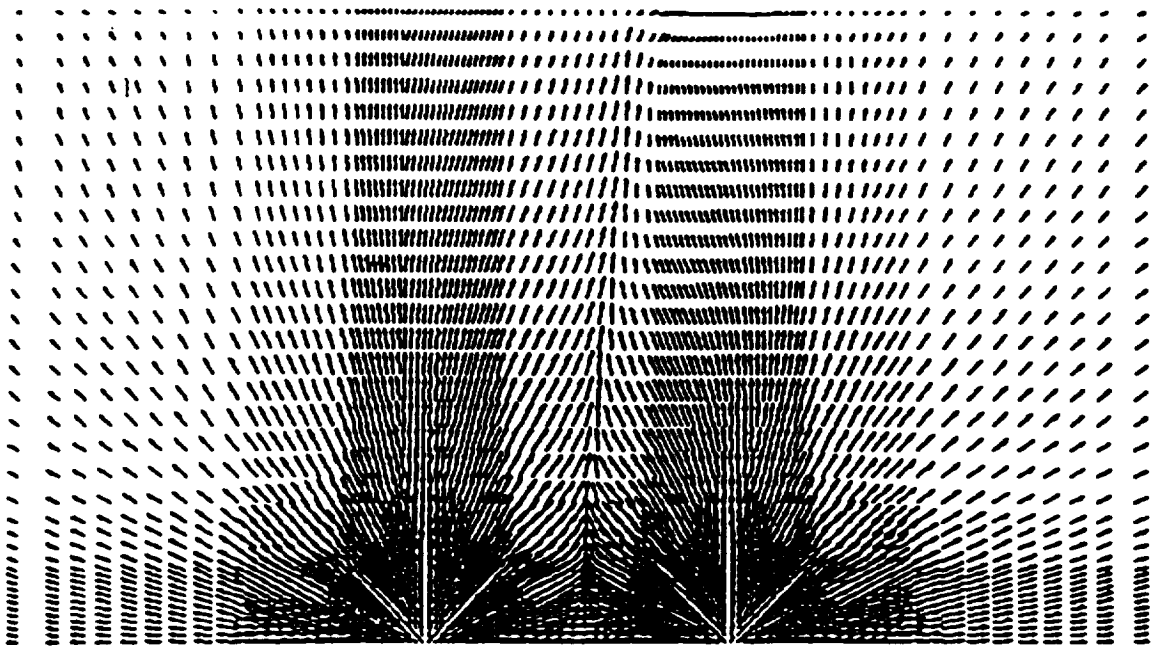

Figure 8. Velocity distribution in the ground plane (x-z plane) of a turbulent impinging jet. The jet temperature is 300 K.

REPORT DOCUMENTATION PAGE

Form Approved
OMB No. 0704-0188

1. AGENCY USE ONLY (*Leave blank*)	2. REPORT DATE	3. REPORT TYPE AND DATES COVERED
	January 1998	Final Contractor Report

4. TITLE AND SUBTITLE

Numerical Investigation of Hot Gas Ingestion by STOVL Aircraft

5. FUNDING NUMBERS

WU–523–26–33
NAG3–1026

6. AUTHOR(S)

S.P. Vanka

7. PERFORMING ORGANIZATION NAME(S) AND ADDRESS(ES)

University of Illinois at Urbana-Champaign
Urbana, Illinois 61801

8. PERFORMING ORGANIZATION REPORT NUMBER

E–10676

9. SPONSORING/MONITORING AGENCY NAME(S) AND ADDRESS(ES)

National Aeronautics and Space Administration
Lewis Research Center
Cleveland, Ohio 44135–3191

10. SPONSORING/MONITORING AGENCY REPORT NUMBER

NASA CR–4769

11. SUPPLEMENTARY NOTES

Project Manager, J.D. Holdeman, Turbomachinery and Propulsion Systems Division, NASA Lewis Research Center, organization code 5830, (216) 433–5846.

12a. DISTRIBUTION/AVAILABILITY STATEMENT

Unclassified - Unlimited
Subject Category: 07 Distribution: Nonstandard

This publication is available from the NASA Center for AeroSpace Information, (301) 621–0390.

12b. DISTRIBUTION CODE

13. ABSTRACT ***(Maximum 200 words)***

This report compiles the various research activities conducted under the auspices of the NASA Grant NAG3–1026, "Numerical Investigation of Hot Gas Ingestion by STOVL Aircraft" during the period of April 1989 to April 1994. The effort involved the development of multigrid based algorithms and computer programs for the calculation of the flow and temperature fields generated by Short Take-off and Vertical Landing (STOVL) aircraft, while hovering in ground proximity. Of particular importance has been the interaction of the exhaust jets with the head wind which gives rise to the hot gas ingestion process. The objective of new STOVL designs to reduce the temperature of the gases ingested into the engine. The present work describes a solution algorithm for the multi-dimensional elliptic partial-differential equations governing fluid flow and heat transfer in general curvilinear coordinates. The solution algorithm is based on the multigrid technique which obtains rapid convergence of the iterative numerical procedure for the discrete equations. Initial efforts were concerned with the solution of the Cartesian form of the equations. This algorithm was applied to a simulated STOVL configuration in rectangular coordinates. In the next phase of the work, a computer code for general curvilinear coordinates was constructed. This was applied to model STOVL geometries on curvilinear grids. The code was also validated in model problems. In all these efforts, the standard k–ε model was used.

14. SUBJECT TERMS	15. NUMBER OF PAGES
STOVL; Hot gas ingestion; CFD; Modeling; Elliptic flows	111
	16. PRICE CODE: A06

17. SECURITY CLASSIFICATION OF REPORT	18. SECURITY CLASSIFICATION OF THIS PAGE	19. SECURITY CLASSIFICATION OF ABSTRACT	20. LIMITATION OF ABSTRACT
Unclassified	Unclassified	Unclassified	

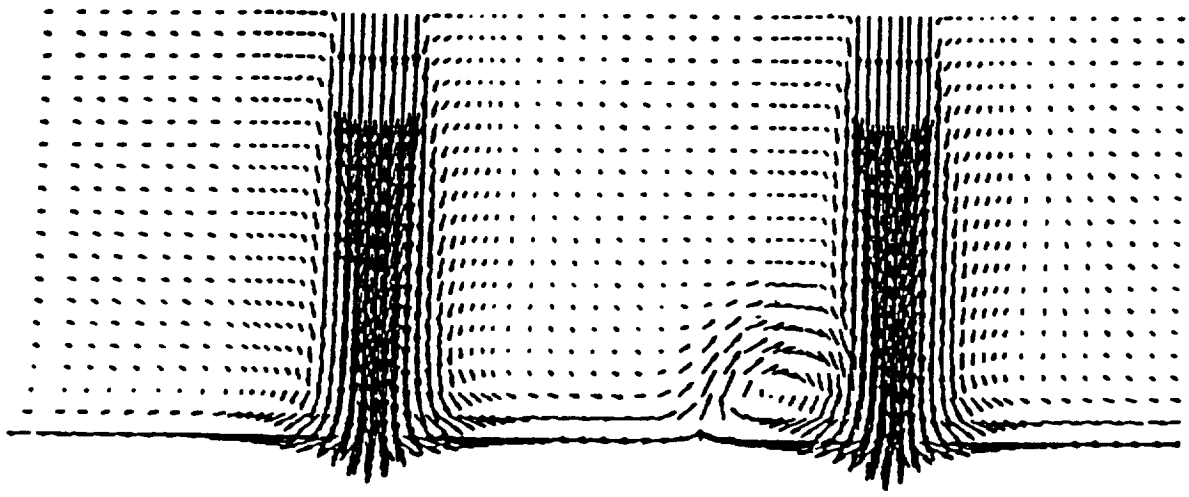

Figure 9. Velocity distribution in the plane of symmetry (x-y plane) for a turbulent impinging jet. The jet temperature is 1000 K.

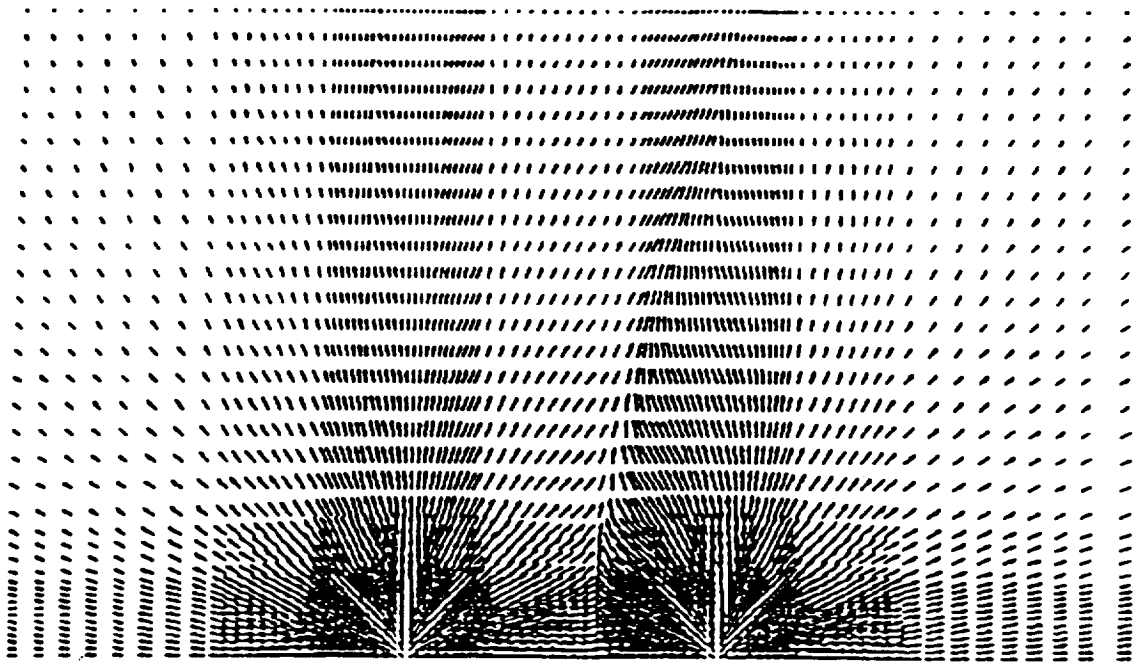

Figure 10. Velocity distribution in the ground plane (x-z plane) of a turbulent impinging jet. The jet temperature is 1000 K.